THE UNIVERSITY *of* EDINBURGH

Neutron scattering studies of helicoidal magnet and 2D magnetic materials

Edmond Chan

Doctor of Philosophy
The University of Edinburgh
May 2023

Abstract

This thesis focuses on the use of complementary neutron scattering techniques to study both statics and dynamics of multiferroic $MnSb_2O_6$ and crystal and magnetic structures of 2D van der Waals magnetic materials.

The first part of this thesis is dedicated to the study of the helicoidal magnet $MnSb_2O_6$ which crystallizes in the trigonal space group $P321$. Its structural chirality is coupled to its magnetic ground state under $T_N \approx 12$ K through symmetric Heisenberg exchanges. One chapter is dedicated to neutron diffraction studies on $MnSb_2O_6$ for a detailed study of both crystal and magnetic structures. While the magnetic ground state could not be unambiguously determined, between a pure cycloidal or a mixture of cycloidal and helical order, the spin rotation plane can be tilted by the application of low external magnetic field. Subsequently, a mechanism based on the coupled structural and magnetic chiralities is proposed to explain the previously reported ferroelectric switching. The following chapter presents the study of the spin dynamics in $MnSb_2O_6$. By performing sum rules analysis on inelastic neutron scattering data, the seven exchange constants based on a Heisenberg model are extracted. Testing the stability of the spin excitations validates the cycloidal ground state.

The last part of the thesis focuses on the structures of 2D van der Waals magnets. In these materials, the magnetic properties are coupled to the stacking of the two-dimensional layers, in particular in $Fe_{3-x}GeTe_2$ and $Fe_{1+x}Te$, where the magnetism can be tuned by the iron concentration. Single crystal neutron diffraction study on $Fe_{3-x}GeTe_2$ is reported as well as spherical neutron polarimetry on $Fe_{1+x}Te$. Finally, X-ray powder diffraction results on the crystal structure of honeycomb layered VI_3 are presented.

Declaration

I declare that this thesis was composed by myself under the supervision of N. Qureshi and C. Stock, that the work contained herein is my own except where explicitly stated otherwise in the text, and that this work has not been submitted for any other degree or professional qualification except as specified.

All the projects discussed in this thesis are the results of collaborative efforts.

- Chapter III and Chapter IV - Powders and single crystals of $MnSb_2O_6$ were synthetized by J. Pásztorová, M. Songvilay and C. Stock.
- Chapter III - The neutron scattering experiments on D3 at Institut Laue-Langevin were performed by C. Stock, J. Pásztorová, M. Songvilay and N. Qureshi. The neutron scattering experiment on RITA-2 at Paul Scherrer Institute was performed by C. Stock, J. Pásztorová and Ch. Niedermeyer. The transmisson polarized optical microscopy was performed by S.-W. Cheong at Rutgers University. This work has been published in [1].
- Chapter IV - The inelastic neutron scattering experiments on MACS at NIST were performed by C. Stock, J. Pásztorová, M. Songvilay and J. A. Rodriguez-Rivera. Section IV.3.6 was composed by H. Lane and C. Stock, and reproduced in this thesis to maintain to completeness of the study. This work has been published in [2].
- Section V.1 - The single crystal neutron diffraction study characterizes samples measured by inelastic neutron scattering on MACS at NIST, performed by H. Lane, C. Stock and J. A. Rodriguez-Rivera, and by scanning tunnel microscopy, performed by C. Trainer, O. Armitage and I. Benedičič at the University of St. Andrews. The full work has been published in [3].
- Section V.3 - Sample preparation was carried out by G. Kaur and C. Stock.

(*Edmond Chan, May 2023*)

Acknowledgements

Almost four years have spent ... and time has come to acknowledge people without whom this thesis work would not have been accomplished!

First, I would like to express my gratitude to my supervisors, Dr. Chris Stock and Dr. Navid Qureshi. I thank them for giving me the opportunity to work on diverse projects, and to participate in numerous neutron scattering experiments. I thank Chris for his kindness and his involvement in my thesis. I am impressed by his enormous knowledge in condensed matter physics, both from the experimental and the theoretical points of view. I thank Navid for his technical expertise on magnetic refinement, and for his availability. His perseverance and his work efficiency are greatly inspiring.

I would like to thank the ILL staff for welcoming me during most of the time of this thesis spent in Grenoble. A special thanks for Henry Fischer and Peter Fouquet for taking care of the ILL Graduate School, as well for Maria Teresa Fernandez Diaz and Thomas Hansen for their support for the Diffraction group.

Most of the work in this thesis result from experiments in large scale facilities so I am grateful to all the scientists and technicians with whom I had the chance to work with. I would like to thank Oscar Fabelo Rosa, Clemens Ritter, Ketty Beauvois, Bachir Ouladdiaf, Anne Stunault and Jose Alberto Rodriguez Velamazan from the ILL; Bertrand Roessli, Alessandra Turrini, Marek Bartkowiak and David William Tam from PSI; Marine Verseils, Jean-Blaise Brubach and Pierre Hemme from Synchrotron SOLEIL.

I would like to thank my collaborators all around the world for fruitful discussions and scientific exchanges. Especially, I would like to thank Roger Johnson from the University College of London, for his help in my diffraction work, and Harry Lane from the University of Edinburgh, for his inputs in my inelastic work. I also thank Manila Songvilay, Laura Chaix and Sophie de Brion from the Institut Néel, for the scientific collarations, and offering me a short insight into THz spectroscopy.

Thanks Yifei and Guratinder for sharing these nice moments during my stay in Edinburgh. I hope we can all meet again in the near future around a dirty chai! Special thanks to didi Guratinder for her care, and for taking time to proofread this manuscript.

I'm glad to belong to this ILL PhD community, and would like to thank all the PhD students that I have met, from the old to the new generation, with whom I had opportunities to share unforgettable memories, from Office 110 to Buenos Aires ... Special mention to the *cuvée* 2019, Oji, Maddy, Carmen and Mo with whom I have shared almost all of my PhD time, and "younger" Fernanda and Esther, for being great support until the end of my writing time.

Merci aux BGs du BCG, pour ces super moments passés à taper des volants, et en dehors des terrains ! Vous avez certainement contribué à mon équilibre physique et mental, et je vous en suis fort reconnaissant.

Merci à papa, à maman, à tonton, à tata, à mon cousin et à ma grande soeur pour leur soutien infaillible, et pour leur confiance dans mes études. Merci d'avoir partagé votre amour et votre courage pour surmonter ces moments difficiles. Merci à la famille tout autour du globe ! 谢谢大家!

Merci Juliette d'avoir été à mes côtés pendant toutes ces années. Je ne sais pas comment j'aurais gravi tous ces sommets sans ta présence. Et j'ai hâte d'explorer ce que nous offrira la vie. Tu es mon amour, tu sais.

Bien sûr, cette thèse est l'accomplissement d'une dizaine d'années d'études, et d'une vingtaine d'années de vie. C'est donc l'occasion de remercier toutes les rencontres qui m'ont forgé.

Merci à tous, du fond du coeur.

献给爸爸

Contents

Chapter I

Introduction

I.1 Overview

Magnetism was already observed by the ancient Greek and Chinese civilizations thousands of years ago. Lodestones were discovered to attract iron, and a compass was the first magnetic technological device, using Earth's magnetic field to guide navigators for centuries [4]. Despite these uses, there was a lack of basic knowledge of this invisible force which was often attributed to mystical reasons [5]. It is only during these last two centuries that our understanding of magnetism has deepened with classical electromagnetism, followed by the theory of relativity. Quantum mechanics has successfully established the foundations of magnetism in solids aiding the exponential discovery of novel materials permitted by the immense development of experimental techniques. In particular, state-of-the-art neutron scattering has been one of the main probe for investigating magnetism in materials. Antiferromagnetic order was first observed in MnO by C. G. Shull (Nobel Prize in Physics in 1994, shared with B. N. Brockhouse) and J. S. Smart in 1949 using neutron diffraction [6], after its prediction in 1936 by Louis Néel (Nobel Prize in Physics in 1970) [7].

In parallel, fundamental research has led to numerous technological applications ranging from simple fridge magnets to magnetic levitation trains. One notable example is the discovery of the Giant Magnetoresistance effect in 1988, independently by Albert Fert [8] and Peter Grünberg [9] who shared the Nobel Prize in Physics in 2007. Depending on the relative magnetization between two thin

ferromagnetic layers sandwiching a nonmagnetic layer, the global resistance of the multilayer changes significantly. This effect is nowadays used for high-sensitive reading heads in hard disk drives, and has paved the way for spintronics, the most promising field to enhance the semiconductors industry, by exploiting the spin degree of freedom in electronics.

This motivation for engineering functional devices and the scientific interest in understanding complex quantum phenomenon would be very limited without the exploration of novel magnetic materials. Improving the energy efficiency in electronics may be a way to limit climate impact, along with political and individual decisions. High-temperature superconductors [10] are therefore promising materials, as they have no resistivity and thus, no energy loss through heating. In this thesis, we will focus on two types of materials: multiferroic and 2D magnetic materials. *Multiferroism* takes advantage of the connection between electric and magnetic orders while *2D magnetism* exhibits the strong quantum fluctuations while reducing the system dimensionality. As shown in Fig. I.1, these fields are hot topics of research, allowed by the advancements in computational power and synthesis methods, leading to more theoretical predictions, and the realization of complex compounds, along with the advances in complementary techniques to characterize the materials, and the growing number of researchers all around the world.

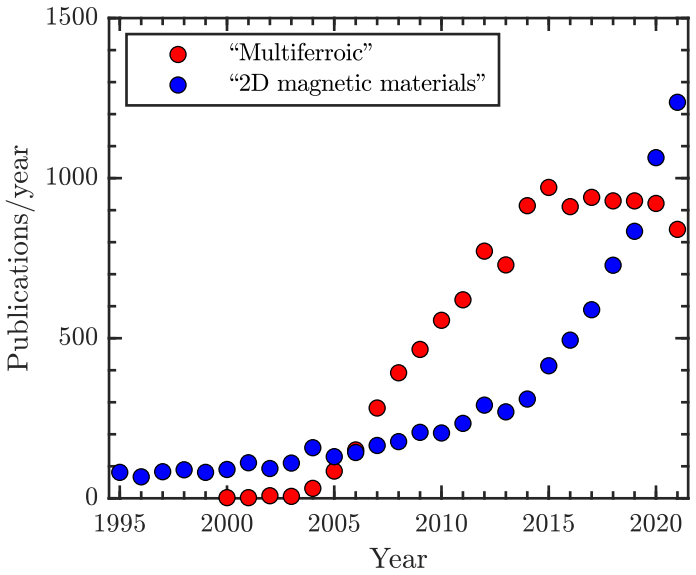

Figure I.1 Evolution of the number of publications per year referenced on Web of Science using the keywords "multiferroic" (red) and "2D magnetic materials" (blue) [11].

This thesis focuses on the characterization of multiferroic $MnSb_2O_6$ using both

neutron diffraction and spectroscopy techniques, and of several 2D magnetic materials using neutron and X-ray diffraction.

Chapter I is an introduction to multiferroics and 2D magnetism materials.

Chapter II presents the basics of the theory of neutron scattering and describes the neutron techniques utilized to accomplish the work presented in this thesis.

Chapter III shows the results of diffraction studies on multiferroic $MnSb_2O_6$. The crystal and magnetic structures are investigated in detail. While the magnetic ground state is found ambiguous, it can be manipulated by the application of an external electric field. A mechanism based on the coupled structural and magnetic chiralities is proposed to explain the previously reported ferroelectric switching. This work has been published in Ref. [1].

Chapter IV concentrates on the inelastic neutron scattering work on $MnSb_2O_6$. An analysis based on the sum rules allows to determine the seven exchange constants considering a Heisenberg model. The stability of the spin-waves is tested and was found in agreement with a cycloidal ground state. This work has been published in Ref. [2].

Chapter V focuses on the diffraction studies of 2D magnetic materials. A single-crystal neutron diffraction study on $Fe_{3-x}GeTe_2$ is reported as well as spherical neutron polarimetry on $Fe_{1+x}Te$. In these compounds, the magnetic properties are highly correlated with the iron concentration. Finally, X-ray powder diffraction results on the crystal structure of honeycomb layered VI_3 are presented. The single-crystal neutron diffraction work on $Fe_{3-x}GeTe_2$ has been combined with neutron spectroscopy and scanning tunnel microscopy studies, and published in Ref. [3].

Chapter VI summarizes the work of this thesis and gives future directions of research.

I.2 Multiferroic materials

While electric and magnetic fields are inextricably tied up by Maxwell equations in classical electromagnetism, the relation between electric and magnetic orders in solids is not obvious. The manipulation of magnetic moments by an electric field, and electric polarization by a magnetic field, known as the *magnetoelectric* effect,

was postulated by Pierre Curie in the end of the 19th century [12]. In 1959, linear magnetoelectric coupling was predicted in the antiferromagnet Cr_2O_3 [13] and experimentally observed a few years later [14, 15]. More strikingly, the complete reversal of electric polarization by the rotation of an external magnetic field was measured in boracite $Ni_3B_7O_{13}I$ in 1966 [16]. This material simultaneously displays ferroelectric and (weak) ferromagnetic orders below 64 K. According to an earlier definition [17], a material is multiferroic when it has two or more primary ferroic orders: ferroelectricity, ferromagnetism or ferroelasticity [18]. In these materials, it is possible to control the orientation states with their conjugate fields (see Fig. I.2). They are particularly interesting if a strong coupling exists between the ferroic orders. Today, the *multiferroic* term is commonly used to refer to magnetoelectric materials combining both electric and magnetic orders due to their practical promises, for example for energy-efficient electrically-driven magnetic memories [19, 20]. The definition has been extended to all kind of magnetic order such as ferrimagnetism or antiferromagnetism [21].

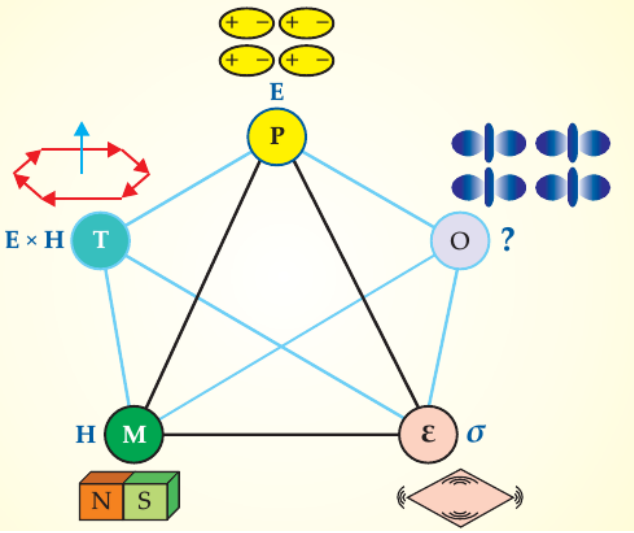

Figure I.2 Primary ferroic ordering: ferroelectricity, ferromagnetism and ferroelasticity are respectively associated to an electric polarization (**P**), magnetization (**M**) and strain ($\boldsymbol{\varepsilon}$), which can be switched by their conjugate electric (**E**), magnetic (**H**) and stress ($\boldsymbol{\sigma}$) fields. Toroidal moments **T** which can be switched by $\mathbf{E} \times \mathbf{H}$ are studied as ferrotoroidicity. *O* represents other possibilities. Figure taken from Ref. [21].

After the first experiments, the research in multiferroic materials has been poor since the 70s. The underlying principle itself was quite a contradiction, since the ferroelectric materials are favored in transition metals with empty *d* orbitals, while magnetism is held by unpaired electrons in partially filled *d* orbitals [22]. From a

symmetry point of view, ferromagnetism breaks the time-reversal symmetry but is invariant by spatial inversion, while ferroelectricity breaks inversion symmetry and is invariant by time-reversal symmetry [23]. These contradictions were raised by Hill (now Spaldin) in 2000 [22] in the paper "*Why are there so few magnetic ferroelectrics?*". This triggered the motivation for a proper understanding of these materials and some experimental breakthroughs in the following years brought a renaissance in the field [23–26]. In 2003, the electric polarization was found enhanced in thin films of $BiFeO_3$, compared to the bulk material [27]. Then, ferroelectricity induced by a magnetic order was found in orthorhombic perovskites $TbMnO_3$ in 2003 [28] and $TbMn_2O_5$ in 2004 [29]. These past twenty years, numerous multiferroic compounds were observed, and many reviews were published [30–35]. As shown in Fig. I.1, multiferroism is still a hot topic and different branches of materials are now explored for deeper understanding and observations [36].

Depending on the microscopic origin of ferroelectricity, multiferroic materials can be divided into two types [37]:

- Type-I: the phase transitions of the ferroic orders are distinct. Generally, different atoms are involved for ferroelectricity and magnetism, so that the magnetoelectric coupling is weak. However, the transition temperatures for these materials can be well above room temperature, an essential criteria for functional devices. Also, the electric polarization is often important. One example is $BiFeO_3$ which is by far the most studied multiferroic [27, 38], which becomes ferroelectric below a Curie temperature $T_C \sim 1103\,K$ and orders antiferromagnetically below a Néel temperature $T_N \sim 643\,K$ [27]. In this material, a pair of Bi^{3+} valence electrons shifts towards the FeO_6 octohedron, giving a spontaneous polarization $P \sim 100\,\mu C/cm^2$ [39]. This is known as the lone-pair mechanism.
- Type-II: the ferroelectric order is induced by a magnetic phase transition. In this case, the magnetoelectric coupling is very strong, but the net electric polarization is generally weak (up to $P \sim 0.3\,\mu C/cm^2$ in $CaMn_7O_{12}$ [40]). Furthermore, the transition temperatures are often far below room temperature. However, more and more spin-driven multiferroics have been discovered since the pioneers $TbMnO_3$ [28] and $TbMn_2O_5$ [29], and finding room temperature materials with a large electric polarization would be a great achievement.

In these type-II multiferroics, the electric polarization was often observed

in materials presenting cycloidal magnetic structures, a noncentrosymmetric ordering which is often found in frustrated magnets stabilized by the competition between the magnetic interactions [32–34, 41].

Using Ginzburg-Landau phenomenological approach, Mostovoy has derived an expression for the electric polarization $\boldsymbol{P}$ as a function of the spatial variation of the magnetization $\boldsymbol{M}$ for a cubic crystal [42]

$$\boldsymbol{P} = \gamma\chi_{\mathrm{e}}[(\boldsymbol{M}\cdot\boldsymbol{\nabla})\boldsymbol{M} - \boldsymbol{M}(\boldsymbol{\nabla}\cdot\boldsymbol{M})], \tag{I.1}$$

where γ is the coupling coefficient and χ_{e} the dielectric susceptibility. A generic expression of the magnetization is given by

$$\boldsymbol{M}(\boldsymbol{r}) = M_1\boldsymbol{e}_1\cos(\boldsymbol{k}\cdot\boldsymbol{r}) + M_2\boldsymbol{e}_2\sin(\boldsymbol{k}\cdot\boldsymbol{r}) + M_3\boldsymbol{e}_3, \tag{I.2}$$

where ($\boldsymbol{e}_1$,$\boldsymbol{e}_2$,$\boldsymbol{e}_3$) form an orthogonal basis where ($\boldsymbol{e}_1$,$\boldsymbol{e}_2$) is the spin rotation plane, M_i is the coefficient associated to each direction i, $\boldsymbol{k}$ is the propagation vector of the magnetic order.[1] If only M_1 or M_2 is non-zero, the order is a *spin-density wave*, as shown in Fig. I.3(a)-(b). If both M_1 and M_2 are non-zero, the order is *helical* for the propagation vector perpendicular to the spin rotation plane, $\boldsymbol{k} \parallel \boldsymbol{e}_3$, shown in Fig. I.3(c), or *cycloidal* for the propagation vector within the the spin rotation plane, $\boldsymbol{k} \perp \boldsymbol{e}_3$, shown in Fig. I.3(d). For an intermediate $\boldsymbol{k}$, the order is *helicoidal*,[2] and a non-zero M_3 results in *conical* magnetic structures [Fig. I.3(e)-(f)]. The average spontaneous polarization is obtained from Eqs.I.1 and I.2:

$$\langle\boldsymbol{P}\rangle = \frac{1}{V}\int \mathrm{d}^3\boldsymbol{r}\boldsymbol{P} = \gamma\chi_{\mathrm{e}}M_1M_2(\boldsymbol{e}_3\times\boldsymbol{k}). \tag{I.3}$$

From this, we can see that the polarization only exists for non-zero M_1 and M_2. Also the $\boldsymbol{k} \perp \boldsymbol{e}_3$ term excludes helical order. As a result, the net electric polarization only occurs for cycloidal order, or more precisely for magnetic structures having a cycloidal component, which includes helicoidal order (when

[1] A description of magnetic structures is given in Appendix B.

[2] The nomenclature of magnetic structures can be confusing in the literature. *Spiral* magnets usually include all kind of orders described by Eq. (I.2) [41], but sometimes only refer to helical order [43]. However, *helical* and *cycloidal* orders are unambiguously defined, and in this thesis, the *helicoidal* order refers to the mixture of both orders [33].

it is not purely a helix), and transverse conical order. In this case, the electric polarization lies in the elliptical rotation plane of the cycloidal component. These situations are summarized in Fig. I.3.

$$\langle \boldsymbol{P} \rangle \propto M_1 M_2 \boldsymbol{k} \times \boldsymbol{e}_3$$

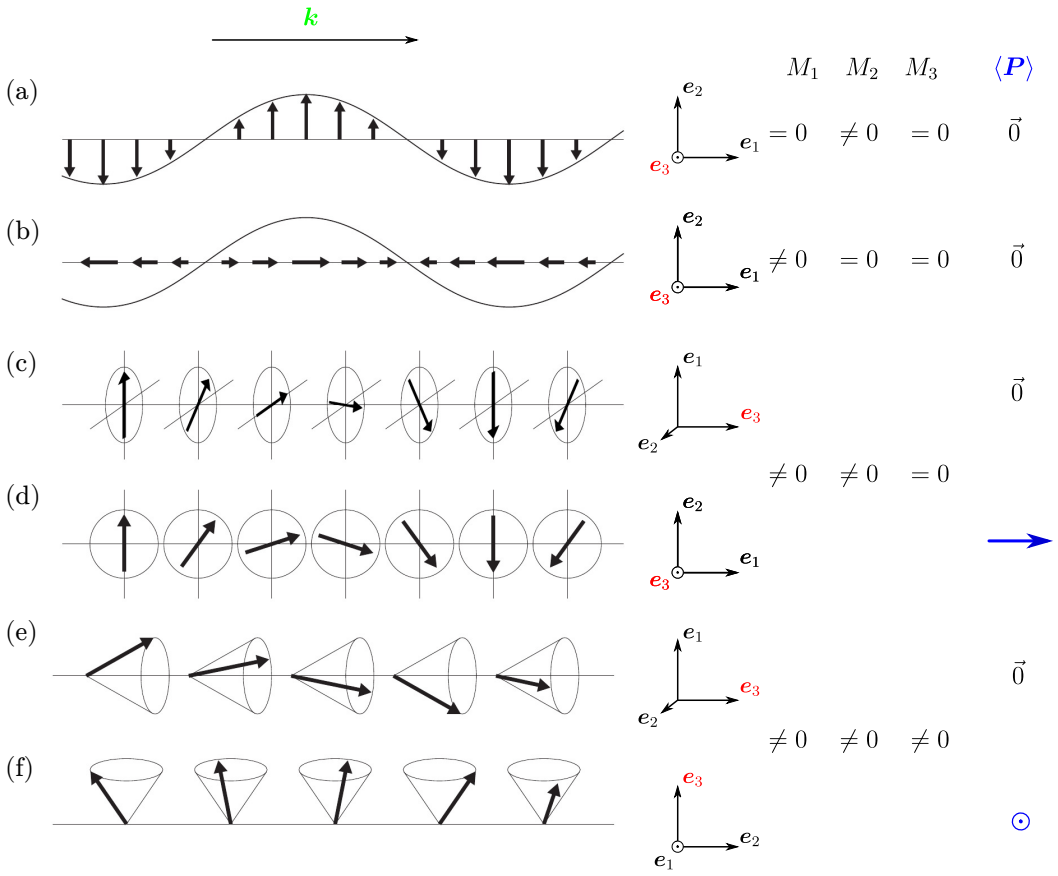

Figure I.3 Different magnetic structures and the resulting electric polarization for (a) a transverse spin-density wave, (b) a longitudinal spin-density wave, (c) a helix (proper screw), (d) a cycloid, (e) a longitudinal cone (helix with a ferromagnetic component), (f) a transverse cone (cycloid with a ferromagnetic component). Figure adapted from Ref. [44].

Two microscopic mechanisms at the origin of electric polarization in noncollinear orders were proposed, arising from spin current [45], and from the antisymmetric exchange interaction [46].

The motion of an electric dipole produces a magnetic field perpendicular to both the direction of motion and the electric polarization. By duality in electromagnetism, the motion of a magnetic dipole, equivalent to a spin current induces an electric polarization [45]. Based on this principle, Katsura, Nagaosa & Balatsky (KNB) proposed that the spin current $\boldsymbol{j}_\mathrm{s} \propto \boldsymbol{S}_i \times \boldsymbol{S}_j$ between noncollinear

spins $\boldsymbol{S}_i$ and $\boldsymbol{S}_j$, connected by the vector $\boldsymbol{e}_{ij}$, induces an electric polarization [47]

$$\boldsymbol{P} \propto \boldsymbol{e}_{ij} \times \boldsymbol{j}_{\mathrm{s}} \propto \boldsymbol{e}_{ij} \times (\boldsymbol{S}_i \times \boldsymbol{S}_j). \tag{I.4}$$

The spin current is obtained from the Heisenberg equation of motion of the spin operator in presence of spin-orbit interaction [32]. This spin current model, or KNB model, is illustrated in Fig. I.4(a) for a superexchange interaction between magnetic ions M1 and M2 with noncollinear spins. The consideration of spin-orbit interaction affects the hybridization between the d orbitals of the magnetic ions and the p orbitals of the oxygen ion resulting in a spin current and therefore an electric polarization [47]

$$\boldsymbol{P} \propto \left(\frac{V}{\Delta}\right)^3 I \boldsymbol{e}_{12} \times (\boldsymbol{S}_1 \times \boldsymbol{S}_2), \tag{I.5}$$

where $I = \langle p_x | \, z \, | d_{xy} \rangle$ is the matrix element, Δ and V are the energy difference and hybridization energy between the orbitals.

(a) Spin current mechanism (b) Inverse Dzyaloshinskii-Moriya mechanism

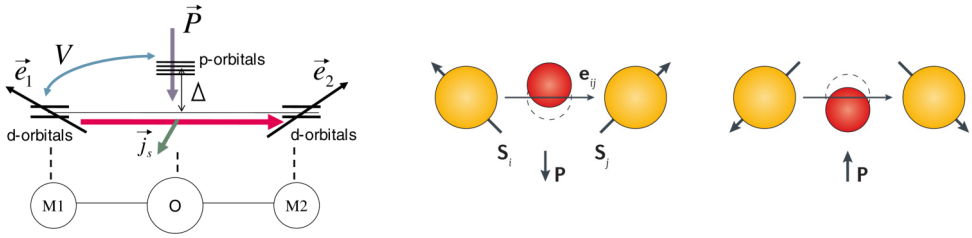

Figure I.4 (a) Spin-current mechanism. Figure taken from Ref. [47]. (b) Inverse Dzyaloshinksii-Moriya mechanism, for two spin configurations leading to different displacements of ions. Figure taken from Ref. [35].

Another mechanism is based on the Dzyaloshinskii-Moriya (DM) interaction [48, 49]. This antisymmetric exchange comes from the relativistic correction to exchange interactions due to spin-orbit coupling, whose Hamiltonian is [50]

$$\hat{\mathcal{H}}_{\mathrm{DM}} = \boldsymbol{D}_{ij} \cdot (\boldsymbol{S}_i \times \boldsymbol{S}_j), \tag{I.6}$$

where $\boldsymbol{D}_{ij}$ is the DM interaction vector between spins $\boldsymbol{S}_i$ and $\boldsymbol{S}_j$, antisymmetric by exchanging indices $i \leftrightarrow j$. This vector is determined by the symmetry of the

system [49, 50]. It vanishes when the crystal field fulfills inversion symmetry with respect to the center between the two magnetic ions. In the absence of inversion symmetry, $\boldsymbol{D}_{ij}$ favors the canting of the neighboring spins. For a perovskite $AB\mathrm{O}_3$ (where B is a magnetic ion), the B-O-B bond is straight in the ideal case (cubic symmetry), but any structural distortion could shift the oxygen ion from the central position, bending the B-O-B bond and giving rise to a DM interaction vector, constrained by symmetry to be [34]

$$\boldsymbol{D}_{ij} \propto \boldsymbol{e}_{ij} \times \boldsymbol{d}_0, \tag{I.7}$$

where $\boldsymbol{e}_{ij}$ is the vector connecting the magnetic ions, and $\boldsymbol{d}_0$ the displacement of the oxygen ion from the central position.

Inversely, noncollinear neighboring spins, for example stabilized by frustration, can favor the displacement of the intermediate ion (typically O^{2-}) in order to minimize the DM energy, as proposed by Sergienko and Dagotto [46]. This can be seen as a fixed spin configuration $\boldsymbol{S}_i \times \boldsymbol{S}_j$ would result in a change in $\boldsymbol{d}_0 \propto \boldsymbol{e}_{ij} \times (\boldsymbol{S}_i \times \boldsymbol{S}_j)$ in Eq. (I.7), to minimize the energy in Eq. (I.6). Hence, this ionic shift of the charge distribution induces an electric polarization

$$\boldsymbol{P} \propto \boldsymbol{e}_{ij} \times (\boldsymbol{S}_i \times \boldsymbol{S}_j). \tag{I.8}$$

This is the inverse DM mechanism, illustrated in Fig. I.4, for two configurations of the spins.

While the inverse DM mechanism is based on a ionic shift, the spin current mechanism is based on the electronic orbitals, but both are based on spin-orbit interaction which makes the induced electric polarization generally small. The effects are similar and in principle, the mechanisms can simultaneously be at the origin of ferroelectricity [34]. In agreement with the phenomenological approach [Eq. (I.3)], a uniform electric polarization only arises in cycloidal magnets. This has been experimentally probed in numerous materials such as the orthorhombic manganites perovskites $R\mathrm{MnO}_3$ (where R = Tb, Dy, Gd) [28, 32, 33]. Also Eq. (I.8) immediately shows the role of the spin vector chirality $\boldsymbol{S}_i \times \boldsymbol{S}_j$ on the electric polarization. Indeed, together with $\boldsymbol{e}_{ij}$, the spin rotation plane gives the direction of the polarization, while the sense of rotation of the spins gives the sign of the polarization along this direction. From this, ferroelectric switching can be

induced by manipulating the magnetic ground state, or by favoring magnetic domains, using an external electric or magnetic field [51–54].

Spin-orbit coupling is also at the origin of the metal-ligand hybridization mechanism. In contrast to the mechanisms described above which implies two magnetic ions, only a single magnetic ion is implied in this case to create a local dipole along the bond direction with the ligand. This mechanism was proposed to be at the origin of the observed electric polarization in the triangular lattice magnet $CuFeO_2$ with a helical order [55]. Moreover, electric polarization can be induced in collinear magnets by exchange striction where the ions shift to minimize symmetric Heisenberg exchanges, for example in the Ising chain magnet Ca_3CoMnO_6 [56].

Multiferroic materials feature complex mechanisms, which are highly dependent on the magnetic structure and the local environment surrounding the magnetic ions. Also the relation between the crystal structure and the underlying magnetoelectric properties can be determining factors. Bulk investigations are therefore essential to have a complete understanding of these systems.

In this thesis we will present results from neutron scattering experiments on the multiferroic candidate $MnSb_2O_6$, which displays a (debated) cycloidal order [57, 58]. Chapter III is dedicated to the diffraction studies of its crystal and magnetic structures, while Chapter IV is focused on the determination of the Heisenberg exchange constants by applying sum rules analysis on inelastic neutron scattering data.

I.3 2D magnetic materials

The experimental realization of graphene in 2004 [59] has provoked the discovery of innumerable 2D materials and brought a boon to this field of research [60–63]. These materials are composed of atomic structures held by strong covalent bonding within 2D layers, and weak van der Waals (vdW) forces along the third direction perpendicular to these layers. This makes them easily cleavable, and even exfoliated down to monolayers by simply using adhesive tape [60]. The variety of electronic, mechanical and optical properties in this class of materials, and the possibility to combine or to create new properties by building heterostructures makes a sandbox for investigating novel physics and engineering

functional devices such as tunnelling transistors, flexible electronics or light-emitting diodes [64–66].

From a fundamental point of view, reducing the dimensionality of a system enhances quantum fluctuations, allowing the observation of new phases and phenomena. Formalized in 1966, the Mermin-Wagner theorem [67] states that long-range magnetic ordering is forbidden in two dimensions for an isotropic Heisenberg system at finite temperature. Indeed, the continuous symmetry leads to gapless spin excitations with a finite density of states. Together with the diverging Bose-Einstein statistics at zero energy and finite temperature, this results in massive thermal fluctuations suppressing any long-range magnetic order. To stabilize a magnetic order, anisotropy is therefore needed to open up a gap in the magnon spectrum and to counter the thermal fluctuations [68]. On the other hand, in 1944, Onsager solved exactly the Ising model in a 2D square lattice, predicting a possible magnetic phase transition at finite temperatures [69]. In the past decades, the study of magnetism in low dimensions has been limited to epitaxy-grown ultrathin magnetic films [70], but their magnetic properties were strongly altered by the interaction with the substrates and the quality of the interfaces [71]. Nonmagnetic 2D materials have been also tuned by introducing vacancies to create local magnetic moments, by applying an electric field to change the band structure, or by building heterostructures with adjacent magnetic materials to transfer their properties by magnetic proximity [72]. However, this results in local or extrinsic magnetic responses [72], and the intrinsic 2D vdW magnetic materials have been only investigated in their bulk form [73] which are only approximate 2D lattices. For a long time, despite the measurements of magnetic order in several bulk 2D materials and some theoretical predictions of their stability down to a monolayer, there was no experimental realization measuring magnetism in monolayers [74].

Things started to evolve in 2016 [68], when Raman measurements indirectly probed magnetism down to a few layers and monolayers of $NiPS_3$ [75] and monolayers of $CrSiTe_3$ [76] and $FePS_3$ [77–79]. But the real beginning of the exploration of "*magnetism in flatland*" [80] is the direct experimental observation in 2017 by magneto-optical Kerr effect (MOKE) microscopy of ferromagnetism order down to a monolayer of CrI_3 [81] and a bilayer of $Cr_2Ge_2Te_6$ [82]. While having similar bulk properties like a Curie temperature $T_C = 61\,K$ below which they become soft ferromagnets, the properties diverge while reducing the dimensionality of both systems. The ferromagnetic (FM) order persists down to

monolayer CrI_3, which is well described by a 2D Ising model with a perpendicular anisotropy, somehow validating Onsager's solution [69]. In accordance with increased fluctuations in low dimensions, the ordering temperature is decreased to $T_C = 45\,K$. In addition, the magnetic order seems layer-dependent, as no magnetization was measured in a bilayer of CrI_3 until a critical applied magnetic field, suggesting an antiferromagnetic coupling between the two layers, while the ferromagnetic order is retrieved in a trilayer of CrI_3 [81]. Similarly, the Curie temperature of $Cr_2Ge_2Te_6$ decreases with the number of layers. In MOKE measurements, a small magnetic field is usually applied to pin the magnetic moments and prevent from the formation of ferromagnetic domains. Contrary to bulk materials, in which this field does not play much on the observed properties [71], the transition temperature could be tuned by varying the value B of the applied magnetic field in low-layer $Cr_2Ge_2Te_6$ samples. For $B = 0.065\,T$, the bilayer sample undergoes a FM transition around $T_C^* = 28\,K$, which could be increased to $T_C^* = 44\,K$ for $B = 0.3\,T$. The anisotropy was estimated to be very small, which makes $Cr_2Ge_2Te_6$ behave nearly like a 2D Heisenberg magnet. In accordance with the Mermin-Wagner theorem [67], magnetic order was not found in a monolayer (which is an ideal 2D lattice) down to the lowest temperature of the measurement, $T = 4.7\,K$ [82].

These two experiments illustrate the strong dependence of the magnetic properties on the number of layers (reflecting the closeness to an ideal 2D lattice), and also the importance of anisotropy to stabilize magnetic order against enhanced thermal fluctuations in low dimensions, in agreement with the theoretical predictions [67, 69]. This triggers the exponential research in intrinsic 2D magnetic materials [68, 72, 83–85]. As for the nonmagnetic van der Waals compounds, this new class of materials provides a wide range of physical properties, from metallic ferromagnets such as Fe_3GeTe_2 [86] to antiferromagnetic insulator such as $FePS_3$ [79]. Multiferroic 2D materials were also predicted theoretically, but still awaiting for an experimental realization [87, 88]. The ultimate goal is to find a high ordering temperature 2D material with high stability under ambient conditions which can be implemented in functional devices in spintronics or magnonics [72]. In order to achieve this, several directions have been proposed, such as enhancing both exchange interactions and magnetocrystalline anisotropy. This can be done by looking for new bulk materials, for example based on $4d$ or $5d$ transition metals which have been relatively unexplored compared to materials based on $3d$ transition metals [84, 85]. Owing to stronger spin-orbit coupling whose interaction with the crystal fields

results in strong single-ion magnetic anisotropy, magnetic ordering at higher temperature could be stabilized in these compounds [85]. The high sensitivity of 2D materials to external constraints such as strain, light, electric and magnetic fields along with the ability to introduce defects or to intercalate atoms or molecules in the vdW gaps gives another direction of research. Furthermore, designing vdW heterostructures [68, 84] expands ever greater the possibilities of investigating new physics and creating new devices. In addition, this constitutes a playground to broaden the understanding in more exotic phases such as quantum spin liquids, topological insulators, unconventionnal superconductors or skyrmions [83].

Alongside the development of computing power allowing faster and more sophisticated *ab-initio* calculations, the experimental achievements were allowed by the improvement of sample preparation, from the synthesis aspect with higher quality chemical vapor transport and molecular beam epitaxy, to accurate micromechanical cleavage techniques [84]. A wide range of optical and electrical methods were also developed or adapted to study magnetism in 2D materials [84, 85]. Yet, it is essential to understand the origin of magnetism in the bulk materials in order to compare the properties down to a few layers. Being sensitive to the magnetic moments and magnetic excitations, neutron scattering remains a powerful probe for 2D magnetism. Diffraction (neutron or X-ray) is also necessary in order to accurately establish the crystal structures which are highly correlated to the magnetic properties.

Chapter V will present the diffraction studies of several 2D magnetic materials: $Fe_{3-x}GeTe_2$, $Fe_{1+x}Te$ and VI_3.

Chapter II

Neutron scattering techniques

Since the discovery of the neutron by James Chadwick in 1932 [89] and the early experiments in 1936 probing Bragg diffraction by crystals, neutron scattering has been facilitated by the development of neutron reactors providing more and more flux [90, 91]. Decades of research and improvement of the facilities and instruments have made neutron scattering techniques among the most useful probes in condensed matter, accredited by awarding the Nobel Prize in Physics to Clifford Shull and Bertram Brockhouse in 1994 for their respective contributions to elastic [6] and inelastic [92] neutron scattering.

Most of the experimental results from this thesis were obtained by using neutron scattering techniques. In this chapter, the basic properties of neutrons will be introduced, followed by an overview of neutron scattering theory, covering both nuclear and magnetic scattering, with a focus on polarized neutrons scattering. Finally, we will focus on the techniques and instruments used during this thesis. Definitions and conventions in the equations are introduced here and adopted in the rest of the manuscript. More exhaustive details on neutron scattering can be found in numerous textbooks [93–99].

II.1 Introduction to neutron scattering

II.1.1 Properties and advantages of neutrons

A neutron is an electrically neutral particle composed of one up quark and two down quarks. From the quantum mechanics perspective, a neutron follows wave-particle duality. The momentum $\boldsymbol{p} = \hbar\boldsymbol{k}$ of a neutron, where $\hbar = h/2\pi$ is the reduced Planck constant, and $\boldsymbol{k}$ is the neutron wavevector, is therefore related to its de Broglie wavelength $\lambda = h/|\boldsymbol{p}|$. As a consequence, the kinetic energy E of a non-relativistic neutron with mass m_n is given by

$$E = \frac{h^2}{2m_\mathrm{n}\lambda^2} = \frac{\hbar^2 k^2}{2m_\mathrm{n}} = k_\mathrm{B}T \tag{II.1}$$

where k_B is Boltzmann constant, and T is the temperature corresponding to the neutron energy. This energy is usually given in units of meV but can be easily converted into a temperature T in K, its speed v in km/s, its wavevector norm k in Å^{-1} and its wavelength λ in Å with the relation:

$$E = 0.08617\ T = 5.227\ v^2 = 2.072\ k^2 = 81.81/\lambda^2. \tag{II.2}$$

Thanks to their fundamental properties, summarized in Table II.1, neutrons are suitable for various experimental investigations for condensed matter [98]:

- Neutrons produced for scattering experiments have typical de Broglie wavelength of several Å (see Table II.2). This corresponds to the interatomic distances in condensed matter, allowing interference effects and thus the extraction of structural information from the material.
- For these wavelengths, the energies of neutrons are much lower than X-rays, and are comparable to the energy of elementary excitations in condensed matter. Hence, dynamical studies allow to study phonons and magnons.
- As neutrons are chargeless particles, there is no Coulomb interaction with the electron cloud of the atoms. This enables them to penetrate deeply and non-destructively into matter and investigate the bulk properties of materials. It is also easier to operate neutron scattering under extreme conditions (high pressure, very low and very high temperatures, high magnetic and electric fields ...) because the shielding involves low loss of

neutrons.

- X-rays interact with the electron cloud, so the scattering cross section is almost varying linearly as a function of the atomic number. On the contrary, neutron scattering is based on the strong nuclear interaction with the atomic nucleus. Therefore, the neutron cross sections vary irregularly due to their strong dependence on the details of the individual nuclear interaction. This allows to distinguish chemical elements with close atomic numbers and also isotopes.
- Finally, neutrons are an outstanding probe of magnetism in condensed matter because they possess a magnetic moment which allows the interaction with the unpaired electrons of magnetic atoms. Neutron beams can further be polarized in order to provide more detailed study and solve complex magnetic structures.

These features make neutron scattering techniques widely used for the study of condensed matter, but also in other fields like nuclear physics, engineering, soft matter and biology.

Table II.1 Basic properties of neutrons. Table adapted from Ref. [99].

Properties	Values
Mass	$m_\mathrm{n} = 1.675 \times 10^{-27}\,\mathrm{kg}$
Charge	$0\,\mathrm{C}$
Spin	$1/2$
Magnetic moment	$1.913\ \mu_\mathrm{N}$
Mean lifetime[1]	$\tau_\mathrm{n} = 878.4(5)\,\mathrm{s}$

II.1.2 Neutron production

Neutrons used for scattering experiments in large-scale facilities are produced in two kinds of sources: nuclear reactors and spallation sources [99]. Nuclear reactors are the historical sources, based on the fission of heavy nuclei like ${}^{235}_{92}\mathrm{U}$ isotopes in a chain reaction:

$$ {}^{235}_{92}\mathrm{U} + {}^{1}_{0}\mathrm{n} \longrightarrow {}^{236}_{92}\mathrm{U} \longrightarrow \mathrm{X} + \mathrm{Y} + N\,{}^{1}_{0}\mathrm{n}. \tag{II.3} $$

[1]The neutron lifetime is classically measured with the beam and the bottle methods, leading in average to $\tau_\mathrm{n} = 879.4(6)\,\mathrm{s}$ and $\tau_\mathrm{n} = 888(2)\,\mathrm{s}$ [100]. It is still unclear whether this 8.6 s difference comes from systematic errors in the experiments, or from unknown physical phenomena. The value in the table is given by the Particle Data Group in 2022 [101].

The $^{235}_{92}$U nucleus absorbs one neutron, and generally splits into 2 lighter elements X and Y, with the release of N neutrons, 2.5 in average. The reaction is self-sustained and a fraction of the produced neutrons with a typical kinetic energy of 2 MeV are released from the reactor core. These neutrons must be slowed down by a moderator in order to be suitable for scattering experiments. A moderator is a medium in which the neutrons are having multiple collisions with the particles, transferring their energy until reaching thermal equilibrium. After that, the neutron energy follows a Maxwell-Boltzmann distribution, whose peak energy density is determined by the moderator temperature. The neutrons coming from these moderators are classified by cold, thermal and hot depending on their energy. This is shown in Table II.2 with typical moderators liquid hydrogen, water and heated graphite used for each range of neutron energy.

Table II.2 Types of neutron sources with their energy and corresponding wavelength ranges (approximative), achieved by a typical moderator at a specific temperature.

Source	Energy	Wavelength	Typical moderator and temperature
Cold	$[0.1, 10]$ meV	$[3, 30]$ Å	H_2, D_2, $T \approx 25$ K
Thermal	$[10, 100]$ meV	$[1, 3]$ Å	H_2O, D_2O, $T \approx 300$ K
Hot	$[100, 500]$ meV	$[0.4, 1]$ Å	graphite, $T \approx 2400$ K

The Institut Laue Langevin (ILL, Grenoble, France) is the most powerful source with its 58 MW high flux reactor (Fig. II.1) producing a continuous flux of neutrons of $1.5 \times 10^{15}\,\mathrm{cm^{-2}s^{-1}}$ delivered to over 40 instruments. The National Institute of Standards and Technology (NIST) through its Center for Neutron Research (NCNR, Gaithersburg, United States) operates a 20 MW reactor for a suite of 30 instruments.

In spallation sources, heavy nuclei (such as tungsten, mercury or lead) are bombarded by high-energy protons (> 1 GeV). Those protons are accelerated by means of different methods: linear accelerators (linacs), cyclotrons and synchrotrons. The target nucleus absorbs the high-energy proton and goes into a short unstable excited state before decaying, emitting around 30 neutrons per incident proton. Similarly to reactor sources, the produced neutrons are thermalized through moderators before being transported to instruments via the beam tubes. Most of the spallation sources, like ISIS (Didcot, United Kingdom) produce pulsed neutron beams due to the periodic accelaration of protons. SINQ at Paul Scherrer Institute (PSI, Villigen, Switzerland) is an exception as it uses a cyclotron with a frequency high enough to produce a

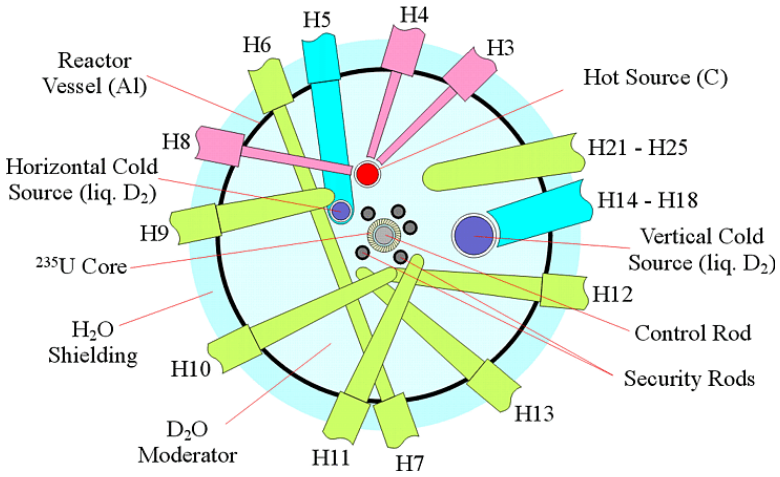

Figure II.1 Schematic of the ILL reactor, with beam tubes connected to cold (blue), thermal (green) and hot (red) sources. Figure taken from Ref. [102].

continuous beam. Despite having a peak neutron flux much higher than in the reactor sources, the time-averaged flux is significantly lower in spallation sources. But the tendency is changing by recent technological improvements while the development of continuous reactor sources is reaching a plateau. The next generation European Spallation Source (ESS, Lund, Sweden) will have a time-averaged neutron flux comparable to the ILL.

II.1.3 Scattering cross section

During a neutron scattering experiment, an incident beam of neutrons with initial wavevector $\boldsymbol{k}_\mathrm{i}$ energy E_i and spin state σ_i interacts with a sample from which the neutron beam scatters. In this thesis, we will focus on crystalline solids, but the sample might be in general, an amorphous solid, a liquid or a gas. In the typical scattering geometry shown in Fig. II.2, a neutron detector counts the scattered neutrons in a solid angle $\mathrm{d}\Omega$ around the neutron final wavevector $\boldsymbol{k}_\mathrm{f}$ in the direction $(2\theta, \phi)$. The intensity measured by the detector is proportional to the partial differential cross section defined as

$$\frac{\mathrm{d}^2\sigma}{\mathrm{d}\Omega\,\mathrm{d}E_\mathrm{f}} = \frac{\begin{array}{c}\text{neutrons scattered per second into } \mathrm{d}\Omega \\ \text{with energy between } E_\mathrm{f} \text{ and } E_\mathrm{f} + \mathrm{d}E_\mathrm{f}\end{array}}{\phi\,\mathrm{d}\Omega\,\mathrm{d}E_\mathrm{f}}, \tag{II.4}$$

where ϕ is the flux of incident neutrons. With this definition, the cross section

σ has the dimension of an area as expected, typically expressed in units of barns (1 barn $= 10^{-24}\,\mathrm{cm}^2$).

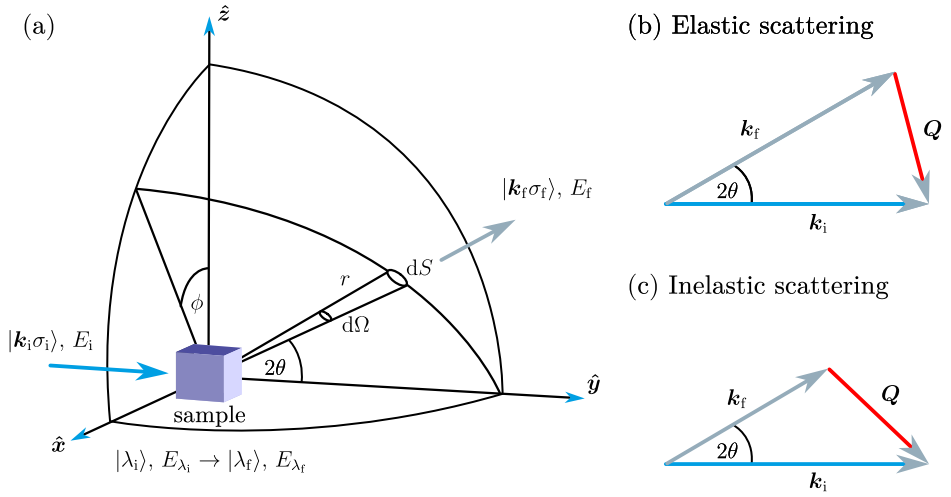

Figure II.2 (a) Classical geometry for a scattering experiment: an incident neutron beam with wavevector $\boldsymbol{k}_\mathrm{i}$ scatters from a sample. A detector is placed in direction $(2\theta, \phi)$, delimited by a solid angle $d\Omega$. Figure adapted from Ref. [93]. Scattering triangle for (b) elastic scattering where $|\boldsymbol{k}_\mathrm{i}| = |\boldsymbol{k}_\mathrm{f}|$ and (c) inelastic scattering where $|\boldsymbol{k}_\mathrm{i}| \neq |\boldsymbol{k}_\mathrm{f}|$.

During the scattering process, the sample goes from initial state λ_i with energy E_{λ_i} to final state λ_f with energy E_{λ_f} with the momentum transfer[2]

$$\boldsymbol{Q} = \boldsymbol{k}_\mathrm{i} - \boldsymbol{k}_\mathrm{f}, \tag{II.5}$$

and an energy transfer

$$E = \hbar\omega = E_\mathrm{i} - E_\mathrm{f} = E_{\lambda_\mathrm{f}} - E_{\lambda_\mathrm{i}}, \tag{II.6}$$

by conservation of the total energy. The scattering is said elastic when no energy is transferred to the sample ($\hbar\omega = 0$). In this case diffraction techniques allow the structural study of materials. When the energy transfer is non-zero, the scattering is said inelastic, and spectroscopy techniques allow to study dynamical properties of matter. $\boldsymbol{Q}$ is commonly named the scattering vector and represented by the scattering triangle in Fig. II.2(b) for elastic scattering and Fig. II.2(c) for inelastic scattering. The scattering angle 2θ is by convention two times the Bragg

[2]We note that the scattering vector can also be defined as the momentum transferred from the sample to the neutron, in this case $\boldsymbol{Q} = \boldsymbol{k}_\mathrm{f} - \boldsymbol{k}_\mathrm{i}$.

reflection angle θ defined later in Fig. II.3.

Considering all the processes which transform the total system (neutron+sample) from initial states $|\boldsymbol{k}_\mathrm{i}\sigma_\mathrm{i}\lambda_\mathrm{i}\rangle$ to final states $|\boldsymbol{k}_\mathrm{f}\sigma_\mathrm{f}\lambda_\mathrm{f}\rangle$, the partial differential cross section can be expressed using Fermi's Golden rule in the first Born approximation:[3]

$$\left(\frac{\mathrm{d}^2\sigma}{\mathrm{d}\Omega\,\mathrm{d}E_\mathrm{f}}\right)_{\boldsymbol{k}_\mathrm{i}\to\boldsymbol{k}_\mathrm{f}} = \frac{k_\mathrm{f}}{k_\mathrm{i}}\left(\frac{m_\mathrm{n}}{2\pi\hbar^2}\right)^2 \sum_{\lambda_\mathrm{i}\sigma_\mathrm{i}} p_{\lambda_\mathrm{i}} p_{\sigma_\mathrm{i}} \sum_{\lambda_\mathrm{f}\sigma_\mathrm{f}} \left|\langle \boldsymbol{k}_\mathrm{f}\sigma_\mathrm{f}\lambda_\mathrm{f}|\,\hat{V}\,|\boldsymbol{k}_\mathrm{i}\sigma_\mathrm{i}\lambda_\mathrm{i}\rangle\right|^2 \delta(\hbar\omega + E_{\lambda_\mathrm{i}} - E_{\lambda_\mathrm{f}}), \tag{II.7}$$

where $\hat{V}$ is the interaction potential operator of the neutrons with the sample which describes the scattering processes, and the Dirac function corresponds to the energy conservation law. The sum is over the sample final states λ_f and the neutron beam final spin state σ_f, and the cross section is averaged over the initial states λ_i of the sample with the weight

$$p_{\lambda_\mathrm{i}} = \frac{\mathrm{e}^{-E_{\lambda_\mathrm{i}}/k_\mathrm{B}T}}{\sum_{\lambda_\mathrm{i}} \mathrm{e}^{-E_{\lambda_\mathrm{i}}/k_\mathrm{B}T}}, \tag{II.8}$$

when the sample is in thermal equilibrium, following the Boltzmann distribution, and the neutron beam initial spin state σ_i with probability p_{σ_i}

Equation II.7 is called the master equation as it rules all the processes encountered during a scattering experiment. The next step of the calculation relies on the matrix element depending on the interaction potential. In condensed matter, neutrons are scattered by the nuclei and from unpaired electrons of magnetic atoms. Thus, the interaction potential can be separated into one part corresponding to nuclear scattering, and the other part corresponding to magnetic scattering.

[3]The theory of scattering by a potential is derived using perturbation theory. For a weak potential, the Born expansion can be limited to the first order which corresponds to single scattering processes. In this case the scattering amplitude is the Fourier transform of the interaction potential as incident and scattered neutrons are considered as plane waves.

II.1.4 Correlation functions

Before focusing on nuclear and magnetic scattering, we can simplify the summation from the master equation. Let's consider any operator $\hat{\mathcal{O}}$ acting on the sample states, we want to evaluate:[4]

$$\sum_{\lambda_\mathrm{i}\lambda_\mathrm{f}} p_{\lambda_\mathrm{i}} \langle\lambda_\mathrm{i}|\, \hat{\mathcal{O}}^\dagger\, |\lambda_\mathrm{f}\rangle\langle\lambda_\mathrm{f}|\, \hat{\mathcal{O}}\, |\lambda_\mathrm{i}\rangle\, \delta(\hbar\omega + E_{\lambda_\mathrm{i}} - E_{\lambda_\mathrm{f}}). \tag{II.9}$$

The Dirac function can be expressed in its integral representation:

$$\delta(\hbar\omega + E_{\lambda_\mathrm{i}} - E_{\lambda_\mathrm{f}}) = \frac{1}{2\pi\hbar}\int_{-\infty}^{+\infty} \mathrm{d}t\, \mathrm{e}^{-\mathrm{i}\omega t}\mathrm{e}^{\mathrm{i}(E_{\lambda_\mathrm{f}}-E_{\lambda_\mathrm{i}})t/\hbar}. \tag{II.10}$$

Then introducing the Hamiltonian $\hat{\mathcal{H}}$ of the scattering system for which the $|\lambda\rangle$ are eigenstates with eigenvalues E_λ, we have $\mathrm{e}^{-\mathrm{i}\hat{\mathcal{H}}t/\hbar}\,|\lambda_\mathrm{i}\rangle = \mathrm{e}^{-\mathrm{i}E_{\lambda_\mathrm{i}}t/\hbar}\,|\lambda_\mathrm{i}\rangle$ and $\langle\lambda_\mathrm{f}|\,\mathrm{e}^{\mathrm{i}\hat{\mathcal{H}}t/\hbar} = \langle\lambda_\mathrm{f}|\,\mathrm{e}^{\mathrm{i}E_{\lambda_\mathrm{f}}t/\hbar}$, combining the two previous equations gives:

$$\frac{1}{2\pi\hbar}\int_{-\infty}^{+\infty} \mathrm{d}t\, \mathrm{e}^{-\mathrm{i}\omega t}\sum_{\lambda_\mathrm{i}\lambda_\mathrm{f}} p_{\lambda_\mathrm{i}} \langle\lambda_\mathrm{i}|\, \hat{\mathcal{O}}^\dagger\, |\lambda_\mathrm{f}\rangle\langle\lambda_\mathrm{f}|\, \mathrm{e}^{\mathrm{i}\hat{\mathcal{H}}t/\hbar}\hat{\mathcal{O}}\mathrm{e}^{-\mathrm{i}\hat{\mathcal{H}}t/\hbar}\, |\lambda_\mathrm{i}\rangle\,. \tag{II.11}$$

Using closure relation over the final states, and the Heisenberg representation operator $\hat{\mathcal{O}}(t) = \mathrm{e}^{\mathrm{i}\hat{\mathcal{H}}t/\hbar}\hat{\mathcal{O}}\mathrm{e}^{-\mathrm{i}\hat{\mathcal{H}}t/\hbar}$, with $\hat{\mathcal{O}}(0) = \hat{\mathcal{O}}$, this gives:

$$\frac{1}{2\pi\hbar}\int_{-\infty}^{+\infty} \mathrm{d}t\, \mathrm{e}^{-\mathrm{i}\omega t}\sum_{\lambda_\mathrm{i}} p_{\lambda_\mathrm{i}} \langle\lambda_\mathrm{i}|\, \hat{\mathcal{O}}^\dagger\hat{\mathcal{O}}(t)\, |\lambda_\mathrm{i}\rangle = \frac{1}{2\pi\hbar}\int_{-\infty}^{+\infty} \mathrm{d}t\, \mathrm{e}^{-\mathrm{i}\omega t}\left\langle \hat{\mathcal{O}}(0)^\dagger\hat{\mathcal{O}}(t)\right\rangle, \tag{II.12}$$

where $\left\langle \hat{\mathcal{O}}^\dagger\hat{\mathcal{O}}(t)\right\rangle = \sum_{\lambda_\mathrm{i}} p_{\lambda_\mathrm{i}} \langle\lambda_\mathrm{i}|\, \hat{\mathcal{O}}^\dagger\hat{\mathcal{O}}(t)\, |\lambda_\mathrm{i}\rangle$ is the correlation function corresponding to the thermal statistical average of the operator $\hat{\mathcal{O}}^\dagger\hat{\mathcal{O}}(t)$.

[4] $\hat{\mathcal{O}}^\dagger$ is the adjoint operator of $\hat{\mathcal{O}}$.

II.2 Nuclear scattering

Neutron scattering from nuclei is due to the strong interaction and can be approximated by the Fermi pseudo-potential:[5]

$$\hat{V}_{\mathrm{N}}(\boldsymbol{r}) = \frac{2\pi\hbar^2}{m_{\mathrm{n}}} \sum_j b_j \delta(\boldsymbol{r} - \hat{\boldsymbol{R}}_j), \tag{II.13}$$

where $\hat{\boldsymbol{R}}_j$ is the position operator of the j-th nucleus, and b_j its scattering length. It is a complex number whose imaginary part is related to energy-dependent absorption. The Fourier transform of this potential is given by

$$\hat{V}_{\mathrm{N}}(\boldsymbol{Q}) = \langle \boldsymbol{k}_{\mathrm{f}} | \, \hat{V}_{\mathrm{N}}(\boldsymbol{r}) \, | \boldsymbol{k}_{\mathrm{i}} \rangle = \frac{2\pi\hbar^2}{m_{\mathrm{n}}} \hat{N}(\boldsymbol{Q}), \tag{II.14}$$

with the nuclear amplitude operator

$$\hat{N}(\boldsymbol{Q}) = \sum_j b_j \mathrm{e}^{\mathrm{i}\boldsymbol{Q}\hat{\boldsymbol{R}}_j}. \tag{II.15}$$

II.2.1 Coherent and incoherent scattering

Assuming no correlation between the nuclear positions and the scattering lengths, the evaluation of the matrix element from Eq. (II.7) with Eq. (II.12) and the Fermi pseudo-potential gives the partial differential cross section for unpolarized neutrons:

$$\left(\frac{\mathrm{d}^2\sigma}{\mathrm{d}\Omega \, \mathrm{d}E_{\mathrm{f}}}\right)_{\mathrm{N}} = \frac{k_{\mathrm{f}}}{k_{\mathrm{i}}} \frac{1}{2\pi\hbar} \int_{-\infty}^{+\infty} \mathrm{d}t \, \mathrm{e}^{-\mathrm{i}\omega t} \sum_{j,j'} \overline{b_j b_{j'}^*} \langle \mathrm{e}^{-\mathrm{i}\boldsymbol{Q}\cdot\hat{\boldsymbol{R}}_{j'}(0)} \mathrm{e}^{\mathrm{i}\boldsymbol{Q}\cdot\hat{\boldsymbol{R}}_j(t)} \rangle, \tag{II.16}$$

where the $\overline{b_j b_{j'}^*}$ translates the average for a large number of nuclei of the scattering lengths over random nuclear spin orientation[6] and isotope distributions.

[5] The true nuclear interaction potential is very short range, but also very strong, so that Born approximation is no longer valid. Yet, the Fermi pseudo-potential describes the expected isotropic scattering far from the nuclei.

[6] In this thesis, we will ignore the interaction between the neutrons and the nuclear spins which order at very low temperature or under very high magnetic fields.

Assuming real scattering lengths we can write

$$\overline{b_j b_{j'}} = \begin{cases} \bar{b}_j \bar{b}_{j'}, & \text{if } j \neq j'. \\ \overline{b_j^2}, & \text{if } j = j'. \end{cases} \tag{II.17}$$

Allowing to rewrite the sums into:

$$\begin{aligned} &\sum_{j,j'} \overline{b_j b_{j'}} \langle \mathrm{e}^{-\mathrm{i}\boldsymbol{Q}\cdot\hat{\boldsymbol{R}}_{j'}(0)} \mathrm{e}^{\mathrm{i}\boldsymbol{Q}\cdot\hat{\boldsymbol{R}}_{j}(t)} \rangle \\ =&\sum_{j\neq j'} \bar{b}_j \bar{b}_{j'} \langle \mathrm{e}^{-\mathrm{i}\boldsymbol{Q}\cdot\hat{\boldsymbol{R}}_{j'}(0)} \mathrm{e}^{\mathrm{i}\boldsymbol{Q}\cdot\hat{\boldsymbol{R}}_{j}(t)} \rangle + \sum_{j} \overline{b_j^2} \langle \mathrm{e}^{-\mathrm{i}\boldsymbol{Q}\cdot\hat{\boldsymbol{R}}_{j}(0)} \mathrm{e}^{\mathrm{i}\boldsymbol{Q}\cdot\hat{\boldsymbol{R}}_{j}(t)} \rangle \\ =&\sum_{j,j'} \bar{b}_j \bar{b}_{j'} \langle \mathrm{e}^{-\mathrm{i}\boldsymbol{Q}\cdot\hat{\boldsymbol{R}}_{j'}(0)} \mathrm{e}^{\mathrm{i}\boldsymbol{Q}\cdot\hat{\boldsymbol{R}}_{j}(t)} \rangle + \sum_{j} (\overline{b_j^2} - \bar{b}_j{}^2) \langle \mathrm{e}^{-\mathrm{i}\boldsymbol{Q}\cdot\hat{\boldsymbol{R}}_{j}(0)} \mathrm{e}^{\mathrm{i}\boldsymbol{Q}\cdot\hat{\boldsymbol{R}}_{j}(t)} \rangle. \end{aligned} \tag{II.18}$$

Thus, one can split the partial differential cross section into:

$$\left(\frac{\mathrm{d}^2\sigma}{\mathrm{d}\Omega\,\mathrm{d}E_\mathrm{f}}\right)_\mathrm{N} = \left(\frac{\mathrm{d}^2\sigma}{\mathrm{d}\Omega\,\mathrm{d}E_\mathrm{f}}\right)_\mathrm{N}^\mathrm{coh} + \left(\frac{\mathrm{d}^2\sigma}{\mathrm{d}\Omega\,\mathrm{d}E_\mathrm{f}}\right)_\mathrm{N}^\mathrm{inc}, \tag{II.19}$$

with the first term corresponding to coherent scattering describing the correlation between different nuclei having average scattering lengths $\bar{b}_j$:

$$\left(\frac{\mathrm{d}^2\sigma}{\mathrm{d}\Omega\,\mathrm{d}E_\mathrm{f}}\right)_\mathrm{N}^\mathrm{coh} = \frac{k_\mathrm{f}}{k_\mathrm{i}} \frac{1}{2\pi\hbar} \int_{-\infty}^{+\infty} \mathrm{d}t\, \mathrm{e}^{-\mathrm{i}\omega t} \sum_{j,j'} \bar{b}_j \bar{b}_{j'} \langle \mathrm{e}^{-\mathrm{i}\boldsymbol{Q}\cdot\hat{\boldsymbol{R}}_{j'}(0)} \mathrm{e}^{\mathrm{i}\boldsymbol{Q}\cdot\hat{\boldsymbol{R}}_{j}(t)} \rangle, \tag{II.20}$$

and the second term corresponds to incoherent scattering describing self-correlations of nuclei having random variations of the scattering lengths:

$$\left(\frac{\mathrm{d}^2\sigma}{\mathrm{d}\Omega\,\mathrm{d}E_\mathrm{f}}\right)_\mathrm{N}^\mathrm{inc} = \frac{k_\mathrm{f}}{k_\mathrm{i}} \frac{1}{2\pi\hbar} \int_{-\infty}^{+\infty} \mathrm{d}t\, \mathrm{e}^{-\mathrm{i}\omega t} \sum_{j} \frac{\sigma_j^\mathrm{inc}}{4\pi} \langle \mathrm{e}^{-\mathrm{i}\boldsymbol{Q}\cdot\hat{\boldsymbol{R}}_{j}(0)} \mathrm{e}^{\mathrm{i}\boldsymbol{Q}\cdot\hat{\boldsymbol{R}}_{j}(t)} \rangle, \tag{II.21}$$

where $\sigma_j^\mathrm{inc} = 4\pi(\overline{b_j^2} - \bar{b}_j{}^2)$ is the incoherent cross section of the j-th atom.

Coherent scattering reflects interferences from the periodicity of the lattice

and can be useful for structural determination (elastic scattering) or to study collective excitations such as phonons (inelastic scattering). On the other hand elastic incoherent scattering gives a constant background which can be used for absolute normalization procedures, as described in Section IV.3.2, while inelastic incoherent scattering provides dynamical properties and can be used to study diffusive systems. These coherent and incoherent scattering lengths and their associated total cross section are tabulated for most of individual isotopes and their natural mix for each chemical element [103].

II.2.2 Elastic nuclear scattering

In this section, we will focus on elastic scattering in crystalline solids. The translational symmetry in an ideal crystal allows to describe its periodic structure as an infinite Bravais lattice. The basis (the same group of atoms) is repeated on each lattice point. It is thus convenient to describe the crystal structure as the 3D repetition of primitive unit cells which are the smallest building blocks of the crystal [104].

In order to take into account this periodicity of the crystal, the position of the j-th atom can be rewritten as:

$$\hat{\boldsymbol{R}}_j(t) = \boldsymbol{R}_{ld}(t) = \boldsymbol{R}_l + \boldsymbol{r}_d + \hat{\boldsymbol{u}}_{l,d}(t), \tag{II.22}$$

where $\boldsymbol{R}_l = n_a\boldsymbol{a} + n_b\boldsymbol{b} + n_c\boldsymbol{c}$ is a real space lattice vector (with $(\boldsymbol{a}, \boldsymbol{b}, \boldsymbol{c})$ the unit cell primitive vectors, and (n_a, n_b, n_c) are integer coordinates), $\boldsymbol{r}_d = x\boldsymbol{a} + y\boldsymbol{b} + z\boldsymbol{c}$ is the equilibrium position of the atom within the unit cell (with $(x, y, z) \in [0; 1[$ the fractional coordinates), and $\boldsymbol{u}_{l,d}(t)$ is the displacement of the atom around its equilibrium position. This allows to rewrite the sum from Eq. (II.20):

$$\begin{aligned} &\sum_{j,j'} \bar{b}_j \bar{b}_{j'} \langle \mathrm{e}^{-\mathrm{i}\boldsymbol{Q}\cdot\hat{\boldsymbol{R}}_{j'}(0)} \mathrm{e}^{\mathrm{i}\boldsymbol{Q}\cdot\hat{\boldsymbol{R}}_j(t)} \rangle \\ =&\sum_{l,l'} \mathrm{e}^{\mathrm{i}\boldsymbol{Q}(\boldsymbol{R}_l - \boldsymbol{R}_{l'})} \sum_{d,d'} \mathrm{e}^{\mathrm{i}\boldsymbol{Q}(\boldsymbol{r}_d - \boldsymbol{r}_{d'})} \bar{b}_d \bar{b}_{d'} \langle \mathrm{e}^{-\mathrm{i}\boldsymbol{Q}\cdot\hat{\boldsymbol{u}}_{l',d'}(0)} \mathrm{e}^{\mathrm{i}\boldsymbol{Q}\cdot\hat{\boldsymbol{u}}_{l,d}(t)} \rangle. \end{aligned} \tag{II.23}$$

By defining $U = -\mathrm{i}\boldsymbol{Q}\cdot\hat{\boldsymbol{u}}_{l',d'}(0)$ and $V = \mathrm{i}\boldsymbol{Q}\cdot\hat{\boldsymbol{u}}_{l,d}(t)$, the aim is to evaluate the thermal average $\langle \mathrm{e}^U \mathrm{e}^V \rangle$. This is done by considering the nuclei in isotropic harmonic potentials [99]. This allows to write

$$\langle \mathrm{e}^{U} \mathrm{e}^{V} \rangle = \mathrm{e}^{-W_{d'} - W_d} \, \mathrm{e}^{\langle UV \rangle}, \tag{II.24}$$

where

$$W_d = \frac{1}{2} \langle (\boldsymbol{Q} \cdot \hat{\boldsymbol{u}}_d)^2 \rangle \tag{II.25}$$

is the Debye-Waller factor describing the thermal motion of the atoms. By translational symmetry there is no more dependence on the lattice index l. The exponential $\mathrm{e}^{\langle UV \rangle}$ can further be expanded as power series in $\langle UV \rangle$ where the n-th term corresponds to the n-phonon process. In this thesis, we are not studying any phonon processes, and can limit the exponential expansion to its zeroth order ($= 1$). There is no more time-dependence in Eq. (II.23), so the time integral in Eq. (II.20) can be written

$$\frac{1}{2\pi\hbar} \int_{-\infty}^{+\infty} \mathrm{d}t \, \mathrm{e}^{-\mathrm{i}\omega t} = \delta(\hbar\omega). \tag{II.26}$$

This is the condition for elastic scattering $\hbar\omega = 0$ for which $k_\mathrm{i} = k_\mathrm{f}$. Moreover, the lattice sum is given by

$$\sum_l e^{\mathrm{i}\boldsymbol{Q}\cdot\boldsymbol{R}_l} = \frac{(2\pi)^3}{v_0} \sum_{\boldsymbol{G}} \delta(\boldsymbol{Q} - \boldsymbol{G}), \tag{II.27}$$

where $G = h\boldsymbol{a}^* + k\boldsymbol{b} + l\boldsymbol{c}$ are the reciprocal lattice vectors and v_0 the volume of the unit cell. Using these two relations and by integrating Eq. (II.20) over the final energy E_f, we finally obtain the diffential cross section for elastic coherent nuclear scattering:

$$\left(\frac{\mathrm{d}\sigma}{\mathrm{d}\Omega} \right)_\mathrm{N}^\mathrm{coh} = N \frac{(2\pi)^3}{v_0} \sum_{\boldsymbol{G}} \delta(\boldsymbol{Q} - \boldsymbol{G}) |F_\mathrm{N}(\boldsymbol{Q})|^2, \tag{II.28}$$

where N is the number of unit cells in the sample. $F_\mathrm{N}(\boldsymbol{Q})$ is the unit cell nuclear structure factor given by

$$F_\mathrm{N}(\boldsymbol{Q}) = \sum_d \bar{b}_d \, \mathrm{e}^{-\mathrm{i}\boldsymbol{Q}\cdot\boldsymbol{r}_d} \mathrm{e}^{-W_d(\boldsymbol{Q})}. \tag{II.29}$$

The delta function $\delta(\boldsymbol{Q} - \boldsymbol{G})$ translates the fact that strong diffraction only happens when the scattering vector is equal to a reciprocal lattice vector. This is known as the Laue condition and is equivalent to Bragg's law (Fig. II.3) [104]:

$$n\lambda = 2d_{hkl} \sin\theta, \tag{II.30}$$

where n is an integer, $\lambda = 2\pi/k_\mathrm{i}$ the wavelength of the incident neutron beam, d_{hkl} the distance between planes labeled by the Miller indices (hkl), and θ is the Bragg reflection angle.

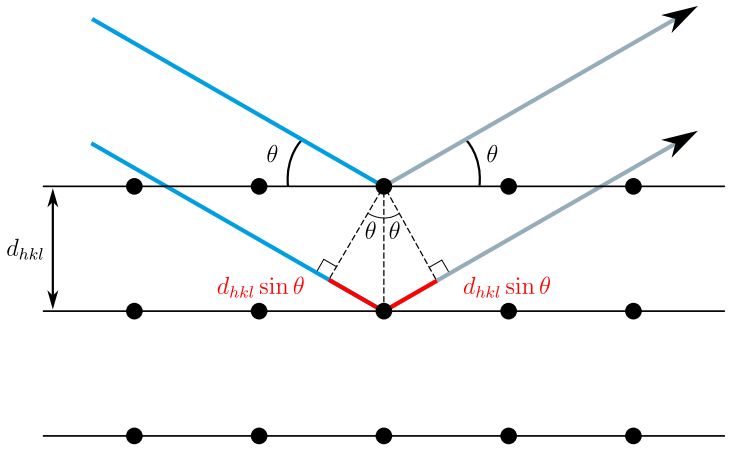

Figure II.3 Illustration of Bragg's law: the incident beams are scattered from a set of planes (hkl) separated by a distance d_{hkl} with a path difference $2d_{hkl} \sin\theta$ between adjacent planes.

We note that for elastic scattering, the norm Q of the scattering vector

$$Q = \sqrt{k_\mathrm{i}^2 + k_\mathrm{f}^2 - 2k_\mathrm{i}k_\mathrm{f} \cos 2\theta} \tag{II.31}$$

is simply (as $k_\mathrm{i} = k_\mathrm{f}$)

$$Q = 2k_\mathrm{i} \sin\theta = 4\pi \frac{\sin\theta}{\lambda} = \frac{2\pi}{d_{hkl}}. \tag{II.32}$$

Assuming isotropic atomic displacements, the Debye-Waller factor can be written [96]

$$W_d = \frac{1}{6} Q^2 \langle u_d^2 \rangle = B_d \frac{\sin^2\theta}{\lambda^2}, \tag{II.33}$$

where $B_d = \frac{8\pi^2}{3}\langle u_d^2 \rangle$ is the isotropic displacement parameter in Å^2. From this it is immediate that the Debye-Waller factor attenuates the scattered intensity as a function of Q. It also acts on the elastic incoherent nuclear scattering which can be calculated in a similar way from Eq. (II.21):

$$\left(\frac{\mathrm{d}\sigma}{\mathrm{d}\Omega}\right)_{\mathrm{N}}^{\mathrm{inc}} = N \sum_d \frac{\sigma_d^{\mathrm{inc}}}{4\pi} \mathrm{e}^{-2W_d}. \tag{II.34}$$

II.3 Magnetic scattering

In this section, we will consider the interaction between the neutrons and the unpaired electrons in the crystal. We will introduce the unpolarized inelastic cross section (the polarized case is treated in next section), and the elastic cross section for magnetic diffraction studies.

II.3.1 Magnetic cross section

Magnetic interaction potential

Magnetic scattering occurs when the neutron at position $\boldsymbol{r}$ interacts with the magnetic field created by an unpaired electron i, at position $\boldsymbol{r}_i$, with the momentum $\hat{\boldsymbol{p}}_i$ and spin $\hat{\boldsymbol{s}}_i$. Their respective magnetic moments are $\hat{\boldsymbol{\mu}}_{\mathrm{n}} = -\gamma\mu_{\mathrm{N}}\hat{\boldsymbol{\sigma}}$ (with $\hat{\boldsymbol{\sigma}}$ the Pauli spin operator) and $\hat{\boldsymbol{\mu}}_i = -g_{\mathrm{e}}\mu_{\mathrm{B}}\hat{\boldsymbol{s}}_i$, with $\gamma = -1.91$ the neutron gyromagnetic ratio, $g_{\mathrm{e}} \approx 2$ the electron spin g-factor, μ_{N} and μ_{B} the nuclear and the Bohr magnetons. The magnetic interaction potential is given by

$$\hat{V}_{\mathrm{M}}(\boldsymbol{r}) = -\hat{\boldsymbol{\mu}}_{\mathrm{n}} \cdot \hat{\boldsymbol{B}}(\boldsymbol{r}), \tag{II.35}$$

where

$$\boldsymbol{B} = \sum_i \frac{\mu_0}{4\pi} \left\{ \boldsymbol{\nabla} \times \left(\frac{\hat{\boldsymbol{\mu}}_i \times \boldsymbol{R}_i}{|\boldsymbol{R}_i|^3} \right) - \frac{2\mu_{\mathrm{B}}}{\hbar} \frac{\hat{\boldsymbol{p}}_i \times \boldsymbol{R}_i}{|\boldsymbol{R}_i|^3} \right\} \tag{II.36}$$

is the magnetic field created by the unpaired electrons, and $\boldsymbol{R}_i = \boldsymbol{r} - \boldsymbol{r}_i$ are the distances between the neutron and the electrons. The contribution from the

unpaired electrons can be separated into two parts: the first term of the equation is due to the electron spins (flux density of a magnetic dipole moment) and the second term is due to their motion (flux density of a non-relativistic charged particle in motion), often refered as the orbital contribution.

The Fourier transform of the magnetic interaction potential in Eq. (II.35) can be calculated giving [93, 95]:

$$\hat{V}_{\mathrm{M}}(\boldsymbol{Q}) = \frac{2\pi\hbar^2}{m_{\mathrm{n}}}\hat{\boldsymbol{\sigma}} \cdot \hat{\boldsymbol{M}}_{\perp}(\boldsymbol{Q}), \tag{II.37}$$

where $\hat{\boldsymbol{M}}_{\perp}(\boldsymbol{Q})$ is the magnetic interaction vector[7] built upon the spin $\hat{\boldsymbol{s}}_i$ and momentum $\hat{\boldsymbol{p}}_i$ of the electrons

$$\hat{\boldsymbol{M}}_{\perp}(\boldsymbol{Q}) = \gamma r_0 \sum_i e^{\mathrm{i}\boldsymbol{Q}\cdot\boldsymbol{r}_i}[\tilde{\boldsymbol{Q}} \times (\hat{\boldsymbol{s}}_i \times \tilde{\boldsymbol{Q}}) + \frac{\mathrm{i}}{\hbar Q}(\hat{\boldsymbol{p}}_i \times \tilde{\boldsymbol{Q}})], \tag{II.38}$$

where $r_0 = \frac{\mu_0 e^2}{4\pi m_{\mathrm{e}}}$ is the classical electron radius, with e and m_{e} the charge and the mass of the electron. $|\gamma r_0| \approx 0.5\times10^{-12}$ cm which makes magnetic scattering cross section usually comparable to the nuclear one. $\tilde{\boldsymbol{Q}} = \boldsymbol{Q}/Q$ is the unit scattering vector. $\hat{\boldsymbol{M}}_{\perp}$ is the projection of $\hat{\boldsymbol{M}}$ perpendicular to the scattering vector $\boldsymbol{Q}$:

$$\hat{\boldsymbol{M}}_{\perp} = \tilde{\boldsymbol{Q}} \times (\hat{\boldsymbol{M}} \times \tilde{\boldsymbol{Q}}) = \hat{\boldsymbol{M}} - (\hat{\boldsymbol{M}} \cdot \tilde{\boldsymbol{Q}})\tilde{\boldsymbol{Q}}. \tag{II.39}$$

Also,

$$\begin{aligned} \hat{\boldsymbol{M}}_{\perp}^{\dagger} \cdot \hat{\boldsymbol{M}}_{\perp} &= [\hat{\boldsymbol{M}}^{\dagger} - (\hat{\boldsymbol{M}}^{\dagger} \cdot \tilde{\boldsymbol{Q}})\tilde{\boldsymbol{Q}}][\hat{\boldsymbol{M}} - (\hat{\boldsymbol{M}} \cdot \tilde{\boldsymbol{Q}})\tilde{\boldsymbol{Q}}] \\ &= \hat{\boldsymbol{M}}^{\dagger} \cdot \hat{\boldsymbol{M}} - (\hat{\boldsymbol{M}}^{\dagger} \cdot \tilde{\boldsymbol{Q}})(\hat{\boldsymbol{M}} \cdot \tilde{\boldsymbol{Q}}) \\ &= \sum_{\alpha\beta} \left(\delta_{\alpha\beta} - \tilde{Q}_{\alpha}\tilde{Q}_{\beta}\right) \hat{M}_{\alpha}^{\dagger}\hat{M}_{\beta}. \end{aligned} \tag{II.40}$$

$\hat{\boldsymbol{M}}(\boldsymbol{Q}) = -\frac{\gamma r_0}{2\mu_{\mathrm{B}}}\hat{\boldsymbol{\mathcal{M}}}(\boldsymbol{Q})$, where $\hat{\boldsymbol{\mathcal{M}}}(\boldsymbol{Q})$ is the Fourier transform of the total magnetization operator $\hat{\boldsymbol{\mathcal{M}}}(\boldsymbol{r}) = \hat{\boldsymbol{\mathcal{M}}}_{\mathrm{S}}(\boldsymbol{r}) + \hat{\boldsymbol{\mathcal{M}}}_{\mathrm{L}}(\boldsymbol{r})$. The spin part is related to the density of electron spin moments $\hat{\boldsymbol{\rho}}_{\mathrm{S}}$:

[7] We have included the factor γr_0 into the magnetic interaction vector to simplify our notations for the theory of polarized neutrons scattering in Section II.4.

$$\hat{\boldsymbol{\mathcal{M}}}_{\mathrm{S}}(\boldsymbol{r}) = -2\mu_{\mathrm{B}}\hat{\boldsymbol{\rho}}_{\mathrm{S}}(\boldsymbol{r}) = -2\mu_{\mathrm{B}}\sum_i \delta(\boldsymbol{r}-\boldsymbol{r}_i)\hat{\boldsymbol{s}}_i, \tag{II.41}$$

which Fourier transform corresponds to the first term of Eq. (II.38). It can be shown similarly that the Fourier transform of the orbital magnetization operator $\hat{\boldsymbol{\mathcal{M}}}_{\mathrm{L}}(\boldsymbol{r})$ corresponds to the second part of Eq. (II.38) [93]. Eq. (II.39) illustrates the fact that magnetic scattering is only sensitive to magnetization perpendicular to the scattering vector $\boldsymbol{Q}$. This can be interpreted from Maxwell's equation $\boldsymbol{\nabla}\cdot\boldsymbol{B}(\boldsymbol{r}) = 0$, which Fourier transform imposes $\boldsymbol{Q}\cdot\boldsymbol{B}(\boldsymbol{Q}) = 0$ [99].

Magnetic master equation

The master equation for magnetic scattering becomes

$$\left(\frac{\mathrm{d}^2\sigma}{\mathrm{d}\Omega\,\mathrm{d}E_{\mathrm{f}}}\right)_{\boldsymbol{k}_{\mathrm{i}}\sigma_{\mathrm{i}}\to\boldsymbol{k}_{\mathrm{f}}\sigma_{\mathrm{f}}} = \frac{k_{\mathrm{f}}}{k_{\mathrm{i}}}\sum_{\lambda_{\mathrm{i}},\sigma_{\mathrm{i}}} p_{\lambda_{\mathrm{i}}}p_{\sigma_{\mathrm{i}}}\sum_{\lambda_{\mathrm{f}},\sigma_{\mathrm{f}}}\left|\langle\sigma_{\mathrm{f}}\lambda_{\mathrm{f}}|\,\hat{\boldsymbol{\sigma}}\cdot\hat{\boldsymbol{M}}_{\perp}(\boldsymbol{Q})\,|\sigma_{\mathrm{i}}\lambda_{\mathrm{i}}\rangle\right|^2\delta(\hbar\omega + E_{\lambda_{\mathrm{i}}} - E_{\lambda_{\mathrm{f}}}). \tag{II.42}$$

The matrix element in Eq. (II.42) can be further separated with the spin operator acting on the neutron spin states, and the magnetic interaction vector acting on the electron states (included in the states λ of the sample):

$$\langle\sigma_{\mathrm{f}}\lambda_{\mathrm{f}}|\,\hat{\boldsymbol{\sigma}}\cdot\hat{\boldsymbol{M}}_{\perp}(\boldsymbol{Q})\,|\sigma_{\mathrm{i}}\lambda_{\mathrm{i}}\rangle = \langle\sigma_{\mathrm{f}}|\,\hat{\boldsymbol{\sigma}}\,|\sigma_{\mathrm{i}}\rangle\cdot\langle\lambda_{\mathrm{f}}|\,\hat{\boldsymbol{M}}_{\perp}(\boldsymbol{Q})\,|\lambda_{\mathrm{i}}\rangle\,. \tag{II.43}$$

For unpolarized neutrons (the polarized case is discussed in Section II.4) performing the sum over initial and final states with $p_{\sigma_{\mathrm{i}}} = 1/2$ in Eq. (II.42) and using properties of Pauli matrices (Appendix A):

$$\sum_{\sigma_{\mathrm{i}}\sigma_{\mathrm{f}}} p_{\sigma_{\mathrm{i}}}\,\langle\sigma_{\mathrm{i}}|\,\hat{\sigma}_\alpha\,|\sigma_{\mathrm{f}}\rangle\langle\sigma_{\mathrm{f}}|\,\hat{\sigma}_\beta\,|\sigma_{\mathrm{i}}\rangle = \sum_{\sigma_i} p_{\sigma_{\mathrm{i}}}\,\langle\sigma_{\mathrm{i}}|\,\hat{\sigma}_\alpha\hat{\sigma}_\beta\,|\sigma_{\mathrm{i}}\rangle = \delta_{\alpha\beta}, \tag{II.44}$$

then introducing the Heisenberg operators in the thermal average from Eq. (II.12) gives the cross section

$$\left(\frac{\mathrm{d}^2\sigma}{\mathrm{d}\Omega\,\mathrm{d}E_\mathrm{f}}\right)_{\boldsymbol{k}_\mathrm{i}\to\boldsymbol{k}_\mathrm{f}} = \frac{k_\mathrm{f}}{k_\mathrm{i}}\sum_{\alpha\beta}\left(\delta_{\alpha\beta}-\tilde{Q}_\alpha\tilde{Q}_\beta\right)S_{\alpha\beta}(\boldsymbol{Q},\hbar\omega), \tag{II.45}$$

where

$$S_{\alpha\beta}(\boldsymbol{Q},\hbar\omega) = \frac{1}{2\pi\hbar}\int_{-\infty}^{+\infty}\mathrm{d}t\,\mathrm{e}^{-\mathrm{i}\omega t}\langle\hat{M}_\alpha^\dagger(\boldsymbol{Q},0)\hat{M}_\beta(\boldsymbol{Q},t)\rangle \tag{II.46}$$

is the partial dynamical structure factor. The factor $\sum_{\alpha\beta}\left(\delta_{\alpha\beta}-\tilde{Q}_\alpha\tilde{Q}_\beta\right)$ before this structure factor is called the orientation factor and selects the magnetization perpendicular to the scattering vector.

Spin-only scattering and dipole approximation

Evaluating the matrix element in Eq. (II.46) can be difficult, but some useful approximations are usually taken. We suppose that the unpaired electrons are localized around to the positions $\hat{\boldsymbol{R}}_{ld}$ of the magnetic ions in the crystalline lattice,[8] and that they have LS coupling. The energy of the neutrons is assumed to be small enough, so that the unpaired electrons have the same spatial wave functions and total spin length before and after scattering. If the magnetization is only due to the spins of the electrons ($L = 0$), we can write from Eq. (II.41) [93]

$$\langle\lambda_\mathrm{f}|\,\hat{\boldsymbol{M}}(\boldsymbol{Q})\,|\lambda_\mathrm{i}\rangle = \gamma r_0\sum_{ld} f_d(\boldsymbol{Q})\,\langle\lambda_\mathrm{f}|\,\mathrm{e}^{\mathrm{i}\boldsymbol{Q}\cdot\hat{\boldsymbol{R}}_{ld}(t)}\hat{\boldsymbol{S}}_{ld}\,|\lambda_\mathrm{i}\rangle\,, \tag{II.47}$$

where the magnetic form factor $f_d(\boldsymbol{Q})$ is the Fourier transform of the electron spin density (normalized so that $f_d(0) = 1$) of the d-th magnetic ion of the unit cell. $\hat{\boldsymbol{S}}_{ld}$ is the total spin operator of the unpaired electrons for each magnetic ion in the crystal. The magnetic form factor can be seen as the smearing of the unpaired electrons around the magnetic ions, attenuating the scattered intensity compared to the scattering from point-like particles [105].

These approximations can be extended, for example for intermediate crystal fields, typically for $3d$ ions studied in this thesis, where the orbital moment is

[8] As defined in Eq. (II.22), the l index refers to the lattice, and d to the atom in the unit cell.

usually quenched. In the dipole approximation (valid for Q^{-1} large compared to the orbital wave function radius), the small spin-orbit coupling can be described by a deviation of the g-factor from its spin-only value $g = 2$, and the matrix element becomes

$$\langle \lambda_\mathrm{f} | \, \hat{\boldsymbol{M}}(\boldsymbol{Q}) \, | \lambda_\mathrm{i} \rangle = \gamma r_0 \sum_{ld} \frac{g}{2} f_d(Q) \, \langle \lambda_\mathrm{f} | \, \mathrm{e}^{\mathrm{i}\boldsymbol{Q}\cdot\hat{\boldsymbol{R}}_{ld}(t)} \hat{\boldsymbol{S}}_{ld} \, | \lambda_\mathrm{i} \rangle \, , \tag{II.48}$$

where the $\hat{\boldsymbol{S}}_{ld}$ are effective spin operators. Assuming an isotropic spatial distribution of the magnetization, the magnetic form factor becomes

$$f_d(Q) = \langle j_0(Q) \rangle + \frac{g-2}{2} \langle j_2(Q) \rangle, \tag{II.49}$$

where $\langle j_n(Q)) \rangle = \int_0^{+\infty} \mathrm{d}r \, j_n(Qr) r^2 R^2(r)$ is the radial integral, $j_n(Qr)$ is the n-th order spherical Bessel function, and $f(r)$ is the radial wave function. The magnetic form factor depends on the oxidation state of the d-th magnetic atom. An analytical approximation of the form factors is tabulated for most of the elements [106].

II.3.2 Inelastic magnetic scattering

Considering that the crystal has only one type of magnetic ion, the magnetic partial differential cross section for unpolarized neutrons is

$$\left(\frac{\mathrm{d}^2\sigma}{\mathrm{d}\Omega \, \mathrm{d}E_\mathrm{f}} \right)_\mathrm{M} = \frac{k_\mathrm{f}}{k_\mathrm{i}} (\gamma r_0)^2 \left(\frac{g f(\boldsymbol{Q})}{2} \right)^2 \mathrm{e}^{-2W(\boldsymbol{Q})} S(\boldsymbol{Q}, E), \tag{II.50}$$

where the term $\mathrm{e}^{-2W(\boldsymbol{Q})}$ involving the Debye-Waller factor was obtained the same way as in Section II.2.2, assuming that the spin directions are independent from the ion positions, which allows to decouple the structural and magnetic correlations. We then only consider the static part of the structural correlation, ignoring any effects from magneto-vibrational scattering [93, 95]:

$$S(\boldsymbol{Q}, E) = \sum_{\alpha,\beta} \left(\delta_{\alpha\beta} - \hat{Q}_\alpha \hat{Q}_\beta \right) S^{\alpha\beta}(\boldsymbol{Q}, E) \tag{II.51}$$

and the dynamical spin correlation function is

$$S^{\alpha\beta}(\boldsymbol{Q},E)=\frac{1}{2\pi\hbar}\int_{-\infty}^{+\infty}\mathrm{d}t\,\mathrm{e}^{-\mathrm{i}\omega t}\sum_{ij}\mathrm{e}^{\mathrm{i}\boldsymbol{Q}\cdot(\boldsymbol{R}_j-\boldsymbol{R}_i)}\langle\hat{S}_i^{\alpha}(0)\hat{S}_j^{\beta}(t)\rangle. \tag{II.52}$$

II.3.3 Elastic magnetic scattering

Similarly as described above for nuclear scattering [Eq. (II.28)], the elastic magnetic differential cross section is obtained by integrating Eq. (II.50) over the final energy:

$$\left(\frac{\mathrm{d}\sigma}{\mathrm{d}\Omega}\right)_{\mathrm{el}}=N\frac{(2\pi)^3}{v_0}\sum_{\boldsymbol{G}\boldsymbol{k}}\delta(\boldsymbol{Q}-\boldsymbol{G}-\boldsymbol{k})|\boldsymbol{F}_{\mathrm{M}_\perp}(\boldsymbol{Q})|^2, \tag{II.53}$$

where again N is the number of structural unit cells, and v_0 the volume cell unit, the sum is over the reciprocal lattice vectors $\boldsymbol{G}$ and the propagation vectors $\boldsymbol{k}$ describing the periodicity of the magnetic structure (see Appendix B). $\boldsymbol{F}_{\mathrm{M}_\perp}(\boldsymbol{Q})$ is the component perpendicular to the scattering vector $\boldsymbol{Q}$ of the unit cell magnetic structure factor

$$\boldsymbol{F}_{\mathrm{M}}(\boldsymbol{Q})=p\sum_d f_d(Q)\boldsymbol{S}_{\boldsymbol{k}d}\mathrm{e}^{\mathrm{i}\boldsymbol{Q}\cdot\boldsymbol{r}_d}\mathrm{e}^{-W_d(\boldsymbol{Q})}, \tag{II.54}$$

where d is the index of the d-th magnetic ion in the position $\boldsymbol{r}_d$ within the unit cell. $\boldsymbol{S}_{\boldsymbol{k}d}$ is the Fourier component associated to propagation vector $\boldsymbol{k}$ in units of μ_{B} and $p=\gamma r_0/2\mu_{\mathrm{B}}=0.2695\times10^{-12}\,\mathrm{cm}/\mu_{\mathrm{B}}$ is the conversion factor from magnetic moments in μ_{B} into scattering length in units of $10^{-12}\,\mathrm{cm}$. $f_d(Q)$ and $\mathrm{e}^{-W_d(\boldsymbol{Q})}$ are the magnetic form factor and Debye-Waller factor defined above.

For a commensurate magnetic structure which can be described by a magnetic unit cell the magnetic differential cross section can be simplified as

$$\left(\frac{\mathrm{d}\sigma}{\mathrm{d}\Omega}\right)_{\mathrm{M}}=N_{\mathrm{M}}\frac{(2\pi)^3}{v_{\mathrm{M}}}\sum_{\boldsymbol{G}_{\mathrm{M}}}\delta(\boldsymbol{Q}-\boldsymbol{G}_{\mathrm{M}})|\boldsymbol{F}_{\mathrm{M}_\perp}(\boldsymbol{Q})|^2, \tag{II.55}$$

where N_{M} is the number of magnetic unit cells, and v_{M} its volume. The sum is over the reciprocal magnetic lattice vectors $\boldsymbol{G}_{\mathrm{M}}$ and the magnetic structure factor

$\boldsymbol{F}_{\mathrm{M}}(\boldsymbol{Q})$ is given by

$$\boldsymbol{F}_{\mathrm{M}}(\boldsymbol{Q}) = p \sum_d f_d(Q) \boldsymbol{S}_d \mathrm{e}^{\mathrm{i}\boldsymbol{Q}\cdot\boldsymbol{r}_d} \mathrm{e}^{-W_d(\boldsymbol{Q})}. \tag{II.56}$$

These expressions of the magnetic cross section are very similar to Eq. (II.28) for the nuclear elastic cross section. In general, the magnetic structure can be seen as a superstructure in the reciprocal space where the magnetic Bragg peaks appears at $\pm\boldsymbol{k}$ around the nuclear Bragg peaks.

II.4 Polarized neutrons

Polarized neutrons are nowadays used in powerful scattering techniques allowing the separation of nuclear and magnetic cross sections, the determination of complex magnetic structures, or the study of magnetic chiralities. The theory of polarized neutron scattering was first developed by Halpern and Johnson in 1939 [107], and the derived equations were probed experimentally in the 50s [108, 109]. However, the studies were limited to ferromagnetic and simple antiferromagnetic structures, omitting some terms in the scattering cross section of a polarized beam, and on the calculation of the final polarization. More general expressions were derived in the 60s independently by Blume [110] and Maleev [111] using the density matrix formalism. In this section, an overview on the polarized neutron scattering theory will be given, followed by an introduction to spherical neutron polarimetry and Schwinger scattering.

II.4.1 Polarized neutron scattering cross section

Incident beam polarization

Using the notations introduced in this chapter, we want to evaluate the matrix element $\langle\sigma_{\mathrm{f}}|\,\hat{V}\,|\sigma_{\mathrm{i}}\rangle$ in the master equation. The initial neutron spin state can be described by a mixture of pure states $|\sigma_{\mathrm{i}}\rangle$ with probability $p_{\sigma_{\mathrm{i}}}$ by the density matrix [112]

$$\hat{\rho} = \sum_{\sigma_\mathrm{i}} p_{\sigma_\mathrm{i}} \left|\sigma_\mathrm{i}\right\rangle\!\left\langle\sigma_\mathrm{i}\right| . \tag{II.57}$$

Then we can define the initial polarization $\boldsymbol{P}_\mathrm{i}$ of the neutron beam as the expectation value of the Pauli spin operator $\hat{\boldsymbol{\sigma}}$ (see Appendix A)

$$\boldsymbol{P}_\mathrm{i} = \langle \hat{\boldsymbol{\sigma}} \rangle_{\hat{\rho}} = \mathrm{Tr}[\hat{\rho}\hat{\boldsymbol{\sigma}}]. \tag{II.58}$$

With this definition $|\boldsymbol{P}_\mathrm{i}| = 0$ for an unpolarized neutron beam, and $|\boldsymbol{P}_\mathrm{i}| = 1$ for a fully polarized beam. Noting that any 2×2 Hermitian matrix can be written as a linear combination of the identity matrix and the Pauli matrices [113, 114]:

$$\hat{\mathcal{O}} = u\hat{\mathbb{1}} + \boldsymbol{v} \cdot \hat{\boldsymbol{\sigma}} \tag{II.59}$$

We can compare $\mathrm{Tr}\,\hat{\rho} = \sum_{\sigma_\mathrm{i}} p_{\sigma_\mathrm{i}} = 1$ and $\mathrm{Tr}\,\hat{\mathcal{O}} = 2u$, to get $u = 1/2$, and $\mathrm{Tr}\left[\hat{\mathcal{O}}\hat{\boldsymbol{\sigma}}\right] = 2\boldsymbol{v}$ to Eq. (II.58) to get $\boldsymbol{v} = 1/2\boldsymbol{P}_\mathrm{i}$. Finally the density matrix for the initial spin state is given by

$$\hat{\rho} = \frac{1}{2}(\hat{\mathbb{1}} + \boldsymbol{P}_\mathrm{i} \cdot \hat{\boldsymbol{\sigma}}). \tag{II.60}$$

By closure relation, the spin part from Eq. II.7 becomes:

$$\sum_{\sigma_\mathrm{i}\sigma_\mathrm{f}} p_{\sigma_\mathrm{i}} \left\langle\sigma_\mathrm{i}\right| \hat{V}^\dagger \left|\sigma_\mathrm{f}\right\rangle\!\left\langle\sigma_\mathrm{f}\right| \hat{V} \left|\sigma_\mathrm{i}\right\rangle = \sum_{\sigma_\mathrm{i}} p_{\sigma_\mathrm{i}} \left\langle\sigma_\mathrm{i}\right| \hat{V}^\dagger\hat{V} \left|\sigma_\mathrm{i}\right\rangle = \mathrm{Tr}\left[\hat{\rho}\hat{V}^\dagger\hat{V}\right]. \tag{II.61}$$

As we want to evaluate the action of the interaction operator $\hat{V} = \hat{u}\hat{\mathbb{1}} + \hat{\boldsymbol{v}} \cdot \hat{\boldsymbol{\sigma}}$ in the spin space, using properties of Pauli matrices (Appendix A) this is equivalent to

$$\mathrm{Tr}\left[\hat{\rho}\hat{V}^\dagger\hat{V}\right] = \hat{u}^\dagger\hat{u} + \hat{\boldsymbol{v}}^\dagger \cdot \hat{\boldsymbol{v}} + \hat{u}^\dagger(\boldsymbol{P}_\mathrm{i} \cdot \hat{\boldsymbol{v}}) + (\boldsymbol{P}_\mathrm{i} \cdot \hat{\boldsymbol{v}}^\dagger)\hat{u} + \mathrm{i}\boldsymbol{P}_\mathrm{i} \cdot (\hat{\boldsymbol{v}}^\dagger \times \hat{\boldsymbol{v}}). \tag{II.62}$$

From the previous sections, we can express the general Fourier transform of the interaction potential as

$$\hat{V}(\boldsymbol{Q}) = \frac{2\pi\hbar^2}{m_\mathrm{n}}(\hat{N} + \hat{\boldsymbol{T}} \cdot \hat{\boldsymbol{\sigma}} + \hat{\boldsymbol{M}}_\perp \cdot \hat{\boldsymbol{\sigma}}), \tag{II.63}$$

where the term $\hat{\boldsymbol{T}}(\boldsymbol{Q}) = \sum_j B_j \hat{\boldsymbol{I}}_j \mathrm{e}^{\mathrm{i}\boldsymbol{Q}\hat{\boldsymbol{R}}_j}$ due to nuclear spins $\hat{\boldsymbol{I}}_j$ of the j-th atom will be neglected in the following. The $\boldsymbol{Q}$-dependence of the operators will be implicit, in order to simplify the notations. With this interaction potential, Eq. II.62 becomes

$$\mathrm{Tr}\left[\hat{\rho}\hat{V}^\dagger\hat{V}\right] = \hat{N}^\dagger\hat{N} + \hat{\boldsymbol{M}}_\perp^\dagger \cdot \hat{\boldsymbol{M}}_\perp + \hat{N}^\dagger(\boldsymbol{P}_\mathrm{i} \cdot \hat{\boldsymbol{M}}_\perp) + (\boldsymbol{P}_\mathrm{i} \cdot \hat{\boldsymbol{M}}_\perp^\dagger)\hat{N} + \mathrm{i}\boldsymbol{P}_\mathrm{i} \cdot (\hat{\boldsymbol{M}}_\perp^\dagger \times \hat{\boldsymbol{M}}_\perp). \tag{II.64}$$

We can generalize the correlation function based on the thermal average of the scatterer states in Eq. (II.12) for any operator $\hat{\mathcal{O}}$ and $\hat{\mathcal{P}}$ and use the following notation for the time-energy Fourier transform:

$$\left\langle \hat{\mathcal{P}}^\dagger\hat{\mathcal{O}} \right\rangle_\omega = \frac{1}{2\pi\hbar}\int_{-\infty}^{+\infty} \mathrm{d}t\, \mathrm{e}^{-\mathrm{i}\omega t} \left\langle \hat{\mathcal{P}}^\dagger(0)\hat{\mathcal{O}}(t) \right\rangle. \tag{II.65}$$

With this notation, from Eq. (II.64) the partial differential cross section becomes

$$\begin{aligned}\frac{\mathrm{d}^2\sigma}{\mathrm{d}\Omega\,\mathrm{d}E_\mathrm{f}} = \frac{k_\mathrm{f}}{k_\mathrm{i}} \Big\{ &\left\langle \hat{N}^\dagger\hat{N} \right\rangle_\omega + \left\langle \hat{\boldsymbol{M}}_\perp^\dagger \cdot \hat{\boldsymbol{M}}_\perp \right\rangle_\omega + \\ &\boldsymbol{P}_\mathrm{i} \cdot \left(\left\langle \hat{N}^\dagger\hat{\boldsymbol{M}}_\perp \right\rangle_\omega + \left\langle \hat{\boldsymbol{M}}_\perp^\dagger\hat{N} \right\rangle_\omega \right) + \mathrm{i}\boldsymbol{P}_\mathrm{i} \cdot \left\langle \hat{\boldsymbol{M}}_\perp^\dagger \times \hat{\boldsymbol{M}}_\perp \right\rangle_\omega \Big\}.\end{aligned} \tag{II.66}$$

Scattered beam polarization

The initial states $|\sigma_\mathrm{i}\rangle$ transform with the interaction operator into states $\hat{V}|\sigma_\mathrm{i}\rangle$. Thus similarly to Eq. II.58, we can define the final polarization of the neutron beam as the expectation value of the neutron spin operator over the final states

$$\sum_{\sigma_\mathrm{i}} p_{\sigma_\mathrm{i}} \langle\sigma_\mathrm{i}|\, \hat{V}^\dagger\hat{\boldsymbol{\sigma}}\hat{V}\, |\sigma_\mathrm{i}\rangle = \mathrm{Tr}\Big[\hat{\rho}\hat{V}^\dagger\hat{\boldsymbol{\sigma}}\hat{V}\Big]. \tag{II.67}$$

As the scattering process is in general non-unitary, this quantity has to be

normalized to get a final polarization $\boldsymbol{P}_\mathrm{f}$ with an amplitude within $[0,1]$ [112]

$$\boldsymbol{P}_\mathrm{f} = \frac{\mathrm{Tr}\left[\hat{\rho}\hat{V}^\dagger\hat{\boldsymbol{\sigma}}\hat{V}\right]}{\mathrm{Tr}\left[\hat{\rho}\hat{V}^\dagger\hat{V}\right]}. \tag{II.68}$$

Similarly to Eq. II.62 we can derive from the Pauli matrices properties (Appendix A) for a general operator acting on the spin space $\hat{V} = \hat{u}\hat{\mathbb{1}} + \hat{\boldsymbol{v}}\cdot\hat{\boldsymbol{\sigma}}$:

$$\begin{aligned}\mathrm{Tr}\left[\hat{\rho}\hat{V}^\dagger\hat{\boldsymbol{\sigma}}\hat{V}\right] = \hat{u}^\dagger\hat{\boldsymbol{v}} + \hat{\boldsymbol{v}}^\dagger\hat{u} + \hat{u}^\dagger\hat{u}\boldsymbol{P}_\mathrm{i} - \boldsymbol{P}_\mathrm{i}(\hat{\boldsymbol{v}}^\dagger\cdot\hat{\boldsymbol{v}}) + \hat{\boldsymbol{v}}^\dagger(\boldsymbol{P}_\mathrm{i}\cdot\hat{\boldsymbol{v}}) + (\boldsymbol{P}_\mathrm{i}\cdot\hat{\boldsymbol{v}}^\dagger)\hat{\boldsymbol{v}} + \\ -\mathrm{i}(\hat{\boldsymbol{v}}^\dagger\times\hat{\boldsymbol{v}}) + \mathrm{i}\hat{u}^\dagger(\hat{\boldsymbol{v}}\times\boldsymbol{P}_\mathrm{i}) + \mathrm{i}(\boldsymbol{P}_\mathrm{i}\times\hat{\boldsymbol{v}}^\dagger)\hat{u}.\end{aligned} \tag{II.69}$$

Applying this with the interaction potential given in Eq. II.63 then multiplying left- and right-hand sides of Eq. II.68 by $\mathrm{Tr}\left[\hat{\rho}\hat{V}^\dagger\hat{V}\right]$ and evaluating the matrix element over the scatter states as described previously (thermal average value and time Fourier transform), we obtain the relation between the final and initial polarizations:

$$\begin{aligned}\boldsymbol{P}_\mathrm{f}\frac{\mathrm{d}^2\sigma}{\mathrm{d}\Omega\,\mathrm{d}E_\mathrm{f}} = \frac{k_\mathrm{f}}{k_\mathrm{i}}\Big\{&\left\langle\hat{N}^\dagger\hat{\boldsymbol{M}}_\perp\right\rangle_\omega + \left\langle\hat{\boldsymbol{M}}_\perp^\dagger\hat{N}\right\rangle_\omega \\ &+\boldsymbol{P}_\mathrm{i}\left\langle\hat{N}^\dagger\hat{N}\right\rangle_\omega - \boldsymbol{P}_\mathrm{i}\left\langle\hat{\boldsymbol{M}}_\perp^\dagger\cdot\hat{\boldsymbol{M}}_\perp\right\rangle_\omega \\ &+\left\langle\hat{\boldsymbol{M}}_\perp^\dagger(\hat{\boldsymbol{M}}_\perp\cdot\boldsymbol{P}_\mathrm{i})\right\rangle_\omega + \left\langle(\hat{\boldsymbol{M}}_\perp^\dagger\cdot\boldsymbol{P}_\mathrm{i})\hat{\boldsymbol{M}}_\perp\right\rangle_\omega \\ &+\mathrm{i}\left\langle\hat{N}^\dagger(\hat{\boldsymbol{M}}_\perp\times\boldsymbol{P}_\mathrm{i})\right\rangle_\omega + \mathrm{i}\left\langle(\boldsymbol{P}_\mathrm{i}\times\hat{\boldsymbol{M}}_\perp^\dagger)\hat{N}\right\rangle_\omega \\ &-\mathrm{i}\left\langle\hat{\boldsymbol{M}}_\perp^\dagger\times\hat{\boldsymbol{M}}_\perp\right\rangle_\omega\Big\}.\end{aligned} \tag{II.70}$$

Eq. (II.66) and Eq. (II.70) are the so-called Blume-Maleev equations [110, 111], generalized here for inelastic scattering cross sections.

II.4.2 Spherical Neutron Polarimetry

Spherical neutron polarimetry (SNP) is a powerful technique used to determine complex magnetic structures and magnetic chiralities, which plainly demonstrates

the benefits of using polarized neutrons [112, 115]. The idea is to measure in three orthogonal directions the final polarization of the neutrons, for incident neutrons polarized along each of the three directions. This allows to measure a 3×3 polarization matrix given by

$$P_{if} = \frac{n_{if} - n_{i\bar{f}}}{n_{if} + n_{i\bar{f}}}, \tag{II.71}$$

where $i, f = x, y, z$ denotes the polarization direction of the incident and scattered neutrons in the local coordinates where $\hat{\boldsymbol{x}}$ is parallel to the scattering vector $\boldsymbol{Q}$, $\hat{\boldsymbol{z}}$ is perpendicular to the scattering plane and $\hat{\boldsymbol{y}}$ completes this right-handed set as shown in Fig. II.4, n_{if} and $n_{i\bar{f}}$ are the number of scattered neutrons with spin parallel and antiparallel to the f-direction.

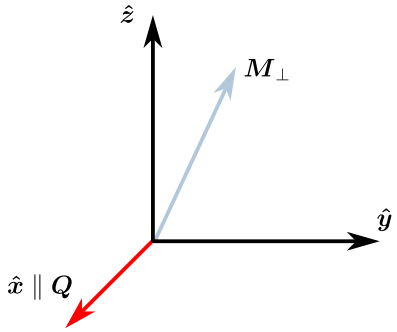

Figure II.4 Local coordinates used in polarimetry, $\hat{\boldsymbol{x}}$ is parallel to the scattering vector $\boldsymbol{Q}$, $\hat{\boldsymbol{y}}$ is in the scattering plane, and $\hat{\boldsymbol{z}}$ is perpendicular to the scattering plane, so that the magnetic interaction vector $\boldsymbol{M}_\perp$ lies on the (yz)-plane.

Now we want to derive the final polarization for the initial polarization in each of the three directions, in the local coordinates. We will introduce the following notations to further simplify the equations:

$$\begin{aligned}
\sigma_{\mathrm{N}} &= \left\langle \hat{N}^\dagger \hat{N} \right\rangle_\omega, \text{ the nuclear term} \\
\sigma_{\mathrm{M}} &= \left\langle \hat{\boldsymbol{M}}_\perp^\dagger \cdot \hat{\boldsymbol{M}}_\perp \right\rangle_\omega, \text{ the magnetic term} \\
M_{ii=yy,zz} &= \left\langle \hat{M}_{\perp i}^\dagger \hat{M}_{\perp i} \right\rangle_\omega, \text{ the magnetic component term} \\
M_{\mathrm{ch}} &= \mathrm{i} \left\langle \hat{\boldsymbol{M}}_\perp^\dagger \times \hat{\boldsymbol{M}}_\perp \right\rangle_\omega, \text{ the magnetic chiral term} \\
M_{yz} &= \left\langle \hat{M}_{\perp y}^\dagger \hat{M}_{\perp z} \right\rangle_\omega + \left\langle \hat{M}_{\perp z}^\dagger \hat{M}_{\perp y} \right\rangle_\omega, \text{ the magnetic cross term} \\
R_{i=y,z} &= \left\langle \hat{N}^\dagger \hat{M}_{\perp i} \right\rangle_\omega + \left\langle \hat{M}_{\perp i}^\dagger \hat{N} \right\rangle_\omega, \text{ the nuclear-magnetic real term} \\
I_{i=y,z} &= \mathrm{i} \left\langle \hat{N}^\dagger \hat{M}_{\perp i} \right\rangle_\omega - \mathrm{i} \left\langle \hat{M}_{\perp i}^\dagger \hat{N} \right\rangle_\omega, \text{ the nuclear-magnetic imaginary term.}
\end{aligned} \tag{II.72}$$

Let's consider $\boldsymbol{P}_\mathrm{i} = P_x\hat{\boldsymbol{x}}$ along the x -axis. In this case, the partial differential cross section is simplified from Eq. II.66:

$$\frac{\mathrm{d}^2\sigma}{\mathrm{d}\Omega\,\mathrm{d}E_\mathrm{f}} = \frac{k_\mathrm{f}}{k_\mathrm{i}}(\sigma_\mathrm{N} + \sigma_\mathrm{M} + P_x M_\mathrm{ch}), \tag{II.73}$$

as $\hat{M}_{\perp x} = 0$ (neutrons are only sensitive to the magnetic moments perpendicular to the scattering vector). The right-hand side of Eq. II.70 also simplifies by identifying the components of the polarization vector:

$$\boldsymbol{P}_\mathrm{f}(\sigma_\mathrm{N} + \sigma_\mathrm{M} + P_x M_\mathrm{ch}) = \begin{pmatrix} P_x(\sigma_\mathrm{N} - \sigma_\mathrm{M}) - M_\mathrm{ch} \\ P_x I_z + R_y \\ -P_x I_y + R_z \end{pmatrix}. \tag{II.74}$$

We obtain $\boldsymbol{P}_\mathrm{f}$ for $\boldsymbol{P}_\mathrm{i} = P_x\hat{\boldsymbol{x}}$ by dividing both sides of the equation, and this gives the first line of the polarization matrix P_{xf}. Doing similar calculations for $\boldsymbol{P}_\mathrm{i}$ along the y- and the z-axis, we can calculate each corresponding final polarization and derive the full polarization matrix [112, 115]:

$$P_{if} = \begin{pmatrix} \frac{P_x(\sigma_\mathrm{N} - \sigma_\mathrm{M}) - M_\mathrm{ch}}{\sigma_\mathrm{N} + \sigma_\mathrm{M} + P_x M_\mathrm{ch}} & \frac{P_x I_z + R_y}{\sigma_\mathrm{N} + \sigma_\mathrm{M} + P_x M_\mathrm{ch}} & \frac{-P_x I_y + R_z}{\sigma_\mathrm{N} + \sigma_\mathrm{M} + P_x M_\mathrm{ch}} \\ \frac{-P_y I_z - M_\mathrm{ch}}{\sigma_\mathrm{N} + \sigma_\mathrm{M} + P_y R_y} & \frac{P_y(\sigma_\mathrm{N} + M_{yy} - M_{zz}) + R_y}{\sigma_\mathrm{N} + \sigma_\mathrm{M} + P_y R_y} & \frac{P_y R_{zy} + R_z}{\sigma_\mathrm{N} + \sigma_\mathrm{M} + P_y R_y} \\ \frac{P_z I_y - M_\mathrm{ch}}{\sigma_\mathrm{N} + \sigma_\mathrm{M} + P_z R_z} & \frac{P_z M_{yz} + R_y}{\sigma_\mathrm{N} + \sigma_\mathrm{M} + P_z R_z} & \frac{P_z(\sigma_\mathrm{N} + M_{zz} - M_{yy}) + R_z}{\sigma_\mathrm{N} + \sigma_\mathrm{M} + P_z R_z} \end{pmatrix}. \tag{II.75}$$

Each element of the polarization matrix P_{if} corresponds to the polarization of the neutron beam along the f-axis, for an initial polarization of the neutron beam along the i-axis.

The first polarimetry technique, named longitudinal polarization analysis (LPA), was introduced by Moon, Riste and Koehler in 1969 [116]. In this case the polarization of the scattered beam is parallel (non spin-flip) or anti-parallel (spin-flip) to the incident beam. This technique basically gives access to the terms in the diagonal of the polarization matrix. This allows to separate nuclear and magnetic scattering, to access the individual components of the

magnetic cross section and the magnetic chiral[9] term [113]. In addition, SNP provides to the full vectorial information of the scattering process with the off-diagonal terms of the polarization matrix, allowing to distinguish spin rotation and creation/annihilation of the beam polarization.

For elastic scattering, the nuclear and magnetic terms σ_{N} and σ_{M} are simply replaced by the amplitude squared of the unit cell nuclear and magnetic structure factors $|F_{\mathrm{N}}|^2$ and $|\boldsymbol{F}_{\mathrm{M}_\perp}|^2$ respectively introduced in Eq. (II.29) and Eq. (II.54). Furthermore, considering a purely magnetic reflection, the nuclear contributions and nuclear-magnetic interference terms vanish, giving:

$$P_{if} = \begin{pmatrix} \dfrac{-P_x|\boldsymbol{F}_{\mathrm{M}_\perp}|^2 - M_{\mathrm{ch}}}{|\boldsymbol{F}_{\mathrm{M}_\perp}|^2 + P_x M_{\mathrm{ch}}} & 0 & 0 \\ \dfrac{-M_{ch}}{|\boldsymbol{F}_{\mathrm{M}_\perp}|^2} & \dfrac{P_y(|F_{\mathrm{M}_\perp y}|^2 - |F_{\mathrm{M}_\perp z}|^2)}{|\boldsymbol{F}_{\mathrm{M}_\perp}|^2} & \dfrac{2P_y\,\mathrm{Re}\{F_{\mathrm{M}_\perp y}F^*_{\mathrm{M}_\perp z}\}}{|\boldsymbol{F}_{\mathrm{M}_\perp}|^2} \\ \dfrac{-M_{ch}}{|\boldsymbol{F}_{\mathrm{M}_\perp}|^2} & \dfrac{2P_z\,\mathrm{Re}\{F_{\mathrm{M}_\perp z}F^*_{\mathrm{M}_\perp y}\}}{|\boldsymbol{F}_{\mathrm{M}_\perp}|^2} & \dfrac{P_z(|F_{\mathrm{M}_\perp z}|^2 - |F_{\mathrm{M}_\perp y}|^2)}{|\boldsymbol{F}_{\mathrm{M}_\perp}|^2} \end{pmatrix}. \quad \text{(II.76)}$$

The polarization matrix provides accurate information on the relative directions and magnitudes of the magnetic moments while unpolarized neutron single-crystal diffraction is only sensitive to the amplitude squared $|\boldsymbol{F}_{\mathrm{M}_\perp}|^2$ of the magnetic structure factor. In general, measuring a few magnetic reflections is sufficient to solve complex magnetic structures [115, 117–119]. In absence of nuclear-magnetic interference, only the relative magnitude of the magnetic moments can be measured. In the presence of magnetic domains, the polarization matrices have to be averaged. In particular, if chiral magnetic domains have the same population, the chiral term will average to zero.

From an experimental point of view, SNP requires a system which can control independently the initial and final polarization directions of the neutron beams and protect them from parasitic magnetic fields. At ILL, the CRYOPAD (Cryogenic Polarization Analysis Device) is used [120–122], and described in Section II.5.3.

[9] In the sense of spin vector chirality defined in Eq. (III.3).

II.4.3 Schwinger scattering

In the reference frame of a moving neutron, the electric field of a non-centrosymmetric crystal creates an effective magnetic field which couples to the neutron spin. This neutron spin-orbit interaction results in a polarization-dependant scattering known as Schwinger scattering [123] which can be used as a probe of the structural handedness of the crystal [124, 125].

In the local coordinates, where $\hat{\boldsymbol{z}} \parallel \boldsymbol{k}_\mathrm{i} \times \boldsymbol{k}_\mathrm{f}$ is perpendicular to the scattering plane, the asymmetric Schwinger structure factor is given by [125]

$$F_\mathrm{SO}(\boldsymbol{Q}) = \mathrm{i}\frac{\gamma r_0}{2}\frac{m_\mathrm{e}}{m_\mathrm{p}} F_\mathrm{E}(\boldsymbol{Q}) \cot(\theta) \hat{\boldsymbol{\sigma}} \cdot \hat{\boldsymbol{z}}, \tag{II.77}$$

where γ is the neutron gyromagnetic ratio, r_0 is the electron classical radius, θ is half of the scattering angle, $\hat{\boldsymbol{\sigma}}$ is the neutron spin operator, and $F_\mathrm{E}(\boldsymbol{Q})$ is the electrostatic unit cell structure factor:

$$F_\mathrm{E}(\boldsymbol{Q}) = \sum_j [Z_j - f_j(\boldsymbol{Q})] \mathrm{e}^{-W_j(\boldsymbol{Q})} \mathrm{e}^{-\mathrm{i}\boldsymbol{Q}\cdot\boldsymbol{r}_j}, \tag{II.78}$$

where Z_j, $f_j(\boldsymbol{Q})$ and $W_j(\boldsymbol{Q})$ are respectively the atomic number, the X-ray atomic form factor [Eq. (II.86)], and the Debye-Waller factor of the j-th atom of the unit cell. The small ratio between the electron and proton mass $m_\mathrm{e}/m_\mathrm{p}$ leads to a weak Schwinger scattering cross section $\propto \frac{\gamma r_0}{2}\frac{m_\mathrm{e}}{m_\mathrm{p}} = -1.46 \times 10^{-4}$ in units of $10^{-12}\,\mathrm{cm}$ (nuclear scattering length) [124]. For a nuclear reflection, the contribution from Schwinger scattering adds to the nuclear structure factor F_N (Eq. II.29) leading to an intensity:

$$I^\pm \propto |F_\mathrm{N}|^2 + |F_\mathrm{SO}|^2 \pm \mathcal{I}, \tag{II.79}$$

where $\mathcal{I} = 2p\,\mathrm{Re}(F_\mathrm{N} F_\mathrm{SO}^*)$ is an interference term and p is the polarization of the incident beam along $\pm\hat{\boldsymbol{z}}$. Measuring both intensities with the incident neutron beam polarized along $\pm\hat{\boldsymbol{z}}$ allows us to compute the flipping ratio:

$$R = \frac{|F_\mathrm{N}|^2 + |F_\mathrm{SO}|^2 + \mathcal{I}}{|F_\mathrm{N}|^2 + |F_\mathrm{SO}|^2 - \mathcal{I}}. \tag{II.80}$$

The flipping ratio technique, very well known to the magnetization density community, affords the extraction of the weak Schwinger scattering and to distinguish structural twins in a single crystal discussed below. Indeed, each twin would lead to a different flipping ratio. For example the flipping ratio is inverted for an inversion twin.

As explained above, Schwinger scattering is weak compared to nuclear scattering. In this case we can simplify the previous equation by dividing both numerator and denominator by $|F_{\mathrm{N}}|^2$, and writting $\epsilon = \mathcal{I}/|F_{\mathrm{N}}|^2$ at first order of $\epsilon \approx |F_{\mathrm{SO}}/F_{\mathrm{N}}|$ we obtain

$$R \approx \frac{1+\epsilon}{1-\epsilon} \approx 1 + 2\epsilon + \mathcal{O}\big(\epsilon^2\big). \tag{II.81}$$

In this case, the flipping ratio of the inversion twin is directly given by $R \approx 1-2\epsilon$. This gives the convenient constraint that the flipping ratios are at equal opposite distance from 1:

$$R(hkl) - 1 = -(R(\bar{h}\bar{k}\bar{l}) - 1). \tag{II.82}$$

II.5 Instruments

Having introduced the theory of neutron scattering, several instrumental techniques from continuous sources used during this thesis will be described in this section.

II.5.1 Powder diffractometer

A powder sample can be seen as a very large number of small crystallites randomly oriented. In average (ideally for grains of a few microns) there are always some crystallites which are correctly oriented to satisfy Bragg's law (Eq. II.30) for each (hkl) plane. Actually each set of planes will scatter the neutrons in a Debye-Scherrer cone centered around the incident beam direction, with the semi-angle 2θ corresponding to the Bragg angle. This is illustrated in Fig. II.5 where the incident beam scatters from the red crystallites at angle $2\theta_1$ and on the green ones at $2\theta_2$ into two diffraction cones.

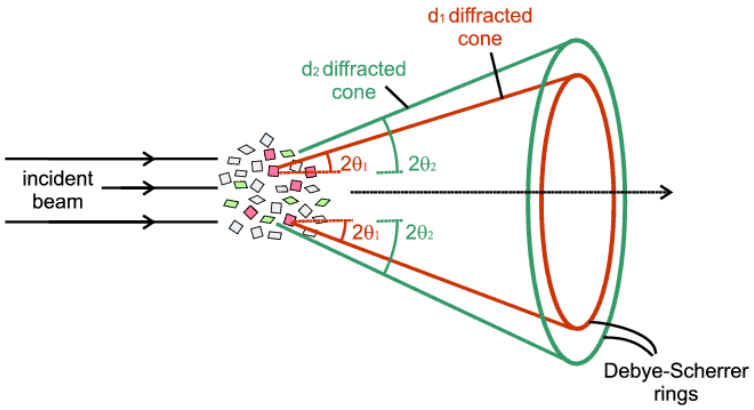

Figure II.5 Neutrons are scattered from red and green crystallites into different scattering angles $2\theta_1$ and $2\theta_2$, forming two Debye-Scherrer cones. Figure taken from Ref. [126].

In steady-state neutron sources, the incoming neutrons pass through a monochromator[10] which selects a unique wavelength, as illustrated in Fig. II.6 for the high-resolution diffractometer D20 at ILL [127] used in this thesis (Section III.4.2.1). Each set of planes (hkl) allows an elastic signal at scattering angle 2θ, which is collected by a range of the microstrip multidetector around the sample.

The result of the measurement is a diffraction pattern showing the scattering intensity as a function of the scattering angle. The Bragg reflections are not perfect shaped as δ-functions as predicted in Eq. II.28 and Eq. II.53 but rather convolutions with the instrumental resolution effects. As a result, diffraction bands are observed corresponding to the intersection between the finite Debye-Scherrer cone and the detectors (the Debye-Scherrer rings shown in Fig. II.5). The peak positions, profile functions, instrumental parameters are taken into account to calculate intensity profiles which are fitted to the observed intensities during a Rietveld refinement [129]. It uses a weighted least squares method to minimize the quantity

$$\chi^2 = \sum_i w_i (y_i^{\text{obs}} - y_i^{\text{cal}})^2, \tag{II.83}$$

where y_i^{obs} and y_i^{cal} are the observed and calculated intensities for the i-th data point, and w_i a weight for the refinement, typically the inverse of the variance

[10] Basically a coalignment of single crystals such as pyrolitic graphite, copper, germanium or silicium. For a given reflection plane, rotating the monochromator at a specific scattering angle allows to select a specific incident wavelength λ according to Eq. (II.30). Higher harmonics λ/n are typically suppressed by graphite or beryllium filters.

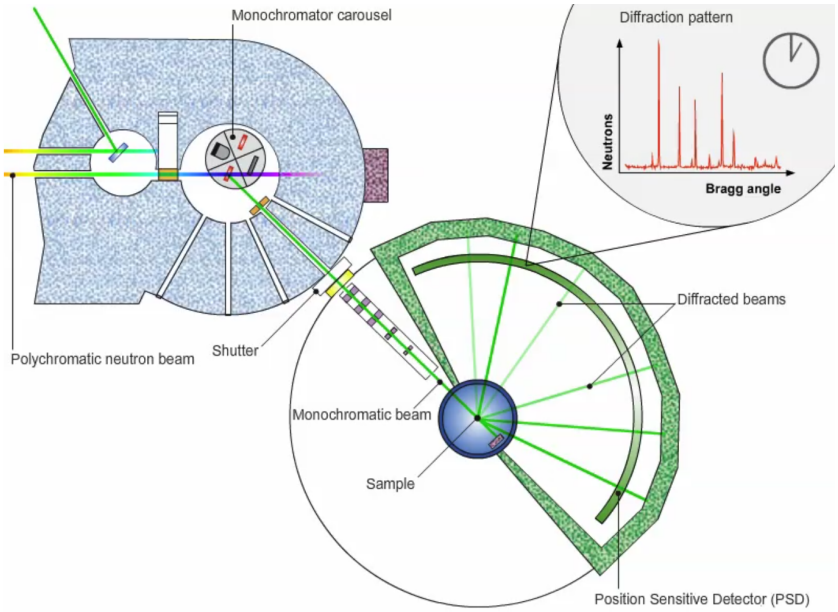

Figure II.6 Diagram of high resolution powder diffractometer D20 at ILL. A monochromatic neutron beam scatters on the polycrystalline sample, and intensity is measured at scattering angles satisfying Bragg's law on the large microstrip multidetector. Figure taken from Ref. [128].

of the observed intensities. The intensities are basically proportional (up to a background term and some correction factors) to the amplitude square of the elastic structure factors $|F_{\boldsymbol{Q}}|^2$, which directly contains information from the crystal and magnetic structures of the material.

II.5.2 Single-crystal diffractometer

In the case the sample is a single crystal, knowing its orientation is crucial in order to control the Bragg scattering. This can be done by using the Laue method. A polychromatic incident (neutron or X-ray) beam is sent on the single crystal for a given orientation. Each set of lattice planes satisfying Bragg's law would scatter the beam onto the 2D detector at a particular angle, resulting in a Laue diffraction pattern composed of a collection of Bragg spots. This pattern gives a picture of the reciprocal space, depending on the crystal symmetry and its orientation, as shown in Fig. II.7. The single crystal is usually fixed on a goniometer, so that it can be oriented to the needed crystallographic axes before the single crystal scattering experiments. During this thesis, we have used OrientExpress at ILL [130], which uses CCD cameras coupled to a large-area neutron scintillator in the

back-reflection geometry, allowing the measurements of neutron Laue pattern in a very short time. We note that Laue diffraction also shows the quality of the sample, a high mosaicity in the crystal giving a spread in the Bragg spots.

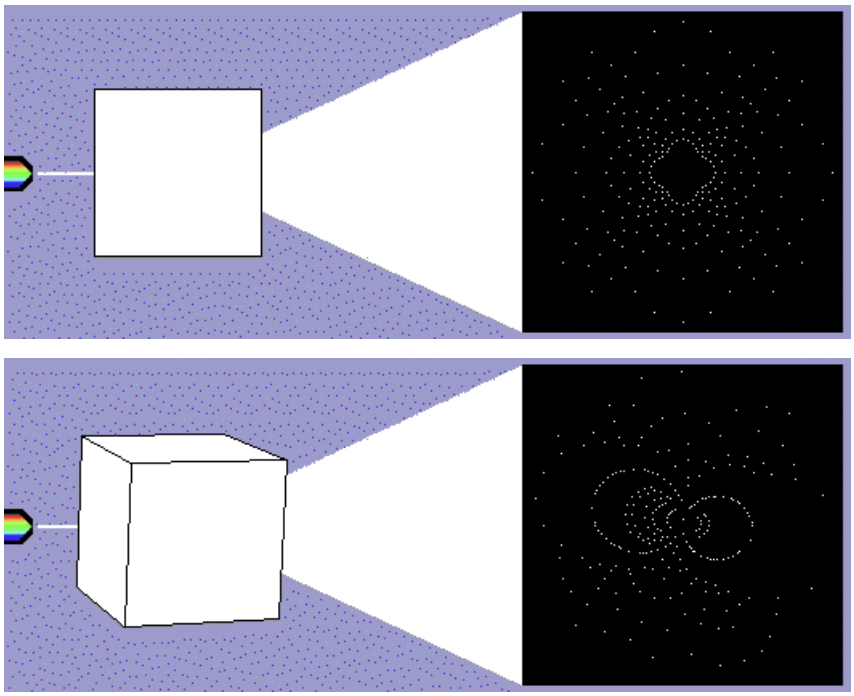

Figure II.7 Laue diffraction patterns for a cubic single crystal for different orientations. Figure taken from Ref. [131].

After being correctly oriented[11], the single crystal can be measured in a a four-circle diffractometer using a monochromatic incident neutron beam. The sample is mounted onto a Eulerian cradle on which it can be reoriented along three rotation angles φ, χ and ω as shown in Fig. II.8. This allows a flexibility in selecting the scattering plane (up to the instrumental limits of the rotation angles). The 2D-detector can be moved along the scattering angle 2θ for the selected Bragg reflection and records the intensity diffracted by the sample, which is usually rotated around the vertical axis (ω-scan) through the settings of the diffraction condition. This whole process is illustrated in Fig. II.8 for the hot neutron four-circle diffractometer D9 at ILL, whose short wavelength allows the accurate measurements of Bragg intensities up to very high momentum transfer. This makes D9 ideal for detailed structural analysis as presented in Section III.4.1.1 and Section V.1.2. We have also used the high flux four-circle diffractometer D10 at ILL which uses thermal neutrons allowing accurate

[11] Actually in four-circle geometry, the sample could be oriented during the experiment by finding reflections, but starting from a known orientation can save a lot of time. On the other hand, having the correct orientation is primordial in normal-beam geometry where the vertical axis of the sample is fixed with respect to the scattering plane.

measurements of magnetic Bragg peaks located at low momentum transfer, as presented in Section III.4.2.2.

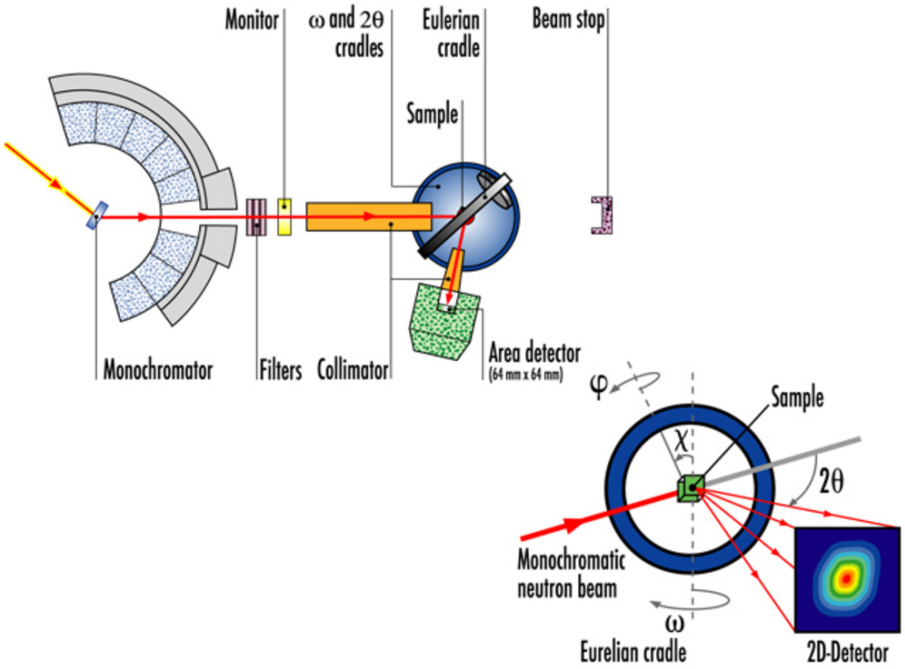

Figure II.8 Diagram of hot neutron four-circle diffractometer D9 at ILL. A monochromatic neutron beam scatters on the single-crystal mounted on an Eulerian cradle which allows to select to desired orientation for Bragg scattering, onto a 2D-detector from which the intensities are integrated. Figure taken from Ref. [132].

The process is repeated for a numerous number of Bragg reflections (typically several hundreds). The collected intensities are integrated taking into account an instrument resolution ellipse. The crystal and magnetic structures can then be refined with a weighted least squares method described in Eq. (II.83), where y_i^{obs} is now the integrated intensity for the i-th Bragg reflection.

In this thesis the refinement of crystal and magnetic structures were performed either on FULLPROF [133] or on MAG2POL [134] softwares, which both allow the analysis of powder and single-crystal diffraction data.

In the process of refinement in these softwares, the goodness of fit can be evaluated by the agreement factors such as the crystallographic R-factor [135]:

$$R_{\text{F}} = 100 \frac{\sum_{\boldsymbol{Q}} \left| F_{\boldsymbol{Q}}^{\text{obs}} - F_{\boldsymbol{Q}}^{\text{cal}} \right|}{\sum_{\boldsymbol{Q}} F_{\boldsymbol{Q}}^{\text{obs}}} \tag{II.84}$$

which indicates the differences between observed and calculated structure factors, or the Bragg factor:

$$R_{\text{Bragg}} = 100\frac{\sum_{\boldsymbol{Q}} \left| I_{\boldsymbol{Q}}^{\text{obs}} - I_{\boldsymbol{Q}}^{\text{cal}} \right|}{\sum_{\boldsymbol{Q}} I_{\boldsymbol{Q}}^{\text{obs}}} \tag{II.85}$$

which indicates the differences between observed and calculated integrated intensities. The sum is over the Bragg contributions to the given phase (allowing to distinguish the nuclear and magnetic refinements for example).

II.5.3 Polarization analysis device

Diffraction techniques using unpolarized neutrons were introduced in the two previous sections. While Schwinger scattering (Section II.4.3) only needs to polarize the incident neutron beam, a polarization analysis device is necessary for Spherical Neutron Polarimetry (Section II.4.2). In this section the use of CRYOPAD (Cryogenic Polarization Analysis Device) [120–122] on the hot neutron single-crystal diffractometer D3 at ILL will be discussed.

The device is pictured in Fig. II.9. The sample is located at the center of the magnetic field free chamber created by two superconducting Meissner shields. The incident monochromatic neutron beam is polarized vertically,[12] the axial guide field turns the neutron polarization axis towards the incident wavevector. Then the incident nutator brings the neutron polarization to any direction perpendicular to the incident wavevector. The combination with the rotation in the secondary precession coil (protected from the nutator magnetic field by the outer Meissner shield) allows the neutron beam to be polarized in any direction in space. After scattering from the sample, and thus a change in the polarization, a similar combination of the primary precession coil and the outgoing nutators allow to pick the polarization which will be analyzed along the final wavevector using a polarized ^{3}He spin filter [137]. The integration of CRYOPAD into the D3 setup is shown in Fig. II.10. We have used CRYOPAD on D3 to perform SNP and Schwinger scattering on $MnSb_2O_6$ (Section III.4) and SNP on $Fe_{1+x}Te$ (Section V.2.2). The data analysis was performed using the MAG2POL software

[12] This is usually done using a Heusler Cu_2MnAl crystal on which we apply a uniform vertical magnetic field to create a single ferromagnetic domain. For the (111) reflection, $F_{\text{N}} \approx -F_{\text{M}_\perp}$, so that the scattered intensity $I^{\pm} \propto |F_{\text{N}} \pm F_{\text{M}_\perp}|^2$ is predominant for spin-down ($-$) neutrons and almost zero for spin-up ($+$) neutrons, producing a highly polarized neutron beam [99].

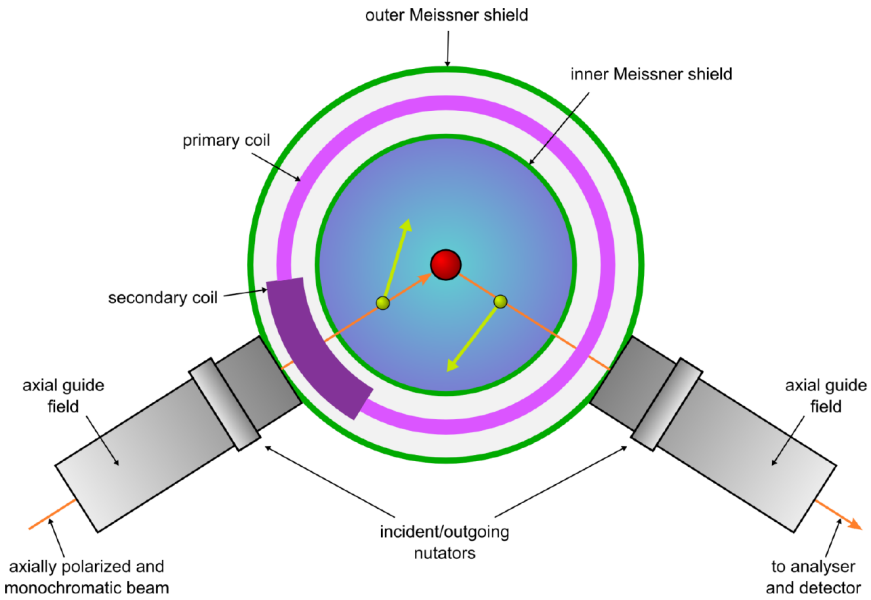

Figure II.9 Diagram of CRYOPAD. The incident and final polarization of the neutron beam are set in any direction thanks to the combination of nutators rotations and coil currents. The sample is located in the cryostat in a zero magnetic field zone. Adapted Figure taken from Ref. [136].

[134].

We note that CRYOPAD can be also used on some spectrometers such as IN12, IN20, IN22 and THALES at ILL in order to perform SNP and access the inelastic cross section. On TASP at PSI, polarization analysis is perfomed using MuPAD (Mu-metal Polarization Analysis Device) [138]. The zero field chamber is created by a non-cryogenic double layered mu-metal cylinder, and the polarization direction of incident and scattered neutron beam is controlled by a set of two precession coils. The polarization of the incident beam, and the polarization analysis of the scattered neutron beam are performed with super-mirror benders [139].

II.5.4 Triple-axis spectrometer

While the diffractometers measure scattering cross sections integrated in final energy (including the inelastic part as a background), a triple-axis spectrometer (TAS) allows the selection of the neutron final energy and thus provides an access to inelastic cross sections. The principle is very similar to previous diffractometers

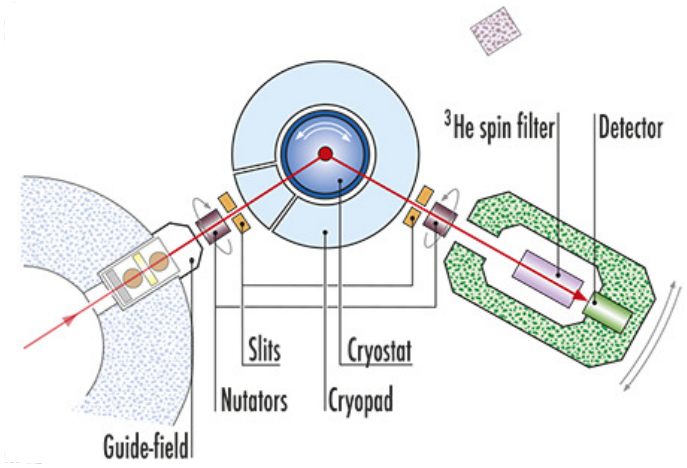

Figure II.10 Diagram of D3 with the CRYOPAD setup. Figure taken from Ref. [136].

and illustrated for TASP at PSI in Fig. II.11. The incident neutron beam is monochromated, then scatters on the sample mounted on a goniometer. Finally, an analyzer (which works the same way as the monochromator) is placed before the detectors. The rotation (around a vertical third axis) of the analyzer scattering angle allows to select the final neutron beam wavelength and thus its energy. Therefore, these spectrometers allow to accurately explore the $(\boldsymbol{Q}, E)$ map and are ideal to study excitations in condensed matter.

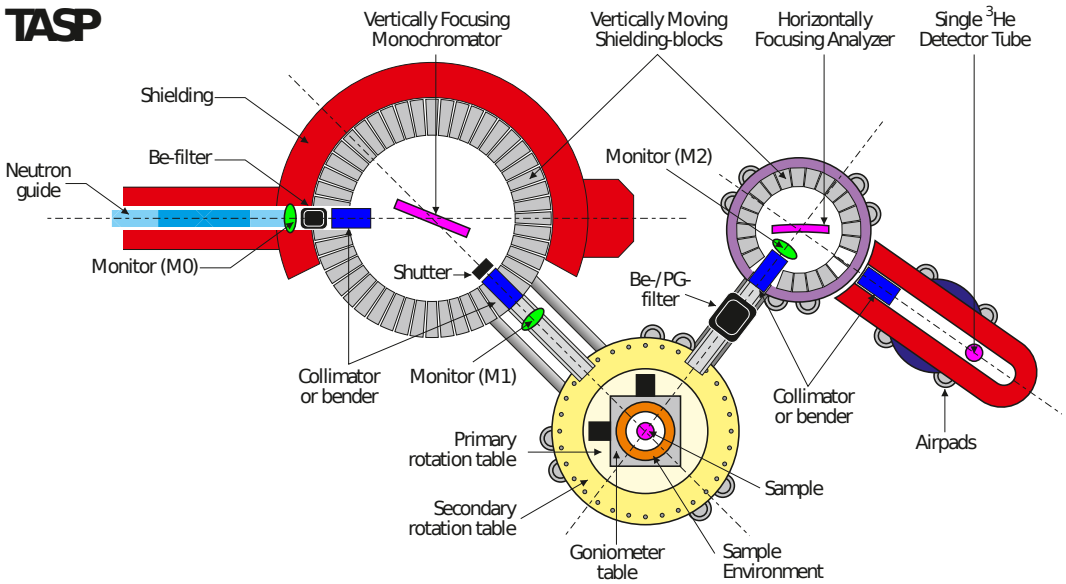

Figure II.11 Diagram of TASP. The monochromator selects the wavelength of the incident neutron beam, which is scattered from the sample. The analyzer selects the final energy, allowing to scan the $(\boldsymbol{Q}, E)$ space. Figure taken from Ref. [140].

In this thesis, we have studied magnetic excitations in $MnSb_2O_6$ (Chapter IV)

using the high flux cold neutron spectrometer MACS [141] at NIST. As inelastic scattering cross sections are generally orders of magnitude smaller than the elastic scattering cross sections, the sample used in spectroscopy must be bigger than for diffraction to increase the scattered intensities. Because of chemistry complications to grow big single crystals, it is possible to coalign arrays of single crystals as a sample for inelastic experiments. This was done for the single crystal experiments on MACS on $MnSb_2O_6$, as shown in Fig. IV.1.

TAS can also be used for more accurate studies of elastic scattering, as the analyzer removes the background from the integrated inelastic scattering. We have used cold TAS RITA-2 (now replaced by CAMEA) at PSI to perform single-crystal diffraction on $MnSb_2O_6$ under an horizontal magnetic field (Section III.4.3).

II.5.5 X-ray powder diffractometer

A laboratory X-ray powder diffractometer (Rigaku SmartLab at the University of Edinburgh) was used to characterize the crystal structure of VI_3 in Section V.3. The theory of X-ray diffraction is similar to neutron diffraction (Section II.2.2) and is therefore not detailed in this thesis. The main difference being that the photons are scattered by the electron clouds of the atoms instead of the point-like nuclei in the case of the neutrons. The scattering length in Eq. (II.29) is replaced by the X-ray atomic form factor (in electron units):

$$f_j(\boldsymbol{Q}) = \int \mathrm{d}^3\boldsymbol{r}\, \rho_j(\boldsymbol{r}) \mathrm{e}^{\mathrm{i}\boldsymbol{Q}\cdot\boldsymbol{r}}, \tag{II.86}$$

where ρ_j is the electron charge density of the j-th atom. An analytical approximation of the form factors are tabulated in Ref. [142]. The form factor decreases with the scattering angle, and for $\theta = 0$, it corresponds to the number of electrons Z_j.

For a X-ray powder diffractometer in the reflection (or Bragg-Brentano) geometry, the X-ray source and the detector are mounted on a goniometer circle, centered on the sample holder, on which the powder sample is uniformly spread. In the $\theta - \theta$ configuration shown in Fig. II.12, the sample is fixed, and X-ray source and detector are moving symmetrically to scan the scattering angle 2θ.

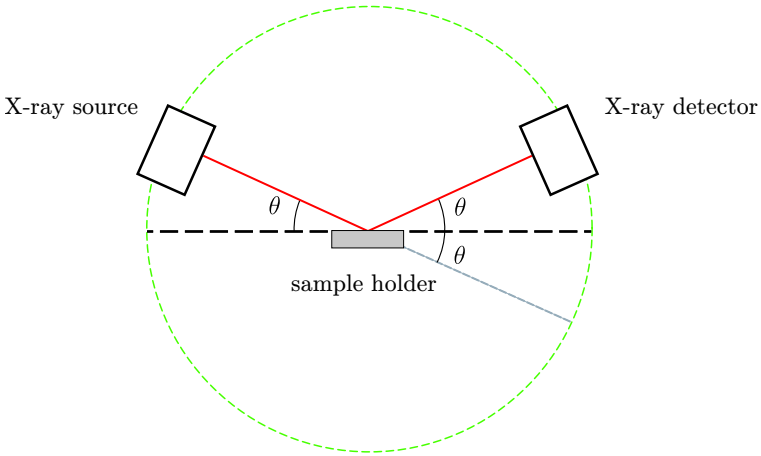

Figure II.12 X-ray powder diffractometer in the Bragg-Brentano geometry, in $\theta - \theta$ mode, where the sample is fixed, and X-ray source and detector moves simultaneously.

Chapter III

Diffraction studies on $MnSb_2O_6$

The next two chapters will be dedicated to the study of $MnSb_2O_6$. Chapter III consists of an introduction to the material followed by results of neutron diffraction experiments. This chapter has been adapted from Ref. [1].

III.1 Introduction

III.1.1 A chiral structure

Coupling magnetism and ferroelectricity would allow the possibility for controlling electric polarization with a magnetic field and magnetic moments with an electric field. However, ferroelectricity and magnetism originate from disparate microscopic mechanisms [25], and such multiferroic materials are rare. Despite these challenges, complex coupling schemes have been intensively studied and sought after for decades, motivated by the interesting physics and promising multifunctional applications [32–35]. For example, noncentrosymmetric magnetic ordering can break inversion symmetry and induce an improper electric polarization via the inverse antisymmetric Dzyaloshinskii-Moriya (DM) interaction [28, 143]. This is the case in cycloidal magnets, often stabilized by the competition of exchange interactions, and where the sense of rotation of the spins can be linked to the sign of the electric polarization [41, 42, 47]. Additional interest can be found in materials having a crystallographic chirality that may naturally stabilize a noncentrosymmetric magnetic structure. For example, iron based

langasite ($Ba_3NbFe_3Si_2O_{14}$ [125, 144–148]) crystallizes in the trigonal space group $P321$, and its structural chirality is coupled to the chirality of its magnetic helix through symmetric Heisenberg exchanges.

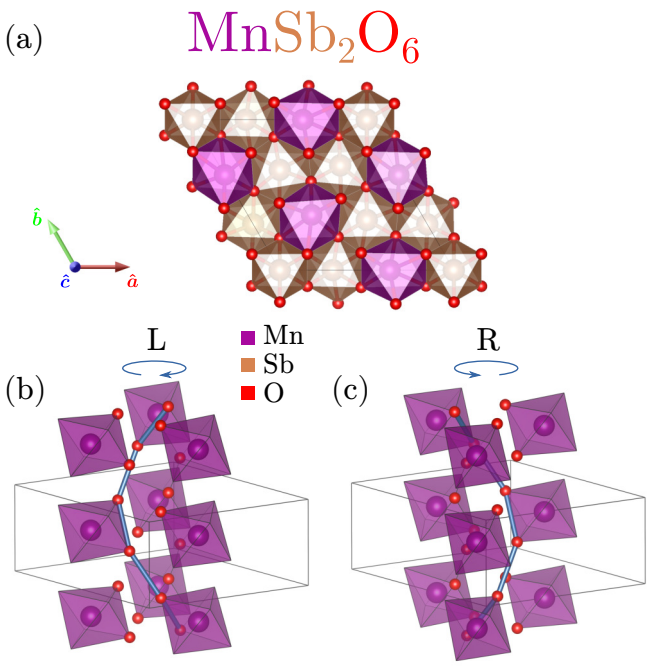

Figure III.1 (a) Crystal structure of chiral $MnSb_2O_6$. The structural chirality can be defined as the helical winding of the Mn-O-O-Mn super-super-exchange path (blue lines) with respect to the c-axis: it is clockwise for left-handed structure (b) and anticlockwise for right-handed structure (c). Figures made using VESTA [149].

Analogous to iron based langasite, $MnSb_2O_6$ crystallizes in the trigonal space group $P321$, which is among the 65 space groups containing only symmetry operations of the first kind: translations, rotations and screw rotations [150]. Referred as the Sohncke groups, they allow chiral crystal structures such as $Ba_3NbFe_3Si_2O_{14}$ and $MnSb_2O_6$. Magnetic manganese ions with a valence of Mn^{2+} give a high spin $S = 5/2$ and orbitally quenched moment, $L \approx 0$ [57]. Isolated MnO_6 octahedra are interconnected by the SbO_6 octahedra, as shown in Fig. III.1(a). The structural chirality can be defined as the helical winding of the Mn-O-O-Mn super-super-exchange (SSE) path along the vertical c-axis. It is left-handed if the winding is clockwise around the c-axis [Fig. III.1(c)], and right-handed if the winding is anti-clockwise [Fig. III.1(d)].

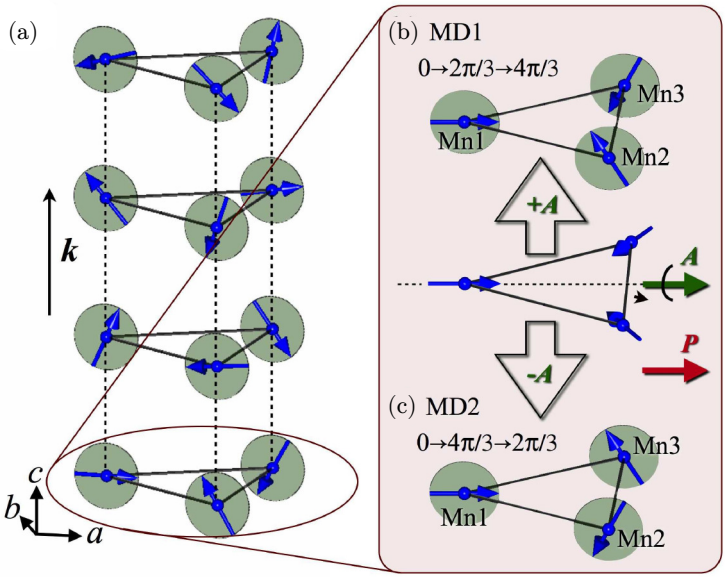

Figure III.2 (a) The magnetic structure of $MnSb_2O_6$ reported in Ref. [57] : Mn atoms form a triangle in the (ab)-plane. The moments are rotating with a cycloidal modulation along the c-axis, and are dephased by $2\pi/3$ within the triangle. The cycloidal polarity $\boldsymbol{P}$ defines the sense of rotation of the cycloids. The axial vector $\boldsymbol{A}$ defines the sense of rotation within the triangle, and can be: (b) parallel, or (c) antiparallel to $\boldsymbol{P}$, defining the magnetic domains MD1 and MD2. Figure taken from Ref. [57].

III.1.2 A polar magnet

Magnetization measurements found long-range magnetic order below $T_N \approx 12\,K$ and some evidence for short-range correlations below 200 K have been provided [151, 152]. Based on earlier neutron powder diffraction experiment the magnetic moments were determined to rotate nearly as cycloids, in the (ac)-plane, with an incommensurate propagation vector $\boldsymbol{k} = (0.015, 0.015, 0.183)$ [151]. Nearest neighbor moments arranged in triangular motifs in the (ab)-plane are dephased by 120°. More recently, Johnson *et al.* measured a propagation vector $\boldsymbol{k} = (0, 0, 0.182)$ and found out that the Mn moments are rotating in the (ac)-plane, forming a pure cycloidal magnetic structure as shown in Fig. III.2 [57]. Two vectors were introduced to describe the sense of rotation of the spins along the cycloidal modulation and within a basal triangle:

- The cycloid polarity was defined as $\boldsymbol{P}_m = \boldsymbol{k} \times (\boldsymbol{S} \times \boldsymbol{S}')$, where $\boldsymbol{S}$ and $\boldsymbol{S}'$ are adjacent spins along the c-axis. $\boldsymbol{P}_m$ is the same for the three Mn atoms in the triangle.
- The magnetic moments of the Mn atoms within triangle are dephased by

$2\pi/3$ and their sense of rotation was defined by the axial vector $\boldsymbol{A} = \boldsymbol{k} \times \boldsymbol{V}$ where $\boldsymbol{V} = \frac{1}{3}(\boldsymbol{S}_1 \times \boldsymbol{S}_2 + \boldsymbol{S}_2 \times \boldsymbol{S}_3 + \boldsymbol{S}_3 \times \boldsymbol{S}_1)$ is the classical chirality vector.

Two distinct magnetic configurations where $\boldsymbol{P}_\mathrm{m}$ and $\boldsymbol{A}$ are parallel or antiparallel were labeled MD1 [Fig. III.2(b)] and MD2 [Fig. III.2(c)]. The sign of the product $\boldsymbol{P}_\mathrm{m} \cdot \boldsymbol{A}$ could be distinguished by single-crystal unpolarized neutron diffraction. They found out a domain fraction MD1(0.8)/MD2(0.2) which was attributed to a non-racemic mixture of two chiral structural domains. In Section III.3.2, we will redefine these vectors and relate them to well-defined, generic magnetic parameters η_C and η_T that couple directly to the crystal chirality σ. In Section III.4.2.2, we will show that the consideration of structural twins is actually necessary to attribute the magnetic domains MD1 and MD2 to chiral structural domains.

III.1.3 Comparison with iron langasite $Ba_3NbFe_3Si_2O_{14}$

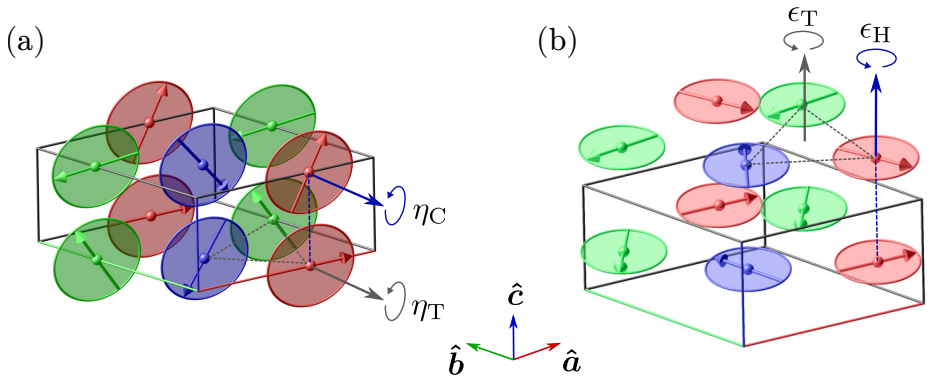

Figure III.3 Magnetic structure of (a) $MnSb_2O_6$ with a cycloidal order and (b) $Ba_3NbFe_3Si_2O_{14}$ with a helical order. Senses of rotation of the spins along the propagation order and within a triangle of magnetic ions are described by magnetic parameters. Figures made using MAG2POL [134].

$MnSb_2O_6$ is structurally and magnetically very similar to $Ba_3NbFe_3Si_2O_{14}$ which also crystallizes in the $P321$ space group [144, 145]. Fe^{3+} are the magnetic ions [in red, green and blue in Fig. III.3(b)] and they also form triangles in the (ab)-plane. The main difference is that the magnetic moments order below $T_\mathrm{N} = 27\,\mathrm{K}$ in the (ab)-plane with an helical modulation with a commensurate propagation vector $\boldsymbol{k} = (0, 0, \sim \frac{1}{7})$ [148], as shown in Fig. III.3(b). In iron langasite, the rotation of the spins along the helix and within a triangle are respectively described by scalar chiralities ϵ_H and ϵ_T. This is similar in $MnSb_2O_6$ where the parameters η_C

and η_T indicate the sense of rotation of the spins, respectively along the c-axis and within a basal triangle, as shown in Fig. III.3(a).

$MnSb_2O_6$ magnetic structure can be seen as a global rotation of $Ba_3NbFe_3Si_2O_{14}$ magnetic moments by $\pm 90°$ around the axial vector $\boldsymbol{A}$ (Fig. III.2) [57]. Only enantiopure single crystals of iron langasite were observed [125, 144]. Moreover, a single magnetic configuration was measured [144], and this was lately explained by the presence of single-ion anisotropy which makes the helix elliptical rather than circular, lifting the degeneracy by favoring one triangular chirality [125]. It is also remarkable that the magnetic structure is rather stabilized by symmetric exchange interaction than DM interaction [145, 146] which often has an important role in noncentrosymmetric materials presenting rotating magnetic structures [153]. For $MnSb_2O_6$, the DM interaction should neither play in the stabilization of the cycloidal order, as it would be perpendicular to a threefold axis, and all the DM vectors would exactly cancel out [57], if there is no structural transition from the paramagnetic $P321$ space group. Hence, the reason why a cycloidal modulation is favored over a helical modulation remains unclear.

III.1.4 Heisenberg model

The magnetic interactions are described by a dominant Heisenberg Hamiltonian

$$\hat{\mathcal{H}} = \sum_{ij} J_{ij} \hat{\boldsymbol{S}}_i \cdot \hat{\boldsymbol{S}}_j, \tag{III.1}$$

with the symmetric exchange constants corresponding to the seven SSE pathways in $MnSb_2O_6$ [57]. The nearest neighbor exchange paths are shown in Fig. III.4, where the oxygen atoms are omitted for clarity. Each manganese and antimony atom is surrounded by six oxygen atoms forming edge-sharing octahedra. In a minimalist model considering only interactions between neighboring Mn^{2+} ions, there are therefore seven exchange constants which need to be considered. Intraplane interactions are shown in Fig. III.4(a) where J_1 connects a triangle of MnO_6 octahedra through a SbO_6 octahedra centered at the origin, and J_2 connects MnO_6 octahedra between these triangles, through an interplane SbO_6 octahedron shown in Fig. III.4(c). Interplane interactions within a Mn triangle connected by J_1 are shown in Fig. III.4(b), where J_4 is the straight interplane exchange interaction, and J_3 and J_5 are diagonal exchange interactions. Similarly,

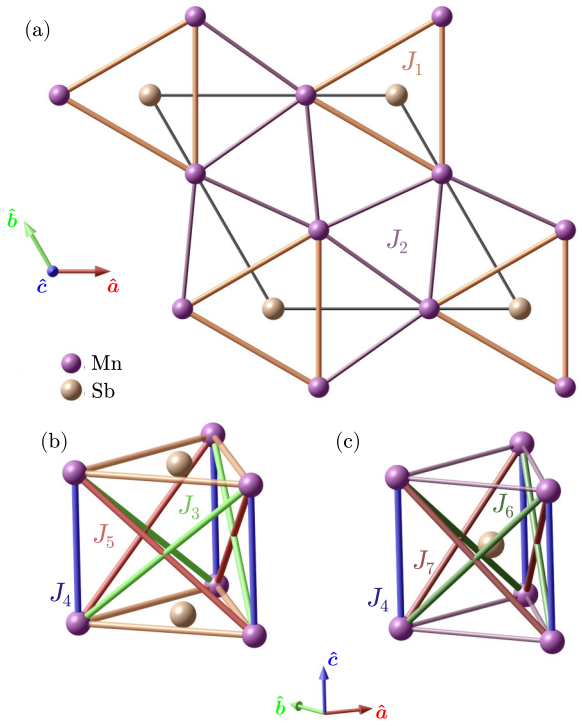

Figure III.4 Drawing of the seven nearest neighbors interactions in $MnSb_2O_6$. (a) Intraplane interactions J_1 connecting triangles of Mn centered at the lattice origin, and J_2 connecting between these triangles. (b) Interplane interactions based on the J_1 triangle, J_4 is the straight interplane interaction, while J_3 and J_5 are diagonal chiral interactions. (c) Interplane interactions based on the J_2 triangle, with J_6 and J_7 as chiral exchange interactions. Oxygen atoms are omitted here for clarity. Figure made using MAG2POL [134].

Figure III.4(c) shows J_6 and J_7, the diagonal exchange interactions connecting a Mn triangle linked by J_2. Interestingly, J_3 and J_6 are related to the right-handed helical winding of the Mn-O-O-Mn SSE pathways [shown in Fig. III.1(c) for J_3], while J_5 and J_7 are related to left-handed SSE pathways [shown in Fig. III.1(b) for J_5]. Thus, these chiral exchange paths are interchanged by applying inversion symmetry operation between structurally left- and right-handed crystals [57]. We note that only the five first exchange constants were necessary to describe the SSE interactions in iron langasite, due to structural differences with $MnSb_2O_6$. Indeed, in $Ba_3NbFe_3Si_2O_{14}$, the Fe-Fe bond distance $d_2 = 5.652\,\text{Å}$ associated with intertriangle interaction J_2 is significantly larger than the Fe-Fe bond distance $d_1 = 3.692\,\text{Å}$ tied to intratriangle interaction J_1 [146]. On the contrary, in $MnSb_2O_6$, the Mn-Mn bond distance $d_2 = 4.845\,\text{Å}$ is smaller than $d_1 = 5.596\,\text{Å}$, as a result the related interplane interactions J_6 and J_7 are expected to be more

significant as they link magnetic Mn^{2+} ions through SSE pathways.

III.1.5 Ferroelectric switching mechanism

As explained in Section I.2, cycloidal magnets can hold an electric polarization

$$\boldsymbol{P} \propto \boldsymbol{r}_{ij} \times (\boldsymbol{S}_i \times \boldsymbol{S}_j), \tag{III.2}$$

where $\boldsymbol{r}_{ij}$ is the distance between two spins at sites i and j. Magnetic domains can exist when the symmetry of the paramagnetic phase is lowered by the ordered magnetic structure. These domains are energetically equivalent, and related by the symmetry operators which are broken during the phase transition [18]. In the case of $MnSb_2O_6$, threefold symmetry is broken by the cycloidal magnetic structure, hence at least three cycloidal domains are expected below T_N. The rotation plane of the cycloids for each magnetic domain defines a cycloidal polarity, related to the other domains by threefold symmetry. In this case, three directions of electric polarization are present in the crystal, as shown in Fig. III.5(a). By applying an electric field greater than the ferroelectric coercitive field in one direction, one could select one domain [Fig. III.5(b)], and by reversing the sign of the electric field, one could switch to a mixture of two polar (thus magnetic) domains [Fig. III.5(c)] [57].

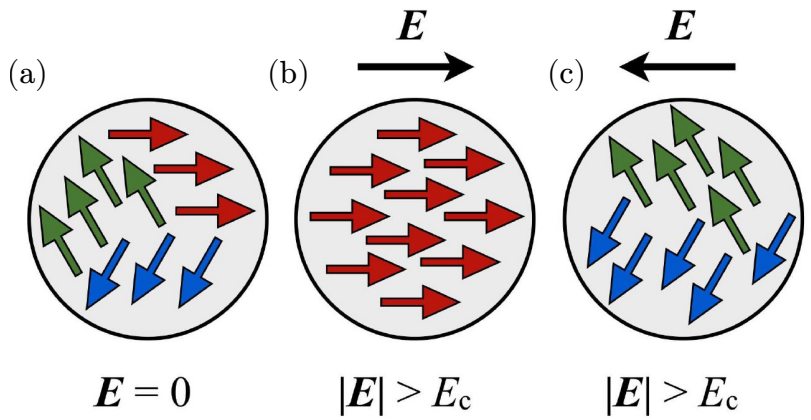

Figure III.5 Unique ferroelectic switching mechanism predicted in $MnSb_2O_6$. (a) Three polar domains exist in $MnSb_2O_6$. Applying a sufficient electric field in one sense or the other allows to switch from (b) a one-domain state to (c) a two-domain state. Figure taken from Ref. [57].

Additional magnetic domains related to the signs of η_C and η_T will also form, as discussed later.

III.1.6 A tilted cycloid model

In 2016, Kinoshita *et al.* measured the (ab)-plane moments of the Mn atoms along the $[1\bar{1}0]$ axis [58]. By measuring the magnetic susceptibility as a function of the angle of an applied magnetic field ($\perp [1\bar{1}0]$), they found out that the cycloidal rotation plane is tilted from the c-axis by an angle $\pm\theta \approx 13°$ as shown in Fig. III.6. Their unpolarized neutron diffraction on single-crystal data agreed with this tilted cycloid model, with a best fit at $\theta = 18(5)°$. An other interesting point is that they found out one dominant magnetic domain (less than 1% of MD2) which was attributed to a single chiral structural domain in their compound. As for the previous interpretation [57], we will show in Section III.4.2.2 that structural twins may be present, and have to be considered for the attribution of the magnetic domains MD1 and MD2 to chiral structural domains.

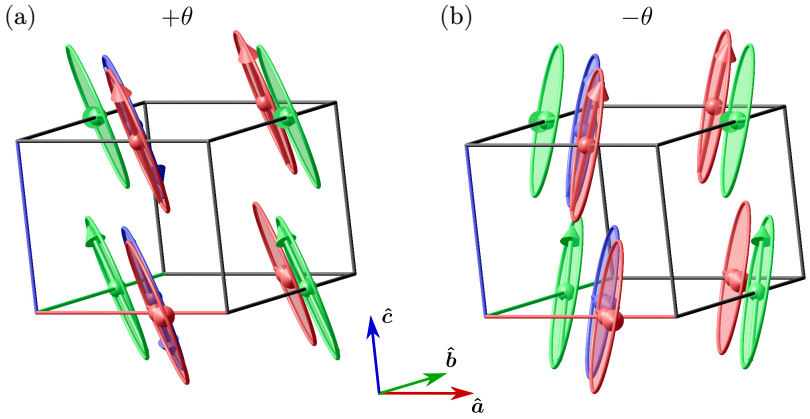

Figure III.6 The tilted cycloid model proposed in Ref. [58]. The moments are aligned along $[1\bar{1}0]$, and tilted from the c-axis by a (a) positive (b) negative angle θ. Figures made using MAG2POL [134].

In addition to the breaking of threefold symmetry from the $P321$ paramagnetic space group, this magnetic structure is also breaking the twofold symmetry. This was not considered in Ref. [57], because the a-axis, which is a twofold symmetry axis, lies within the spin rotation plane. Here, the moments are perpendicular to the twofold axis [110]. Therefore, this leads to six equivalent magnetic domains which can be characterized by an electric polarization $\boldsymbol{P}$ (parallel or antiparallel to the cycloidal polarity $\boldsymbol{P}_m$). This is illustrated in Fig. III.7(a).

The key point is that twofold symmetry inverts the tilt of the rotation plane and

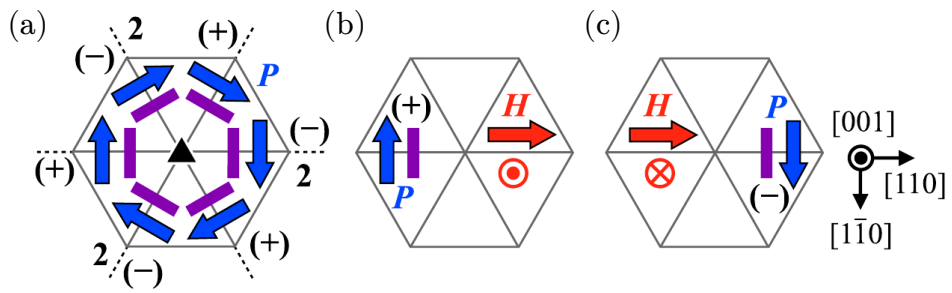

Figure III.7 (a) Six magnetic domains are present with different electric polarization $\boldsymbol{P}$, the tilt of the cycloidal plane for each domain is indicated by (±). Applying a magnetic field (b) out of the plane towards [001], (c) out of the plane towards −[001] favors (b) a positive tilt, (c) a negative tilt, for which the polarization are inverted. From Ref. [58].

the cycloidal polarities $\boldsymbol{P}_{\mathrm{m}}$. For example the domains shown in Fig. III.7(b) and (c) are related by twofold symmetry along [110]. This allows to easily select one of the six domains by applying a magnetic field: (1) perpendicular to the rotation plane to select the threefold domain, (2) directed positively [Fig. III.7(b)] or negatively [Fig. III.7(c)] out of the (001) plane to select the twofold domain. As one domain corresponds to one electric polarization, this allows an unique control of the ferroelectric domain with a magnetic field. This polarization selection was measured and studied in details in Ref. [58], and they showed that a low magnetic field $B \approx 0.3\,\mathrm{T}$ is sufficient to select the magnetic domain. However, according to this theory, based on the tilted cycloid ground state, the positive tilt (+) is favoring $\boldsymbol{P}_{\mathrm{m}}$ along $-[1\bar{1}0]$, while negative tilt (-) is favoring $\boldsymbol{P}_{\mathrm{m}}$ along $[1\bar{1}0]$ as shown in Fig. III.7(b)-(c). In principle, for both positive and negative tilt, $\boldsymbol{P}_{\mathrm{m}}$ along $\pm[1\bar{1}0]$ should be energetically equivalent, and one should consider twelve polar domains instead of six. This was done in our SNP study presented in Section III.4.2.3, and we propose a theory based on DM interaction to favor the polar domains in Section III.5.

III.1.7 Outline

Unpolarized and polarized neutron diffraction were used to study both powders and single crystals of $MnSb_2O_6$ in order to study in detail both crystal and magnetic structure. A mixture of chiral structural domains in our single crystal is found while there is no clear evidence of the tilted model for the magnetic ground state. Through magnetic diffraction under an applied magnetic field,

it is shown that it is possible to manipulate the magnetic structure with small magnetic fields. Finally an alternative mechanism for the appearance of electric polarization will be proposed, based on the DM interaction under an external magnetic field and coupled chiralities. This mechanism does not require a tilted cycloid ground state for ferroelectric domain switching in an applied magnetic field.

This chapter is based upon five sections including this introduction. After describing the materials preparation and neutron instrumentation used for diffraction studies in Section III.2, twinning afforded by the $P321$ symmetry and various structural and magnetic chiralities in $MnSb_2O_6$ will be defined in Section III.3. In Section III.4, the experimental results will be presented, followed by Section III.5 with a phenomenological theory for ferroelectric switching previously observed.

III.2 Experimental details

In this section we describe the materials preparation and neutron scattering experiments used to study both powders and single crystals of $MnSb_2O_6$.

III.2.1 Materials preparation

Materials preparation followed the procedure outlined in Ref. [154]. Powders of $MnSb_2O_6$ were prepared by mixing stoichiometric amounts of pure $MnCO_3$ and Sb_2O_3. After mixing through grinding, the powder was pressed into a pellet and heated up to 1000°C with the process repeated with intermediate grinding. It was found that heating the pellet to higher temperatures introduced the impurity $Mn_2Sb_2O_7$. Single crystals of $MnSb_2O_6$ were prepared using the flux method. Starting ratios for single-crystal growth were (by weight) 73% of flux V_2O_5, 20% of polycrystalline $MnSb_2O_6$ and 7% of B_2O_3. The powder was ground and pressed into a pellet and flame sealed in a quartz ampoule under vacuum (less than $1e^{-4}$ Torr). B_2O_3 was used to lower the melting temperature of the V_2O_5 flux. Back filling the ampoules with $\approx$ 200 mTorr of Argon gas was found to noticeably improve crystal sizes. Quartz ampoules were then heated to 1000°C at a rate of 60°C/hour and soaked at this temperature for 24 hours. The furnace was then cooled to 700°C at a rate of 2°C/hour and held for 24 hours, before it was switched

off and allowed to cool to room temperature. Crystal sizes in the range from a few millimeters to nearly a centimeter were obtained through this procedure.

Powders and single crystals of $MnSb_2O_6$ were synthetized by J. Pásztorová, M. Songvilay and C. Stock.

III.2.2 Neutron diffraction

The crystal and magnetic structures of $MnSb_2O_6$ were studied on the four-circle diffractometers D9 [155] and D10 [156] (ILL, Grenoble) using a single crystal sample of dimensions $\sim 3 \times 2 \times 0.2$ mm^3 (hexagonal shape). On D9, a monochromatic neutron beam of wavelength $\lambda = 0.836$ Å was selected by the (220) reflection of a Cu monochromator in transmission geometry. On D10, a wavelength of $\lambda = 2.36$ Å was selected from a vertically focusing pyrolytic graphite monochromator. The same single crystal was previously characterized using the CRYOgenic Polarization Analysis Device (CRYOPAD)[122] on the spin-polarized hot neutron diffractometer D3 [157] (ILL, Grenoble) using a wavelength $\lambda = 0.85$ Å selected by the (111) reflection of a Cu_2MnAl Heusler monochromator. The good quality of the single crystal was confirmed by neutron Laue diffraction. Powder diffraction was performed on the high-intensity two-axis diffractometer D20 [158] (ILL, Grenoble) on ~ 17 g of powder, using a wavelength $\lambda = 2.41$ Å selected by the (002) reflection of a pyrolitic graphite HOPG monochromator in reflection position. Single-crystal diffraction under an external magnetic field was performed on the cold triple-axis spectrometer RITA-2 (now replaced by CAMEA, SINQ, Villigen), using a horizontal cryo-magnet MA7 with wavelength $\lambda = 4.9$ Å monochromated with a vertically focused pyrolitic graphite PG002 monochromator. The use of a horizontal field was necessary given the need to apply the magnetic field along the c-axis, parallel to the magnetic propagation vector which is kinematically constrained to be in the horizontal plane.

While conventional powder and single-crystal neutron diffraction was used in this work, we relied as well heavily on the use of less standard techniques: Schwinger scattering and spherical neutron polarimetry, to gain extra information into the complex crystal and magnetic structures of $MnSb_2O_6$. These techniques were introduced in Section II.4.2 and Section II.4.3.

The neutron scattering experiments on D3 at Institut Laue-Langevin were performed before the beginning of this thesis by C. Stock, J. Pásztorová, M.

Songvilay and N. Qureshi. The neutron scattering experiment on RITA-2 at Paul Scherrer Institute was performed before the beginning of this thesis by C. Stock, J. Pásztorová and Ch. Niedermeyer.

III.2.3 Transmission polarized optical microscopy

The transmisson polarized optical microscopy presented in Section III.4.1.3 was performed by S.-W. Cheong at Rutgers University.

III.3 Theory and definitions

Given the complexity of the magnetic and crystal structure in $MnSb_2O_6$, we outline in this section the various definitions for the structural and magnetic chiralities and twins. This is required for presenting powder and single-crystal neutron diffraction results discussed below.

III.3.1 Definition of twins

Twinning occurs when two or more single crystals of the same species are intergrown in different orientations, related by the so-called twin laws [159, 160]. When the twin operation belongs to the point group of the lattice but not to the point group of the crystal, the twinning is called twinning by merohedry. In this case, the crystal lattices of the two twins overlap in both direct and reciprocal space [161]. As all Bravais lattices are centrosymmetric, the noncentrosymmetric basis of $MnSb_2O_6$ (space group $P321$) is expected to form inversion twins. Furthermore, the absence of improper rotations in $P321$ (*e.g.* mirror plane) implies the inversion twins will have opposite structural chiralities (known as enantiomorphs). It follows that the reciprocal lattice of one twin is the inverse of the other, *i.e.* $(hkl) \rightarrow (\bar{h}\bar{k}\bar{l})$. In the case of the $P321$ space group additional merohedral twinning associated with twofold rotation around the c-axis, *i.e.* $(hkl) \rightarrow (\bar{h}\bar{k}l)$, is also allowed [162]. We note that these twins related by twofold rotation have the same chirality. Combining the twofold rotation with the inversion twin leads to a fourth twin $(hk\bar{l})$. In order to distinguish the structural chirality of these four possible merohedral twins, we will subsequently use the labels L(hkl), L$(\bar{h}\bar{k}l)$, R$(\bar{h}\bar{k}\bar{l})$ and R$(hk\bar{l})$, where L(R) refers to the left(right)-

handedness of the crystal structure, defined by the helical winding of the Mn-O-O-Mn super-super-exchange pathways in Fig. III.1(b)-(c).

III.3.2 Definition of structural and magnetic chiralities

In crystallography, chirality can be defined as the property of an object "being non-superposable by pure rotation and translation on its image formed by inversion through a point" [150]. On the other hand, the definition of magnetic chirality is not obvious because the time reversal operation (T) has to be considered in addition to parity operation (P). Barron proposed a more general definition: "True chirality is possessed by systems that exist in two distinct enantiomeric states that are interconverted by space inversion but not by time reversal combined with any proper spatial rotation"[163]. In this meaning only helical magnetic structures are truly chiral [33, 112]. However, spin "chirality" is commonly used to refer to the sense of rotation of the spins with respect to a crystallographic reference often taken to be an oriented link between two atomic sites, say $\boldsymbol{r}_{ij}$, and can thus describe the spin configuration of cycloidal structures and triangular networks [164].

The cross-product of two spins at sites i and j defines a vector chirality

$$\boldsymbol{V}_{ij} = \boldsymbol{S}_i \times \boldsymbol{S}_j \tag{III.3}$$

which is a T-even axial vector (*i.e.* P-even), changing sign on exchange of indices $i \leftrightarrow j$. This chirality vector is well-defined by providing the oriented link between two spins.

For clarification and to understand our diffraction data, we redefine the vectors introduced in Ref. [57] in the context of $MnSb_2O_6$. To do this, we consider an orthonormal basis $\mathsf{R} = (\hat{\boldsymbol{x}}, \hat{\boldsymbol{y}}, \hat{\boldsymbol{z}})$ where $\hat{\boldsymbol{x}}$ lies along the a-axis, $\hat{\boldsymbol{z}}$ along the c-axis and $\hat{\boldsymbol{y}}$ completes the right-handed basis set of vectors. We define the spin rotation plane using two vectors $\hat{\boldsymbol{u}}$ and $\hat{\boldsymbol{v}}$, where we take $\hat{\boldsymbol{u}} \equiv \hat{\boldsymbol{x}}$ in the following. In order to account for a tilt of the spin rotation plane we introduce θ as the tilt angle about $\hat{\boldsymbol{u}}$ such that $\hat{\boldsymbol{v}} = [0, -\sin\theta, \cos\theta]$. We note that in our analysis, $\hat{\boldsymbol{u}}$ could take any direction in the (ab)-plane, and the definition of the tilt angle θ can be generalized. By definition, any two spins $\boldsymbol{S}_i$ and $\boldsymbol{S}_j$, lie within the uv-plane, so their cross product must lie along $\pm\hat{\boldsymbol{n}} = \hat{\boldsymbol{u}} \times \hat{\boldsymbol{v}} = [0, -\cos\theta, -\sin\theta]$

(Fig. III.8). Note that when $\theta = 0$, the spins rotate in a plane containing $\hat{\boldsymbol{z}}$ and we obtain a proper cycloid [Fig. III.3(a)]. When $\theta = 90°$, the spins rotate in a plane perpendicular to $\hat{\boldsymbol{z}}$ defining a proper helix, as reported in $Ba_3NbFe_3Si_2O_{14}$ [Fig. III.3(b)]. Intermediate values of θ give a generic helicoidal structure that can be decomposed into an admixture of helical and cycloidal parts.

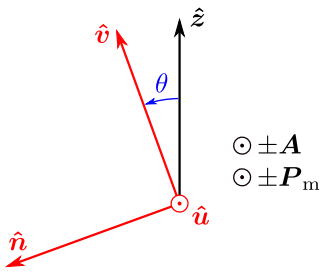

Figure III.8 $\hat{\boldsymbol{u}}$ and $\hat{\boldsymbol{v}}$ are the main axis of the helicoidal spin structure envelope. Any cross product of spins lies along $\hat{\boldsymbol{n}}$. $\boldsymbol{A}$ and $\boldsymbol{P}_{\mathrm{m}}$ lie along $\hat{\boldsymbol{u}}$.

The spin configuration within a basal triangle of Mn^{2+} ions is described by the classical vector chirality $\boldsymbol{V}_{\mathrm{T}} = \frac{1}{3}(\boldsymbol{S}_1 \times \boldsymbol{S}_2 + \boldsymbol{S}_2 \times \boldsymbol{S}_3 + \boldsymbol{S}_3 \times \boldsymbol{S}_1)$ where the indices are given by right hand rule around the axial vector $\hat{\boldsymbol{z}}$ defined as parallel to the positive c-axis. Similarly, a vector chirality $\boldsymbol{V}_{\mathrm{C}} = \boldsymbol{S}_\alpha \times \boldsymbol{S}_\beta$ can be introduced to describe the rotation of the spins along the c-axis, relatively to the polar vector $\boldsymbol{r}_{\alpha\beta}$ where α and β refer to two neighboring layers along the c-axis. We can now redefine the axial vector $\boldsymbol{A}$ and the polar vector $\boldsymbol{P}_{\mathrm{m}}$ used to characterize the cycloidal magnetic structure of $MnSb_2O_6$ (see Section III.1.2) in Ref. [57] as

$$\begin{cases} \boldsymbol{A} = \hat{\boldsymbol{z}} \times \boldsymbol{V}_{\mathrm{T}} = [\eta_{\mathrm{T}} \cos\theta, 0, 0] \\ \boldsymbol{P}_{\mathrm{m}} = \boldsymbol{r}_{\alpha\beta} \times \boldsymbol{V}_{\mathbf{C}} = [\eta_{\mathrm{C}} \cos\theta, 0, 0], \end{cases} \tag{III.4}$$

where η_{T} and η_{C} are T-even P-even and T-even P-odd parameters associated with the magnetic configuration within the (ab)-plane triangular motifs and on propagation along the c-axis, respectively. Importantly, both parameters are conserved upon rotation by θ. We can similarly redefine the triangular chirality ϵ_{T} and spin helicity ϵ_{H} used to characterize the helical magnetic structure of $Ba_3NbFe_3Si_2O_{14}$ in Ref. [144] as

$$\begin{cases} \epsilon_{\mathrm{T}} = \hat{\boldsymbol{z}} \cdot \boldsymbol{V}_{\mathrm{T}} = -\eta_{\mathrm{T}} \sin\theta \\ \epsilon_{\mathrm{H}} = \boldsymbol{r}_{\alpha\beta} \cdot \boldsymbol{V}_{\mathbf{C}} = -\eta_{\mathrm{C}} \sin\theta, \end{cases} \tag{III.5}$$

These expressions allow us to use η_{T}, η_{C}, and θ to parametrize a generic helicoidal magnetic structure as shown in Fig. III.3(a) for $\theta = 0$. The vector quantities of Eq. (III.4) capture the cycloidal component projected into the (ac)-plane, and the scalar quantities of Eq. (III.5) capture the helical part projected into the (ab)-plane. We note that the helical part is odd in θ, while the cycloidal part is even.

III.3.3 Magnetic structure description

Considering the two perpendicular unit vectors $\hat{\boldsymbol{u}}$ and $\hat{\boldsymbol{v}}$ that define the spin rotation plane, we can describe the magnetic moment for a Mn atom at site $j = (1, 2, 3)$ on a given triangular motif, in layer α (along the c-axis), and with an angle $\phi_{\alpha j}$ [58]:

$$\begin{cases} \boldsymbol{\mu}_{\alpha j} = M_u \cos\phi_{\alpha j}\hat{\boldsymbol{u}} + M_v \sin\phi_{\alpha j}\hat{\boldsymbol{v}} \\ \phi_{\alpha j} = 2\pi\eta_{\mathrm{C}} k_{\mathrm{z}}\alpha + \eta_{\mathrm{T}}(j-1)\dfrac{2\pi}{3}, \end{cases} \tag{III.6}$$

M_u and M_v describe the shape of the ellipse (circular for $M_u = M_v$), k_{z} is the vertical component of the propagation vector $\boldsymbol{k} = (0, 0, k_{\mathrm{z}})$. η_{C} and η_{T} describe the sense of rotation of the spins respectively along the positive c-axis, and within a Mn^{2+} triangle, following the definitions above. A full description of the magnetic structure is given in Appendix C, along with its implementation in refinement softwares.

The first magnetic structure proposed in Ref. [57] has $\hat{\boldsymbol{u}}$ lying along the crystallographic a-axis, and $\hat{\boldsymbol{v}}$ along the c-axis. This magnetic structure preserves the twofold symmetry (magnetic space group $B21'$). This is not the case in the model proposed in Ref. [58], with $\hat{\boldsymbol{u}} \parallel [1\bar{1}0]$, which lowers the symmetry of the magnetic space group to $P11'$ owing to the breaking of the twofold symmetry. However, the tilting of $\hat{\boldsymbol{v}}$ from the c-axis reported in Ref. [58], by an angle θ, is also allowed in the $B21'$ space group as long as the twofold symmetry is preserved. Both models consider the presence of threefold domains, and for each of them, the magnetic moments in Eq. (III.6) are transformed by rotating $\hat{\boldsymbol{u}}$ and $\hat{\boldsymbol{v}}$ by 120° around the c-axis.

III.3.4 Invariant from Heisenberg interactions

If we consider a Heisenberg Hamiltonian with seven SSE pathways as described above and illustrated in Fig. III.4, the classical mean-field energy can be derived as a function of the propagation vector $k_z > 0$:

$$E_0(k) = -\frac{1}{2}(J_1 + 2J_2) + J_4 \cos(2\pi\eta_C k_z) + J_R \cos(2\pi\eta_C k_z + \eta_T \frac{2\pi}{3}) + J_L \cos(2\pi\eta_C k_z - \eta_T \frac{2\pi}{3}), \quad \text{(III.7)}$$

where $J_R = J_3 + 2J_6$ sums the right-handed interactions and $J_L = J_5 + 2J_7$ sums the left-handed interactions. Minimizing Eq. (III.7) with respect to the propagation vector gives for the ground state:

$$\tan(2\pi\eta_C k_z) = \frac{\eta_T\sqrt{3}(J_R - J_L)}{J_R + J_L - 2J_4}. \quad \text{(III.8)}$$

As left-handed and right-handed exchange paths are switched between the enantiomorphs, the quantity $J_R - J_L$ changes sign upon inversion symmetry. Thus taking the DFT values for the exchange constants from Ref. [57], a sign analysis of Eq. (III.8) gives the invariant:

$$\sigma\eta_C\eta_T = +1, \quad \text{(III.9)}$$

where $\sigma = +1$ for a left-handed crystal structure (L), and $\sigma = -1$ for a right-handed crystal structure (R). This is similar to iron langasite, where the structural chirality is linked to the pair of magnetic chiralities readily obtained by substituting $\theta = 90°$ into Eq. (III.5) [144].

III.4 Results and discussion

Having outlined the experimental neutron diffraction techniques and the definitions relevant for the discussion of $MnSb_2O_6$, we now present the experimental results. We first discuss the crystal and then the low temperature magnetic structure.

III.4.1 Crystal structure

III.4.1.1 Single-crystal neutron diffraction

For a given Bragg reflection $\boldsymbol{Q}$, the inversion twin will scatter with a nuclear structure factor $F_{\mathrm{N}}(-\boldsymbol{Q})$. In absence of resonant scattering, Friedel's law is valid, and both twins will scatter the same nuclear intensity $\propto |F_{\mathrm{N}}(\boldsymbol{Q})|^2$. Inversion twins are thus indistinguishable by unpolarized neutrons. On the other hand, twofold twins reveal different nuclear structure factors depending on the (hkl) indices so their domain population can be refined using unpolarized neutrons if the appropriate Bragg reflections are measured. We collected intensities from 430 nuclear reflections at 50 K on the four-circle diffractometer D9. Rocking scans show nicely resolved Bragg peaks, with a full width at half-maximum $\sim 0.4°$ in ω. The data were refined using FULLPROF [133]. The parameters scale, extinction, atomic positions, displacements, as well as domain population for twofold twins were refined, showing that our single crystal has no twofold twins as one nuclear intensity domain was refined to a population of 0.991(3). Our refinement results (detailed in Table III.1) agree with the known crystal structure previously studied by neutron powder diffraction at room temperature [151].

As the threefold symmetry from paramagnetic $P321$ space group is broken by the cycloidal structure in the magnetic phase [57], this could relate to a symmetry lowering of the nuclear space group below T_{N}. To investigate this possibility of a structural distortion coinciding with T_{N}, a separate set of 318 Bragg reflections was measured at 2 K (below $T_{\mathrm{N}} \approx 12$ K), leading to 75 inequivalent groups of reflections. If the crystal symmetry is reduced, the equivalent reflections in $P321$ should no longer be equivalent within each group of reflections. For example, reflections (h, k, l), $(k, -h-k, l)$ and $(-h-k, h, l)$ are related by threefold symmetry along the c-axis and are thus equivalent in $P321$. In the case where the threefold symmetry is broken, these three kind of reflections are no more equivalent. In addition, three structural domains rotated by 120° are expected. If these threefold domains are exactly equi-populated, the intensities scattered from each domain will average out, making them impossible to be distinguished from a single threefold symmetric domain. Else, the intensities of reflections within a group of $P321$-equivalent reflections will differ. The internal R-factor is $R_{\mathrm{int}} = 4.1\%$ for the data reduction in $P321$ symmetry, which indicates that the differences of intensities for $P321$-equivalent reflections are not measurable

Table III.1 Structural parameters of $MnSb_2O_6$ single crystal measured on D9, refined with FULLPROF [133] within nuclear space group $P321$ (No. 150)

$T = 50\,\mathrm{K}$ Measured, independent, observations with equivalent reflections: 430, 406, 44						
$R_{\mathrm{int}} = 8.78\%$ $R_{\mathrm{F}} = 4.87\%$ $R_{\mathrm{Bragg}} = 4.69\%$ $\chi^2 = 1.31$						
$a = b = 8.784(8)$ Å $c = 4.724(6)$ Å						
Atoms	Wyckoff	x	y	z	B_{iso} (Å^2)	Occ.
Mn	3e	0.6319(3)	0.0000	0.0000	0.19(3)	1
Sb1	1a	0.0000	0.0000	0.0000	0.06(3)	1
Sb2	2d	0.3333	0.6667	0.5059(4)	0.04(3)	1
Sb3	3f	0.3050(3)	0.0000	0.5000	0.09(2)	1
O1	6g	0.1046(3)	0.8917(3)	0.7626(2)	0.24(2)	1
O2	6g	0.4711(2)	0.5891(2)	0.7286(2)	0.19(2)	1
O3	6g	0.2258(3)	0.7804(3)	0.2805(2)	0.16(2)	1
$T = 2\,\mathrm{K}$ Measured, independent, observations with equivalent reflections: 845, 529, 423						
$R_{\mathrm{int}} = 4.09\%$ $R_{\mathrm{F}} = 5.27\%$ $R_{\mathrm{Bragg}} = 5.40\%$ $\chi^2 = 1.37$						
$a = b = 8.791(2)$ Å $c = 4.718(1)$ Å						
Atoms	Wyckoff	x	y	z	B_{iso} (Å^2)	Occ.
Mn	3e	0.6329(3)	0.0000	0.0000	0.30(3)	1
Sb1	1a	0.0000	0.0000	0.0000	0.16(3)	1
Sb2	2d	0.3333	0.6667	0.5061(5)	0.09(3)	1
Sb3	3f	0.3050(2)	0.0000	0.5000	0.09(2)	1
O1	6g	0.1047(2)	0.8920(3)	0.7628(2)	0.27(1)	1
O2	6g	0.4710(2)	0.5889(2)	0.7285(2)	0.25(2)	1
O3	6g	0.2253(3)	0.7799(2)	0.2804(2)	0.23(2)	1

given our setup. In addition, the data was refined including the threefold domains in $P1$ symmetry, but this did not significantly improve the refinement. In the end 845 nuclear reflections were measured at 2 K, and were well refined in $P321$ space group as shown in Fig. III.9(b), in comparison to the 50 K refinement in Fig. III.9(a). From this, there is no significant evidence of breaking of $P321$ symmetry below Néel temperature. Detailed refinement results for both temperatures are listed in Table III.1.

III.4.1.2 Schwinger scattering

To characterize the chiral domains, Schwinger scattering was measured on D3 on nine Bragg reflections at $T = 3\,\mathrm{K}$ on the same single crystal characterized on D9, for which only two out of four possible twins were measured to be present as explained above. Absolute indexation was determined on D9 by comparing the nuclear intensities of Bragg reflections. This was not done on D3 (as only flipping ratios were measured), so the reflections can be indexed with a twofold rotation between D3 and D9 experiments. Thus, either $\{\mathrm{L}(hkl),\ \mathrm{R}(\bar{h}\bar{k}\bar{l})\}$, or $\{\mathrm{L}(\bar{h}\bar{k}l),$

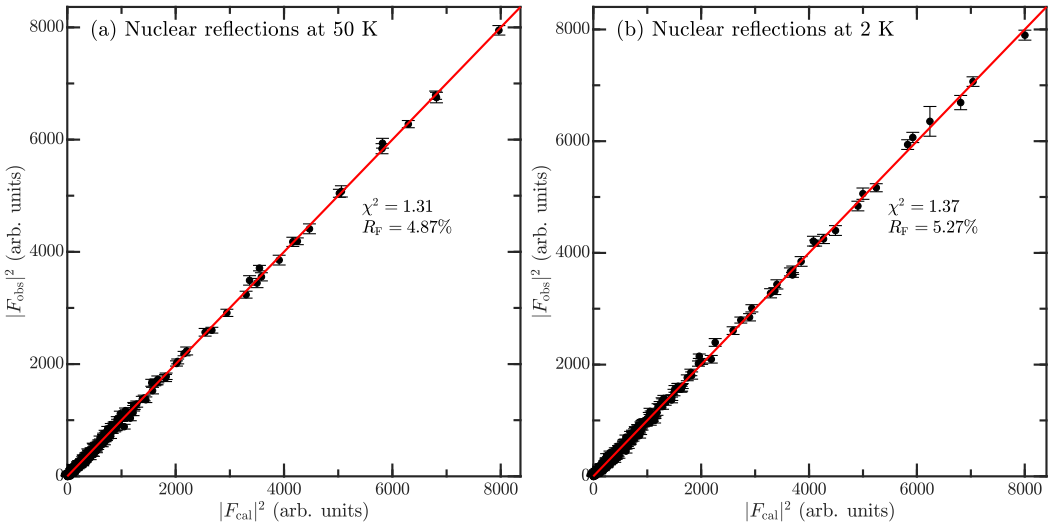

Figure III.9 Observed versus calculated intensities in $P321$ space group for nuclear reflections measured at (a) 50 K, (b) 2 K.

R($hk\bar{l}$)} are the twins present (with the indexation from D3 experiment).

The experimental flipping ratios are then fitted to a linear combination of the theoretical ones (calculated with the atomic positions from D9 data refinement at 2 K), as shown in Fig. III.10. The best fit is obtained considering the twins L($\bar{h}\bar{k}l$) and R($hk\bar{l}$), giving 0.54(2) of left-handed structural domain, and 0.46(2) of right-handed domain. The error bars are quite large in this experiment, but the flipping ratios being close but different than 1 within uncertainties indicate that there is a mixture of chiral inversion twins in the crystal. For an enantiopure, the flipping ratios should be close to one set of predicted flipping ratios, which shows much more pronounced asymmetries as exemplified by the (511) and (153) reflections. The results are thus different from enantiopure $Ba_3NbFe_3Si_2O_{14}$ single crystals which were previously studied [125, 144, 146].

III.4.1.3 Transmission polarized optical microscopy

Chiral structural domains in a single crystal can also be measured with a polarized optical microscope. Due to the optical activity in chiral compounds, the polarization plane of a linearly polarized light is rotated after traveling through the sample [165]. The sense of rotation depends on the handedness of the considered domains, which can be distinguished by observing the transmitted light through an analyzer [166, 167].

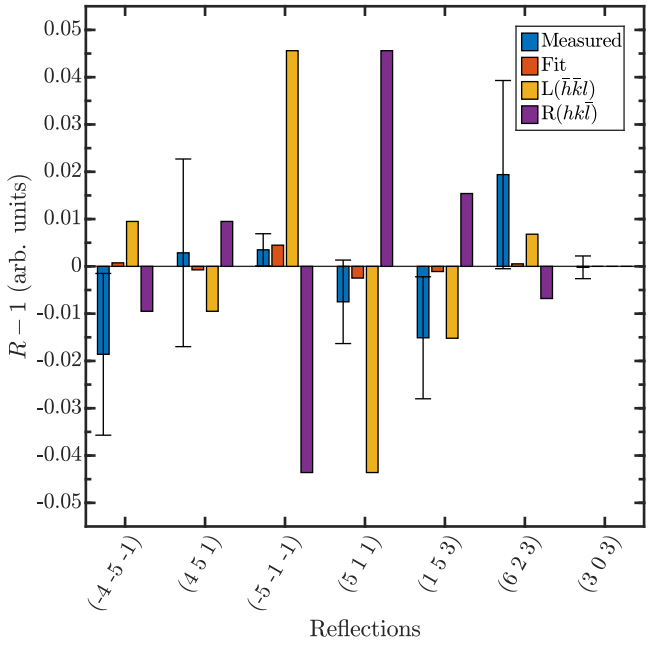

Figure III.10 Measured flipping ratios are fitted to a linear combination of the theoretical flipping ratios for two structural twins.

A different sample of $MnSb_2O_6$, synthesized following the same procedure described in Section III.2.1, was observed under a transmission polarized optical microscope. The directions of the polarizer and analyzer are shown in blue and red in Fig. III.11(a)-(b), forming an angle $\theta = 90 \pm 3°$. These images show several domains with opposite chirality. The constrast between neighboring domains is reverted by rotating the analyzer from $\theta = 93°$ to $\theta = 87°$ because the polarization plane of the transmitted light is rotated in the opposite sense for opposite chirality domains in the sample. Fig. III.11(c) shows the difference of intensity between Fig. III.11(a) and Fig. III.11(b), clearly revealing the chiral areas in the single crystal.

Given the same chemical synthesis, our other single crystals, including the one studied under neutron diffraction, are likely to have a similar behavior. They are expected to be a mixture of chiral structural domains, which is consistent with our Schwinger scattering analysis described above.

III.4.1.4 Magneto-structural effects

Neutron powder diffraction was performed on D20 from 2.5 K to 89.5 K (see Appendix D for more details). The crystal structure was refined sequentially as a

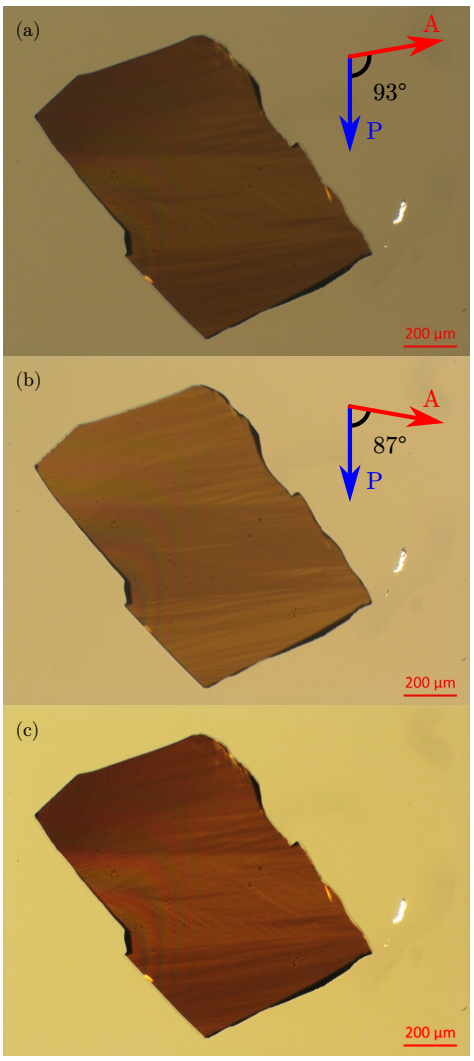

Figure III.11 Transmission polarized optical microscopy images of a single crystal of $MnSb_2O_6$: for different angles between the polarizer (P) and analyzer (A) in (a) and (b). (c) Images substracted, showing the chiral domains in the sample.

function of temperature using FULLPROF [133]. While no symmetry breaking of the $P321$ paramagnetic space group was evidenced by our studies, as discussed above, structural changes induced by the phase transition are visible from the powder diffraction data refinement. Fig. III.12(a) shows the refined volume of the unit cell as a function of temperature. The volume decreases sharply under $T_N \approx 12\,K$, demonstrating a deviation from the linear thermal expansion of the unit cell upon magnetic ordering. Actually, this results from the contraction of both a and c lattice constants. Similarly, changes in bond distances are caused by magneto-elastic effects, as shown in Fig. III.12(b) for the distance between Mn atom (in purple) and symmetry equivalent O1 atoms (in red). More results

on the MnO_6 octahedral distortion as a function of temperature are presented in Appendix D.3. We note that the unit cell volume shows some anomalies in Fig. III.12(a) around 3 K and 10 K. We have over-plotted the different diffraction patterns and could not observe any shift in the peaks positions. We think that these jumps are numerical artifacts rather than real lattice parameters shifts.

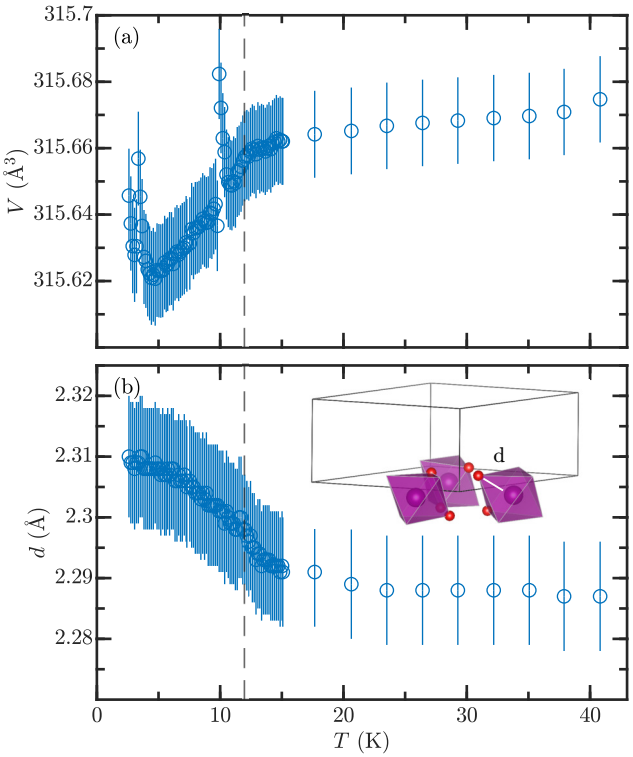

Figure III.12 Refinement results from D20. Temperature dependence of: (a) the unit cell volume, (b) the bond length between Mn (in purple) and symmetry equivalent O1 atoms (in red). $T_N \approx 12$ K is shown in dashed gray lines.

III.4.2 Magnetic structure

III.4.2.1 Order parameter

Neutron powder diffraction is not sensitive to the direction of the magnetic moments in the (ab)-plane, and neither to the magnetic chiralities. Yet the magnitude of the magnetic moments can be refined from D20 powder diffraction data, as a function of temperature. The cycloid was constrained to be circular ($M_u = M_v$) and the refined moments are shown in Fig. III.13. The data in the critical region ($8\,\mathrm{K} < T < 12\,\mathrm{K}$) are fitted to a power law $\propto (T - T_N)^\beta$,

with the critical exponent fixed to $\beta = 0.369$ (solid red curve) as expected for the nonfrustrated 3D Heisenberg model [168], and to $\beta = 0.25$ (dashed blue curve) measured for iron langasite [146] and XY-like stacked-triangular magnets [169]. The critical behavior near $T_N = 11.94(1)$ K is in agreement with the 3D Heisenberg model as suggested previously in Ref. [151]. Therefore $MnSb_2O_6$ does not have the same universality class as iron langasite and other layered-triangular magnets.

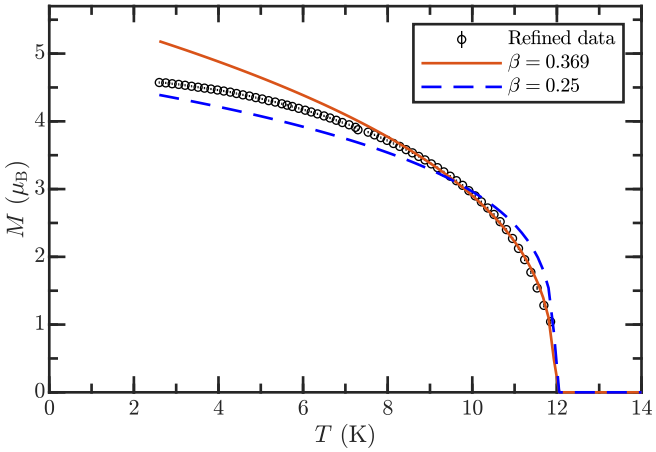

Figure III.13 Refined magnetic moments from D20 as a function of temperature, fitted to a power law $\propto (T - T_N)^\beta$ with the critical exponent β fixed for 3D Heisenberg model (solid red curve) and for 2D XY model (dashed blue curve).

III.4.2.2 Unpolarized single-crystal diffraction

From the invariant derived in Eq. (III.9) ($\sigma\eta_C\eta_T = 1$), a given structural chirality σ is compatible with two pairs of magnetic configurations (η_C, η_T). We can label the structural and magnetic configurations as $\sigma(\eta_C, \eta_T)$, which gives four possibilities L(1, 1), L(−1, −1), R(−1, 1), R(1, −1). L(1, 1) and L(−1, −1) configurations lead to the same magnetic intensities, and R(−1, 1), R(1, −1) are the respective configurations of their inversion twins, as η_C is P-odd and η_T P-even from Eq. (III.4). Magnetic intensities of inversion twins satisfy Friedel's law, so the four configurations are undistinguishable by unpolarized neutrons. However, as mentioned above, twofold structural twins can exist in the $P321$ space group, leading to a different set of nuclear and magnetic intensities (see Table III.2).

In previous studies, unpolarized neutron single-crystal diffraction data were refined with a mixture of two sets of calculated magnetic intensities, attributed

Twin	$\sigma = \eta_C \eta_T$	$\lvert F_N \rvert^2$	$\lvert \boldsymbol{F}_{M_\perp} \rvert^2$	R
L(hkl)	$+1$	N_1	M_1	R_1
L($\bar{h}\bar{k}l$)	$+1$	N_2	M_2	R_2
R($\bar{h}\bar{k}\bar{l}$)	-1	N_1	M_1	R_3
R($hk\bar{l}$)	-1	N_2	M_2	R_4

Table III.2 Summary of the possible twins and their sensitivity to nuclear ($\lvert F_N \rvert^2$) and magnetic diffraction ($\lvert \boldsymbol{F}_{M_\perp} \rvert^2$), and Schwinger scattering (flipping ratio R). Different subscripts denote different values. The twins present in our single crystal are highlighted in red.

to two chiral structural domains. In light of the present study, one should actually assign these two sets of intensities to at least two twofold domains, with a potential further mixture of chiral domains to which the experiment was not sensitive. In Ref. [57], the single-crystal neutron diffraction magnetic refinement shows a 0.8(1)MD1:0.2(1)MD2 domain fraction of the calculated intensities, which corresponds to a fraction 0.8 of twins {L(hkl), R($\bar{h}\bar{k}\bar{l}$)}, and 0.2 of twins {L($\bar{h}\bar{k}l$), R($hk\bar{l}$)}. In absence of a method (Schwinger scattering or anomalous X-ray scattering) sensitive to the inversion twins, one cannot conclude on the population of all four domains. A similar issue arose in Ref. [58], where only one set of magnetic intensities was found and attributed to an enantiopure crystal, but could actually include a mixture of a twin and its chiral inversion twin.

The same single crystal characterized on D3 and D9 was measured on D10. The magnetic structure was refined using MAG2POL [134] (cross-checked with FULLPROF [133], giving similar results), with 256 magnetic reflections collected at 2 K. The scale and extinction parameters are refined using 145 nuclear reflections (40 inequivalent, giving $R_F = 4.88\%$). A single domain in terms of magnetic intensities was found, meaning the absence of twofold structural twins and confirming our results from D9. These intensities are consistent with two twins related by inversion symmetry, shown in red in Table III.2, which can be distinguished by Schwinger scattering (see Section III.4.1.2). Extinction parameters can be significantly different for nuclear and magnetic reflections, due to multiple magnetic domains having smaller sizes than the structural domains [170]. This is the case from our refinement, where the extinction parameters refined with the magnetic intensities are found smaller than the one refined with the nuclear intensities. To keep a consistent comparison between the magnetic structure models, the extinction parameters were set to zero for the magnetic refinement described below.

Name	$\hat{\boldsymbol{u}}$	M_u	M_v	θ (°)	p_1	p_2	p_3	R_F (%)
A	$\hat{\boldsymbol{a}}$	4.5(1)	4.7(1)	0	1	0	0	19.26
B	$\hat{\boldsymbol{a}}$	5.7(1)	3.7(1)	0	0.40	0.20(3)	0.40(3)	15.29
C	$\hat{\boldsymbol{a}}$	5.6(3)	3.8(3)	9(28)	0.40	0.20(5)	0.40(3)	15.31
D	$[1\bar{1}0]$	5.7(1)	3.7(1)	0	0.27	0.27(3)	0.46(3)	15.29
E	$[1\bar{1}0]$	5.9(2)	3.8(3)	15(14)	0.28	0.25(4)	0.47(4)	15.26

Table III.3 Refined parameters obtained for non-tilted and tilted cycloidal models. The directions of the threefold domains of each magnetic model is illustrated in red (A, B, C) and blue (D, E) in Fig. III.14.

The refinement results using different magnetic structure models labeled from A to E are listed in Table III.3. While including the threefold domains (A→B) with populations p_1, p_2, and p_3 improves the goodness of fit, there is no observable difference between models with the in-plane main axis $\hat{\boldsymbol{u}}$ of the cycloid along the a-axis and along $[1\bar{1}0]$ (B→D). Similarly, allowing a tilt around the a-axis (B→C), and around $[1\bar{1}0]$ (D→E) does not significantly improve the fit. This is because the in-plane direction $\hat{\boldsymbol{u}}$ of the spin rotation plane, and the tilt angle θ are correlated with the magnetic domain fractions, which makes no much difference in terms of goodness of fit between models B, C, D and E. Our best fit with the model considered in Ref. [58] is obtained with a tilt angle $\theta = +15(14)°$ (Fig. III.15), compared to previously found $\theta = 18(5)°$. However, two equi-populated tilt domains with $\theta = \pm 18(5)$ were considered in Ref. [58] while in our refinement, a single tilt domain $\theta > 0$ was more consistent. Based on our single-crystal diffraction data, we however do not observe a significant improvement in the resulting fit with inclusion of a tilt in the magnetic structure.

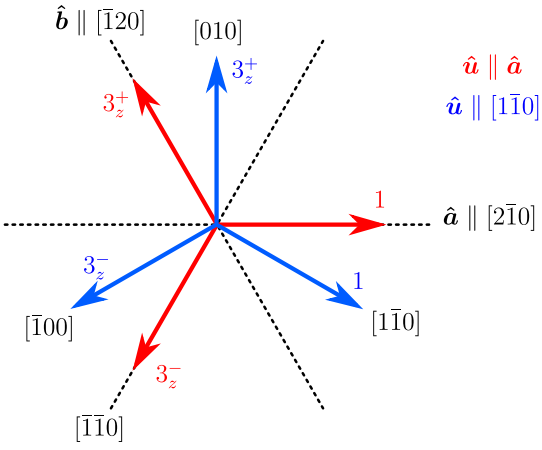

Figure III.14 Directions of the threefold domains for the spin envelop axis $\hat{\boldsymbol{u}}$ along $\hat{\boldsymbol{a}}$ (red) or $[1\bar{1}0]$ (blue).

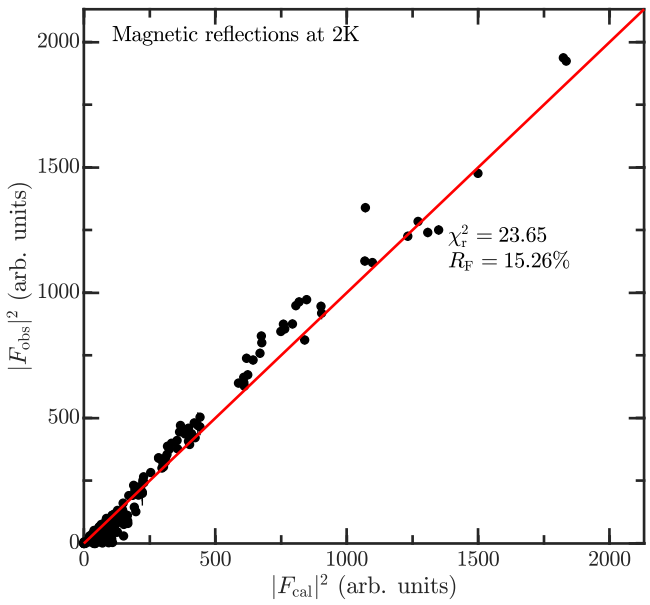

Figure III.15 Observed versus calculated intensities for magnetic reflections measured at 2 K.

III.4.2.3 Spherical neutron polarimetry

SNP was performed on D3, using the same experimental setup as for the Schwinger experiment with the exception of a ^{3}He spin filter necessary for the polarization analysis of the final neutron beam. The full polarization matrices of five magnetic Bragg reflections were measured at $T = 3$ K. CRYOPAD [122] is used to protect the sample from any external magnetic fields, and to select independently the initial and final polarization directions of the neutrons. In the case of $MnSb_2O_6$, SNP is sensitive to the threefold magnetic domains and the cycloidal parameter η_C, while the triangular parameter η_T can not be distinguished. The measured polarization matrices were fitted using MAG2POL [134] to a linear combination of the possible polarization matrices as $P_{meas} = \sum_i \alpha_i P_i$ with α_i, P_i, the population and polarization matrix of the i-th magnetic domain.

The magnetic moments were first refined in the ac-plane ($\hat{\boldsymbol{u}} = \hat{\boldsymbol{a}}$ and $\hat{\boldsymbol{v}} = \hat{\boldsymbol{c}}$). In the absence of a nuclear contribution to the scattered intensity, SNP is not sensitive to the size of the magnetic moments. Therefore, since in this experiment purely magnetic satellites are investigated, only the ratio $e = M_v/M_u$, known as the ellipticity, can be deduced. Considering the model proposed in Ref. [57], threefold and $\eta_C = \pm 1$ domain populations are refined, leading to six

polarization matrices to consider. The refinement results for this model are shown in Table III.4. The cycloids are found elliptical along the basal direction with $e = 0.92(1)$ and $\chi^2_{\rm r} = 7.14$. The population for the third threefold domain with $\eta_{\rm C} = +1$ was fixed to 0 in order to avoid fit divergence and unphysical results.

$\eta_{\rm C}$	1	3^+_z	3^-_z	Sum
$+1$	0.20(1)	0.20(1)	0	0.40(2)
-1	0.09(1)	0.09(1)	0.42(2)	0.60(2)
Sum	0.29(1)	0.28(1)	0.42(2)	1

$\chi^2_{\rm r}$	7.14
e	0.92(1)

Table III.4 Refined parameters for the non-tilted cycloid model.

The SNP data were then fitted to the tilted cycloid model proposed in Ref. [58]. In this case, the positive and negative tilt of the angle θ have to be taken account because it changes the rotation plane and leads to different polarization matrices. This doubles the number of polarization matrices to include, resulting in 12 domain populations to refine (threefold $\times\{\eta_{\rm C} = \pm 1\} \times \pm\theta$). The vectors $\hat{\boldsymbol{u}}$ and $\hat{\boldsymbol{v}}$ of each of these 12 magnetic domains are related by symmetry operators and the absolute values of M_u are constrained to be the same for each magnetic domain (the same for M_v), so that each magnetic domain keeps the same magnetic moment size. This also constrains the absolute value of the tilt angle to be the same for $\theta > 0$ and $\theta < 0$ domains. The results are shown in Table III.5. Again, the domains returning unphysical values in a first refinement step were fixed to zero in the following. The positive tilt domains are predominant, with a population of 0.89(4), giving $\theta = 14(7)^\circ$ which is consistent with the best fit from the D10 data. However, this tilted model only slightly improves the goodness of fit to $\chi^2_{\rm r} = 6.68$.

$\eta_{\rm C}$	θ	1	3^+_z	3^-_z	Sum
-1	+	0.08(1)	0.32(3)	0	0.40(3)
$+1$	-	0.01(2)	0.07(2)	0.04(2)	0.12(3)
-1	-	0	0	0	0
$+1$	+	0.14(1)	0	0.35(2)	0.49(2)
Sum		0.23(2)	0.39(4)	0.39(2)	1

$\chi^2_{\rm r}$	6.68
e	0.96(8)
θ	14(7)°

Table III.5 Refined parameters for the tilted cycloid model.

Our diffraction study of the magnetic structure of $MnSb_2O_6$ evidences a mixture of threefold magnetic domains and magnetic polarities. In the absence of a substantial improvement in R-factors on inclusion of the model with in-plane

moments along $[1\bar{1}0]$, we propose that the model with moments along $\hat{\boldsymbol{a}}$ is the ground state because it has a higher symmetry (not breaking twofold symmetry). The tilt is still allowed by symmetry, as pointed out in Section III.3.3. Thus the possibility of a tilted cycloidal structure is not ruled out by symmetry considerations our experiments. In Section III.5 we discuss the appearance of a macroscopic electric polarization reported in Ref. [58] and propose a different mechanism without invoking the need of a tilted cycloid ground state.

III.4.3 Magnetic field dependence

Before discussing the electric polarization we finally investigate the magnetic field response of the magnetic structure in $MnSb_2O_6$ owing to its importance in any domain switching. Magnetic phase transitions induced by low magnetic fields (below 2 T) were observed previously in $MnSb_2O_6$ bulk magnetization measurements [58, 152]. This was explained by a very small anisotropy stabilizing the cycloidal magnetic ground state, which can be easily overcome by applying a magnetic field, changing the spin structure to another state. In order to complement these macroscopic measurements, neutron diffraction was performed on RITA-2 using a horizontal magnetic field, on a single crystal of $MnSb_2O_6$, aligned in the $(H, 0, L)$ scattering plane such that the magnetic field could be aligned either along the c or a-axes. A single high intensity magnetic peak, $\boldsymbol{Q} = (1, 0, 1) - \boldsymbol{k}$ was scanned over a range of temperatures (between 1.75 and 11.5 K) and magnetic fields (between 0 and 5 T), applied parallel and perpendicular to the c-axis. Unpolarized neutrons are sensitive to the magnetic moments perpendicular to the scattering vector $\boldsymbol{Q}$, so a change of the measured intensity can be a direct proof of a change in the magnetic structure.

Fig. III.16 shows the results for the magnetic field applied along the c-axis. Fig. III.16(a)-(c) show reciprocal space scans along the L direction of the $\boldsymbol{Q} = (1, 0, 1) - \boldsymbol{k}$ magnetic peak at $T = 1.75\,\mathrm{K}$. The intensities are fitted to a skewed Gaussian:

$$I(L) \propto \left\{1 + \mathrm{erf}\left[\frac{\gamma(L - L_0)}{\sigma\sqrt{2}}\right]\right\} \exp\left\{\frac{-(L - L_0)^2}{2\sigma^2}\right\}, \qquad \text{(III.10)}$$

where γ is the skewness parameter, σ and L_0 are the Gaussian standard deviation and center. The mean values of the skew Gaussian are shown in dashed gray lines

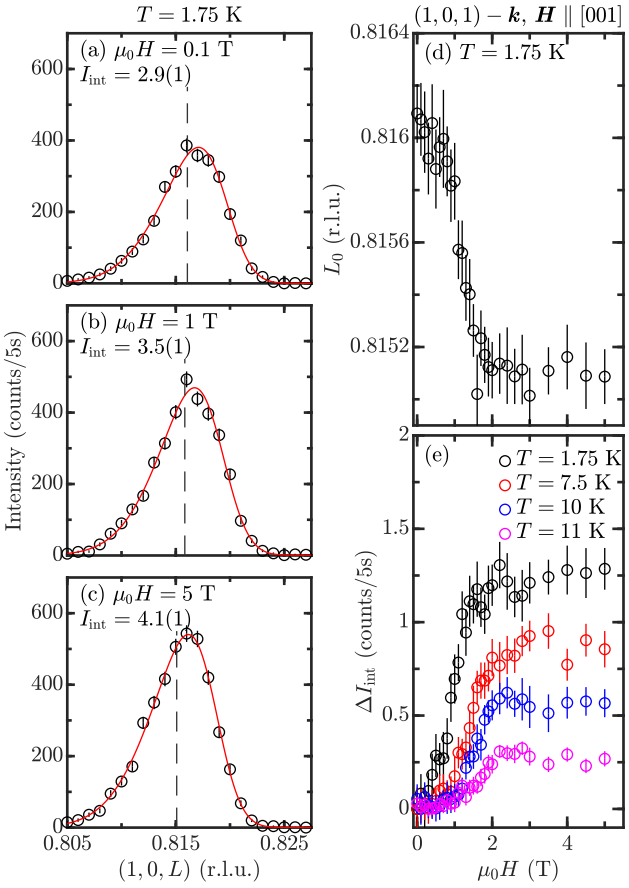

Figure III.16 The magnetic field is applied along the c-axis. (a)-(c) Scans at $T = 1.75\,\mathrm{K}$ along the $(00L)$ direction for different values of magnetic field. The mean position of the skewed Gaussian fits are shown in dashed lines and depend on the applied field. (d) Summary of the field dependence of the propagation vector at $T = 1.75\,\mathrm{K}$. (e) Integrated intensities of the magnetic peak $\boldsymbol{Q} = (1, 0, 1) - \boldsymbol{k}$ as a function of the magnetic field. The zero-field intensity is subtracted from each respective curve for a clearer comparison of the field-induced intensity increase.

and change with the magnetic field. A nuclear reflection (201) was also monitored as a function of the magnetic field and does not present any shift along the L direction. This means that the shift of the magnetic peak $\boldsymbol{Q} = (1, 0, 1) - \boldsymbol{k}$ is caused by a change of the propagation $\boldsymbol{k}$ and not of the lattice parameter c. This is summarized in Fig. III.16(d) where the propagation vector evolution can clearly be observed until a threshold magnetic field (around 2 T). Magneto-elastic effects can be induced by a change in the magnetic structure as illustrated in the change in bond distances at $T_{\rm N}$ discussed above and shown in Fig. III.12. A change in the bond distances would result in a change in the strength of the

exchange constants, which consequently change the propagation vector in order to minimize the ground state energy, from Eq. (III.8).

In Fig. III.16(e), the integrated intensities are displayed as a function of the magnetic field, for different temperatures. The zero-field intensity is subtracted from each respective curve, in order to compare the data on the same scale as the magnetic intensity diminishes when the temperature increases. The integrated intensities increase with the magnetic field until a threshold value (different for each temperature) and then remain constant. For a cycloidal magnetic ground state, when no external field is applied, one main axis of the spin ellipse lies in the (ab)-plane, and the other one along the c-axis. Applying a magnetic field $\boldsymbol{H} \parallel \boldsymbol{c}$ is expected to flop the spin rotation plane from a cycloid to a helix, where the latter is oriented perpendicular to the magnetic field. The gradual increase of the intensity shows that the cycloid plane is continously tilted from the c-axis. For $T = 1.75\,\mathrm{K}$, the observed intensities (with a magnetic field $< 2\,\mathrm{T}$) of reflection $\boldsymbol{Q} = (1,0,1) - \boldsymbol{k}$ match with calculated intensities for a circular helicoidal magnetic structure (with the main axis $\hat{\boldsymbol{u}} \parallel \boldsymbol{a}$ and $\hat{\boldsymbol{v}}$ rotated around $\hat{\boldsymbol{u}}$ by an angle θ, see Section III.3.2) as shown in Fig. III.17. The observed intensities were normalized to the intensity at 2.25 T, while the calculated intensities were normalized to the intensity at $\theta = 90°$. The matching of these normalized intensities indicates that the spin structure goes from a nearly pure cycloid state to a nearly pure helix state which is analogous to the zero field magnetic structure of iron based langasite. At $T = 1.75\,\mathrm{K}$, the tilt angle of the spin rotation plane seems to increase linearly with the magnetic field, whereas the tilt starts at higher magnetic field for higher temperatures.

The results are different when the magnetic field is rotated by 90° and applied in the ab-plane. In this case, the in-plane main axis of the cycloid will tend to be perpendicular to the magnetic field and the magnetic domains are simply reoriented in the ab-plane. As mentioned above, magnetic diffraction is not very sensitive to the direction of the in-plane main axis, because the intensities of the magnetic peaks do not change significantly between two directions of this axis. This is especially true for the magnetic peak $\boldsymbol{Q} = (1,0,1) - \boldsymbol{k}$, where the measured intensities are constant as a function of the magnetic field (Fig. III.18(a)). Contrary to previous thermodynamic magnetization measurements [152] the in-plane reorientation of the spin structure cannot be detected in this experiment. The propagation vector also remains constant, within error, as a function of the magnetic field (Fig. III.18(b)-(e)), indicating the absence of measurable magneto-

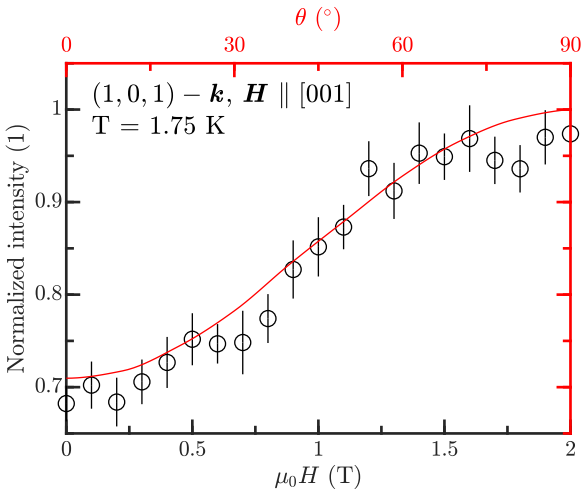

Figure III.17 (black points) Normalized integrated intensity of the measured magnetic peak $\boldsymbol{Q} = (1, 0, 1) - \boldsymbol{k}$ as a function of the magnetic field applied parallel to the c-axis at $T = 1.75\,\mathrm{K}$. (red curve) Simulated magnetic intensity as a function of the tilt angle θ of the spin rotation plane from the c-axis.

elastic effects in this case. We note that the difference in L_0 values between the two different field directions is an experimental artefact resulting from not being able to refine a zero offset in the scattering angle. This is due to only being able to measure a single Bragg peak owing to kinematic constraints imposed by the horizontal magnetic field geometry.

III.5 Theory for an electric polarization

In their work, Kinoshita *et al.* have measured the pyroelectric current in a single crystal of $MnSb_2O_6$ along $\hat{\boldsymbol{u}} \parallel [1\bar{1}0]$ under a magnetic field rotating in the $(1\bar{1}0)$ plane [58]. An electric polarization was measured for the magnetic field slightly off the (ab)-plane and was attributed to the selection of a tilted polar domain. This polarization is reversed when the magnetic field is applied on the other side of the (ab)-plane, favoring the opposite tilted polar domain. This mechanism relied on the tilted cycloid model considered as the ground state in $MnSb_2O_6$. In this section we discuss a phenomenological theory for the domain switching observed in Ref. [58] under the application of a magnetic field in the absence of a zero-field tilt as discussed in our diffraction results outlined above.

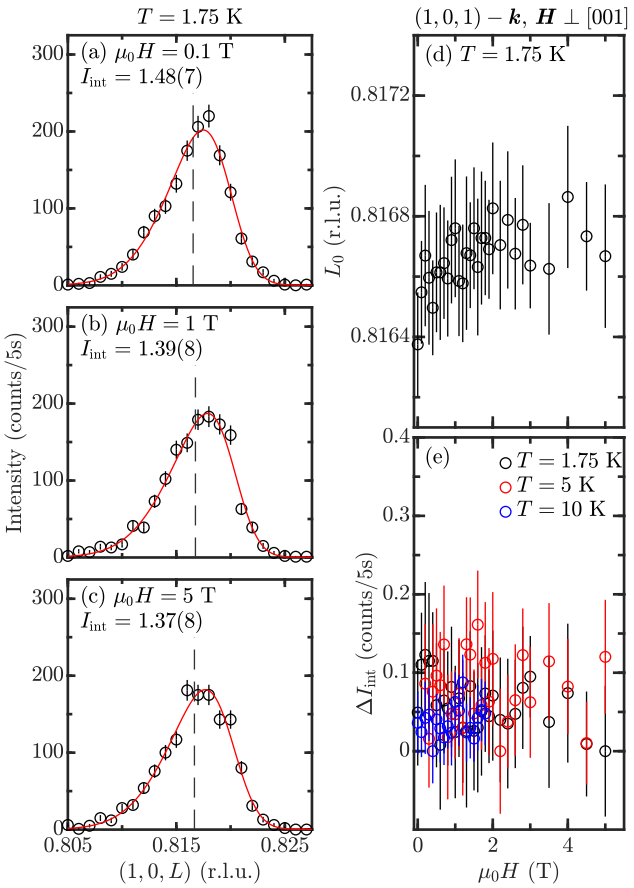

Figure III.18 The magnetic field is applied perpendicular to the c-axis. (a)-(c) Scans at $T = 1.75\,\mathrm{K}$ along the $(00L)$ direction for different values of magnetic field. The mean position of the skewed Gaussian fits are shown in dashed lines and remain constant. (d) Summary of the field dependence of the propagation vector at $T = 1.75\,\mathrm{K}$. (e) Integrated intensities of the magnetic peak $\boldsymbol{Q} = (1, 0, 1) - \boldsymbol{k}$ as a function of the magnetic field. The zero-field intensity is subtracted from each respective curve for a clearer comparison of the data.

As is the case for many compounds having a cycloidal magnetic structure, $MnSb_2O_6$ is predicted to hold an electric polarization (see Section I.2) through the inverse DM interaction [42] or spin-current induced [47] mechanisms which predict an electric polarization $\boldsymbol{P}$ given by

$$\boldsymbol{P} \propto \boldsymbol{r}_{ij} \times (\boldsymbol{S}_i \times \boldsymbol{S}_j) \tag{III.11}$$

which couples to the magnetic polarity $\boldsymbol{P}_{\rm m}$ in the phenomenological free energy

through a term $\propto \lambda \boldsymbol{P}_{\mathrm{m}} \cdot \boldsymbol{P}$. Therefore the electric polarization $\boldsymbol{P}$ lies parallel or antiparallel to to the magnetic polarity $\boldsymbol{P}_{\mathrm{m}}$ depending on the sign of the coupling constant λ [57].

Using our definitions in Eq. (III.4) and Eq. (III.5), we can build trilinear invariants based upon Heisenberg exchange interactions from Eq. (III.9):

$$\begin{aligned} \sigma \epsilon_H \epsilon_T = &\quad \sigma \eta_{\mathrm{C}} \eta_{\mathrm{T}} \sin^2(\theta) \\ \sigma \boldsymbol{P}_{\mathrm{m}} \cdot \boldsymbol{A} = &\quad \sigma \eta_{\mathrm{C}} \eta_{\mathrm{T}} \cos^2(\theta), \end{aligned} \tag{III.12}$$

Again, this shows the equivalence between the scalar and vector coupling schemes from iron langasite and $MnSb_2O_6$, and also the mixture of both with the spin rotation plane tilt angle θ. These invariants imply that the polarization $\boldsymbol{P}$, does not change sign with θ, based on Heisenberg exchanges alone.

However, we can consider a uniform DM interaction with $\boldsymbol{D}_{\alpha\beta}$ parallel to the c-axis. $\boldsymbol{D}_{\alpha\beta}$ is a T-even axial vector that changes sign on exchange of indices. Its sign will also depend upon the structural chirality σ, hence we can write $\boldsymbol{D}_{\alpha\beta} \propto \sigma \boldsymbol{r}_{\alpha\beta}$ where $\boldsymbol{r}_{\alpha\beta}$ is the bond vector between spins at sites α and β along the c-axis. Following Eq. (III.5), the magnetic energy is then given by

$$\begin{aligned} E_{\mathrm{DM}} &= \boldsymbol{D}_{\alpha\beta} \cdot (\boldsymbol{S}_\alpha \times \boldsymbol{S}_\beta) \\ &\propto \sigma \boldsymbol{r}_{\alpha\beta} \cdot \boldsymbol{V}_{\mathbf{C}} \\ &\propto \sigma \eta_{\mathrm{C}} \sin\theta, \end{aligned} \tag{III.13}$$

Therefore, for a given structural domain with a fixed σ, when the sign of θ is inverted (through the application of a magnetic field) the uniform DM interaction will favor a change of sign of η_{C} which in turn results in the sign of $\boldsymbol{P}_{\mathrm{m}}$ being inverted, from Eq. (III.4). This will change the direction of the electric polarization $\boldsymbol{P}$. The only condition for having a non-zero polarization is an imbalance of structural chiral domains for a given tilt angle θ. This mechanism does not need the magnetic ground state to be tilted. Indeed, the ground state could be a pure cycloid stabilized by Heisenberg exchanges, where the anisotropy overcomes this small DM term. When an external magnetic field is applied slightly out of the (ab)-plane, this would overcome the anisotropy and tilt the spin rotation plane. In this case the DM term would lift the degeneracy of $\pm\eta_{\mathrm{C}}$ domains, and give rise to a non-zero electric polarization for a given structural

domain. We note that the DM term is allowed owing to the large distortion of the oxygen octahedra surrounding the Mn^{2+} ions [50].

From our diffraction data under magnetic field, we know that a small magnetic field (around 2 T) is sufficient to reorient the spin rotation plane perpendicular to the magnetic field, which is consistent with a small single-ion anisotropy in our compound and is consistent with the values used in Ref. [58] in their macroscopic measurement of electric polarization. However, Ref. [58] has considered the tilted cycloid ground state as essential for selecting the polar domains with an external magnetic field applied perpendicularly to the spin rotation plane. This explanation does not work in the case that *magnetic* domains with polarity $\pm\eta_C$ have the exact same populations, because the overall polarization would compensate. As $\pm\eta_C$ domains are degenerate from Heisenberg model, our mechanism based on a uniform DM interaction is more general. In particular and in the context of $MnSb_2O_6$, this mechanism does not depend on a tilted ground state, and requires an imbalance in structural chiral domains and the underlying coupling between magnetic and structural chiralities.

III.6 Conclusions

In this chapter, we have performed a combination of unpolarized and polarized neutron diffraction experiments on $MnSb_2O_6$. The study of the crystal structure shows no evidence for the breaking of the paramagnetic crystallographic space group at the magnetic transition. The consideration of structural twins in our work shows that our single crystal is a non-racemic mixture of chiral structural domains. There is no evidence of a helicoidal magnetic ground state, but diffraction under magnetic field shows the possibility to manipulate the spin structure with low magnetic fields. Finally, we propose that a uniform DM interaction, combined with the underlying coupling between structural and magnetic chiralities, is sufficient to explain an electric polarization switching mechanism which was previously measured.

Chapter IV

Sum rules on $MnSb_2O_6$

This chapter presents results from inelastic neutron scattering experiments on $MnSb_2O_6$. This chapter has been adapted from Ref. [2].

IV.1 Introduction

Magnetic materials that lack an inversion center potentially host coupled magnetic and ferroelectric order parameters while also providing a framework for unusual magnetic excitations like directionally anisotropic (or nonreciprocal) spin-waves [148, 171]. Determining these magnetic interactions that provide the basis for coupled structural and magnetic properties is often complicated and based on many parameter fits from complex magnetic ground states [33, 42]. In this chapter we investigate the magnetic excitations in powder and in an array of single crystals of the helicoidal magnet $MnSb_2O_6$ with the goal of extracting the symmetric exchange constants from the Heisenberg model presented in Section III.1.4. Given the complexity of the excitation spectrum, the number of predicted exchange constants, and the ambiguities of the magnetic structure (tilted versus untilted ground state as discussed in Section III.4.2), we apply a first moment (Hohenberg-Brinkman) sum rule [172] analysis to extract the symmetric exchange constants and compare the results to the excitation spectrum from mean field linear spin-wave theory. This approach only depends on the relative orientation of neighboring magnetic moments and does not depend on whether the overall magnetic structure is tilted or untilted as discussed below. We

also demonstrate a generalized methodology for obtaining symmetric Heisenberg exchange constants from multiplexed neutron scattering where extensive regions of momentum and energy transfers are sampled.

The results presented in this chapter are based upon six sections. In Section IV.3.1, we present the excitation spectra from both powder and single crystals of $MnSb_2O_6$. After describing our absolute normalization process in Section IV.3.2, the total (zeroth) moment sum rule is applied to show we have captured all the magnetic spectral weight in our experiments. Section IV.3.4 will show the use of the first moment sum rule to extract, and Section IV.3.5 to determine the exchange constants from the Heisenberg model. Finally we apply Green's functions on a rotating frame to generate spin-wave spectra based on our derived exchange constants in Section IV.3.6. Using the values of the symmetric exchange constants from sum rules of neutron scattering, we refine the parameters to obtain a good description of the neutron inelastic spectra. Based on the Green's functions neutron response, the stability of spin-wave excitations is further tested for the proposed magnetic structures.

IV.2 Experimental details

IV.2.1 Materials preparation

Powders and single crystals of $MnSb_2O_6$ were synthetized by J. Pásztorová and C. Stock, following the procedure detailed in Section III.2.1.

IV.2.2 Neutron spectroscopy

To investigate the magnetic dynamics, neutron spectroscopy was performed on the MACS (NIST, Gaithersburg) triple-axis spectrometer [141] on both single crystals and powder samples. 1.3 g of single crystals were aligned in the (HHL) scattering plane on both sides of four aluminium plates and coated with viscous hydrogen free Fomblin oil, as shown in Fig. IV.1. A select fraction of the crystals were aligned with Laue diffraction and the remainder were aligned using polarized optical microscopy based on the crystal morphology. These single crystals were synthesized the same way as the samples measured in our previous studies in

Chapter III, where we have performed Schwinger scattering and transmission polarized optical microscopy and found only a small imbalance of chiral structural domains in the single crystals. This small imbalance distinguishes $MnSb_2O_6$ from the enantiopure single crystals of iron based langasite previously studied [134, 144, 145]. During the coalignment of the single crystals used here for spectroscopy, great care was taken to align the relative a and b inplane axes, the choice of what constituted $\pm$ [001] was done at random. For the purposes here we consider the average crystal structure to be an equal mixture of the differing chiral domains. We will show in Section IV.3.4 that our analysis holds no matter the proportion of chiral structural domains. To probe the dynamics in our array of single crystals, the final energy was fixed to either E_f=2.4 meV or 3.7 meV with BeO and Be filters, respectively, being used on the scattered side to filter out higher order neutrons from the monochromator. For all results presented here the pyrolytic graphite PG(002) monochromator was focused both horizontally and vertically. The lattice parameters were measured to be $a = b = 8.733\,\text{Å}$ and $c = 4.697\,\text{Å}$. For powder measurements, a 16.3 g sample was used with E_f=3.7 meV and a BeO filter on the scattered side.

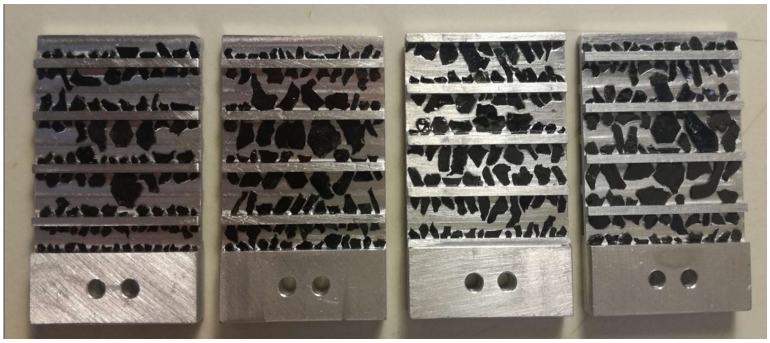

Figure IV.1 1.3 g of single crystals of $MnSb_2O_6$ aligned on four Al plates, and coated with Fomblin oil for inelastic neutron scattering.

The inelastic neutron scattering experiments on MACS at NIST were performed before the start of this thesis by C. Stock, J. Pásztorová, M. Songvilay and J. A. Rodriguez-Rivera.

IV.3 Results and discussion

In this section, we will first present the neutron scattering data for both powders and single crystals of $MnSb_2O_6$, before detailing our absolute normalization

process. Then, zeroth and first moment sum rules are applied to our inelastic data allowing the extraction of the symmetric exchange constants. We will finally use Green's functions on a rotating frame to compare the resulting spin-wave spectra to the experimental ones and to test the stability of proposed magnetic structures.

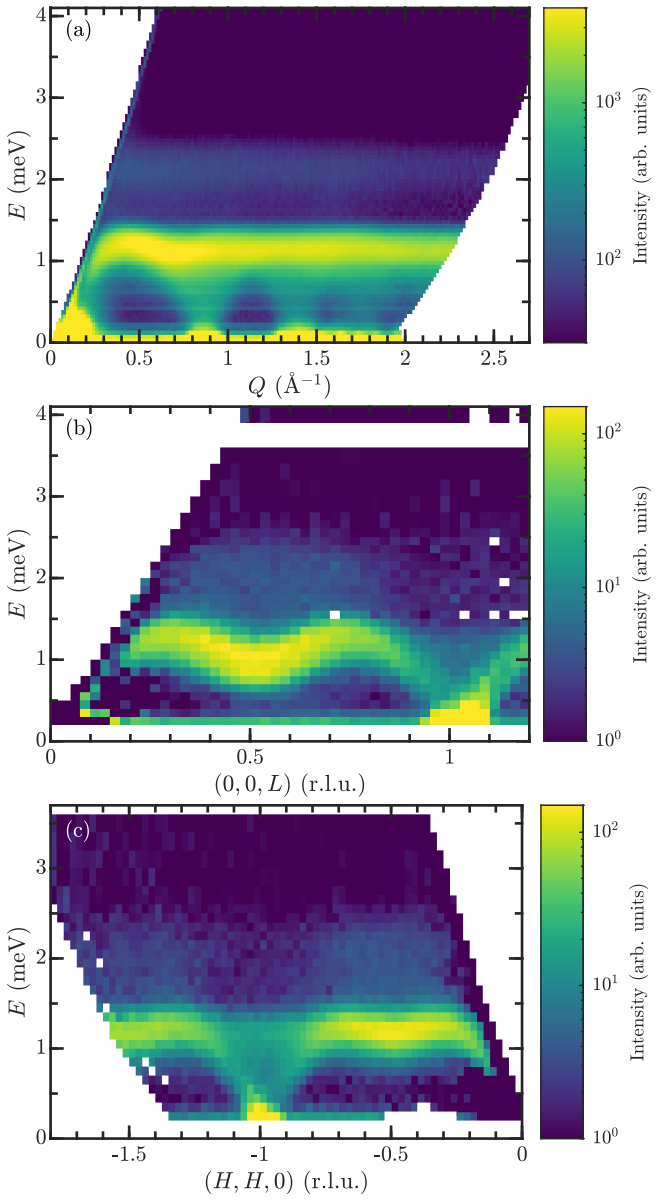

Figure IV.2 (a) Powder averaged inelastic neutron scattering spectrum taken on MACS at $T = 1.4\,\mathrm{K}$. (b)-(c) Single crystal inelastic neutron scattering spectrum from the $E_\mathrm{f} = 3.7\,\mathrm{meV}$ dataset at $T = 1.4\,\mathrm{K}$. The logarithmic intensity scales are chosen to show the two components to the scattering and in particular the higher energy weak scattering displayed at ~ 2 meV.

IV.3.1 Excitation spectra

IV.3.1.1 Total excitation spectra

The excitation spectra of both powders and single crystals of $MnSb_2O_6$ at $T = 1.4\,\mathrm{K}$ are shown in Fig. IV.2, with the $E_\mathrm{f} = 3.7\,\mathrm{meV}$ MACS setup. The powder data in Fig. IV.2(a) display intense low energy magnetic scattering extending from the elastic line to ~ 1 meV, and a weaker band of excitations at approximately twice this value at ~ 2 meV. The single crystal data displayed in Fig. IV.2(b)-(c) illustrate two different types of scattering: one with intense dispersive fluctuations that are well defined both in momentum and energy at low energies, and the other with a weaker momentum and energy broadened continuum of scattering extending to larger energy transfers. This continuum of scattering is most apparent at the zone boundaries in the single crystal data. Given the kinematics of these two types of scattering, we associate the lower energy dispersive fluctuations with one-magnon scattering and the higher energy continuum with two-magnon scattering. While two-magnon scattering is expected to be most prominent in $S = 1/2$ magnets [173–181], it is a direct result of the uncertainty associated with non-commuting observables and has been studied extensively in other large-S magnets [182–184]. We discuss this cross section later in the paper in the context of the zeroth moment sum rule and show indeed that these two components of scattering originate from single and multi magnon processes.

IV.3.1.2 Powder low-energy spectrum

Results of the low-energy powder inelastic neutron scattering experiment performed on MACS, with fixed final energy $E_\mathrm{f} = 3.7\,\mathrm{meV}$ are shown in Fig. IV.3. The powder averaged spin-wave dispersion at $T = 1.4\,\mathrm{K}$, below the Néel magnetic ordering transition, is presented in Fig. IV.3(a), showing low-energy spin dynamics below $E \approx 1.4\,\mathrm{meV}$. These dynamics are highly dispersive from the magnetic ordering wavevector and are gapless within experimental resolution ($\Delta E \approx 0.15\,\mathrm{meV}$). In contrast, above $T_\mathrm{N} \approx 12\,\mathrm{K}$, the magnetic scattering is considerably broadened both in momentum and energy indicative of spatially and temporally short-range correlations. This paramagnetic scattering is very strong due to high spin $S = 5/2$ of Mn^{2+} magnetic ions, as shown in Fig. IV.3(b) with the spectrum measured at $T = 25\,\mathrm{K}$. Both experimental datasets below

and above the magnetic ordering temperature also display a decay in intensity with increasing momentum transfer, characteristic of magnetic scattering. The powder averaged spectra establish the presence of dispersive magnetic dynamics and the energy scale of the spin excitations.

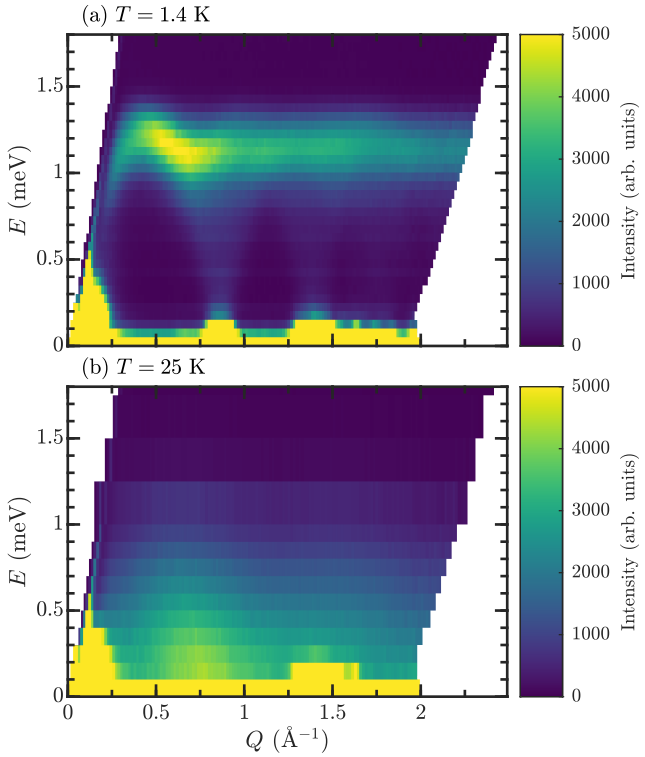

Figure IV.3 Powder inelastic neutron scattering spectrum of the one-magnon cross section at (a) $T = 1.4\,\mathrm{K}$ (below T_N) and (b) $T = 25\,\mathrm{K}$ (above T_N).

IV.3.1.3 Single crystal low-energy spectrum

Results of single crystal inelastic neutron scattering performed on MACS with a fixed final energy $E_\mathrm{f} = 2.4\,\mathrm{meV}$ are displayed in Fig. IV.4 and Fig. IV.5 at $T = 1.4\,\mathrm{K}$ below T_N. The data are illustrative of dispersive dynamics originating from the magnetic ordering wavevector. Constant energy slices at $E = 0.1\,\mathrm{meV}$ and $E = 1.25\,\mathrm{meV}$ are shown in Fig. IV.4(a) and (b). Spin-wave dispersion along $(-1,-1,L)$ and $(H,H,0)$ are respectively shown in Fig. IV.5(a) and Fig. IV.5(b). Spin-wave branches emerging from nuclear Bragg peak (-1,-1,0) and also its magnetic satellites (-1,-1,0)$\pm\boldsymbol{k}$ are visible in Fig. IV.4(a) and Fig. IV.5(a). Within the instrumental resolution ($\Delta E \approx 0.1\,\mathrm{meV}$), all modes seem gapless, which is consistent with the low anisotropy measured from electron spin resonance [152],

and observed from the tunability of the magnetic structure by small magnetic fields presented in Section III.4.3 and in Ref. [58].

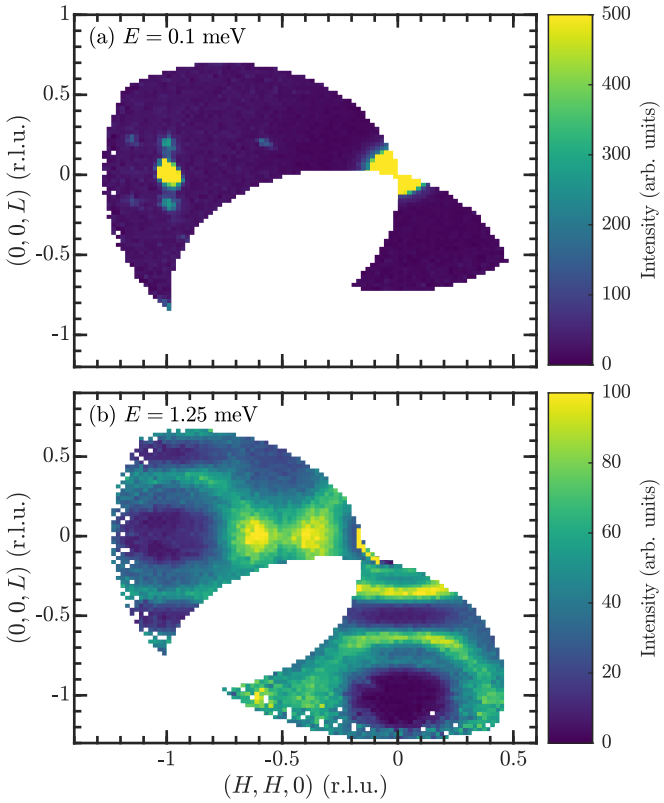

Figure IV.4 MACS single crystal inelastic neutron scattering spectra at $T = 1.4\,\mathrm{K}$: constant energy slices for (a) $E = 0.1\,\mathrm{meV}$ and (b) $E = 1.25\,\mathrm{meV}$. The weak scattering in (a) at $(H, H) \sim$ -0.5 and displaced at $(H, H) \sim$ -1.1 originate from some crystals misaligned by $\sim 60°$ in the multi crystal mount.

As already presented in Fig. IV.2(b)-(c), inelastic neutron scattering data were also obtained on MACS with the same array of single crystals, but with a fixed final energy $E_\mathrm{f} = 3.7\,\mathrm{meV}$. In the following, the dataset used for each analysis will be mentioned.

IV.3.2 Absolute normalization of magnetic cross section

In order to directly compare the magnetic scattering intensities from the different datasets, they have to be converted into absolute units. This is particularly important given our goal of applying sum rules of neutron scattering to obtain the magnetic exchange constants in absolute units of energy. Through this we will apply the zeroth moment sum rule to demonstrate that all of the magnetic

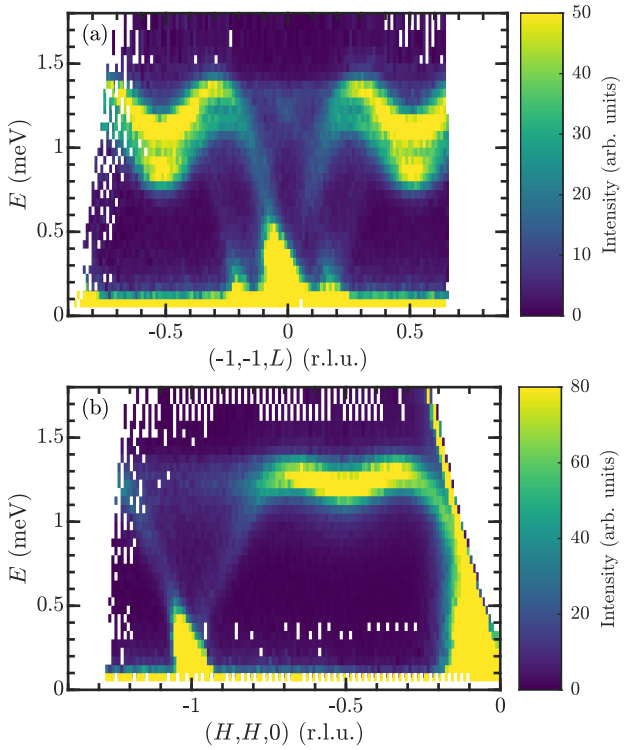

Figure IV.5 MACS single crystal inelastic neutron scattering spectra at $T = 1.4\,\mathrm{K}$: spin-wave dispersion along (a) $(-1,-1,L)$ and (b) $(H,H,0)$.

spectral weight is measured in the experiments discussed above. We then apply the first moment sum rule to obtain the symmetric exchange constants. In this section, we describe our normalization process, adapted from Ref. [185] and Ref. [186] and introduce our definition for the dynamical structure factor $S(\boldsymbol{Q}, E)$.

The intensity measured during the experiment $I(\boldsymbol{Q}, E)$ (in counts) is related to the differential cross section via a convolution with an instrumental-dependent resolution function R,

$$I(\boldsymbol{Q}, E) = \int \mathrm{d}\boldsymbol{Q}_0 \, \mathrm{d}E_0 \, \frac{\mathrm{d}^2\sigma}{\mathrm{d}\Omega \, \mathrm{d}E_\mathrm{f}}(\boldsymbol{Q}_0, E_0) R(\boldsymbol{Q} - \boldsymbol{Q}_0, E - E_0). \tag{IV.1}$$

By assuming a slow variation of this resolution function in the region of study (over the narrow energy range probed in this study), it can be approximated by a constant R_0, which allows us to decouple the intensity into

$$I(\boldsymbol{Q}, E) \approx R_0 \frac{\mathrm{d}^2\sigma}{\mathrm{d}\Omega \, \mathrm{d}E_\mathrm{f}}(\boldsymbol{Q}_0, E_0). \tag{IV.2}$$

During the data reduction, the intensity is normalized to the monitor counts based on a low efficiency detector placed in the incident beam after the monochromator and before the sample. The efficiency of which is inversely dependent to the speed of the incident neutrons, which is proportional to k_i, giving the normalized intensity (in counts/mon):

$$\bar{I}(\boldsymbol{Q}, E) = k_\mathrm{i} I(\boldsymbol{Q}, E) = k_\mathrm{i} R_0 \frac{\mathrm{d}^2\sigma}{\mathrm{d}\Omega\, \mathrm{d}E_\mathrm{f}}(\boldsymbol{Q}, E). \tag{IV.3}$$

Having related the measured scattering intensity to the cross section, we now focus on the magnetic differential cross section for unpolarized neutrons and identical magnetic ions. Assuming isotropic spin excitations, we can define the dynamic structure factor $S(\boldsymbol{Q}, E) = S^{xx} = S^{yy} = S^{zz}$, where $S^{\alpha\beta}$ is the dynamic spin correlation function related to the Fourier transform of the spin-spin correlation function as defined in Eq. (II.52). Neglecting the Debye-Waller factor gives the following double differential cross section:

$$\frac{\mathrm{d}^2\sigma}{\mathrm{d}\Omega\, \mathrm{d}E_\mathrm{f}}(\boldsymbol{Q}, E) = N \frac{k_\mathrm{f}}{k_\mathrm{i}} \left(\frac{\gamma r_0}{2}\right)^2 (g|f(\boldsymbol{Q})|)^2 2S(\boldsymbol{Q}, E), \tag{IV.4}$$

where N is the number of unit cells, $\gamma r_0/2 \approx 0.2695 \times 10^{-12}\,\mathrm{cm}$ is the typical magnetic scattering length, g is the Landé factor and $f(\boldsymbol{Q})$ the magnetic form factor. Combining Eq. IV.3 and IV.4 we get the dynamical structure factor (in meV^{-1}) from the measured intensity by

$$S(\boldsymbol{Q}, E) = \frac{\bar{I}(\boldsymbol{Q}, E)}{|gf(\boldsymbol{Q})|^2 (\frac{\gamma r_0}{2})^2 2 N k_\mathrm{f} R_0}. \tag{IV.5}$$

We can write directly the numerical values of the magnetic cross section $(\gamma r_0/2)^2$ into the equation:

$$S(\boldsymbol{Q}, E) = \frac{13.8(\mathrm{b}^{-1}) \bar{I}(\boldsymbol{Q}, E)}{|gf(\boldsymbol{Q})|^2 2 N k_\mathrm{f} R_0}. \tag{IV.6}$$

The key for normalizing the magnetic intensity is thus to evaluate this instrumental-dependent factor $N k_\mathrm{f} R_0$ expressed in (meV)(counts/mon)(b^{-1}).

There are several ways reported in the literature for obtaining this instrument calibration factor. One possibility is to evaluate the incoherent scattering from the

elastic line of a known standard compound (for example as done in Ref. [187]). By energy integrating the measured intensity close to elastic energy transfer, far from any magnetic or nuclear Bragg peak, we obtain, as $k_\mathrm{i} = k_\mathrm{f}$ for elastic scattering,

$$\int_{-\epsilon}^{+\epsilon} \mathrm{d}E\, \bar{I}(\boldsymbol{Q}, E) = N k_\mathrm{f} R_0 \sum_i (b_i^\mathrm{inc})^2, \tag{IV.7}$$

where b_i^inc is the incoherent scattering length of atom i, and the sum is over the unit cell. Vanadium having a large incoherent scattering cross section compared to its coherent one, it is usually used as a standard sample to normalize inelastic neutron scattering data. We have measured the vanadium sample in the same geometry and instrumental configuration as our $MnSb_2O_6$ powder sample. With N_V the number of vanadium atoms and its incoherent scattering length $b_\mathrm{V}^\mathrm{inc} = 6.35\,\mathrm{fm}$ [103], we can write

$$N_\mathrm{V} k_\mathrm{f} R_0 = \frac{\int_{-\epsilon}^{+\epsilon} \mathrm{d}E\, \bar{I}_\mathrm{V}(\boldsymbol{Q}, E)}{(b_\mathrm{V}^\mathrm{inc})^2}. \tag{IV.8}$$

By writing $N_\mathrm{V} = m_\mathrm{V}/(A_\mathrm{r}(V) m_\mathrm{u})$ with m_V the mass of the vanadium sample, $A_\mathrm{r}(V)$ the relative atomic mass of vanadium, and m_u the atomic mass constant, we can write the ratio $N/N_\mathrm{v} = \frac{m/A_\mathrm{r}(\mathrm{MnSb_2O_6})_\mathrm{cell}}{m_\mathrm{V}/A_\mathrm{r}(V)}$ with m the mass of the $MnSb_2O_6$ sample, and $A_\mathrm{r}(\mathrm{MnSb_2O_6})_\mathrm{cell}$ the relative mass of a unit cell (three formula units of $MnSb_2O_6$ per unit cell), the normalization factor becomes

$$N k_\mathrm{f} R_0 = \frac{m/A_\mathrm{r}(\mathrm{MnSb_2O_6})_\mathrm{cell}}{m_\mathrm{V}/A_\mathrm{r}(V)} \frac{\int_{-\epsilon}^{+\epsilon} \mathrm{d}E\, \bar{I}_\mathrm{V}(\boldsymbol{Q}, E)}{0.403\,\mathrm{b}}. \tag{IV.9}$$

This equation allows us to obtain the instrumental calibration factor from the incoherent cross section centered at the elastic ($E = 0$) position. We note that an alternate way to obtain this calibration constant is to measure the elastic incoherent cross section from the sample given manganese has a comparatively large incoherent cross section. We did not take this approach in this experiment as we found the elastic line where incoherent scattering is present in our single crystal geometry was contaminated by scattering from hydrogen free (yet fluorine based) Fomblin oil. Fomblin, while having a comparatively small incoherent cross section in comparison to hydrogen, has a non-negligible coherent liquid-like cross section.

This cross section is difficult to disentangle from the purely Mn^{2+} incoherent cross section and therefore we relied on a separate vanadium standard of known mass.

IV.3.3 Total moment sum rule

Having established the procedure for calibration of the instrument, we now discuss the sum rules of neutron scattering. Magnetic neutron scattering is governed by sum rules which are satisfied by integrating the dynamical spin correlation function $S^{\alpha\beta}(\boldsymbol{Q}, E)$ over energy and momentum transfer [172]. In particular the energy moments, $\int_{-\infty}^{+\infty} E^n S^{\alpha\beta}(\boldsymbol{Q}, E)\,\mathrm{d}E$ are given theoretically [172, 188], with $n = 0, 1$ the zeroth and first moment. Full derivations of these sum rules can be found in Ref. [189].

The zeroth moment sum rule is often referred to as the total moment sum rule and corresponds to the integral of all the magnetic spectral weights [185, 190–192]:

$$\frac{3\int \mathrm{d}^3\boldsymbol{Q} \int \mathrm{d}E\, S(\boldsymbol{Q}, E)}{\int \mathrm{d}^3\boldsymbol{Q}} = N_\mathrm{m} S(S+1), \tag{IV.10}$$

where $N_\mathrm{m} = 3$ is the number of magnetic ions per unit cell. This quantity can be considered as a conservation rule and allows us to confirm whether we have experimentally measured all of the spectral weight. This rule has become particularly important in itinerant compounds near potential critical points [193]. We will apply this zeroth moment sum rule to our powder data, which was normalized using a vanadium standard sample, following the process described above. In this case, the total moment can be written as

$$I = \frac{\int \mathrm{d}Q\, Q^2 \int \mathrm{d}E\, S(Q, E)}{\int \mathrm{d}Q\, Q^2} = S(S+1) \tag{IV.11}$$

with $Q = |\boldsymbol{Q}|$. In order to estimate the spectral contributions from one-magnon and two-magnon scattering, we can introduce the momentum integrated intensity:

$$\tilde{I}(E) = \frac{3\int \mathrm{d}Q\, Q^2 S(Q, E)}{\int \mathrm{d}Q\, Q^2}, \tag{IV.12}$$

which measures the magnetic density of states [191, 192]. Then the integral

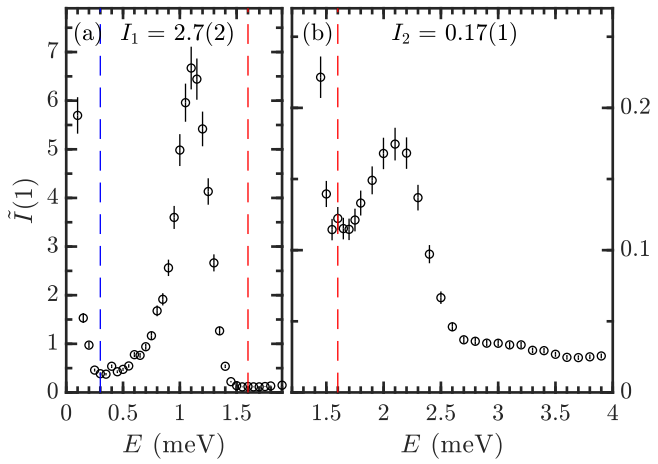

Figure IV.6 Momentum integrated intensities as a function of the energy, for (a) $E \in [0, 1.9]$ meV, and (b) $E \in [1.3, 4]$ meV. The intensities are integrated between the dashed blue (0.4 meV) and red (1.6 meV) lines to get the one-magnon spectral weight I_1, and above the red lines to 4 meV to get the two-magnon spectral weight I_2.

$\int_{E_{\min}}^{E_{\max}} \mathrm{d}E\, \tilde{I}(E)$ gives the spectral weight for the energy interval $[E_{\min}, E_{\max}]$. Figure IV.6 shows the momentum integrated intensities as a function of the energy. As discussed above, the magnetic intensity consists of two components with a low-energy component which consists of harmonic excitations well defined in momentum and energy and a second considerably weaker component which is broadened in momentum and energy transfer. These correspond to single [Fig. IV.6(a)] and two-magnon [Fig. IV.6(b)] dynamics and are separated in the powder averaged data. We can see that the one- and two-magnon contributions crossover around 1.6 meV (red dashed line), but since the intensities are quite low at this energy we consider 1.6 meV as the upper bound of the one-magnon scattering, and 0.3 meV as its lower bound (blue dashed line).

To extract numerical values for the integrated zeroth moments from our powder data we average the data in momentum. Accounting from the momentum powder average, the Q-dependence of the integrated intensity is given by [190, 194]

$$\mathcal{L}(Q_{\max}) = \frac{\int_0^{Q_{\max}} \mathrm{d}Q\, Q^2 \int \mathrm{d}E\, S(Q,E)}{\int_0^{Q_{\max}} \mathrm{d}Q\, Q^2} \tag{IV.13}$$

and is shown in Fig. IV.7 for both (a) one-magnon and (b) two-magnon contributions discussed above. The momentum average in this plot allows us to account for limited kinematic coverage of the detectors at low momentum

transfers (see low momentum transfers in Fig. IV.3). From Fig. IV.7, we can see that $\mathcal{L}(Q_{\max})$ approximately fully saturates close to $2\,\text{Å}^{-1}$ thereby illustrating that approximately all of the spectral weight has been sampled.

Based on this momentum average of the powder data, the spectral weight $I_1 = 2.7(2)$ for one-magnon scattering is then calculated by integrating the intensity between 0.3 meV [dashed blue line in Fig. IV.6(a)], and 1.6 meV (dashed red line in Fig. IV.6). The two-magnon spectral weight is obtained by integrating between 1.6 and 4 meV, leading to $I_2 = 0.17(1)$.

	Theory	Experiment
Total	$S(S+1) = 8.75$	8.2(2)
Elastic	$\langle S_z \rangle^2 = 5.3$	
One-magnon	$(S - \Delta S)(1 + 2\Delta S) = 3.2$	2.7(2)
Two-magnon	$\Delta S(\Delta S + 1) = 0.2$	0.17(1)

Table IV.1 Contributions of the different components of the scattering for $S = 5/2$ and $\Delta S = 0.2$ deduced from neutron powder diffraction.

The elastic (static) scattering contribution to the total moment is $\langle S_z \rangle^2$ where z indicates the direction of the Mn^{2+} spin in the rotated local frame. From our neutron powder diffraction (previously outlined in Section III.4.2.1) the ordered moment is $g\langle S_z \rangle = 4.6\,\mu_B$ at 2.6 K leading to $\langle S_z \rangle^2 = 5.3$, and a spin reduction from the expected full saturated moment corresponding to $S = 5/2$ of $\Delta S = S - \langle S_z \rangle = 0.2$. This missing component from the experimental $\langle S_z \rangle$ by conservation of spectral weight is expected to reside in the multimagnon component of the neutron dynamics corresponding to longitudinal fluctuations.

Based on this elastic spectral weight, the theoretical total, one-magnon, and two-magnon contributions can be computed [183, 195]. They are compared with those obtained experimentally in Table IV.1. The experimental total moment is 8.2(2), which is to be compared to the expected value of 8.75 for $S = 5/2$. The discrepancies can be due to the relatively small Q-range measured during this experiment and experimental systematic issues such as the use of an external vanadium standard or small variations in the resolution function over the energy range probed here. Given the small energy and momentum ranges, and that we have integrated the intensity over all momentum and energy, we do not expect that changes in the resolution to be important. However, the results are in good agreement illustrating the relative weights of one- and two-magnon cross sections

and the energy range over which the magnetic dynamics are present in $MnSb_2O_6$. This also confirms our assignment of the higher energy component to longitudinal two-magnon scattering and also illustrates all of the spectral weight is sampled in the dynamic range of our experiments.

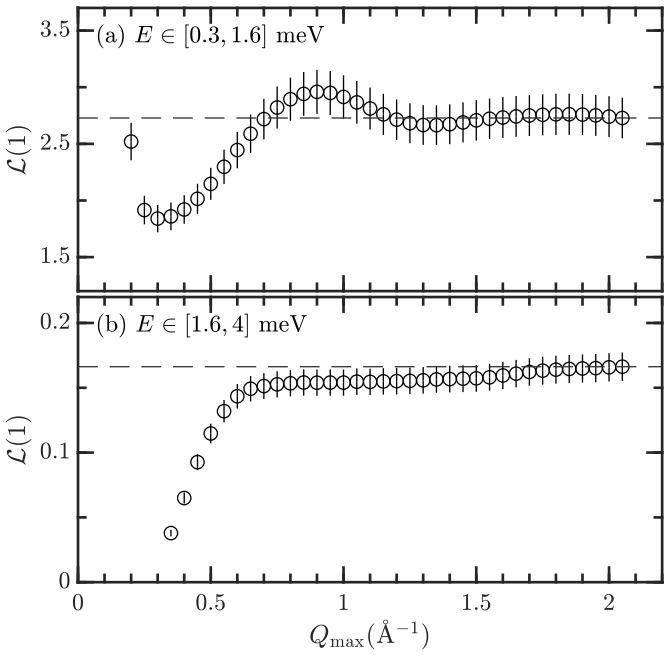

Figure IV.7 Integrated intensities as a function of $Q_{\max}$ the momentum integration upper bound, for (a) one-magnon and (b) two-magnon scattering. The dashed lines indicate the final values for $Q_{\max} = 2.05\,\text{Å}$.

IV.3.4 First moment sum rule

The previous discussion of the zeroth moment sum rule has established several points relevant for the rest of the paper. First, we established the energy range of the magnetic dynamics in $MnSb_2O_6$. Second, we have established the relative spectral weights of the single and two-magnon cross sections and found these to be in good agreement with missing spectral weight observed in diffraction experiments. Third, we have established and verified a calibration procedure for the powder data.

IV.3.4.1 Theory

In this section, we discuss the first moment sum rule and how it can be applied to extract symmetric exchange constants. The first moment is defined for general dynamic spin correlation function $S^{\alpha\beta}(\boldsymbol{Q}, E)$ as

$$\begin{aligned}\langle E\rangle(\boldsymbol{Q}) &\equiv \int_{-\infty}^{\infty} \mathrm{d}E\, E\; S^{\alpha\beta}(\boldsymbol{Q}, E) \\ &= \int_{-\infty}^{\infty} \mathrm{d}E\, \langle[\hat{S}^{\alpha}(\boldsymbol{Q}, E), \hat{\mathcal{H}}]\hat{S}^{\beta}(-\boldsymbol{Q}, 0)\rangle \\ &= \langle[\hat{S}^{\alpha}(\boldsymbol{Q}), \hat{\mathcal{H}}]\hat{S}^{\beta}(-\boldsymbol{Q})\rangle.\end{aligned} \tag{IV.14}$$

For nuclear scattering from a monotonic system, this reduces to $\frac{\hbar^2 Q^2}{2M}$, where M is the mass of the scattering nucleus [196, 197]. For magnetic systems and in the case for symmetric-only exchange where the Hamiltonian has the form $\hat{\mathcal{H}} = \sum_{i,j} J_{ij}\hat{\boldsymbol{S}}_i \cdot \hat{\boldsymbol{S}}_j$, the Hohenberg-Brinkman first moment sum rule is given by [172, 185, 190–192]

$$\begin{aligned}\langle E\rangle(\boldsymbol{Q}) &= \int \mathrm{d}E\, E\; S(\boldsymbol{Q}, E) \\ &= -\frac{2}{3}\sum_{i,j} n_{ij} J_{ij} \langle \hat{\boldsymbol{S}}_i \cdot \hat{\boldsymbol{S}}_j\rangle [1 - \cos(\boldsymbol{Q}\cdot \boldsymbol{d}_{ij})],\end{aligned} \tag{IV.15}$$

where $\langle \hat{\boldsymbol{S}}_i \cdot \hat{\boldsymbol{S}}_j\rangle$ is the ground-state equal-time correlation function of spins $\hat{\boldsymbol{S}}_i$ and $\hat{\boldsymbol{S}}_j$ at sites i and j, n_{ij} is the multiplicity of J_{ij}, the exchange constant associated to the bond vector $\boldsymbol{d}_{ij}$. This equation assumes symmetric-only exchange as we anticipate is dominant for $3d$ magnetic transition metal ions in the absence of spin-orbit coupling. Anisotropic terms in the magnetic Hamiltonian appear as constants to this equation for the first moment, however, given the lack of an orbital degree of freedom in Mn^{2+} in an octahedra, we expect such terms to be small in comparison to the symmetric Heisenberg exchange and therefore neglect them here.

Knowing the crystal and magnetic structure of a compound gives the bond vectors $\boldsymbol{d}_{ij}$ and the correlators $\langle \hat{\boldsymbol{S}}_i \cdot \hat{\boldsymbol{S}}_j\rangle$. Then, measuring the first moment for different $\boldsymbol{Q}$ values allows to fit the exchange constants, which correspond to the amplitudes of the sinusoidal oscillations. We note that Eqn. IV.15 only depends on the relative orientation of neighboring spins which has been modelled previously using

neutron diffraction. For the following, in terms of notation, the spin component $S(S+1)$ will be included in the exchange constants instead of the correlators and the exchange constants are in units of meV.

In $MnSb_2O_6$, seven nearest neighbors exchange interactions are considered and expected to be relevant, as shown in Fig. III.4, related to a total of 30 Mn-Mn bonds per unit cell. The first thing to evaluate is the ground-state correlation functions $\langle \hat{\boldsymbol{S}}_i \cdot \hat{\boldsymbol{S}}_j \rangle$ for each of the bonds. The magnetic ground state of $MnSb_2O_6$ is unclear, rather reported as a pure cycloid in Ref. [57] or tilted from the c-axis in Ref. [58]. But in both cases, the spin structure is helicoidal with the spins co-rotating in the same plane as described in Section III.3.3. Thus, the scalar product can be simply evaluated by $\cos \Delta\theta_{ij}$, with $\Delta\theta_{ij}$, the angle difference between the spins in the same rotation plane. The exchange interactions are listed in Table IV.2 with their associated multiplicities, bond distances, and ground-state correlators, with $k = 0.182$ the propagation vector component along the c-axis. We emphasize that this method only depends on relative orientation of neighboring spins and not on details for the tilted and non tilted helicoidal structures. Indeed, the $\langle \hat{\boldsymbol{S}}_i \cdot \hat{\boldsymbol{S}}_j \rangle$ correlators are the same in both models. Therefore, this method allows us an independent means of measuring the exchange constants without details of the long-range magnetic structure that is relevant for spin-wave calculations. We discuss this point later in the context of stability of the long-wavelength excitations once we have obtained the exchange constants from the first moment analysis.

Furthermore, we note that the correlators for diagonal paths actually depend on the sense of rotations of the spins, and thus on the magnetic parameters η_{C} and η_{T}. From the energy invariant, these magnetic parameters are related to the structural chirality by $\sigma = \eta_{\mathrm{C}}\eta_{\mathrm{T}}$ [Eq. (III.9)]. Thus the correlators for the diagonal exchange paths are $\cos(2\pi(\eta_{\mathrm{C}}k \pm \eta_{\mathrm{T}}/3)) = \cos(2\pi(k \pm \sigma/3))$ for left- J_5, J_7 $(+)$ and right-handed J_3, J_6 $(-)$ exchange interactions. The diagonal exchange interactions are interchanged by inversion symmetry, which corresponds to an inversion of σ. Thus, ground-state correlators are invariant for a given exchange constant. Thus the analysis holds independently of the structural and magnetic domains populations. This is convenient as a mixture of structural and magnetic domains was previously measured in a single crystal of $MnSb_2O_6$ as shown in Chapter III.

For a fixed scattering vector $\boldsymbol{Q}$, the cosine frequency will only depend on the bond distances. We can therefore define the parameters γ associated to each of

J_i	n_i	d_i (Å)	$\Delta\theta_{ij}$	$c_{ij} = \langle \hat{\boldsymbol{S}}_i \cdot \hat{\boldsymbol{S}}_j \rangle = \cos \Delta\theta_{ij}$
J_1	3	$d_1 = 5.5961$	$2\pi/3$	$c_1 = -0.5$
J_2	6	$d_2 = 4.8445$		
J_3	3	$d_\mathrm{i} = 7.3235$	$2\pi(k + \epsilon_\mathrm{T}/3)$	$c_\mathrm{R} = -0.995$
J_4	3	$d_4 = 4.7241$	$2\pi k$	$c_4 = 0.414$
J_5	3	$d_\mathrm{i} = 7.3235$	$2\pi(k - \epsilon_\mathrm{T}/3)$	$c_\mathrm{L} = 0.58$
J_6	6	$d_\mathrm{e} = 6.7666$	$2\pi(k + \epsilon_\mathrm{T}/3)$	$c_\mathrm{R} = -0.995$
J_7	6		$2\pi(k - \epsilon_\mathrm{T}/3)$	$c_\mathrm{L} = 0.58$

Table IV.2 Summary of the exchange interactions J_i, with their multiplicity in the unit cell n_i, the related bond distance d_i, the spin angle difference $\Delta\theta_{ij}$ and the associated ground-state correlation functions c_{ij}. Subindices i and e refer to the diagonal bond distances internal and external to the triangle of Mn interconnected by J_1. Subindices L and R refer to left- and right-handed correlation functions.

the five distinct bond lengths, which are functions of the exchange constants and ground-state correlation functions:

$$\begin{cases} \gamma_1 = J_1 c_1 & \text{(IV.16a)} \\ \gamma_2 = J_2 c_1 & \text{(IV.16b)} \\ \gamma_4 = J_4 c_4 & \text{(IV.16c)} \\ \gamma_\mathrm{i} = J_3 c_\mathrm{R} + J_5 c_\mathrm{L} & \text{(IV.16d)} \\ \gamma_\mathrm{e} = J_6 c_\mathrm{R} + J_7 c_\mathrm{L}, & \text{(IV.16e)} \end{cases}$$

where the c_i are calculated from the co-rotating helicoidal magnetic structure[1] and displayed in Table IV.2.

IV.3.4.2 Single-crystal data

Having discussed the equations and theory for the first moment sum rule applied to $MnSb_2O_6$, we now apply this to our single crystal sample aligned in the (HHL) scattering plane. We can simplify the calculation of the first moment by fixing $H = H_0$ and varying L (L-scan), or fixing $L = L_0$ and varying H (H-scan). This leads to two different analyses. The L-scan analysis will be detailed in the following section, while the H-scan analysis is presented in Appendix E.2.

The data is extracted along an L-scan, considering $\boldsymbol{Q} = (H_0, H_0, L)$ with L

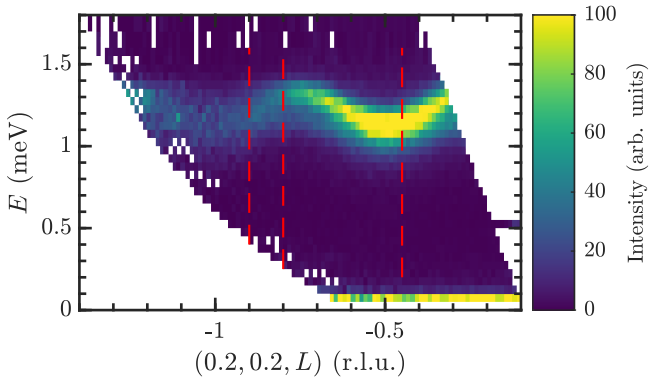

Figure IV.8 MACS single crystal inelastic neutron scattering spectrum: spin-wave dispersion along $(0.2, 0.2, L)$. The red dashed lines indicate constant-$\boldsymbol{Q}$ scans shown in Fig. IV.9(a)-(c).

varying and a given H_0. In the following we will consider the $E_\mathrm{f} = 2.4\,\mathrm{meV}$ dataset, as an example, we take $H_0 = 0.2$. The spin-wave dispersion along $(0.2, 0.2, L)$ is shown in Fig. IV.8. For each interaction indexed by spins i and j, the corresponding term in the first moment cosine from Eq. (IV.15) can be written as

$$\boldsymbol{Q} \cdot \boldsymbol{d}_{ij} = 2\pi H_0(d_{ij,x} + d_{ij,y}) + 2\pi L d_{ij,z}, \tag{IV.17}$$

where the distances d_{ij} are expressed in lattice units, and the scattering vector in reciprocal lattice units. Using trigonometric identities to expand the cosine term, and summing Eq. (IV.15) over the 30 bonds in the unit cell, a general formula for the first moment is derived, for a fixed H_0:

$$\langle E \rangle(H_0, L) = A(H_0)\cos(2\pi L) + C(H_0), \tag{IV.18}$$

where A and C are two H_0-dependent functions of the γ parameters, given by

$$A(H_0) = \frac{2}{3}[(1 + 2c(H_0))\gamma_i + 3\gamma_4 + 2\Sigma_c(H_0)\gamma_e] \tag{IV.19}$$

$$C(H_0) = -\frac{2}{3}[2(1 - c(H_0))\gamma_1 + \ldots \\ 2(3 - \Sigma_c(H_0))\gamma_2 + 3\gamma_i + 3\gamma_4 + 6\gamma_e], \tag{IV.20}$$

where,

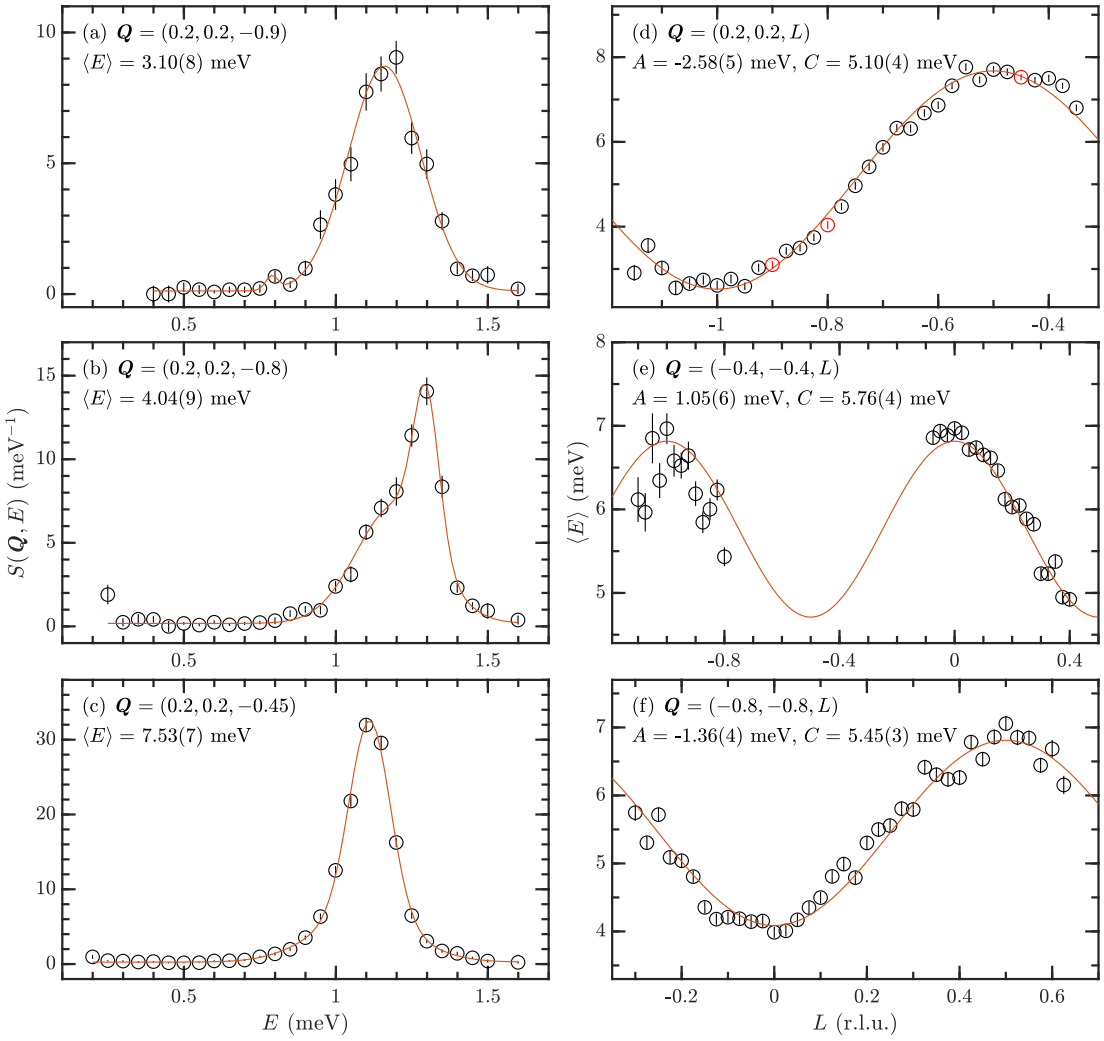

Figure IV.9 (a)-(c) Constant-$\boldsymbol{Q}$ scans for different $\boldsymbol{Q} = (0.2, 0.2, L)$, indicated with dashed red lines in Fig. IV.8. A fit to a double gaussian is shown in red, and the first moment is calculated from trapezoidal integration where the background is removed from the gaussian fit. (d) First moment as a function of L for $H_0 = 0.2$, fitted to its theoretical expression (red curve). The red data points corresponds to the first moments calculated in the cuts plotted in (a)-(c). (e)-(f) First moment as a function of L for (e) $H_0 = -0.4$ and (f) $H_0 = -0.8$, fitted to theoretical expression in red.

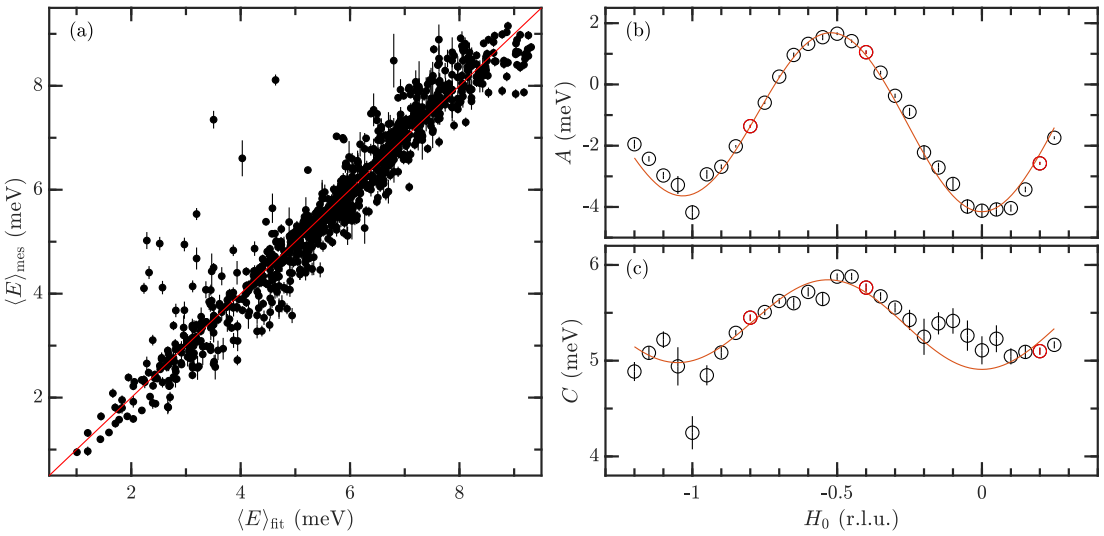

Figure IV.10 (a) Measured first moments versus fitted first moments for L-scan analysis, for the $E_{\rm f} = 2.4\,$meV dataset. A total of 969 $\langle E\rangle(\boldsymbol{Q})$ were taken into account. (b)-(c) Fitting of coefficients (b) A and (c) C giving the γ parameters. The red data points show the values calculated in Fig. IV.9(d)-(f).

$$c(H_0) = \cos(2\pi H_0 \delta_1)$$
$$\Sigma_c(H_0) = \cos(2\pi H_0 \delta_2) + \cos(2\pi H_0 \delta_3) + \cos(2\pi H_0 \delta_4)$$

are H_0-dependent harmonic oscillations, and

$$\delta_1 = 3(1 - r_x)$$
$$\delta_2 = 1$$
$$\delta_3 = 2 - 3r_x$$
$$\delta_4 = 3r_x - 1$$

are Mn-Mn interatomic distances (in r.l.u.) projected in the (ab)-plane. $r_x = 0.6329$ is the a-axis coordinate of the Mn atom at Wyckoff site $3e$, taken from the single-crystal neutron diffraction refinement at $T = 2\,$K from Table III.1.

From Eq. (IV.18), for a specific H_0, we can compute the first moment as a function of L, and fit the coefficients $A(H_0)$ and $C(H_0)$ for a scan along (H_0, H_0, L). The next step is to repeat the same process for several H_0, and fit the γ parameters in coefficients A and C with Eq. (IV.19) and Eq. (IV.20).

Examples of calculations of the first moment for different L, for $\boldsymbol{Q} = (0.2, 0.2, L)$

are shown in Fig. IV.9(a)-(c). These constant-$\boldsymbol{Q}$ scans are indicated in red dashed lines in Fig. IV.8. Most of the $S(\boldsymbol{Q}, E)$ are well fitted by two Gaussians, shown in red in the figures, but to take into account any deviation from a two-mode spectrum, the numerical integration of the first moment from Eq. (IV.15) was performed using a trapezoidal integration, with the background removed from these two-Gaussian fits. The calculation is performed above 0.2 meV to get rid of any contribution from elastic scattering, and below 1.6 meV to only capture contribution from one-magnon scattering. This criterion is arbitrary, and low-energy scattering can be miscalculated. Actually, due to Eq. (IV.15), lowest energy points contribute less to the first moment (given a low magnetic intensity at low energy), so the differences are not significant within uncertainties. More information concerning the numerical integration and the differences between the methods of integration are given in Appendix E.1.

These first moments are calculated for a range of L, as shown in Fig. IV.9(d) where first moments computed in Fig. IV.9(a)-(c) are highlighted in red. For this specific $H_0 = 0.2$, the A and C parameters are obtained from the fit (red curve) to Eq. (IV.15). The H_0-dependence of A and C is then obtained by repeating the same procedure for different H_0, as illustrated in Fig. IV.9(e)-(f) for $H_0 = -0.4$ and $H_0 = -0.8$.

Finally, a total of 969 first moments $\langle E \rangle(\boldsymbol{Q})$ were calculated from the MACS $E_\mathrm{f} = 2.4\,\mathrm{meV}$ dataset for this analysis and are shown as a function of the fitted first moment in Fig. IV.10(a). Finally the γ parameters are obtained by fitting A and C to Eq. (IV.19) and Eq. (IV.20) as shown in Fig. IV.10(b)-(c), where the red data points are the coefficients calculated in Fig. IV.9(d)-(f). We note from Eq. (IV.18) that some remaining background can be included in the computation of C, as well as small contributions from anisotropic terms in the magnetic Hamiltonian, as discussed above. For this reason, the H_0-independent part of Eq. (IV.20) is not fitted to get the parameters γ_4, γ_i and γ_e, which are rather fitted with Eq. (IV.19), where A represents the amplitude of the first moment cosine variation.

A similar analysis can be performed by considering a fixed L_0 and varying along H and is detailed in Appendix E.2, giving another set of fitted γ parameters. Then, these two analyses were performed again with the second single crystal dataset, with $E_\mathrm{f} = 3.7\,\mathrm{meV}$, giving two other sets of γ parameters. This is detailed in Appendix E.3. These fitted γ parameters are shown in Fig. IV.11, where they have been normalized to γ_e obtained from the L-scan analysis for each dataset, in order to get rid of any scale issue coming from the absolute normalization process

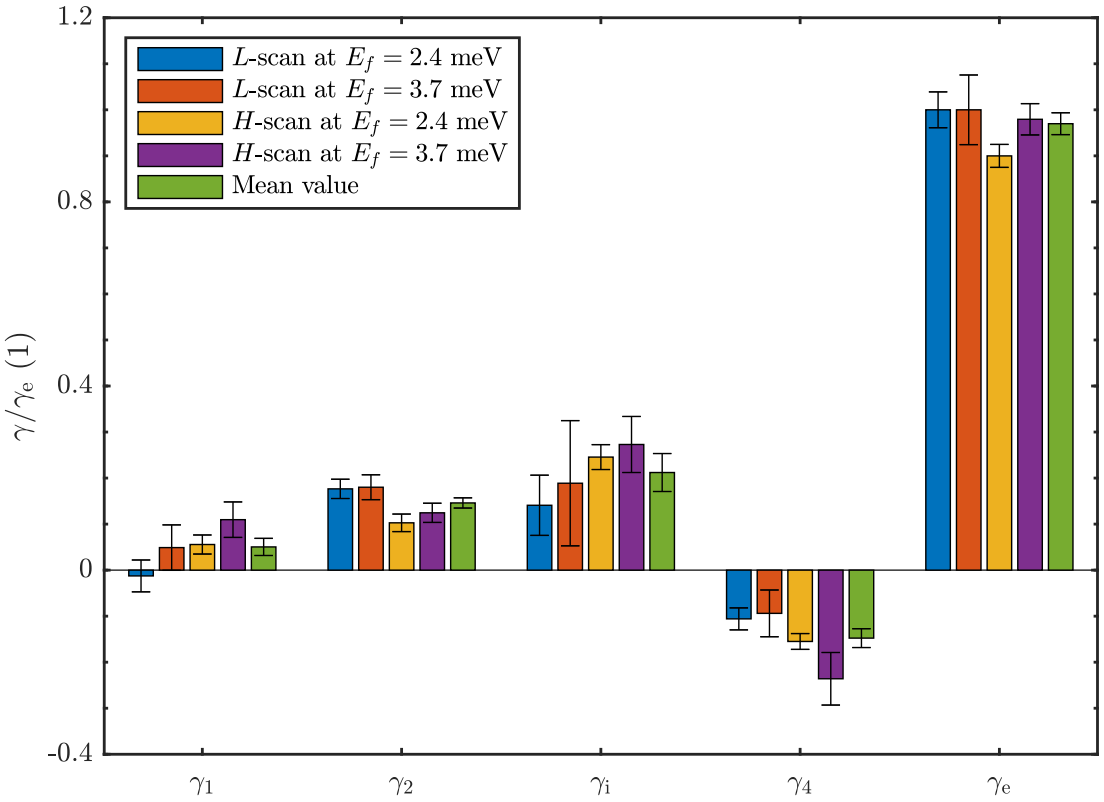

Figure IV.11 Fitted parameters for the different analysis and dataset, normalized to γ_e obtained in the L-scan analysis from the $E_f = 2.4$ meV dataset. Mean values (green bars) are calculated averaging over the four analysis.

and to directly compare the fitted parameters. We discuss below how we obtain the overall scaling factor to obtain units of meV.

IV.3.4.3 Powder data

As described in Section IV.3.1.2, powder inelastic neutron scattering was also performed on MACS and first moment sum rule can also be applied to these data.

For polycrystalline samples, the intensity measured is related to the powder averaged $S(|\boldsymbol{Q}|, E) = \int \mathrm{d}\Omega_{\boldsymbol{Q}}\, S(\boldsymbol{Q}, E)/4\pi$ of the dynamic structure factor. This gives the powder averaged first moment sum rule [190, 192]:

$$\begin{aligned}\langle E\rangle(|\boldsymbol{Q}|) &= \int \mathrm{d}E\, E S(|\boldsymbol{Q}|, E) \\ &= -\frac{2}{3}\sum_{i,j} n_{ij} J_{ij} \langle \hat{\boldsymbol{S}}_i \cdot \hat{\boldsymbol{S}}_j \rangle \left\{ 1 - \frac{\sin(|\boldsymbol{Q}||\boldsymbol{d}_{ij}|)}{|\boldsymbol{Q}||\boldsymbol{d}_{ij}|} \right\}.\end{aligned} \tag{IV.21}$$

As for the single crystal analysis, for a fixed $Q = |\boldsymbol{Q}|$, the sine frequency only depends on the bond lengths, which are the same for diagonal exchange paths as listed in Table IV.2, resulting in five distinct bond distances. We can further simplify the first moment by summing over these distinct bond distances:

$$\langle E\rangle(Q) = -\frac{2}{3}\sum_{i} n_i \gamma_i \left\{ 1 - \frac{\sin(Q|\boldsymbol{d}_i|)}{Q|\boldsymbol{d}_i|} \right\}, \tag{IV.22}$$

where $i \in [1, 5]$ is related to the i-th bond length and the γ_i are defined in Eq. (IV.16). Due to the very close bond distances (especially $d_2 = 4.8445\,\text{Å}$ and $d_4 = 4.7241\,\text{Å}$), and the relatively small Q-range probed in the experiment (from 0.3 to 2.05 Å^{-1}), we were not able to conveniently fit the γ parameters, because of high correlations in the fitting process. However, we can compare the first moment extracted from the powder inelastic neutron scattering with the theoretical one calculated using the γ parameters obtained from the single crystal analysis described above.

The first step for extracting the first moment from the experimental data is to define the region of integration for the energy. For the powder, the first moment was integrated for $E \in [0.3, 1.6]$ meV to get rid of the elastic and two-magnon

scattering. This is justified by the spectral weight calculated in the total moment sum rule analysis described in Section IV.3.3. Due to gapless modes in the one-magnon spectrum, around $0.8\,\text{Å}^{-1}$ and $1.4\,\text{Å}^{-1}$, as shown in Fig. IV.3(a), the contribution from elastic scattering and one-magnon can be mixed. However, this mixture happens at low energies and low intensities, so that deviations from the actual first moment are small. As for the single crystal analysis, the data were integrated numerically using a trapezoid integration, and the background was removed by fitting with two Gaussians. The theoretical γ parameters calculated from the single crystal first moment sum rule analysis were rescaled to match the scale of the first moment observed in the powder experiment, as we know the powder data have been fairly normalized as it captures all the magnetic spectral weight as detailed in Section IV.3.3. The magnetic form factor is also taken into account during this rescaling process.

The theoretical first moment calculated from the γ parameters obtained from the single crystal sum rules analysis is shown in red in Fig. IV.12, and matches well the first moment computed from the powder experiment. The contribution from each exchange constant associated to their bond distance is shown in thin lines (normalized to the powder computed first moment). From this, we can see how the contributions from J_2 and J_4 to the first moment are close, which makes the fit difficult within this small wavevector range probed during this experiment.

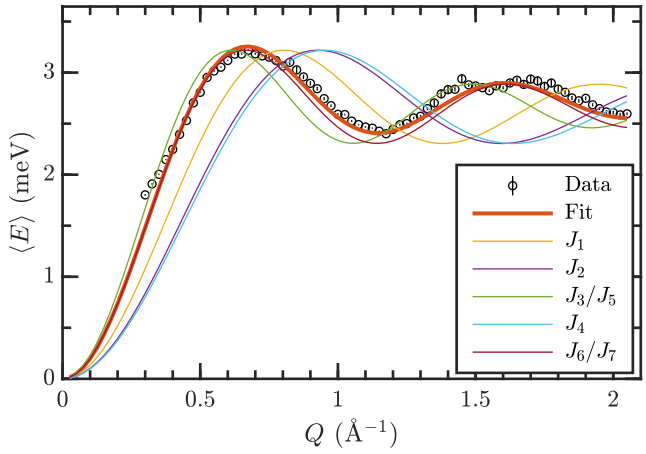

Figure IV.12 (Data points) First moment computed from the powder data, as a function of the scattering vector amplitude. (red thick curve) First moment calculated from the γ parameters fitted in the single crystal first moment sum rule analysis. (thin curves) Contributions to the first moment from the different exchange paths, normalized to the powder computed first moment.

IV.3.5 Determination of exchange constants

In the first moment sum rules analysis, we have used the five γ parameters which are related to the seven exchange constants. γ_1, γ_2 and γ_4 are uniquely related to J_1, J_2 and J_4, and can be deduced from Eqs. (IV.16a) to (IV.16c), leaving J_3, J_5, J_6 and J_7. γ_i and γ_e are related in Eqs. (IV.16d) and (IV.16e) to these four chiral exchange constants. Considering the energy minimization using the experimental propagation vector from diffraction [1], these four unknown exchange constants can be written into three linearly independent equations,

$$\begin{cases} \tan 2\pi k = \sqrt{3}\dfrac{J_3 - J_5 + 2(J_6 - J_7)}{J_3 + J_5 + 2(J_6 + J_7 - J_4)} & \text{(IV.23a)} \\ \gamma_\mathrm{i} = J_3 c_\mathrm{R} + J_5 c_\mathrm{L} & \text{(IV.23b)} \\ \gamma_\mathrm{e} = J_6 c_\mathrm{R} + J_7 c_\mathrm{L}. & \text{(IV.23c)} \end{cases}$$

This analysis presents an ambiguity given the presence of three equations and four unknown exchange constants. This ambiguity is intrinsic originating from many of the exchange parameters corresponding to the same bond distances which is the the basis of the first moment sum rule analysis discussed above. In particular, the exchange constants J_3 (J_6) and J_5 (J_7) correspond to the same bond distance and only differ by the SSE pathway defined by the crystal chirality. We therefore need further information to close this set of equations and seek this through a comparison between calculated and measured single crystal excitation spectra, focusing on the overall bandwidth and excitations near the zone boundary.

By calculating the excitation spectra using linear spin-wave theory software SpinW [198] with an simulated instrumental resolution $\Delta E \approx 0.1\,\mathrm{meV}$, we can see that the upper magnon branch along $(H, H, 0)$ is largely affected by a change of the J_3 exchange parameter. We note that the calculation was done assuming an untilted structure [cycloidal ground state shown in Fig. III.3(a)], however, the scattering near the top of the single magnon branch was found not to be sensitive to the tilting of the magnetic moments. Analyzing the scattering near the top of the single magnon branch near the magnetic zone boundary therefore provides an independent means of fixing J_3. The experimental spectrum from MACS $E_\mathrm{f} = 2.4\,\mathrm{meV}$ dataset is shown in Fig. IV.13(a), and compared to calculated spectra for different values of J_3 in Fig. IV.13(b)-(d), where we can observe a significant change of the position and structure of the upper mode. In particular,

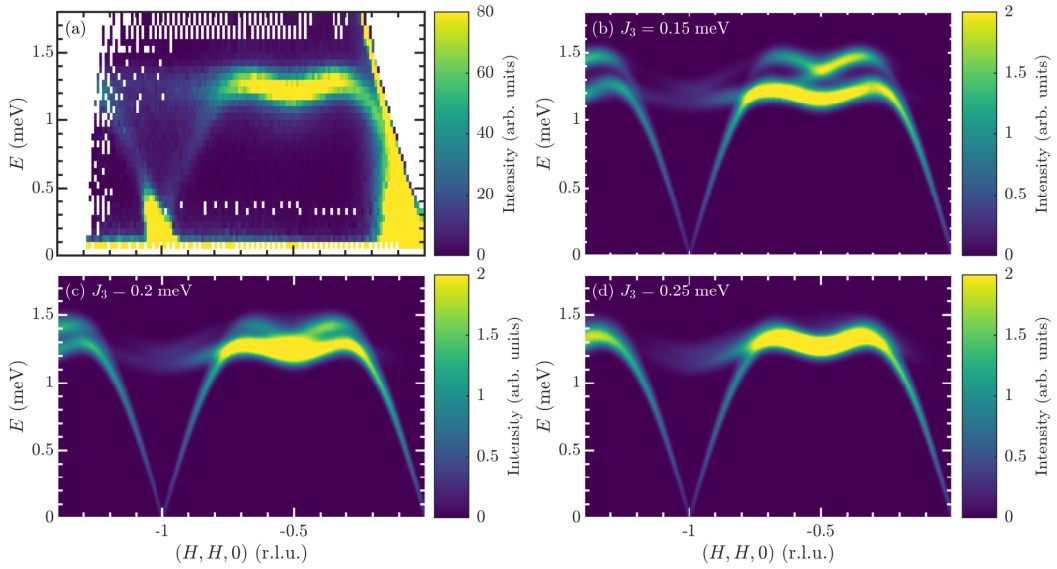

Figure IV.13 Spin-wave dispersion along $(H, H, 0)$ for: (a) MACS single crystal inelastic neutron scattering spectrum. (b)-(d) Inelastic neutron scattering spectrum calculated from linear spin-wave theory by fixing different J_3 values. The other parameters for these calculations are listed in Table E.1.

tuning J_3 affects the maximum energy of the one-magnon band and also the splitting of multiple bands at the maximum energy of the single magnon bands as observed in the H-scans. Given our experimental data [Fig. IV.13(a)] and to close off the set of Eqns. IV.23, we assume no observable splitting of bands in the H-scans and a maximum single-magnon energy excitation given by experiment. These two observations fix both the absolute value of J_3 and also an overall scaling factor taking the data to absolute units of meV. For these calculations, J_5, J_6 and J_7 are obtained by fixing J_3 in Eq. (IV.23) resulting in a system of three equations and three unknowns with γ_i and γ_e the mean values obtained in the single crystal sum rules analysis shown in Fig. IV.11. We have chosen to fix J_3 as it has the lesser influence on the ordering wavevector which is seen by partially differentiating Eq. (IV.23a). Finally, the exchange constants obtained by fixing J_3 with the best agreement are listed in Table IV.3. The uncertainty associated to J_3 is an estimation based on the instrumental resolution of how far from $J_3 = 0.25\,\mathrm{meV}$ we can observe the band splitting. From this estimated error, and the least-square refinement of γ_i and γ_e, we subsequently compute the uncertainties associated to $J_{5,6,7}$. The obtained exchange constants are compared with the values calculated from DFT from Ref. [57]. First we can see that the interactions are overall lower in energy than expected from the DFT calculations.

	J_1	J_2	J_3	J_4	J_5	J_6	J_7
DFT [57]	0.77	1.47	2.2	1.16	0.4	1.94	0.4
Sum rules	0.10(4)	0.29(2)	0.25(2)	0.35(5)	0.07(8)	0.97(3)	0.03(5)
Refined	0.10	0.29	0.25	**0.25**	0.07	0.97	**-0.023**

Table IV.3 Symmetric J exchange constants obtained by DFT calculations [57] and the mean values from the four single crystal sum rules analyses (normalized to γ_e and then rescaled to experimental data, in meV, note that all values of J in the table are multiplied by $S(S+1)$ with $S = 5/2$). The refined parameters using Green's function approach are highlighted in red.

Then, the left-handed interactions J_3 and J_6 are dominant in comparison to right-handed J_5 and J_7, as expected to impose the structural chirality of $MnSb_2O_6$.

From mean field theory, the Curie-Weiss temperature can be estimated by summing the exchange constants over the nearest neighbors of a Mn^{2+} ion [199]

$$\Theta_{CW} = -\frac{S(S+1)}{3k_B}\left[2(J_1 + J_3 + J_4 + J_5) + 4(J_2 + J_6 + J_7)\right]. \tag{IV.24}$$

We note that this equation is not linearly independent from the system in Eq. (IV.23), and thus cannot be used to uniquely determine the four chiral exchange constants J_3, J_5, J_6, and J_7. Furthermore, the Curie-Weiss temperature obtained from magnetic susceptibility on $MnSb_2O_6$ powder, $\Theta_{CW} = -19.6\,K$ in Ref. [57] and $\Theta_{CW} = -23\,K$ in Ref. [152] have a difference $\Delta T = 3.4\,K$ corresponding to an energy difference of $\Delta E \approx 0.3\,meV$, which is significant given the low energy scale of the exchange constants in $MnSb_2O_6$ (see Table IV.2). This variation in experimentally reported results is justifiable given the choice of the linear regime when fitting mean-field Curie Weiss law and reflects the experimental uncertainty. For these reasons, we have not used the experimental Curie-Weiss temperatures as a hard constraint for the exchange constants. On the contrary, we can compute afterwards $\Theta_{CW} = -26(1)\,K$, which reasonably agrees with the measured ones, given the experimental variations.

IV.3.6 Comparison to spin-wave theory

This section was composed by H. Lane and C. Stock, and partially reproduced from Ref. [2] in this thesis to maintain the completeness of the study.

In the previous sections we have applied the first moment sum rule to extract the complex series of Heisenberg exchange constants in $MnSb_2O_6$. In this section we compare these results to a mean-field linear spin-wave theory to compare results and also to test for stability of the ground state magnetic structure. We use the Green's function formalism for this. While this technique for calculating magnetic excitations is more versatile in cases where the low-energy response is determined by a series of single-ion states (such as the case in rare earths or in the presence of spin-orbit coupling like in, for example, Co^{2+} [200] or V^{3+} [201] based compounds), it is also useful to test for stability of harmonic long-wavelength magnetic excitations with changes in the local magnetic environment. In this section we first briefly outline the use of the Green's function technique and then we apply it to calculate the spin excitation spectrum, comparing sum rule results presented above to experiment, then refining results. We then test stability of the proposed magnetic structure and interactions based on the series of exchange constants extracted with the first moment sum rule and refined values. In particular, we discuss the stability of long-wavelength magnetic fluctuations for tilted helicoidal structures.

IV.3.6.1 Green's functions on a rotating frame

The basic technique for applying the Green's function approach has been outlined in several previous papers. The technique was applied to collinear systems CoO [200] in the presence of spin-orbit coupling with Co^{2+} ($S = \frac{3}{2}$, l_{eff}=1) ions, and $CaFe_2O_4$ [202] based on a spin-only ground state of Fe^{3+} ($S = \frac{5}{2}$) ions. This methodology was recently extended to the noncollinear magnetic structure of $RbFe^{2+}Fe^{3+}F_6$ which involved coupled spin-only Fe^{3+} ($S = \frac{5}{2}$) and orbitally degenerate Fe^{2+} ($S = 2$, l_{eff}=1) ions. In terms of $MnSb_2O_6$ where only a spin-degree of freedom exists (Mn^{2+} with $S = \frac{5}{2}$), we quote only the key results here. Further details can be found in Refs. [203] and [2]. The methodology here is to use the Green's functions results from the collinear cases and transform to a local rotating frame of reference for use in incommensurate magnets like $MnSb_2O_6$.

We now apply this theory to $MnSb_2O_6$, which comprises a triangular motif of

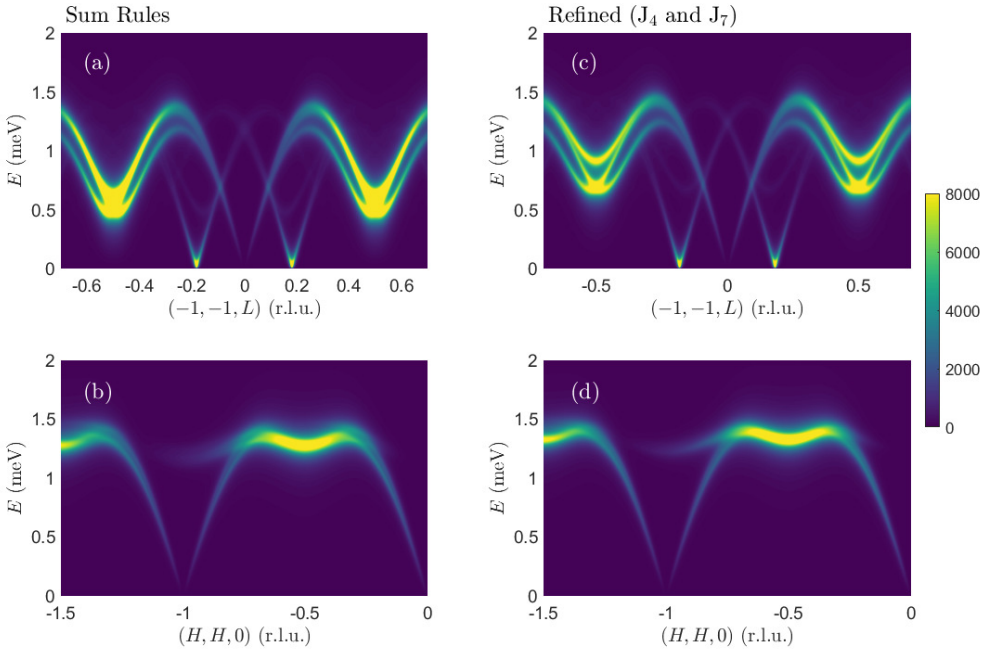

Figure IV.14 The theoretical dispersive neutron scattering results based on our theoretical calculations using Green's functions taking an untilted magnetic ground state [see Fig. III.3(a)]. (a)-(b) display calculations with the exchange parameters fixed from those derived using the first-moment sum rule described in the main text. (c)-(d) show calculations but refining J_4 to give agreement with experiment at the zone boundary and J_7 refined to keep the ordering wavevector consistent with experiment.

coupled Mn^{2+} ($3d^5$) ions. In an intermediate octahedral field, the single-ion ground state of Mn^{2+} is ^6S ($S = 5/2$, $L \approx 0$) and the orbital moment is quenched. As a result, the effect of spin-orbit coupling and crystallographic distortions are small and may be neglected. The single-ion Hamiltonian is thus remarkably simple and consists solely of the molecular mean field created by the magnetic coupling to neighboring ions, which breaks time reversal symmetry, $\mathcal{H}_{\rm SI} = h_{\rm MF}\hat{S}_z$. This "Zeeman-like" term acts to split the 6-fold degenerate $|S = 5/2, m\rangle$ states. At low temperatures (as illustrated in Fig. 7 of Ref. [202]) when only the ground state is populated, only one transition is allowed under the constraints of dipole selection rules of neutron scattering. We note that this approach is equivalent to semi-classical linear spin-wave theory.

IV.3.6.2 Comparison to Experiment

Inputting the symmetric exchange constants derived from the first moment sum rule into the Green's function calculation with an untilted magnetic structure, we derive the predicted neutron scattering excitation spectrum in Fig. IV.14(a)-(b). This calculation is done with no anisotropic terms. Symmetric exchange is expected to be dominant here owing to the lack of an orbital degree of freedom for Mn^{2+}. The general results are in good qualitative agreement with experiment, however the calculated zone-boundary excitations are clearly in disagreement with experiment with the calculation predicting lower energy excitations than observed in experiment at the zone boundary.

To address this, there are two noteworthy points of our first moment sum rule analysis. First, on inspection of Fig. IV.11, the values of γ_4, which fixes J_4 maybe dominated by the H-scan experiment performed with $E_f = 3.7\,\text{meV}$. In comparison to iron based langasite, this value for J_4 is also considerably larger in $MnSb_2O_6$ [146]. We therefore consider a case when this value is lowered in Fig. IV.14(c)-(d). To ensure the same ordering wavevector we correspondingly tune J_7 given the relatively large error bar in our analysis and also the large sensitivity of the magnetic ordering wavevector to this exchange constant (Eqn. IV.23a). After refining $J_{4,7}$ (to within one-two sigma of the calculated error bar from the first moment sum rule analysis) we obtain a good description of the data (both along the L and H directions) with sum rule and refined exchange parameters illustrated in Table IV.3 (refined values from this step highlighted in red).

IV.3.6.3 Stability analysis

Having derived a set of symmetric exchange constants from the first moment sum rule and written down a response function theory for the spin waves in terms of Green's functions, we discuss stability of the ground state fixed by the magnetic structure. As presented in Chapter III, there have been two magnetic structures proposed in the literature involving a tilting of the plane of the helicoid at an angle away from the c-axis [Ref. [58] and Fig. III.6] and one without tilting [Ref. [57] and Fig. III.3(a)]. While initially it was proposed that the observed polar domain switching in $MnSb_2O_6$ requires a tilted structure, other work based on neutron diffraction has suggested that it is not a requirement. While in Chapter III we have argued for the existence of an untilted structure, the goodness of fit to the

diffraction data was not markedly worse for the tilted case making the results arguably ambiguous (Section III.4.2). Here we evaluate the stability of the long-wavelength magnetic excitations as a function of tilting the vertical axis of the spin rotation plane given our exchange constants derived from the first moment rule. We emphasize that the exchange constants derived above from the first moment sum rule depend only on the relative orientation of neighboring spins and is independent of the static magnetic structure being tilted or not. Given the good description of the data to a symmetric-only exchange model, we test here how stable these excitations are when the static magnetic structure is gradually tilted.

The Green's function calculation predicts the energy and momentum values of stable harmonic excitations through the imaginary part of the response, given a magnetic ground state and a set of symmetric exchange constants. In the first moment analysis presented above, the exchange constants are derived based on relative orientation of the magnetic moments, and does not depend on global details like tilting of the overall magnetic structure. Our Green's function analysis, however, does require this tilting as the magnetic ground state determines the local molecular field on each site.

Given that the Green's function approach predicts stable harmonic excitations as a function of momentum and energy, in this section we search for stable long-wavelength excitations as a function of tilting of the spin rotation plane given our derived exchange parameters based on the first moment rule. We focus on L-scans as calculations of the excitation spectrum along H were found to not noticeably change with tilting the spin rotation plane away from the c-axis over the range of 0-15°. We note that such H-scans were used above to fix one of the exchange parameters and the overall calibration constant to take the data to absolute units of meV. The two assumptions behind that step, namely the energy value of the top of the single-magnon band and the splitting, are not found to observably change with tilting in our calculations.

In Fig. IV.15, we search for long-wavelength excitations given our sum rule exchange constants as a function of tilting of the vertical main axis of the spin rotation plane away from the c-axis at an angle θ. The long-wavelength excitations ($q \rightarrow 0$) are calculated for several tilt angles and shown in Fig. IV.15(a)-(c), based on the set of parameters derived from the sum rule analysis. Given that the sum rules and the fixing of the value of J_3 described above is independent of the tilting of the static magnetic moments, in our stability

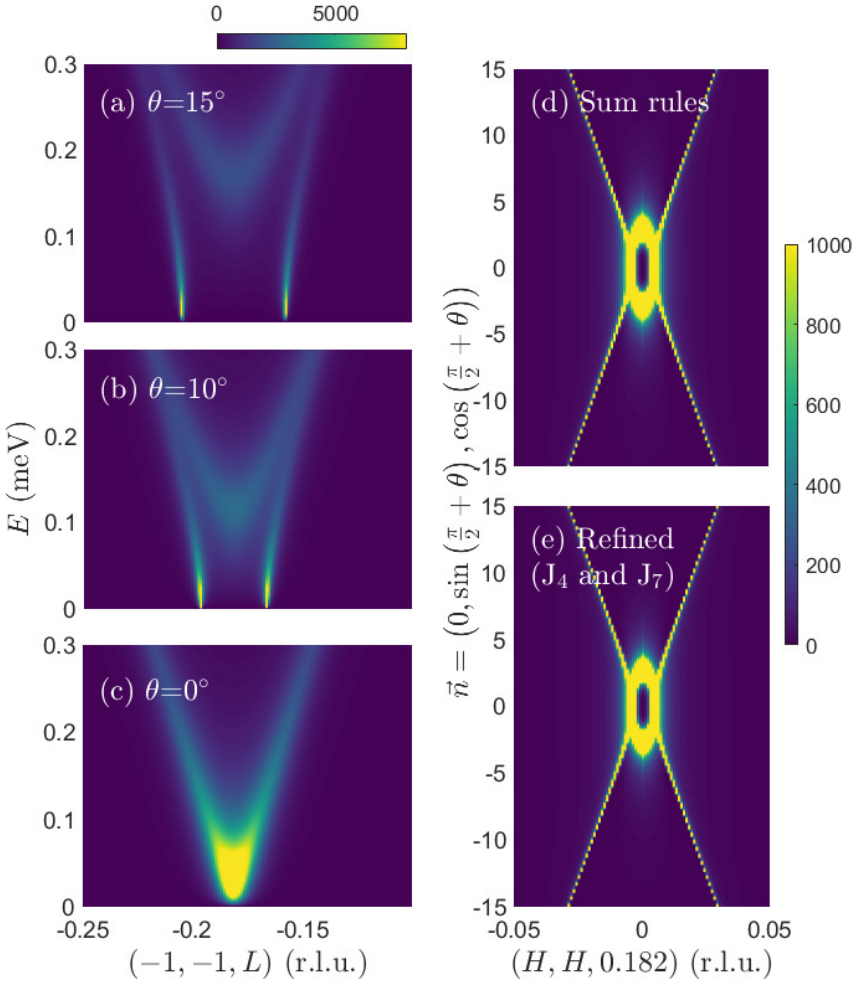

Figure IV.15 Calculations investigating the stability of long-wavelength spin-waves as a function of tilting the spin rotation plane away from the c-axis. Calculations of the neutron response for tilts of $\theta = 15°$ (a), $10°$ (b), and $0°$ (c) are displayed with low-energy, long-wavelength excitations only stable for tilts of $\theta \sim 0°$. This is further illustrated in panels (d)-(e) that display the response at low energies as a function of tilt-angle of the spin rotation plane away from the c-axis. We emphasize that these calculations are done for a magnetic Hamiltonian with *symmetric-only* exchange constants. No anisotropic terms are included in the magnetic Hamiltonian as discussed in the main text.

calculations described here we fix the exchange constants to these determined values and vary the long-range static magnetic structure. On increased tilting, the exchange parameters derived from sum rules show no stable long-wavelength excitations, indicative that the derived exchange parameters combined with a tilted helicoid is unstable. This is further displayed in Fig. IV.15(d)-(e) which plot calculated constant energy cuts (integrating calculated data below 0.02 meV) as a function of tilting of the cycloid away from the c-axis for both the cases of exchange constants derived from sum rules, and refined values discussed above. In both cases, increased tilting of the helicoid results in unstable long-wavelength excitations. Based on this analysis, we suggest that the derived exchange constants are consistent with an untilted ($\theta = 0$) magnetic structure. However, we emphasize that this analysis is based only a Hamiltonian with *symmetric-only* exchange constants as expected based on the high-spin value of Mn^{2+}. We cannot rule out the possibility of small anisotropic or more complex magnetic exchange terms that may arise from the distorted framework surrounding the magnetic ions (see Appendix D.3). In Section III.4.3 we have shown with diffraction under magnetic field the possibility to manipulate the spin structure in $MnSb_2O_6$ and that the appearance of electric polarization does not require a tilted structure as raised in Ref. [58]. Therefore, the stability analysis above is consistent with our neutron diffraction analysis. The elastic scattering outlined in our previous paper and the spin excitations can be modeled and understood in terms of a symmetric-only exchange model on an untilted structure.

IV.4 Conclusions

In this chapter, we have studied structurally chiral polar magnet $MnSb_2O_6$, with magnetic interactions being described by seven symmetric Heisenberg exchanges in the magnetic Hamiltonian. We have presented a method using the first moment sum rule, and have applied this to extract the exchange constants from multiplexed neutron data. This method only depends on the correlators (angles) between neighboring spins and not the tilting of the overall spin rotation plane. Using Green's functions on a rotating frame, we have reproduced the spin-wave spectra, which are in good agreement with the measured ones and discussed refined values. Finally, we investigated the stability of the magnetic structure in terms of long-wavelength magnetic excitations present at low energies and suggest that the pure cycloid is favored in terms of stability given the derived exchange

constants from the first moment sum rule.

Chapter V

Diffraction studies of 2D van der Waals magnetic materials

This chapter is dedicated to the diffraction studies of 2D van der Waals (vdW) magnetic materials which were introduced in Section I.3. This chapter includes the studies of three different materials: $Fe_{3-x}GeTe_2$, $Fe_{1+x}Te$ and VI_3. The determination of the crystal and magnetic structures of $Fe_{3-x}GeTe_2$ by single-crystal neutron diffraction is presented in Section V.1. In Section V.2, we discuss the Spherical Neutron Polarimetry (SNP) results of $Fe_{1+x}Te$ to track the temperature dependence of its magnetic structure. Finally, we investigate the structural transitions in VI_3 as a function of temperature, probed using X-ray powder diffraction and the results are presented in Section V.3.

V.1 $Fe_{3-x}GeTe_2$

V.1.1 Introduction

$Fe_{3-x}GeTe_2$ was initially found to have a high Curie temperature $T_C = 230\,K$ [86]. This itinerant ferromagnetic material has been intensively studied during these last years for its interesting magnetic properties, such as large anomalous Hall effect [204–206] or large magnetic anisotropic energy, which is promising for high-density storage applications [207–209]. Additionally, it was predicted to be stable down to a monolayer [208] which was later proved experimentally [210]

with a Curie temperature being tunable above room temperature by ionic gating [206], making it a potential candidate for spintronics applications based on vdW heterostructures [211].

$Fe_{3-x}GeTe_2$ crystallizes in the $P6_3/mmc$ space group (No. 194), and is composed of substructures of $Fe_{3-x}Ge$ sandwiched between two Te layers (covalent bonds), which are separated by a vdW gap as shown in Fig. V.1(a). The Fe atoms lie on two inequivalent sites Fe1 at $(0, 0, z)$ (Wyckoff position $4e$) and Fe2 at $(\frac{2}{3}, \frac{1}{3}, \frac{3}{4})$ (Wyckoff position $2c$) and form a multilayer honeycomb network shown in Fig. V.1(b). The iron deficiency x was only found on the Fe2 site and significantly impacts the structural and magnetic properties of $Fe_{3-x}GeTe_2$. Both the magnetic anisotropy and the Curie temperature decrease on decreasing the Fe2 site occupancy, due to the variation of magnetic interactions induced by changes in the lattice constants. The ordering temperatures are reported between 140 K and 230 K for varying Fe stoichiometric values from $3 - x = 2.75$ (Fe-deficient) to $3 - x = 3.1$ (Fe-doped) compounds [212].

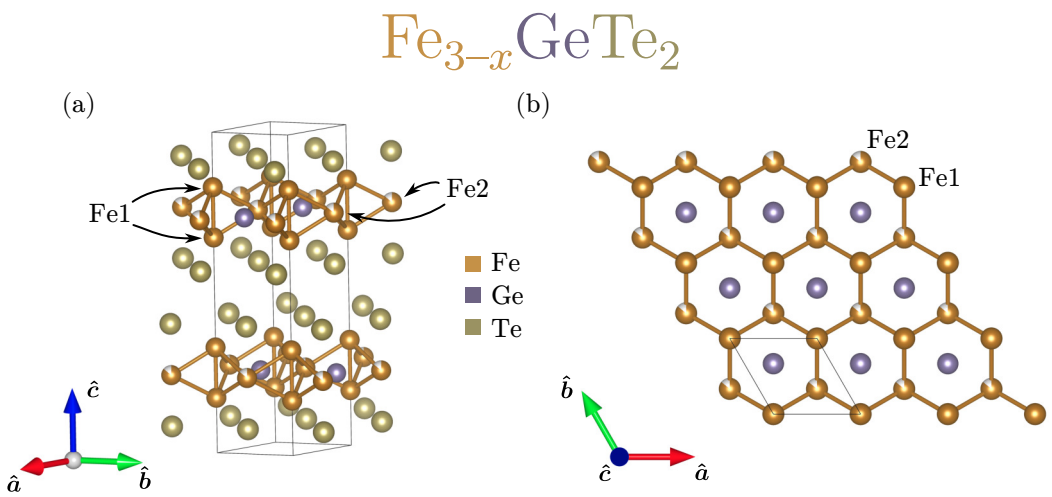

Figure V.1 Crystal structure of $Fe_{3-x}GeTe_2$: (a) $Fe_{3-x}Ge$ slabs sandwiched between Te layers, (b) noncoplanar honeycomb network formed by Fe atoms in inequivalent Fe1 and Fe2 sites. Vacancies are only found on the Fe2 site. Only the Fe1-Fe2 bonds are shown for clarity. Figure made using VESTA [149].

The origin of magnetism in $Fe_{3-x}GeTe_2$ is still unclear. A ferromagnetic order along the c-axis was commonly observed by magnetization measurements [207] or neutron diffraction [212–214]. An additional antiferromagnetic (AFM) transition was found at 152 K below the ferromagnetic (FM) transition at 214 K [215]. It was later shown theoretically that the $Fe_{3-x}GeTe_2$ low temperature ground state should be FM only for $0.11 < x < 0.36$ [216]. The magnetic moments

were found to be different between Fe1 and Fe2 sites for Fe-rich $Fe_{2.9}GeTe_2$ samples [212, 213], indicating a mixed valence Fe^{3+} and Fe^{2+} between the two sites [86, 206]. However, for Fe-deficient $Fe_{2.75}GeTe_2$ samples, the refinement is not giving significantly different magnetic moments [212]. Furthermore, the reduced moments obtained with neutron diffraction [212, 213] agree with the itinerant character of magnetism in $Fe_{3-x}GeTe_2$, while the importance of localized magnetic moments was pointed out by examining its electronic band structure [217].

The iron concentration highly depends on the choice of sample synthesis. While flux-grown samples have typically higher occupancies $3-x \approx 2.75$ [212, 214, 218, 219] and thus lower T_C, the samples grown by chemical vapor transport (CVT) are rather Fe-rich $3-x > 2.8$ with higher T_C [207, 212, 213, 215]. But the main drawback here is that the CVT-grown samples are smaller than the flux-grown ones [212, 219]. For this reason only flux-grown $Fe_{3-x}GeTe_2$ were studied in earlier inelastic neutron scattering experiments [218, 219].

This section is dedicated to the neutron diffraction study of a CVT-grown $Fe_{3-x}GeTe_2$ single crystal. Inelastic neutron scattering was previously performed on coaligned samples from the same batch. The experiment was carried out on MACS [141], at NIST by H. Lane, C. Stock and J. A. Rodriguez-Rivera. Scanning tunnelling microscopy (STM) was later performed on another single crystal from the same batch by C. Trainer, O. Armitage and I. Benedičič at the University of St. Andrews. Fluctuations of the Fe concentration hugely influence the underlying magnetism, hence its prior knowledge is essential for the correct interpretation and comparison with the literature. This is the aim of this single-crystal neutron diffraction study which in addition allows us to confirm the crystal and magnetic structures of our CVT-grown samples. The combined STM imaging and inelastic neutron scattering investigations were published in Ref. [3] and the diffraction results shown in this section are adapted from the Supplemental Material of Ref. [3]

V.1.2 Single-crystal neutron diffraction

Experimental details

The single-crystal neutron diffraction experiment was performed on the hot neutron four-circle diffractometer D9, at ILL [220]. Incoming neutron wavelength $\lambda = 0.836$ Å was selected by the Cu(220) monochromator, allowing to observe the Bragg peaks up to high momentum transfers. A single crystal of Fe_3GeTe_2 of approximate dimensions $3 \times 3 \times 2$ mm^3 was characterized at four different temperatures: 300 K (paramagnetic phase), 98 K, 60 K and 30 K (ferromagnetic phase).

Structure refinement

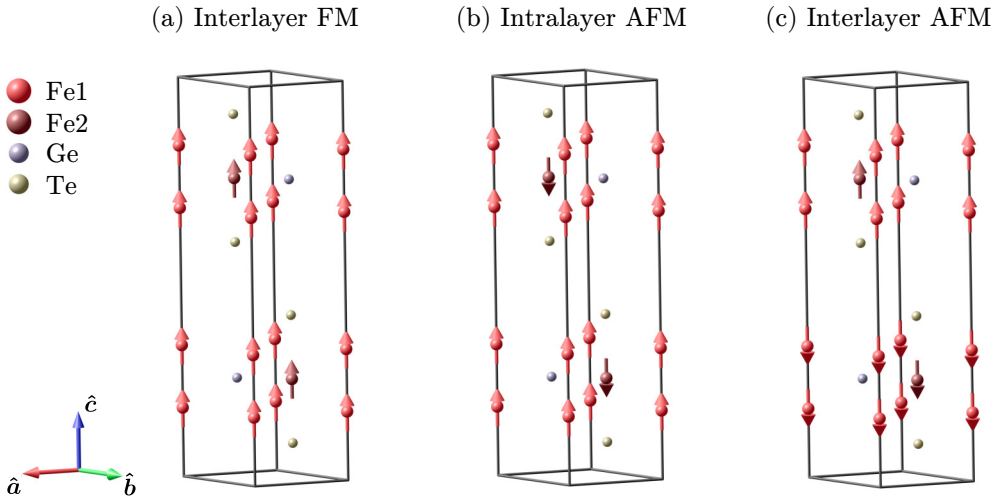

Figure V.2 Magnetic models for $Fe_{3-x}GeTe_2$ (a) Interlayer FM, (b) Intralayer AFM (magnetic moments in opposite directions between Fe1 and Fe2 sites), (c) Interlayer AFM (magnetic moments in opposite directions between adjacent layers). Figure made using MAG2POL [134].

Both crystal and magnetic structures were refined using FULLPROF [133]. The crystal structure was refined in the $P6_3/mmc$ space group (No. 194). Scale, extinction parameters, atomic positions and individual isotropic displacements were refined at each temperature, except at 30 K where the scale and extinction parameters were fixed from the 60 K refinement, given the lower number of

reflections measured.[1] The occupancy of interstitial Fe2 (Wyckoff position $2c$) was refined, and an iron concentration $3 - x = 2.86(3)$ was found at $T = 60\,\mathrm{K}$ in agreement with the three other datasets. $Ni_{3-x}GeTe_2$ is structurally analog to $Fe_{3-x}GeTe_2$. In this non-magnetic compound, Ni atoms were also found in the vdW gap $(0, 0, \frac{1}{2})$ (Wyckoff position $2a$) with an occupancy of 0.25(1), in addition to a full occupancy at Wyckoff position $4e$ and an occupancy of 0.70(1) at Wyckoff position $2a$, leading to a total Ni stoichiometry $3 - x = 2.95(1)$ [86]. Refinement considering an interlayer Fe atom at this position was not successful, suggesting the absence of occupation in the vdW gap contrary to $Ni_{3-x}GeTe_2$.

The best magnetic refinement was obtained using magnetic space group $P6_3/mm'c'$ (No. 194.270) with FM order along the c-axis as shown in Fig. V.2(a). The magnetic moments for Fe1 and Fe2 were constrained to be the same, leading to $\mu = 1.6(2)\,\mu_\mathrm{B}$ at 30 K. The refined parameters for these crystal and magnetic structure refinements are listed in Tab. V.1, and the associated observed intensities versus calculated ones are shown in Fig. V.3. Selected bond distances and angles are presented in Table V.2.

The interlayer AFM model [Fig. V.2(c)] proposed in Ref. [215] was tested using $P6_3'/mm'c$ space group (No. 194.266) but the refinement was not successful. Another magnetic model allowed in $P6_3/mm'c'$ space group is the intralayer AFM model [Fig. V.2(b)], with the moments for Fe1 and Fe2 sites constrained to be opposite in sign. The agreement factors for this refinement are comparable with the ones from the interlayer FM model. However, the magnetic moment was highly correlated to other parameters such as the Fe2 occupancy and the iron anisotropic displacement parameters. Finally, the refinement with different magnetic moments for Fe1 and Fe2 (lifting the FM constraint) in $P6_3/mm'c'$ space group did not reach convergence. Therefore, the interlayer FM model with the same magnetic moments for Fe1 and Fe2 sites yields the best agreement in this study. The reduced magnetic moment $\mu = 1.6(2)\mu_\mathrm{B}$ at 30 K, leading to an effective spin $S \approx 0.8$ instead of $S = 5/2$ or $S = 2$ for localized Fe^{2+} and Fe^{3+}, confirms the itinerant nature of ferromagnetism in $Fe_{3-x}GeTe_2$ [207, 212, 213] The iron stoichiometry, $3 - x = 2.86(3)$ is consistent with larger a and smaller c lattice parameters compared to Fe-deficient samples from Ref. [212]. It also agrees with a high $T_\mathrm{C} = 215(2)\,\mathrm{K}$ previously measured on BT4 (NIST) by tracking the intensity of the magnetic Bragg peak (1 0 0) as a function of temperature shown

[1] The least-squares optimization converged with a higher scale factor [1344(38) at 30 K vs. 1248(44) at 60 K] and with an unphysical negative diagonal extinction parameter in the Becker-Coppens model.

Table V.1 Parameters of a $Fe_{3-x}GeTe_2$ single-crystal refined with FULLPROF within nuclear space group $P6_3/mmc$ (No. 194) and magnetic space group $P6_3/mm'c'$ (No. 194.270).

$T = 300\,\mathrm{K}$ Measured reflections, unique, observed ($I > 2\sigma$): 480, 159, 154							
$R_{\mathrm{int}} = 1.95\%$ $R_{\mathrm{F}} = 6.93\%$ $R_{\mathrm{Bragg}} = 6.10\%$ $\chi^2 = 4.53$							
$a = b = 3.9920(2)$ Å $c = 16.343(3)$ Å							
Atoms	Wyckoff	x	y	z	B_{iso} (Å^2)	Occ.	M_z
Fe1	$4e$	0.000	0.000	0.6715(3)	0.67(3)	1	/
Fe2	$2c$	0.667	0.333	0.750	0.83(7)	0.86(2)	/
Ge	$2d$	0.333	0.667	0.750	1.91(8)	1	/
Te	$4f$	0.667	0.333	0.5900(7)	0.82(4)	1	/
$T = 98\,\mathrm{K}$ Measured reflections, unique, observed ($I > 2\sigma$): 382, 128, 126							
$R_{\mathrm{int}} = 1.6\%$ $R_{\mathrm{F}} = 6.42\%$ $R_{\mathrm{Bragg}} = 6.22\%$ $\chi^2 = 7.72$							
$a = b = 3.9794(5)$ Å $c = 16.304(3)$ Å							
Atoms	Wyckoff	x	y	z	B_{iso} (Å^2)	Occ.	M_z
Fe1	$4e$	0.000	0.000	0.6718(2)	0.31(3)	1	1.4(3)
Fe2	$2c$	0.667	0.333	0.750	0.63(9)	0.87(3)	1.4(3)
Ge	$2d$	0.333	0.667	0.750	1.7(1)	1	/
Te	$4f$	0.667	0.333	0.5894(3)	0.35(4)	1	/
$T = 60\,\mathrm{K}$ Measured reflections, unique, observed ($I > 2\sigma$): 645, 189, 188							
$R_{\mathrm{int}} = 1.52\%$ $R_{\mathrm{F}} = 9.03\%$ $R_{\mathrm{Bragg}} = 8.25\%$ $\chi^2 = 13.7$							
$a = b = 3.9785(5)$ Å $c = 16.286(4)$ Å							
Atoms	Wyckoff	x	y	z	B_{iso} (Å^2)	Occ.	M_z
Fe1	$4e$	0.000	0.000	0.6718(3)	0.24(2)	1	1.5(4)
Fe2	$2c$	0.667	0.333	0.750	0.51(7)	0.86(3)	1.5(4)
Ge	$2d$	0.333	0.667	0.750	1.57(9)	1	/
Te	$4f$	0.667	0.333	0.5896(7)	0.25(3)	1	/
$T = 30\,\mathrm{K}$ Measured reflections, unique, observed ($I > 2\sigma$): 200, 76, 76							
$R_{\mathrm{int}} = 1.44\%$ $R_{\mathrm{F}} = 5.21\%$ $R_{\mathrm{Bragg}} = 4.44\%$ $\chi^2 = 4.04$							
$a = b = 3.9779(1)$ Å $c = 16.281(2)$ Å							
Atoms	Wyckoff	x	y	z	B_{iso} (Å^2)	Occ.	M_z
Fe1	$4e$	0.000	0.000	0.6720(3)	0.23(3)	1	1.6(2)
Fe2	$2c$	0.667	0.333	0.750	0.4(1)	0.86(2)	1.6(2)
Ge	$2d$	0.333	0.667	0.750	1.73(9)	1	/
Te	$4f$	0.667	0.333	0.5891(3)	0.24(4)	1	/

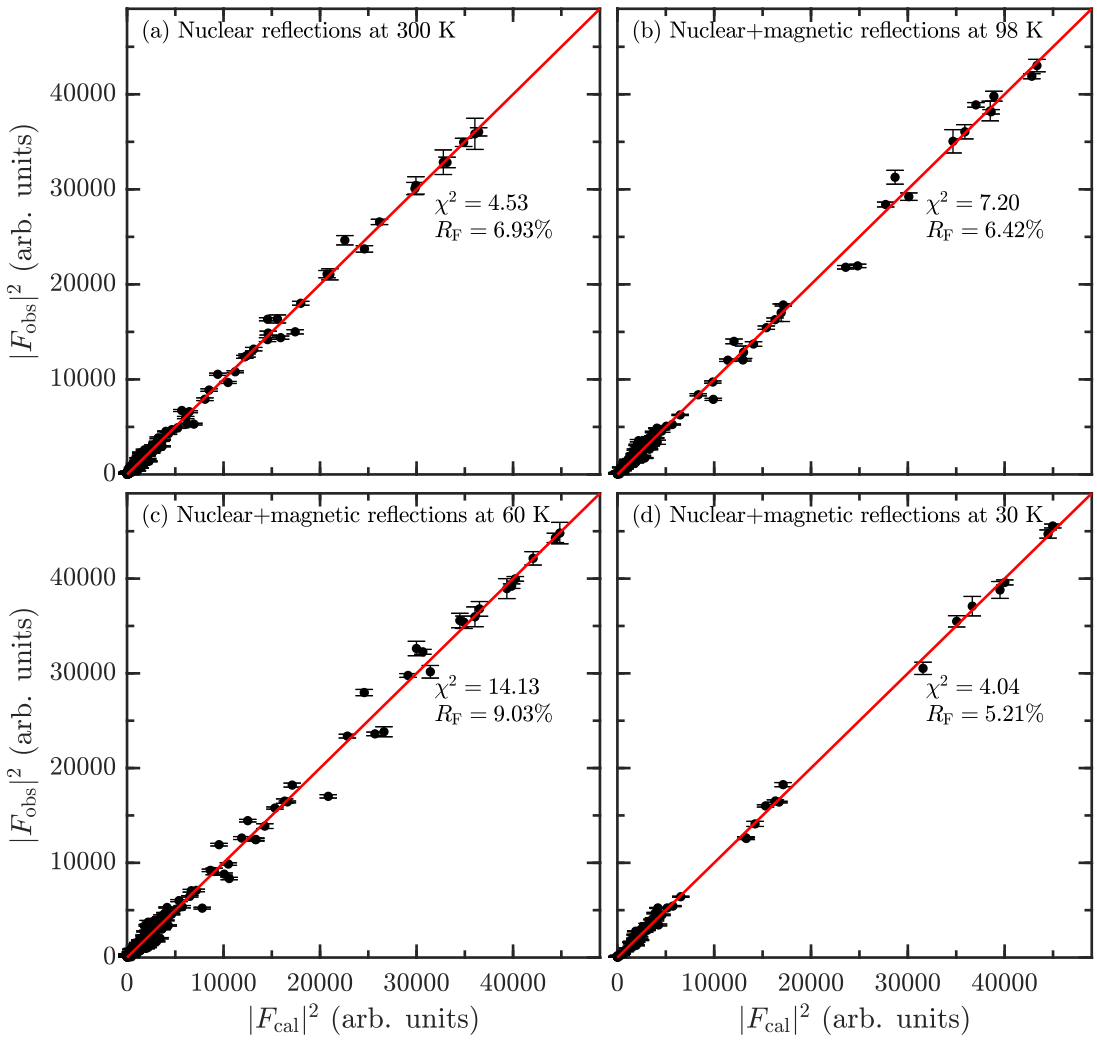

Figure V.3 Observed versus calculated intensities for: (a) nuclear reflections measured at 300 K, (b)-(d) both nuclear and magnetic reflections measured at (b) 98 K, (c) 60 K and (d) 30 K, corresponding to Table V.1, with interlayer FM model shown in Fig. V.2(a).

Table V.2 Selected bond distances and angles calculated from the refinements presented in Table V.1.

Bond distance (Å)	300 K	98 K	60 K	30 K
Fe1-Fe1	2.563(7)	2.558(7)	2.562(7)	2.555(7)
Fe1-Fe2	2.637(2)	2.611(2)	2.612(2)	2.610(2)
Fe1-Ge1	2.637(2)	2.611(2)	2.612(2)	2.610(2)
Fe1-Te1	2.663(6)	2.644(6)	2.643(6)	2.650(6)
Fe2-Te1	2.62(1)	2.63(1)	2.62(1)	2.64(1)
Angle (°)	300 K	98 K	60 K	30 K
Fe1-Fe1-Fe2	60.9(2)	60.7(2)	60.6(2)	60.7(2)
Fe1-Fe2-Fe1	58.1(2)	58.7(2)	58.7(2)	58.6(2)
Fe2-Fe1-Fe2	98.4(1)	98.0(1)	98.0(1)	98.1(1)
Fe1-Fe2-Fe2	40.8(1)	41.0(1)	41.0(1)	41.0(1)

in Fig. V.4, and $T_C = 218\,\mathrm{K}$ from magnetization measurements on a single crystal from the same batch [3].

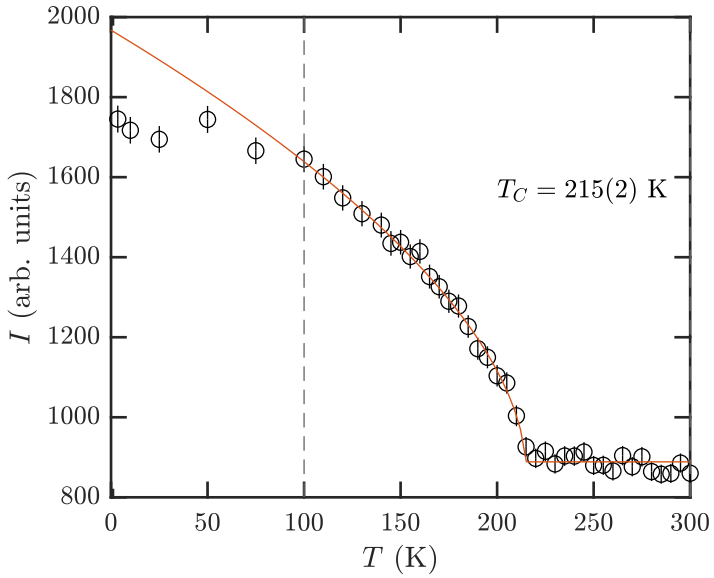

Figure V.4 Intensity of (1 0 0) peak as a function of temperature measured on BT4. The data over 100 K (dashed line) is fitted to a power law (red line), giving $T_C = 215(2)\,\mathrm{K}$. Adapted from [3].

V.1.3 Relating spin-polarized STM imaging and inelastic neutron scattering

The low-Q magnon dispersion measured on MACS was well-modeled by a 2D ferromagnetic spin wave model with a large exchange constant $J = 43(10)\,\mathrm{meV}$

and a small single-ion anisotropy $K = 0.6(1)$ meV [221]. However, the dynamics are quite different from those observed in flux-grown $Fe_{3-x}GeTe_2$ samples [218, 219]. In particular, the magnetic excitations presented a 3D character in Ref. [218] with a higher single-ion anisotropy in iron-deficient $Fe_{2.75}GeTe_2$ compounds. Ferromagnetic domain walls at the surface layer of our $Fe_{2.86(3)}GeTe_2$ sample were investigated by spin-polarized STM. The width of these domain walls is directly related to the magnetic exchange interaction J and to the anisotropy K. Since anisotropy increases at the surface where symmetry is reduced [222] and exchange coupling reduces due to the lack of atoms in the surface layer, the ratio K/J is expected to be greater at the surface than in the bulk material. Yet, calculations from the values found by inelastic neutron scattering show a ratio K/J of the same magnitude at both the surface and the bulk of $Fe_{3-x}GeTe_2$ [3]. This indicates that magnetic properties in 2D materials are only slightly and not tremendously changed at the surface layers [3].

The neutron scattering experiments confirm the importance of iron concentration in the magnetic properties of $Fe_{3-x}GeTe_2$. In addition, the surface measurements provide information on how these properties are altered by increased anisotropy, which is also expected while studying lower layers $Fe_{3-x}GeTe_2$ compounds.

V.2 $Fe_{1+x}Te$

V.2.1 Introduction

The discovery of high-temperature superconductivity in a family of materials based on iron in 2008 [223] paved the way for even more intense research in unconventional superconductivity [224–228]. The chalcogenide system $Fe_{1+x}Te_{1-y}M_y$ (where M = S, Se) is particularly interesting due to the simplicity of its layered crystal structure, becoming superconducting by anion substitution on the Te site [229–231]. Electronic and magnetic properties can be chemically tuned by the amount x of interstitial iron between the FeTe layers and the amount y of anion substitution. It was shown that both variables are important for the appearance of superconducting phases [232–235]. Given the interplay between structural, electronic and magnetic properties, the understanding of the non-superconducting parent phase $Fe_{1+x}Te$ is essential.

$Fe_{1+x}Te$ crystallizes at room temperature in the tetragonal $P4/nmm$ space group

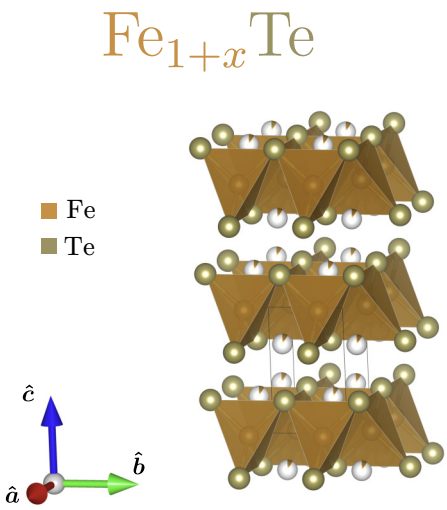

Figure V.5 High temperature crystal structure of $Fe_{1+x}Te$: interstitial iron (in white and brown) located between weakly bonded layers of $FeTe_4$ tetrahedra. Figure made using VESTA [149].

(No. 129). The amount x of interstitial iron is located between vdW layers of edge-sharing $FeTe_4$ tetrahedra as shown in Fig. V.5. This material exhibits a rich magnetic-crystallographic phase diagram as shown in Fig. V.6 depending on both temperature and iron occupancy [236–239]

- For $x < 0.12$, a bicollinear AFM structure orders along the b-axis ($T_N = 67\,K$ for $x = 0.068$ [229]) at the same temperature as a structural transition from tetragonal $P4/nmm$ to monoclinic $P2_1/m$ (No. 11) space group. This magnetic ground state consists of stripes of moments with a FM coupling within the stripes, and an AFM coupling between the stripes, with a commensurate propagation vector $\boldsymbol{k} = (\frac{1}{2}, 0, \frac{1}{2})$, illustrated in Fig. V.7(a).
- For $x > 0.12$, the crystal symmetry is lowered from tetragonal $P4/nmm$ to orthorhombic $Pmmn$ (No. 59) space group. The structural transition temperature coincides with an incommensurate helical ordering with propagation vector $\boldsymbol{k} = (\delta, 0, \frac{1}{2})$ (where $\delta \approx 0.38$ for $x = 0.141$ [240]) as shown in Fig. V.7(c).
- For critical $x \approx 0.12$, the magnetic ground state is an incommensurate collinear spin-density wave (SDW) shown in Fig. V.7(d), with a mixture of the reported crystallographic phases [232, 241].

In addition, STM measurements performed on the surface layers of $Fe_{1+x}Te$

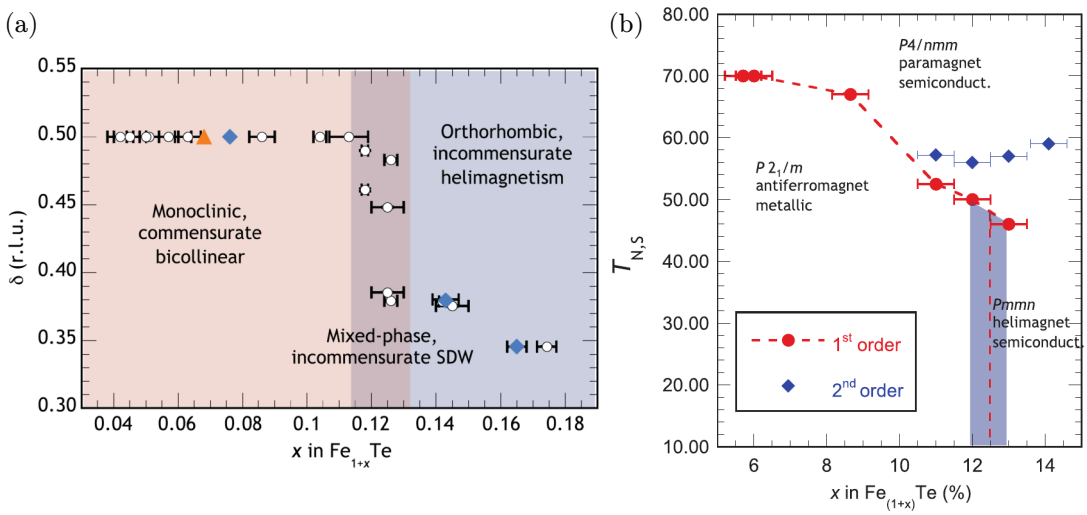

Figure V.6 Phase diagrams of $Fe_{1+x}Te$. (a) δ component of the propagation vector $\boldsymbol{k} = (\delta, 0, \frac{1}{2})$ for low temperature ground state, as a function of the iron occupancy. (b) Néel temperature as a function of the iron occupancy. Figures taken from [236] and [242].

($x \approx 0.1$) samples revealed a canting $\theta = 29.8(13.7)^\circ$ of the spins in the (bc)-plane [Fig. V.7(b)] in comparison to the original bicollinear AFM structure [Fig. V.7(a)] [243, 244]. However, spherical neutron polarimetry (SNP) performed on $Fe_{1.09}Te$ shows no canting [$\theta = 0(5)^\circ$] in the bulk material. This evidences slightly different properties between bulk and surface magnetism due to out of plane magnetocrystalline anisotropy [244], as pointed out in Section V.1.3 for $Fe_{3-x}GeTe_2$.

In a $Fe_{1.09(1)}Te$ single crystal, an incommensurate propagation vector $\boldsymbol{k} = (\delta, 0, \frac{1}{2})$ corresponding to the SDW order [Fig. V.7(d)] was previously observed in vicinity of the Néel temperature [232]. At 57 K, $\delta = 0.421(1)$ and the value moves towards the bicollinear AFM value $\delta = \frac{1}{2}$ around 46 K below which it is locked. This competition between incommensurate and commensurate collinear order was also evidenced by inelastic neutron scattering using polarization analysis, performed on single crystals of $Fe_{1.057(7)}Te$ [239]. Anisotropic fluctuations along the b-axis (parallel to the low-temperature ordered magnetic moment) were measured at 70 K close to T_N. Contrary to the low-temperature fluctuations which are located at commensurate $\boldsymbol{Q} = (0.5\ 0\ 0.5)$, the high-temperature fluctuations were found at incommensurate $\boldsymbol{Q} = (0.45\ 0\ 0.5)$, indicating the presence of the SDW phase near the Néel temperature. In the previous SNP experiment conducted in [244], the measurements were only performed at base temperature (2 K). Given the

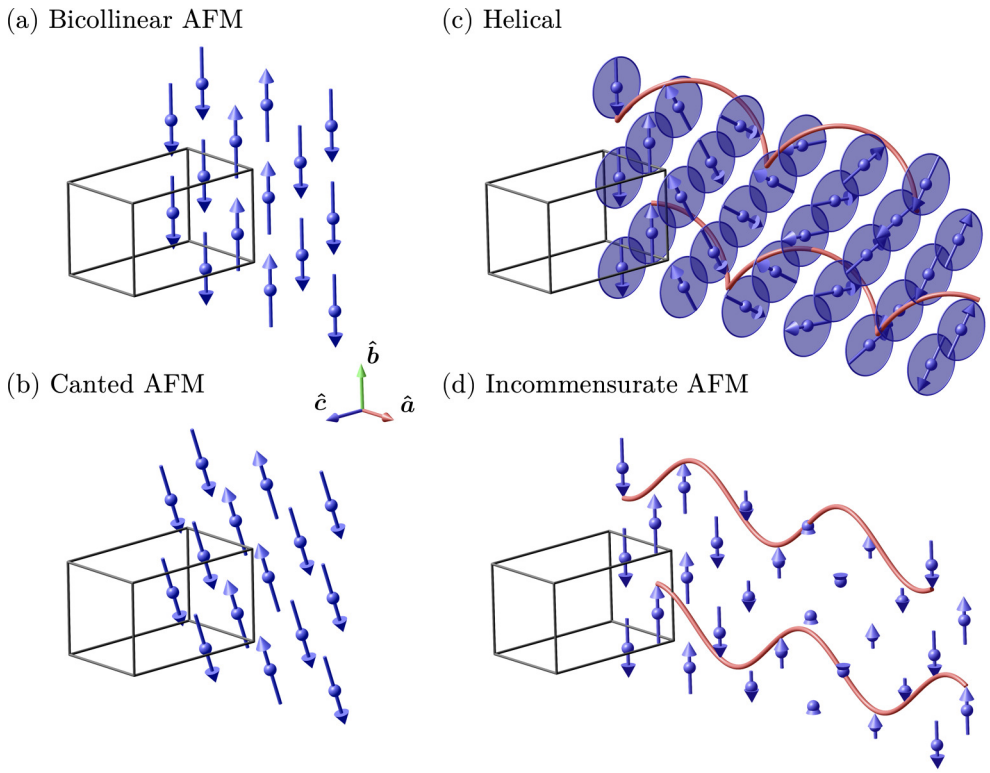

Figure V.7 Reported magnetic ground states for $Fe_{1+x}Te$: (a) bicollinear AFM found in low $x < 0.12$ compounds, (b) canted AFM (in the (bc)-plane) measured on the surface layer of $Fe_{1.1}Te$ samples, (c) helical incommensurate order found in high $x > 0.12$ compounds, (d) collinear spin-density wave order at intermediate $x \approx 0.12$ iron concentration. Only moments near $z = 0$ are shown for clarity. Figures made using MAG2POL [134].

complex phase diagram in $Fe_{1+x}Te$ and the observations in Refs. [232] and [239], it is also important to study the temperature dependence of the magnetic structure.

In this section, we will present the investigation on the magnetic structure of a single crystal of $Fe_{1.057(7)}Te$ (from the same batch as in Ref. [239]) with a focus close to the Néel temperature. We have used SNP to be sensitive to chiral scattering (see Section II.4.2) due to the possibility of a helical order.

V.2.2 Polarized neutron diffraction

Experimental details

The SNP experiment was performed using CRYOPAD on the hot neutron diffractometer D3, at ILL [245] using a wavelength $\lambda = 0.85\,\text{Å}$ selected by the (111) reflection of a Cu_2MnAl Heusler monochromator. The sample is a cylindrical single crystal of approximate height 4 mm and diameter 7 mm, mounted in the $(H0L)$ scattering plane. The b-axis is the vertical axis in the local coordinates (see Section II.4.2). As shown in Fig. V.8, magnetic scattering is only sensitive to the component of the magnetic structure factor perpendicular to the scattering vector. In the case of collinear magnetic structures like the bicollinear commensurate AFM [Fig. V.7(a)] or the incommensurate AFM [Fig. V.7(d)], the magnetic structure factor lies on the z-axis, so that $|\boldsymbol{F}_{\text{M}_\perp}| = |F_{\text{M}_\perp z}|$. Any presence of magnetic moments apart from the b-axis would result in a non-zero $F_{\text{M}_\perp y}$ component (depending on the measured magnetic reflection), giving $|F_{\text{M}_\perp z}| < |\boldsymbol{F}_{\text{M}_\perp}|$. This could be a sign of helical ordering [Fig. V.7(c)] or canted AFM [Fig. V.7(b)].

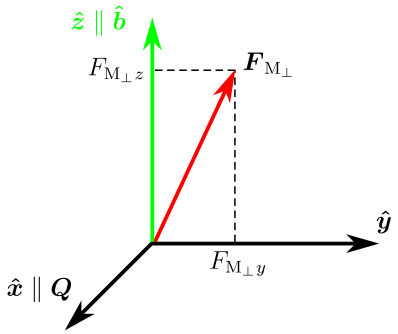

Figure V.8 Polarimetry local coordinates for $Fe_{1+x}Te$. The scattering vector $\boldsymbol{Q}$ lies in the $(H0L)$ scattering plane, and the vertical axis is along $\hat{\boldsymbol{b}}$.

Temperature dependence of the propagation vector

In order to determine whether the magnetic order is commensurate or incommensurate close to the Néel temperature, scans along $(H\ 0\ 0.5)$ were measured as a function of temperature, as shown in Fig. V.9(a). The Néel temperature was found around 70 K [Fig. V.9(b)] and the propagation vector does not change as a function of temperature [Fig. V.9(c)], contrary to the evolution

from incommensurate $\boldsymbol{k} = (\delta, 0, \frac{1}{2})$ to commensurate $\boldsymbol{k} = (\frac{1}{2}, 0, \frac{1}{2})$ reported in Refs. [236] ($\delta = 0.421(1)$ at 57 K) and [239] ($\delta = 0.45$ at 70 K). Moreover, the sample was aligned in the paramagnetic phase in the tetragonal unit cell. The monoclinic distortion at T_N leads to a misalignment resulting in a difference from the exact AFM order for which $\delta = 0.5$.

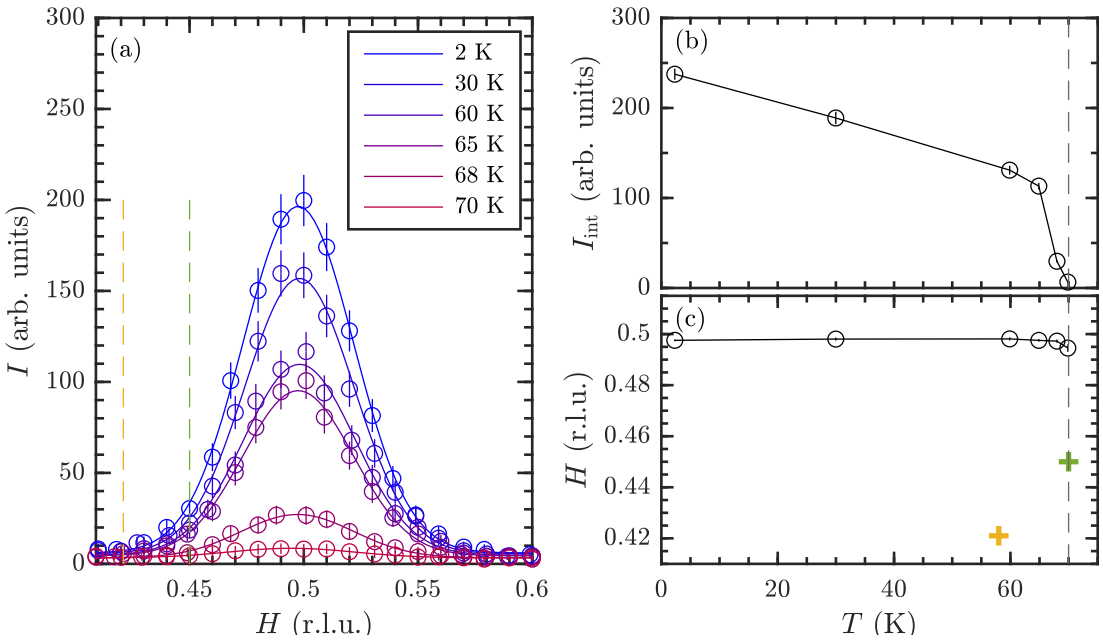

Figure V.9 (a) H-scans along (H 0 0.5) for different temperatures, fitted to Gaussians (continuous lines). Temperature dependence of (b) the integrated intensities, (c) the center of the magnetic reflection. $T_N \approx 70$ K is indicated in dashed gray lines. The reported values $\delta = 0.421(1)$ at 57 K [236] and $\delta = 0.45$ at 70 K [239] are shown in yellow and green in (a) dashed lines, (c) crosses.

Having established the commensurability of the magnetic structure in our $Fe_{1.057(7)}Te$ single crystal, which rules out both the SDW order and the helical order, we looked at the temperature dependence of the polarization matrices to investigate on the possibility of a canted AFM structure [Fig. V.7(c)].

Polarization matrices

For a pure elastic magnetic reflection, in absence of any chiral terms,[2] the polarization matrix for a fully polarized incident beam is given by:

[2] A helical magnetic ground state would have necessitated $\boldsymbol{k} \neq (\frac{1}{2}\ 0\ \frac{1}{2})$, and if so, we would have observed chiral terms in addition to the reduction of the amplitude of the diagonal elements of the polarization matrix from 1.

$$P_{if} = \begin{pmatrix} -1 & 0 & 0 \\ 0 & -\dfrac{|F_{\mathrm{M}_\perp z}|^2 - |F_{\mathrm{M}_\perp y}|^2}{|\boldsymbol{F}_{\mathrm{M}_\perp}|^2} & \dfrac{2\,\mathrm{Re}\left\{F_{\mathrm{M}_\perp y} F^*_{\mathrm{M}_\perp z}\right\}}{|\boldsymbol{F}_{\mathrm{M}_\perp}|^2} \\ 0 & \dfrac{2\,\mathrm{Re}\left\{F_{\mathrm{M}_\perp z} F^*_{\mathrm{M}_\perp y}\right\}}{|\boldsymbol{F}_{\mathrm{M}_\perp}|^2} & \dfrac{|F_{\mathrm{M}_\perp z}|^2 - |F_{\mathrm{M}_\perp y}|^2}{|\boldsymbol{F}_{\mathrm{M}_\perp}|^2} \end{pmatrix}. \tag{V.1}$$

As illustrated in Fig. V.8, magnetic moments fully aligned along the b-axis would only give a $F_{\mathrm{M}_\perp z}$ component. Any canting from the b-axis would result in a non-zero $F_{\mathrm{M}_\perp y}$ component, and the reduction of the amplitude of the diagonal elements $P_{yy} = -P_{zz}$ from 1. In addition, the structural transition from tetragonal to monoclinic symmetry in $\mathrm{Fe}_{1+x}\mathrm{Te}$ would lead to four structural domains. In the case of equi-populated domains, the off-diagonal elements P_{yz} and P_{zy} would average to zero [244], leading to the diagonal polarization matrix

$$P_{if} = \begin{pmatrix} -1 & 0 & 0 \\ 0 & -x & 0 \\ 0 & 0 & x \end{pmatrix}, \tag{V.2}$$

where $x = 1$ if the moments are along $\hat{\boldsymbol{b}}$ and $x < 1$ if they are canted. The polarization matrices for three magnetic reflections $(\frac{1}{2}\ 0\ \frac{1}{2})$, $(\frac{3}{2}\ 0\ \frac{1}{2})$ and $(\frac{1}{2}\ 0\ \frac{3}{2})$ were measured at five different temperatures. They were corrected to the initial polarization on D3 $p_0 = 0.935$. The decay of the ^{3}He spin filter efficiency was tracked by measuring at regular time intervals the P_{zz} matrix element of the nuclear Bragg peak (2 0 0).[3] This is taken into account in the polarization matrices shown in Table V.3.

Finally, all the polarization matrices fairly correspond to Eq. (V.2), where $x = 1$. We note that some off-diagonal terms are non-zero within the calculated statistical uncertainties. This is particularly true for P_{xz} which should vanish for a pure magnetic reflection. The presence of an nuclear-magnetic interference contribution (due to an eventual structural modulation with the same propagation vector) to P_{xz} can be discarded as this would lead to $P_{xz} = -P_{zx}$ [see Eq. (II.75)]. Non-zero values for P_{zx} are also found, but they do not correspond to a chiral term which would necessitate $P_{yx} = P_{zx}$. Actually, as mentionned above, the single crystal was aligned in its tetragonal phase. Below the monoclinic distortion, there

[3] $P_{zz} = 1$ for a nuclear peak and perfect initial and final neutron beam polarization.

Table V.3 Polarization matrices for different reflections at different temperatures.

$\boldsymbol{Q}$	$T = 2\,\mathrm{K}$	$T = 30\,\mathrm{K}$
$(\frac{1}{2}\ 0\ \frac{1}{2})$	$\begin{pmatrix} -0.985(4) & 0.036(7) & 0.099(7) \\ -0.002(7) & -0.983(4) & 0.093(7) \\ 0.111(7) & 0.070(7) & 0.981(4) \end{pmatrix}$	$\begin{pmatrix} -0.993(5) & 0.029(8) & 0.080(8) \\ 0.004(8) & -0.980(5) & 0.090(8) \\ 0.117(8) & 0.069(8) & 0.983(5) \end{pmatrix}$
$(\frac{3}{2}\ 0\ \frac{1}{2})$	$\begin{pmatrix} -0.97(2) & 0.02(3) & 0.10(3) \\ 0.02(3) & -0.93(2) & 0.02(3) \\ 0.13(3) & 0.03(3) & 1.01(2) \end{pmatrix}$	$\begin{pmatrix} -1.01(2) & 0.04(3) & 0.13(3) \\ -0.00(3) & -1.00(3) & 0.05(3) \\ 0.14(3) & 0.07(3) & 1.03(3) \end{pmatrix}$
$(\frac{3}{2}\ 0\ \frac{3}{2})$	$\begin{pmatrix} -0.97(3) & 0.06(4) & 0.14(4) \\ 0.02(4) & -0.96(3) & 0.13(4) \\ 0.12(4) & 0.04(4) & 0.98(3) \end{pmatrix}$	$\begin{pmatrix} -0.99(3) & 0.06(4) & 0.00(4) \\ 0.02(4) & -1.06(4) & 0.16(4) \\ 0.03(4) & 0.05(4) & 0.97(3) \end{pmatrix}$
$\boldsymbol{Q}$	$T = 60\,\mathrm{K}$	$T = 65\,\mathrm{K}$
$(\frac{1}{2}\ 0\ \frac{1}{2})$	$\begin{pmatrix} -0.976(7) & 0.02(1) & 0.10(1) \\ 0.00(1) & -0.983(7) & 0.07(1) \\ 0.10(1) & 0.09(1) & 0.979(7) \end{pmatrix}$	$\begin{pmatrix} -0.973(7) & 0.045(9) & 0.097(9) \\ 0.004(9) & -0.976(7) & 0.092(9) \\ 0.122(9) & 0.095(9) & 0.984(7) \end{pmatrix}$
$(\frac{3}{2}\ 0\ \frac{1}{2})$	$\begin{pmatrix} -0.98(3) & 0.06(4) & 0.08(4) \\ 0.06(4) & -1.00(3) & 0.03(3) \\ 0.16(4) & 0.11(4) & 0.97(3) \end{pmatrix}$	$\begin{pmatrix} -0.97(3) & 0.02(3) & 0.11(3) \\ 0.03(3) & -0.96(3) & -0.00(3) \\ 0.11(4) & 0.08(3) & 0.96(3) \end{pmatrix}$
$(\frac{3}{2}\ 0\ \frac{3}{2})$	$\begin{pmatrix} -1.06(5) & -0.08(5) & 0.04(5) \\ 0.05(5) & -0.92(5) & 0.11(5) \\ 0.08(6) & 0.25(6) & 0.90(5) \end{pmatrix}$	$\begin{pmatrix} -0.98(3) & 0.03(4) & 0.12(4) \\ 0.01(4) & -0.98(4) & 0.06(4) \\ 0.11(4) & 0.04(4) & 0.93(4) \end{pmatrix}$
$\boldsymbol{Q}$	$T = 68\,\mathrm{K}$	
$(\frac{1}{2}\ 0\ \frac{1}{2})$	$\begin{pmatrix} -0.93(2) & 0.04(2) & 0.11(2) \\ 0.01(2) & -0.93(2) & 0.09(2) \\ 0.10(2) & 0.08(2) & 0.98(2) \end{pmatrix}$	
$(\frac{3}{2}\ 0\ \frac{1}{2})$	$\begin{pmatrix} -1.00(5) & 0.01(6) & 0.15(5) \\ 0.05(5) & -0.80(6) & -0.06(6) \\ 0.09(6) & 0.05(5) & 0.93(6) \end{pmatrix}$	
$(2\ 0\ 0)$	$\begin{pmatrix} 0.994(6) & -0.006(6) & -0.030(7) \\ -0.044(7) & 0.999(6) & -0.005(7) \\ -0.007(7) & 0.032(7) & 0.999(5) \end{pmatrix}$	

could be a disalignment leading to a deviation from $\boldsymbol{x} \parallel \boldsymbol{Q}$, and the appearance of non-zero diagonal terms. Another reason could be the underestimation of the experimental errors. Indeed, only statistical uncertainties were computed but additional systematic errors could come from the incomplete polarization of the incoming neutron beam and small misalignments of the polarization direction with respect to the sample (typical precision of 2° [122]). A full error analysis is detailed in the Appendix of Ref. [119], and is not taken into account in our study.

As a conclusion, contrary to the SDW phase in vicinity to the Néel temperature reported in $Fe_{1.09(1)}Te$ in Ref. [236], and indicated in $Fe_{1.057(7)}Te$ in Ref. [239], or the canted AFM structure reported in Ref. [244] at the surface layers of $Fe_{1+x}Te$ samples, the magnetic structure in our $Fe_{1.057(7)}Te$ single crystal seems to be uniquely commensurate bicollinear AFM below $T_N \approx 70\,K$. As shown in the phase diagram in Fig. V.6, this is consistent with the fact that $Fe_{1.057(7)}Te$ compound is deep in the bicollinear phase in terms of interstitial iron. X-ray powder diffraction was performed by G. Kaur and C. Stock on Rigaku SmartLab at the University of Edinburgh to study the structural transitions as a function of temperature. Acoustic phonons were studied by inelastic neutron scattering performed by C. Stock and U. Stuhr on EIGER at PSI [246], using $Fe_{1.057(7)}Te$ samples from the same batch. These datasets are currently being analyzed in order to provide detailed information on the crystal structure of our compound and a proper understanding of our observations on the magnetic structure.

V.3 VI_3

V.3.1 Introduction

Finding materials exhibiting ferromagnetism down to monolayers is essential for engineering functional spintronic devices based on vdW heterostructures. Transition metal trihalides MX_3 (where M is a metal cation and X a halide) crystallizing in honeycomb layers are potential candidates [84, 247]. Among them CrI_3 has been widely studied these last years in comparison to its vanadium analog VI_3 [248–254].

VI_3 was first studied in the 1960s and its crystallographic structure was found to be BiI_3 type in the rhombohedral $R\bar{3}$ space group (No. 148) [255, 256]. More detailed studies were carried out in the recent years after the prediction of a FM

order and the stability of monolayers of VI_3 with DFT calculations [257]. However the crystal structure of VI_3 is still controversial. Son *et al.* [258] first found VI_3 to crystallizes at room temperature in the trigonal $P\bar{3}1c$ space group (No. 163) with a structural transition at $T_1 = 79.0(5)$ K into monoclinic $C2/c$ space group (No. 17). Tian *et al.* [259] proposed a monoclinic $C2/m$ space group (No. 15) at high temperature, followed by a structural transition at $T_1 = 79$ K into rhombohedral $R\bar{3}$ space group (like CrI_3). On the contrary, Kong *et al.* [260] determined a rhombohedral $R\bar{3}$ at room temperature, and noticed a "subtle" phase transition at $T_1 = 78$ K. However, they all had measured a ferromagnetic transition $T_C \approx 50$ K by magnetization measurements and agreed on the semiconductor character of VI_3. Later Doležal *et al.* [261] and Marchandier *et al.* [262] corroborated the rhombohedral $R\bar{3}$ symmetry for high temperature. In addition to this $T_1 = 78$ K structural transition and the $T_C \approx 50$ K ferromagnetic transition they have also observed a second structural transition at $T_2 = 32$ K. This low-temperature phase was well refined in the triclinic $P\bar{1}$ space group in Ref. [262], but is is unclear whether this structural transition comes with a second ferromagnetic transition as reported in Ref. [263]. A summary of the crystal structures reported for the different structural phases of VI_3 is presented in Table V.4.

In all the different reported structures, VI_3 is based on edge-sharing VI_6 octohedra forming a honeycomb network in a layer in the (ab)-plane, as shown in Fig. V.10(a), with the vanadium atoms occupying two-thirds of the octahedral positions [262]. However the stacking of these vdW layers differs between the models with an exact ABC stacking for the rhombohedral $R\bar{3}$ model, shown in Fig. V.10(b), and a quasi-ABC stacking for the monoclinic $C2/m$ model [259].

Furthermore, magnetism in VI_3 is also complex and ambiguous. V^{3+} magnetic ions have two valence electrons in the three-degenerate t_{2g} orbitals, leading to $(S = 1, l_{\text{eff}} = 1)$ [201, 260]. Different values for the magnetic moments were found by magnetization measurements in VI_3 [258–260, 264–266], sometimes suggesting the canting of the easy-axis anisotropy away from the c-axis [260, 265, 266]. This is supported by the reduced magnetic moments of V^{3+} $\mu \approx 1.3(1)\,\mu_B$ at $T = 6$ K determined by powder and single-crystal neutron diffraction [266]. Contrary to CrI_3, where the Cr^{3+} orbital moment is quenched in the octahedral crystal field, orbital ordering and strong spin-orbit coupling is expected in VI_3 [267, 268]. However the nature of orbital ordering is discussed, as the orbital moment

[4]Refinement in $P\bar{3}m1$ space group for the high temperature phase, and in monoclinic $C2/m$ space group for the intermediate phase were attempted, but they did not match the peaks accounted from the vanadium honeycomb superstructure.

Table V.4 Summary of the reported crystal structures of VI_3. Space group and lattice parameters are given along with the temperature of the measurements, and the phase transition temperatures.

Paper	High temperature		First transition		Second transition
Son *et al.* [258] Powder XRD	$P\bar{3}1c$ (No. 163) 300 K $a = 6.8987(10)$ Å $c = 13.2897(1)$ Å	$T_1 = 79.0(5)$ K	$C2/c$ (No. 15) 40 K $a = 6.9354(3)$ Å $b = 11.9069(5)$ Å $c = 13.1865(1)$ Å $\beta = 90.403(2)°$	$T_C = 50.0(1)$ K	
Tian *et al.* [259] Single crystal XRD	$C2/m$ (No. 12) 100 K $a = 6.8416(3)$ Å $b = 11.8387(6)$ Å $c = 6.9502(4)$ Å	$T_1 \approx 79$ K	$R\bar{3}$ (No. 148) 60 K $a = 6.8325(6)$ Å $c = 19.6776(2)$ Å	$T_C \approx 50$ K	$R\bar{3}$ (No. 148) 40 K $a = 6.8351(7)$ Å $c = 19.696(2)$ Å
Kong *et al.* [260] Single crystal XRD	$R\bar{3}$ (No. 148) 100 K $a = 6.8879(3)$ Å $c = 19.8139(9)$ Å	$T_1 \approx 78$ K	Subtle phase transition seen in specific heat measurements	$T_C \approx 49$ K	
Doležal *et al.* [261] Single crystal XRD	$R\bar{3}$ (No. 148) 250 K $a = 6.9257(3)$ Å $c = 19.9185(13)$ Å	$T_1 \approx 79$ K	Monoclinic (peak splitting)	$T_2 \approx 32$ K	Triclinic (peak splitting)
Marchandier *et al.* Synchrotron Powder XRD [262]	$R\bar{3}$ (No. 148)[4] 250 K $a = 6.9277(2)$ Å $c = 19.9389(2)$ Å	$T_1 \approx 76$ K	$P\bar{1}$ (No. 2) 60 K $a = 7.7359(2)$ Å $b = 7.6886(2)$ Å $c = 7.6968(2)$ Å $\alpha = 53.1933(5)°$ $\beta = 53.0168(7)°$ $\gamma = 53.4732(7)°$	$T_2 \approx 32$ K	$P\bar{1}$ (No. 2) 9 K $a = 7.7268(2)$ Å $b = 7.6808(2)$ Å $c = 7.6985(2)$ Å $\alpha = 53.1280(2)°$ $\beta = 53.0863(3)°$ $\gamma = 53.5022(3)°$

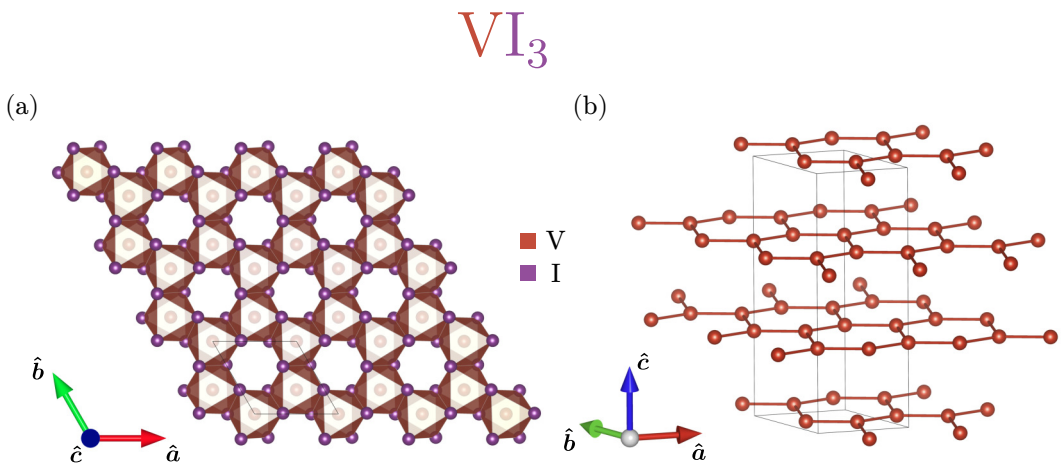

Figure V.10 Crystal structure of VI_3 in the $R\bar{3}$ space group: (a) layer of edge-sharing VI_6 octohedra in a honeycomb network, (b) ABC stacking of the VI_6 honeycomb layers, where iodine atoms are omitted for clarity. Figures made using VESTA [149].

was predicted to be anti-parallel [267, 268] or parallel to the spin moment [269]. Moreover, the presence of two magnetically non-equivalent V sites was suggested by nuclear magnetic resonance measurements [263] and theoretically [270]. Using inelastic neutron scattering, H. Lane *et al.* have modeled the observed magnetic excitations with multi-spin-orbit levels calculations considering two sites with oppositely distorted octahedra of VI_6 [201]. This was later supported by X-ray magnetic circular dichroism measurements [271].

As the magnetic properties are highly correlated to the crystal structure in VI_3, a detailed study is necessary to characterize the samples measured in Ref. [201]. This is the aim of the X-ray diffraction experiment presented in this section, using powder ground from single crystals synthesized the same way as in Ref. [201].

V.3.2 X-ray powder diffraction

Experimental details

The sample growth and preparation were carried by G. Kaur and C. Stock. Single crystals of VI_3 were grown using CVT method [256]. Due to the air-sensitivity[5] of the samples, they were ground in an inert atmosphere provided by a nitrogen

[5] A study of the stability of a single crystal of VI_3 under air exposure is presented in the Supplemental Material of Ref. [261].

gas filled glovebox. The powder was purified using a sublimation apparatus on a hotplate around 40 °C overnight to get rid of excess iodine precursor. This step is important given that these crystals were grown using CVT method and the transport agent is iodine. Powders of VI_3 were then uniformly spread on a sample holder made out of aluminium and chromium alloy. The sample holder was mounted on a Oxford PheniX cryostat, using copper grease to ensure high thermal conductivity. The measurements were performed on the Rigaku SmartLab X-ray powder diffractometer, at the University of Edinburgh, in the Bragg-Brentano geometry, using a Cu K-α1 radiation with a wavelength $\lambda = 1.5406\,\text{Å}$. Note that, this experiment is a part of the commissioning project of the X-ray diffractometer with the cryostat setup.

Full diffraction patterns with a 2θ-range $[5, 120]^\circ$ were measured at 12, 28, 60 and 100 K. A temperature dependence from 20 K to 150 K of the 2θ-range $[42.5, 57]^\circ$ was measured, to track the peak splittings due to the structural transitions. The raw datasets are presented in Appendix F.

Temperature dependence

Three diffraction peaks in the $[42.5, 57]^\circ$ 2θ-range were fitted on MATLAB to a single- or a double-Lorentzian for different temperatures. This is illustrated for four different temperatures in Fig. V.11, where the 2θ-axis has been transformed into Q-axis. A peak splitting occurs around 80 K for $(3\ 0\ 0)_\text{h}$ [Fig. V.11(a)] and $(3\ 0\ 6)_\text{h}$ [Fig. V.11(b)], where the subscript indicates the Miller indices in the hexagonal cell. This evidences the first structural transition, from rhombohedral to monoclinic space group. However, no more splitting was observed at lower temperature, within our instrumental resolution, contrary to the reported structural transition reported at $T_2 = 32\,\text{K}$ [261, 262]. The (0 0 12) peak is simply shifted as a function of the temperature, as shown in Fig. V.11(c).

These diffraction peaks are fitted to a single- or a double-Lorentzian as shown in Fig. V.11(d)-(f). For the double-Lorentzian fits, the width were fixed from the low temperature fitted parameters. The temperature dependence of the centers of the fitted peaks is shown in Fig. V.12.

From the peak centers of $(3\ 0\ 0)_\text{h}$ and (0 0 12) reflections, we can deduce the lattice parameters in the monoclinic unit cell [261]. This is presented in Fig. V.13. The first structural transition is clearly seen in Fig. V.13(a) as probed by the peak

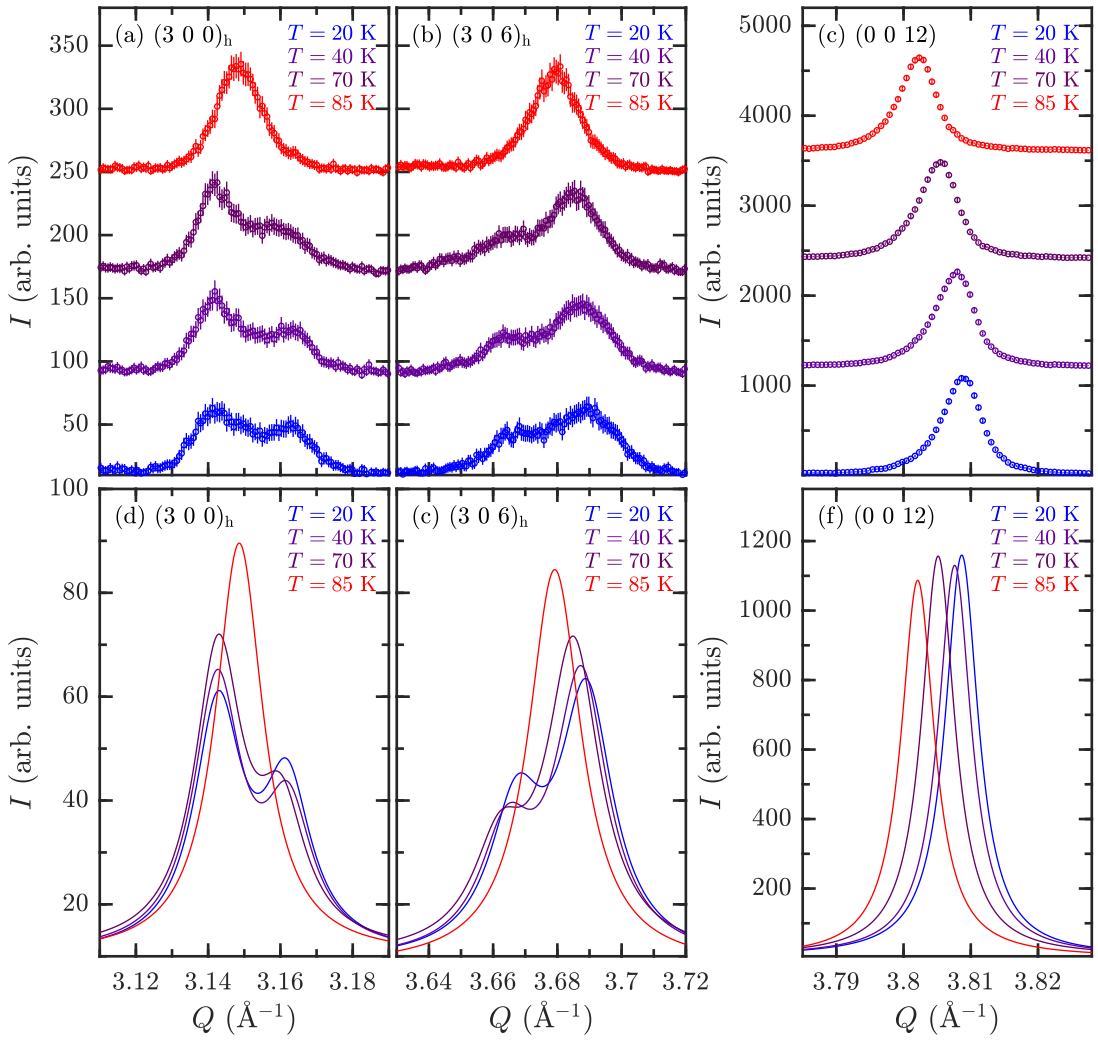

Figure V.11 Stacked plots of diffraction peaks for several temperatures corresponding to: (a) $(3\ 0\ 0)_{\mathrm{h}}$, (b) $(3\ 0\ 6)_{\mathrm{h}}$, where the subscripts indicate the hexagonal unit cell, and (c) (0 0 12). Corresponding single- and double-Lorentzian fit for (d) $(3\ 0\ 0)_{\mathrm{h}}$, (e) $(3\ 0\ 6)_{\mathrm{h}}$, and (f) (0 0 12).

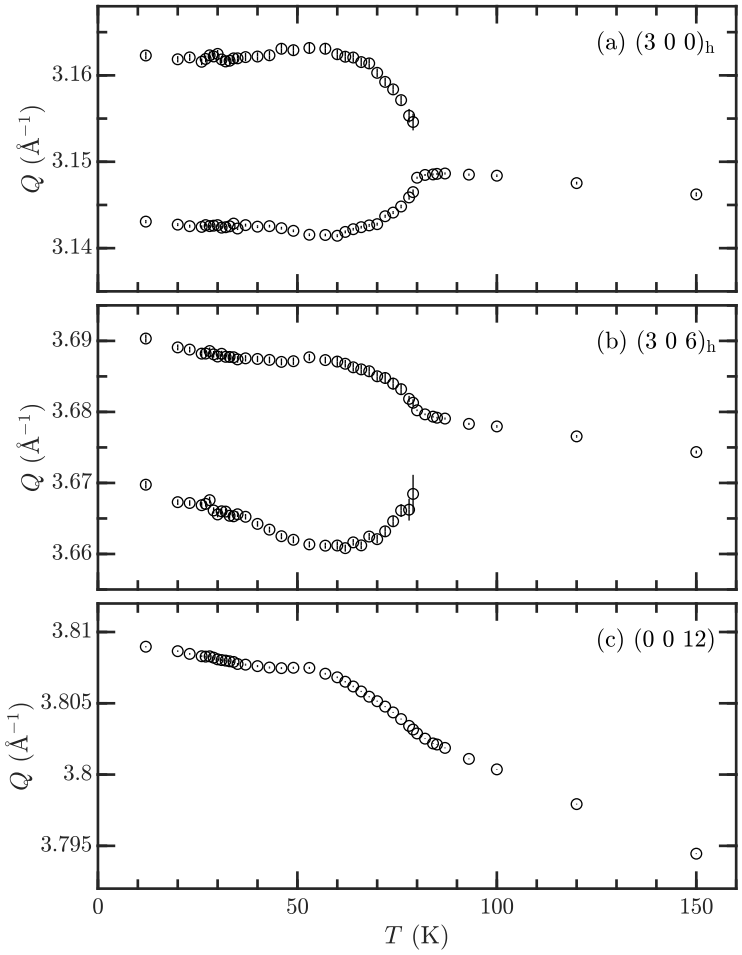

Figure V.12 Temperature dependence of the centers of the diffraction peaks (some fits are shown in Fig. V.11) corresponding to: (a) $(3\ 0\ 0)_{\mathrm{h}}$, (b) $(3\ 0\ 6)_{\mathrm{h}}$, where the subscripts indicate the hexagonal unit cell, and (c) (0 0 12).

splitting with different monoclinic lattice parameters a_{m} and b_{m} ($b_{\mathrm{m}} = \sqrt{3}a_{\mathrm{m}}$ if the monoclinic unit cell is congruent with the hexagonal cell). It is also indicated by an inflection in the lattice parameter c (corresponding to the stacking of three vdW layers) shown in Fig. V.13(b). The ferromagnetic transition can also be observed at $T_{\mathrm{C}} = 50\,\mathrm{K}$ by an inflection in all three of the lattice parameters, probing the magnetoelastic coupling coming along with the magnetic ordering. But as mentioned above, there is no evidence in our data of an other transition around $T_2 = 32\,\mathrm{K}$. Ongoing work shows that VI_2 has a structural transition at this temperature, and previous observations could be related to VI_2 impurities in the measured VI_3 samples.

With this study, we have successfully observed the first structural transition in VI_3, corresponding to the temperatures reported in the literature ensuring

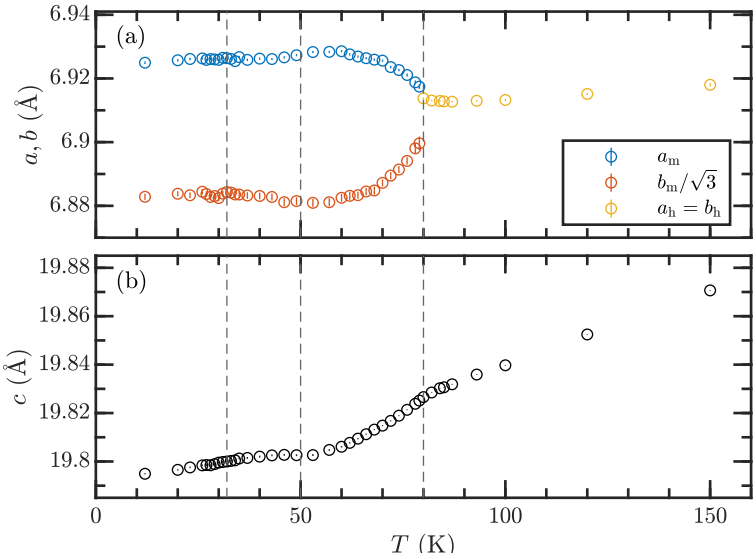

Figure V.13 Lattice parameters as a function of temperature in VI_3: (a) a and b, $a_h = b_h$ correspond to the hexagonal unit cell above $T_1 = 80\,K$ (dashed lines) while a_m and b_m correspond to the monoclinic unit cell, (b) c in the hexagonal unit cell, corresponding to the stacking of three vdW layers. The reported $T_C = 50\,K$ and the lower structural transition temperature $T_1 = 32\,K$ are also indicated in dashed lines.

a correct temperature calibration of the cryostat in the measurement presented in the thesis.[6] Rietveld refinements of the full diffraction patterns are in progress, with the ultimate objective to track down the octahedral distortions modeled in Ref. [201], as the main point of this diffraction study was to motivate the presence of the two sites from neutron spectroscopy.

V.4 Conclusions

In this chapter, we have presented results of diffraction studies on three 2D van der Waals magnetic materials which show strong interplay between structural, electronic and magnetic properties. In both $Fe_{3-x}GeTe_2$ and $Fe_{1+x}Te$ the magnetic properties are highly correlated to the iron deficiency x. Single-crystal diffraction

[6] In a previous measurement under the same conditions, we have observed the peak splitting around 30 K (sample temperature indicated by the software). However the temperature of the cryostat shield was higher than usual. By stopping the cryostat and purging it before cooling back to 12 K, we observed the same peak splitting at 80 K in agreement with the literature. This indicates an offset of $\sim 50\,K$ between the two measurements. Greatest care and further tests are therefore needed to ensure the stability of this new experimental setup.

on $Fe_{3-x}GeTe_2$ determined both crystal and magnetic structures of $Fe_{3-x}GeTe_2$ allowing to characterize the Fe-rich samples measured during inelastic neutron scattering and scanning tunnelling microscopy experiments. Spherical neutron polarimetry on $Fe_{1+x}Te$ showed no temperature-dependence of the magnetic structure in our compound, contrary to the competition between commensurate and incommensurate antiferromagnetic order reported earlier. X-ray powder diffraction successfully captured the higher temperature structural transition in VI_3 but was not sensitive to the lower temperature transition reported in the literature.

Chapter VI

Conclusions and outlook

In this thesis, we have studied two types of novel magnetic materials: multiferroic $MnSb_2O_6$, and 2D magnetic $Fe_{3-x}GeTe_2$, $Fe_{1+x}Te$ and VI_3 using complementary neutron scattering techniques and X-ray diffraction.

Chapter III was dedicated to the crystal and magnetic structure determination of multiferroic $MnSb_2O_6$. We have observed no evidence for the breaking of the paramagnetic $P321$ space group as derived by single-crystal and powder neutron diffraction. Previous studies were not considering the possible presence of structural twins in their single crystals. We have used polarized neutrons to measure Schwinger scattering and have unambiguously determined the population of chiral structural domains. The magnetic ground state, exhaustively studied by unpolarized single-crystal diffraction, and spherical neutron polarimetry, remained ambiguous, due to the mixture of threefold domains, and polar domains. Yet, we have performed diffraction experiments under an external magnetic field, and shown that the magnetic structure can be tuned by low magnetic fields. This led us to consider that a uniform Dzyaloshinskii-Moriya interaction, combined with the underlying coupling between structural and magnetic chiralities, favors a polar domain in the presence of a magnetic field which tilts the spin rotation plane. This alternative explanation of the previously measured electric polarization is valid for both proposed ground states.

Given the possibility to manipulate the magnetic structure with low magnetic fields, and therefore to reduce the number of magnetic domains, the next step would be the detailed study of the magnetic structure by pinning the polar domains (with magnetic or electric field) [51–54]. This was actually attempted

during the thesis on TASP (PSI), where we have perfomed spherical neutron polarimetry under an electric field. However, we have not observed any switching of the chiral (polar) domains. The single crystal of $MnSb_2O_6$ was mounted on a high voltage sample stick [272], and connected to an electrode by fixing a wire with silver paint, but we have repeatedly stated that the connection was lost when we removed the stick from the cryostat (without knowing if the wire went off before the measurements, during, or when we removed the stick). This was partially due to the non-sticky surface of the sample, and a more elaborated sample mounting would be necessary for future experiments. Pinning the magnetic domains would help determining the actual magnetic ground state in $MnSb_2O_6$. Furthermore, this would provide a microscopic proof of the multiferroic character of the compound, supporting the pyroelectric current measurements performed previously.

In Chapter IV, we have studied the dynamics of $MnSb_2O_6$. We have developed an analysis based on the first moment sum rule to evaluate the seven Heisenberg exchange constants in $MnSb_2O_6$, taking advantage of the multiplexed inelastic neutron scattering data collected on MACS. This analysis is independent from the tilt of the spin rotation plane, as the first moment sum rule considers the correlators between neighboring spins. Based on the extracted exchange constants, we have reproduced the spin excitations, using Green's functions on a rotating frame, which are in good agreement with the measured spectra. Finally, we have shown that the pure cycloidal order is favored in terms of stability of the magnetic excitations given the extracted exchange constants.

The advantage of the first moment sum rule analysis is that no assumption on the strength of the exchange constants is necessary. Therefore, it is very useful to study the magnetic interactions in magnetic materials well described by a Heisenberg model, and having a complex magnetic network. The analysis being based on the correlators and the distances between neighboring spins, it would be particularly powerful for systems presenting lower symmetry and therefore different distances between the spins. In this case, inelastic neutron scattering on a powder sample could be used to obtain the exchange constants. For closer distances between the spins, as in $MnSb_2O_6$, larger datasets should be collected on single crystals (using for example multiplexed neutron instrumentation), in order to decorrelate the sinusoidal variations of the first moment in all the directions of the reciprocal space.

Research on the dynamical magnetoelectric effects led to the observation, in the

THz range, of novel hybrid excitations, the so-called electromagnons [273]. These are magnons that can be driven by an electric field. The dual phenomenon, atomic vibrations having both an electric and magnetic character have been observed in iron langasite $Ba_3NbFe_3Si_2O_{14}$ [274]. This is due to its peculiar chiral crystallographic structure, and no other experimental signature has been observed so far in other materials. Given the structural similarity of $MnSb_2O_6$, it is a good candidate to sustain such excitations. A first experiment on the AILES beamline (Synchrotron SOLEIL, Saclay, France) has been performed during this thesis work, and more investigations are ongoing to explore these novel excitations.

Chapter V was dedicated to the structural and magnetic studies of three 2D van der Waals magnetic materials using neutron and X-ray diffraction.

In Section V.1, single-crystal neutron diffraction allowed to determine the iron occupancy of the investigated $Fe_{2.86(2)}GeT_2$ sample. The refinement of both crystal and magnetic structures was found to be consistent with the literature. Given the important role of the iron occupancy in the magnetic properties of this material, this characterization was essential to relate with the neutron spectroscopy and the scanning tunnel microscopy experiments perfomed on the same batch of single crystals, which results were published in Ref. [3].

In Section V.2, we have studied the non-superconducting parent phase $Fe_{1+x}Te$, which also has a rich phase diagram depending on the iron deficiency x, using spherical neutron polarimetry. The magnetic structure was found temperature-independent below the Néel temperature in the studied $Fe_{1.057(7)}Te$ single crystal, showing the absence of competition between commensurate and incommensurate antiferromagnetic order for low iron occupancy compounds, staying in their bicollinear antiferromagnetic phase. These results fix our sample of $Fe_{1+x}Te$ in the phase diagram, and will be combined with the study of the monoclinic distortion using X-ray powder diffraction, and of acoustic phonons using inelastic neutron scattering. In particular, a soft acoustic branch which slope is sensitive to an elastic constant related to the breaking of the fourfold structural symmetry was observed in $Fe_{1+x}Te$.

In Section V.3, we have tracked several nuclear peaks of VI_3 as a function of temperature, using X-ray powder diffraction, showing clear splittings, proof of the first structural transition observed in the literature. This structural transition, as well as the ferromagnetic transition are also indicated in the temperature evolution of the lattice parameters. Further Rietveld refinements are in process

in order to validate the model based on the presence of two vanadium sites, to explain the spectra observed in previous inelastic neutron scattering experiments [201].

Appendix A

Properties of Pauli matrices

For spin 1/2 particles, spin operator are usually represented by the 2×2 Hermitian Pauli matrices. The Pauli spin operator $\hat{\boldsymbol{\sigma}}$ is

$$\hat{\boldsymbol{\sigma}} = (\hat{\sigma}_x, \hat{\sigma}_y, \hat{\sigma}_z), \tag{A.1}$$

where the Pauli matrices are

$$\hat{\sigma}_x = \begin{pmatrix} 0 & 1 \\ 1 & 0 \end{pmatrix} \tag{A.2}$$

$$\hat{\sigma}_y = \begin{pmatrix} 0 & -\mathrm{i} \\ \mathrm{i} & 0 \end{pmatrix} \tag{A.3}$$

$$\hat{\sigma}_z = \begin{pmatrix} 1 & 0 \\ 0 & -1 \end{pmatrix}. \tag{A.4}$$

Product of two Pauli matrices:

$$\hat{\sigma}_\alpha \hat{\sigma}_\beta = \delta_{\alpha\beta} + \mathrm{i}\epsilon_{\alpha\beta\gamma}\hat{\sigma}_\gamma. \tag{A.5}$$

Dot product for any vector $\boldsymbol{a}$ and $\boldsymbol{b}$:

$$(\boldsymbol{a}\cdot\hat{\boldsymbol{\sigma}})(\boldsymbol{b}\cdot\hat{\boldsymbol{\sigma}}) = (\boldsymbol{a}\cdot\boldsymbol{b})\mathbb{1} + \mathrm{i}(\boldsymbol{a}\times\boldsymbol{b})\cdot\hat{\boldsymbol{\sigma}}. \tag{A.6}$$

Trace relations:

$$\mathrm{Tr}(\sigma_\alpha) = 0 \tag{A.7}$$

$$\mathrm{Tr}(\sigma_{\alpha\beta}) = 2\delta_{\alpha\beta} \tag{A.8}$$

$$\mathrm{Tr}(\sigma_{\alpha\beta\gamma}) = 2\mathrm{i}\epsilon_{\alpha\beta\gamma} \tag{A.9}$$

$$\mathrm{Tr}(\sigma_{\alpha\beta\gamma\delta}) = 2(\delta_{\alpha\beta}\delta_{\gamma\delta} - \delta_{\alpha\gamma}\delta_{\beta\delta} + \delta_{\alpha\delta}\delta_{\beta\gamma}). \tag{A.10}$$

Appendix B

Description of magnetic structures

The magnetic moment for the j-th atom in the unit cell indexed by the lattice vector $\boldsymbol{R}_l$ is given in Fourier decomposition as

$$\boldsymbol{\mu}_j(\boldsymbol{R}_l) = \frac{1}{2}\sum_{\boldsymbol{k}}(\boldsymbol{S}_{\boldsymbol{k}j}\mathrm{e}^{-\mathrm{i}\boldsymbol{k}\cdot\boldsymbol{R}_l} + \boldsymbol{S}_{-\boldsymbol{k}j}\mathrm{e}^{\mathrm{i}\boldsymbol{k}\cdot\boldsymbol{R}_l}), \tag{B.1}$$

where $\boldsymbol{S}_{-\boldsymbol{k}j} = \boldsymbol{S}^*_{\boldsymbol{k}j}$ so that the magnetic moment is real. In the case of a single propagation vector, the sum over $\boldsymbol{k}$ and the related indexes can be removed:

$$\boldsymbol{\mu}_j(\boldsymbol{R}_l) = \frac{1}{2}(\boldsymbol{S}_j\mathrm{e}^{-\mathrm{i}\boldsymbol{k}\cdot\boldsymbol{R}_l} + \boldsymbol{S}^*_j\mathrm{e}^{\mathrm{i}\boldsymbol{k}\cdot\boldsymbol{R}_l}). \tag{B.2}$$

Assuming a helicoidal magnetic structure where the spins lie in the plane formed by orthogonal unit vectors $\hat{\boldsymbol{u}}$ and $\hat{\boldsymbol{v}}$ the Fourier coefficient of atom j is $\boldsymbol{S}_j = (S_{uj}\boldsymbol{u}_j + S_{vj}\mathrm{i}\boldsymbol{v}_j)\mathrm{e}^{-\mathrm{i}2\pi\phi_j}$, where ϕ_j is the phase of the magnetic moment of atom j. From this, the magnetic moment can be written as

$$\boldsymbol{\mu}_j(\boldsymbol{R}_l) = \frac{1}{2}[(S_{uj}\boldsymbol{u}_j + \mathrm{i}S_{vj}\boldsymbol{v}_j)\mathrm{e}^{-\mathrm{i}\boldsymbol{k}\cdot\boldsymbol{R}_l}\mathrm{e}^{-\mathrm{i}2\pi\phi_j} + (S_{uj}\boldsymbol{u}_j - \mathrm{i}S_{vj}\boldsymbol{v}_j)\mathrm{e}^{\mathrm{i}\boldsymbol{k}\cdot\boldsymbol{R}_l}\mathrm{e}^{\mathrm{i}2\pi\phi_j}], \tag{B.3}$$

and regrouping the exponential factors allows to write the cosine and sine

decomposition

$$\boldsymbol{\mu}_j(\boldsymbol{R}_l) = S_{uj}\boldsymbol{u}_j \cos(\boldsymbol{k}\cdot\boldsymbol{R}_l + 2\pi\phi_j) + S_{vj}\boldsymbol{v}_j \sin(\boldsymbol{k}\cdot\boldsymbol{R}_l + 2\pi\phi_j). \tag{B.4}$$

We note that Eq. (B.1) is defined using the same convention as in FULLPROF, for example. In MAG2POL the definition of the magnetic moment is

$$\boldsymbol{\mu}_j(\boldsymbol{R}_l) = \frac{1}{2}\sum_{\boldsymbol{k}}(\boldsymbol{S}_{\boldsymbol{k}j}\mathrm{e}^{\mathrm{i}\boldsymbol{k}\cdot\boldsymbol{R}_l} + \boldsymbol{S}_{-\boldsymbol{k}j}\mathrm{e}^{-\mathrm{i}\boldsymbol{k}\cdot\boldsymbol{R}_l}), \tag{B.5}$$

in which case the Fourier coefficient is rather $\boldsymbol{S}_j = (S_{uj}\boldsymbol{u}_j + S_{vj}\mathrm{i}\boldsymbol{v}_j)\mathrm{e}^{\mathrm{i}2\pi\phi_j}$ and the magnetic moment is given by:

$$\boldsymbol{\mu}_j(\boldsymbol{R}_l) = S_{uj}\boldsymbol{u}_j \cos(\boldsymbol{k}\cdot\boldsymbol{R}_l + 2\pi\phi_j) - S_{vj}\boldsymbol{v}_j \sin(\boldsymbol{k}\cdot\boldsymbol{R}_l + 2\pi\phi_j). \tag{B.6}$$

Appendix C

Magnetic moments in $MnSb_2O_6$

As described in Section III.3.3 the magnetic moment of an Mn atom at site $j = (1, 2, 3)$, in a layer α (along the c-axis), and with an angle $\phi_{\alpha j}$ can be described by

$$\begin{cases} \boldsymbol{\mu}_{\alpha j} = M_u \cos\phi_{\alpha j}\hat{\boldsymbol{u}} + M_v \sin\phi_{\alpha j}\hat{\boldsymbol{v}} \\ \phi_{\alpha j} = 2\pi\eta_{\mathrm{C}} k_z \alpha + \eta_{\mathrm{T}}(j-1)\dfrac{2\pi}{3}. \end{cases} \tag{C.1}$$

$\hat{\boldsymbol{u}}$ and $\hat{\boldsymbol{v}}$ are orthogonal unit vectors which describe the main axes of the spin rotation plane (which is an ellipse).

We can introduce an orthonormal basis $\mathcal{R} = (\hat{\boldsymbol{x}}, \hat{\boldsymbol{y}}, \hat{\boldsymbol{z}})$ where $\hat{\boldsymbol{x}}$ lies along the a-axis, $\hat{\boldsymbol{z}}$ along the c-axis and $\hat{\boldsymbol{y}}$ completes the right-handed set. For the magnetic model proposed in Ref. [57] and pictured in Fig. III.3(a), $\hat{\boldsymbol{u}} = \hat{\boldsymbol{x}}$ and $\hat{\boldsymbol{v}} = \hat{\boldsymbol{z}}$. In order to describe a tilted cycloid structure and to allow any direction $\hat{\boldsymbol{u}}$ in the (ab)-plane, we can introduce two rotation matrices. The first one is a rotation around $\hat{\boldsymbol{x}}$ to describe the vertical tilt of the cycloid by an angle θ as illustrated in Fig. C.1(a):

$$R_\theta = \begin{pmatrix} 1 & 0 & 0 \\ 0 & \cos\theta & -\sin\theta \\ 0 & \sin\theta & \cos\theta \end{pmatrix}. \tag{C.2}$$

And the second one is a rotation around $\hat{\boldsymbol{z}}$ to describe the rotation of the in-plane

main axis by an angle χ as illustrated in Fig. C.1(b):

$$R_\chi = \begin{pmatrix} \cos\chi & -\sin\chi & 0 \\ \sin\chi & \cos\theta & 0 \\ 0 & 0 & 1 \end{pmatrix}. \tag{C.3}$$

From starting $\hat{\boldsymbol{u}}_0 = \hat{\boldsymbol{x}}$ and $\hat{\boldsymbol{v}}_0 = \hat{\boldsymbol{z}}$ we can describe all kind of tilted structures. $\hat{\boldsymbol{n}} = \hat{\boldsymbol{u}} \times \hat{\boldsymbol{v}}$ completes the orthonormal set and normal to the spin rotation plane. Applying first R_θ and then R_χ, the general expression of these basis vectors are given by

$$\hat{\boldsymbol{u}} = \begin{pmatrix} \cos\chi \\ \sin\chi \\ 0 \end{pmatrix}, \hat{\boldsymbol{v}} = \begin{pmatrix} \sin\chi\sin\theta \\ -\cos\chi\sin\theta \\ \cos\theta \end{pmatrix}, \hat{\boldsymbol{n}} = \begin{pmatrix} \sin\chi\cos\theta \\ -\cos\chi\cos\theta \\ -\sin\theta \end{pmatrix}. \tag{C.4}$$

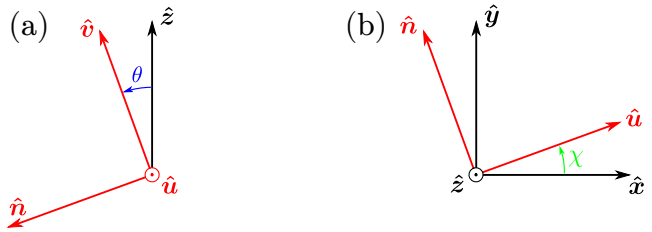

Figure C.1 (a) Here, $\hat{\boldsymbol{u}} = \hat{\boldsymbol{x}}$, θ is the rotation angle around $\hat{\boldsymbol{x}}$. (b) Here, $\hat{\boldsymbol{v}} = \hat{\boldsymbol{z}}$, χ is the rotation angle around $\hat{\boldsymbol{z}}$.

With this general formalism the spin chirality vector associated to the propagation of the magnetic order along the c-axis is given by

$$\boldsymbol{V}_\mathrm{C} = \boldsymbol{\mu}_{\alpha j} \times \boldsymbol{\mu}_{\alpha+1 j} = M_u M_v (\hat{\boldsymbol{u}} \times \hat{\boldsymbol{v}}) \sin(\phi_{\alpha+1 j} - \phi_{\alpha j}) = M_u M_v \sin(2\pi k_\mathrm{z}) \eta_\mathrm{C} \hat{\boldsymbol{n}}. \tag{C.5}$$

Similarly the triangular spin chirality vector is given by

$$\boldsymbol{V}_\mathrm{T} = \boldsymbol{\mu}_{\alpha j} \times \boldsymbol{\mu}_{\alpha j+1} = M_u M_v (\hat{\boldsymbol{u}} \times \hat{\boldsymbol{v}}) \sin(\phi_{\alpha j+1} - \phi_{\alpha j}) = M_u M_v \sqrt{3}/2 \eta_\mathrm{T} \hat{\boldsymbol{n}}. \tag{C.6}$$

Thus η_C and η_T are well describing the senses of rotation of the spins around the

$\hat{\boldsymbol{n}}$ axis as they change sign according to the senses of rotation.

In the refinement softwares used for modeling and refining magnetic structure (MAG2POL [134] and FULLPROF [133]), the sign of the first term of $\phi_{\alpha j}$ is determined by the dot product with the lattice vector $\boldsymbol{k} \cdot \boldsymbol{R}_{\mathrm{L}}$ and cannot be refined, so we need to rewrite Eq. (C.1) into

$$\begin{cases} \boldsymbol{\mu}_{\alpha j} = M_u \cos \phi'_{\alpha j} \hat{\boldsymbol{u}} + \eta_{\mathrm{C}} M_v \sin \phi'_{\alpha j} \hat{\boldsymbol{v}} \\ \phi'_{\alpha j} = \eta_{\mathrm{C}} \phi_{\alpha j} = 2\pi k_{\mathrm{z}} \alpha + \eta_{\mathrm{C}} \eta_{\mathrm{T}} (j-1) \dfrac{2\pi}{3}. \end{cases} \tag{C.7}$$

In this case the magnetic parameters can be encoded in the signs of the Fourier coefficients and of the magnetic phases. Also, the magnetic moments are often expressed in the direct space $\mathcal{R}_{abc}$ of the crystal lattice. In the case of $MnSb_2O_6$ or in general for a trigonal unit cell, we have to convert to $\hat{\boldsymbol{a}} = \hat{\boldsymbol{x}}$, $\hat{\boldsymbol{b}} = \sqrt{3}/2\hat{\boldsymbol{y}} - 1/2\hat{\boldsymbol{x}}$ and $\hat{\boldsymbol{c}} = \hat{\boldsymbol{z}}$. For a vector $\boldsymbol{M}$ its conversion from the direct space to the orthonormal basis $\mathcal{R}$ is given by:

$$\begin{pmatrix} M_x \\ M_y \\ M_z \end{pmatrix}_{\mathcal{R}} = \begin{pmatrix} 1 & -1/2 & 0 \\ 0 & \sqrt{3}/2 & 0 \\ 0 & 0 & 1 \end{pmatrix} \begin{pmatrix} M_a \\ M_b \\ M_c \end{pmatrix}_{\mathcal{R}_{abc}}. \tag{C.8}$$

Inversely,

$$\begin{pmatrix} M_a \\ M_b \\ M_c \end{pmatrix}_{\mathcal{R}_{abc}} = \begin{pmatrix} 1 & 1/\sqrt{3} & 0 \\ 0 & 2/\sqrt{3} & 0 \\ 0 & 0 & 1 \end{pmatrix} \begin{pmatrix} M_x \\ M_y \\ M_z \end{pmatrix}_{\mathcal{R}}. \tag{C.9}$$

Thus for the tilted model from Ref. [58] with $\hat{\boldsymbol{u}} \parallel [1\bar{1}0]$, i.e. for $\chi = -30°$ and letting θ as a free parameter. From Eq. (C.4) and Eq. (C.9).

$$\hat{\boldsymbol{u}} = \begin{pmatrix} \sqrt{3}/2 \\ -1/2 \\ 0 \end{pmatrix}_{\mathcal{R}} = \frac{1}{\sqrt{3}} \begin{pmatrix} 1 \\ -1 \\ 0 \end{pmatrix}_{\mathcal{R}_{abc}} , \hat{\boldsymbol{v}} = \begin{pmatrix} -\sin\theta/2 \\ -\sqrt{3}/2\sin\theta \\ \cos\theta \end{pmatrix}_{\mathcal{R}} = \begin{pmatrix} -\sin\theta \\ -\sin\theta \\ \cos\theta \end{pmatrix}_{\mathcal{R}_{abc}} .$$

(C.10)

Working with the basis vectors:

$$\boldsymbol{B}_1 = \begin{pmatrix} 1 \\ -1 \\ 0 \end{pmatrix}_{\mathcal{R}_{abc}} , \boldsymbol{B}_2 = \mathrm{i} \begin{pmatrix} 1 \\ 1 \\ 0 \end{pmatrix}_{\mathcal{R}_{abc}} , \boldsymbol{B}_3 = \mathrm{i} \begin{pmatrix} 0 \\ 0 \\ 1 \end{pmatrix}_{\mathcal{R}_{abc}} . \tag{C.11}$$

Associated to the coefficients C_1, C_2, C_3 (refinable during the data analysis). Along with the magnetic phase $\phi_j = \eta_{\mathrm{C}}\eta_{\mathrm{T}}(j-1)\frac{2\pi}{3}$, and constraining $M_v > 0$, this gives 4 refinable parameters for 5 physical quantities M_u, M_v, θ, η_{C}, η_{T}. With the relations:

$$\begin{cases} M_u = C_1\sqrt{3}, dM_u = dC_1\sqrt{3} \\ M_v = \sqrt{(C_2^2 + C_3^2)}, dM_v = \sqrt{\frac{{C_2}^2}{M_v} dC_2^2 + \frac{{C_2}^2}{M_v} dC_3^2} \\ \theta = \mathrm{atan}[-C_2/C_3]. \end{cases} \tag{C.12}$$

Appendix D

Powder neutron diffraction on $MnSb_2O_6$

This appendix supplies more information on the powder neutron diffraction experiment on $MnSb_2O_6$ performed on D20, presented in Chapter III.

D.1 Datasets

The datasets were measured between 2.6 K and 89.4 K, with fine temperature steps below 15 K (85 temperatures between 2.6 K and 15.1 K) and coarse steps above (26 temperatures between 17.7 K and 89.4 K). Raw diffraction patterns are shown in Fig. D.1 for selected temperatures. Magnetic peaks appear below $T_N \approx 12\,K$.

D.2 Refinement results

The data were refined sequentially using FULLPROF [133]. Zero shift, scale, asymmetry, UVW and shape parameters were refined at 2.6 K, and then fixed during the sequential refinement. Background parameters, lattice constants, atomic positions (within the $P321$ space group) and overall displacement factor were refined at each temperature. A magnetic phase was also considered, where the magnetic moment magnitude M of the Mn^{2+} ions is refined following

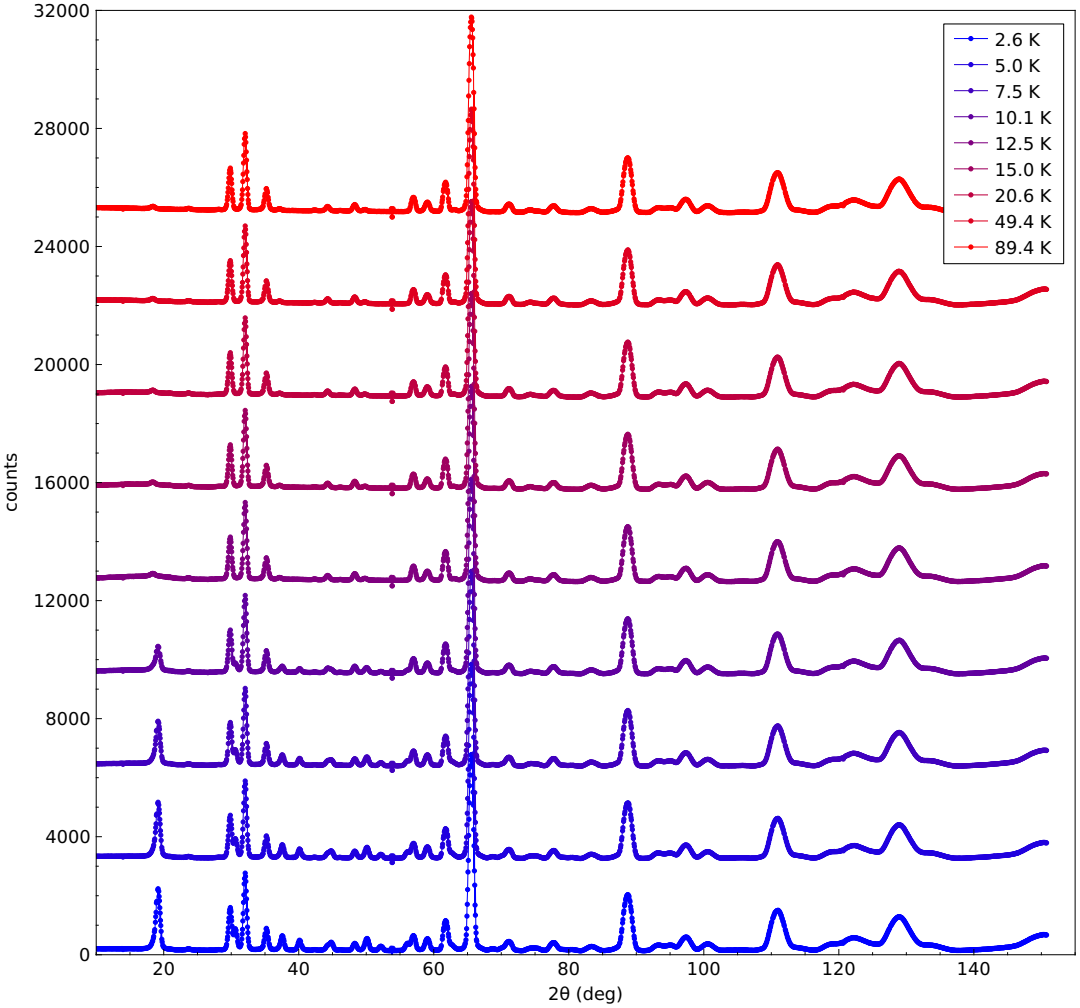

Figure D.1 Stacked plots of the D20 diffraction patterns for selected temperatures.

Eq. (III.6) considering a circular spin rotation envelop of the cycloids $M = M_u = M_v$. In the process of the sequential refinement, this second phase is also refined above the actual Néel temperature (giving $M = 0$ within uncertainties above $T_N = 12\,K$). Examples of the refinement are shown in Fig. D.2, with the corresponding results listed in Table D.1.

Refining separately M_u and M_v (elliptical envelop) did not improve the fit. Also, for this refinement, $\hat{\boldsymbol{u}}$ was taken along the a-axis, and $\hat{\boldsymbol{v}}$ along the c-axis, as powder diffraction is not sensitive to the in-plane direction of the spin rotation plane.

Table D.1 Refined parameters from powder neutron diffraction performed on D20 for selected temperatures.

$T = 2.6\,K$						
$R_{Bragg}(nuc) = 2.06\%$ $R_{Bragg}(mag) = 5.93\%$ $\chi^2 = 104$						
$a = b = 8.7901(2)$ Å $c = 4.7171(2)$ Å $B_{iso} = 0.08(2)$ Å^2						
Atoms	Wyckoff	x	y	z	M (μ_B)	Occ.
Mn	$3e$	0.6318(7)	0.0000	0.0000	4.57(2)	1
Sb1	$1a$	0.0000	0.0000	0.0000	/	1
Sb2	$2d$	0.3333	0.6667	0.487(3)	/	1
Sb3	$3f$	0.3039(5)	0.0000	0.5000	/	1
O1	$6g$	0.105(1)	0.8943(6)	0.7595(5)	/	1
O2	$6g$	0.469(1)	0.5859(5)	0.7267(7)	/	1
O3	$6g$	0.2287(7)	0.781(1)	0.2803(7)	/	1
$T = 49.4\,K$						
$R_{Bragg}(nuc) = 2.23\%$ $R_{Bragg}(mag) = 143\%$ $\chi^2 = 83.4$						
$a = b = 8.7904(2)$ Å $c = 4.7175(1)$ Å $B_{iso} = 0.11(1)$ Å^2						
Atoms	Wyckoff	x	y	z	M (μ_B)	Occ.
Mn	$3e$	0.6322(6)	0.0000	0.0000	0.1(3)	1
Sb1	$1a$	0.0000	0.0000	0.0000	/	1
Sb2	$2d$	0.3333	0.6667	0.491(3)	/	1
Sb3	$3f$	0.3046(5)	0.0000	0.5000	/	1
O1	$6g$	0.105(1)	0.8918(5)	0.7605(5)	/	1
O2	$6g$	0.469(1)	0.5867(4)	0.7273(7)	/	1
O3	$6g$	0.2305(6)	0.780(1)	0.2799(6)	/	1

D.3 MnO_6 octahedral distortion

Each MnO_6 octahedron is composed of a Mn atom surrounded by six O atoms with three inequivalent Wyckoff positions as shown in Fig. D.3. The distances (calculated from the refinement) between the Mn atom and the O atoms within an octahedron are shown in Fig. D.4 as a function of the temperature, showing a sharper evolution below $T_N \approx 12\,K$, indicating magnetostructural effects and

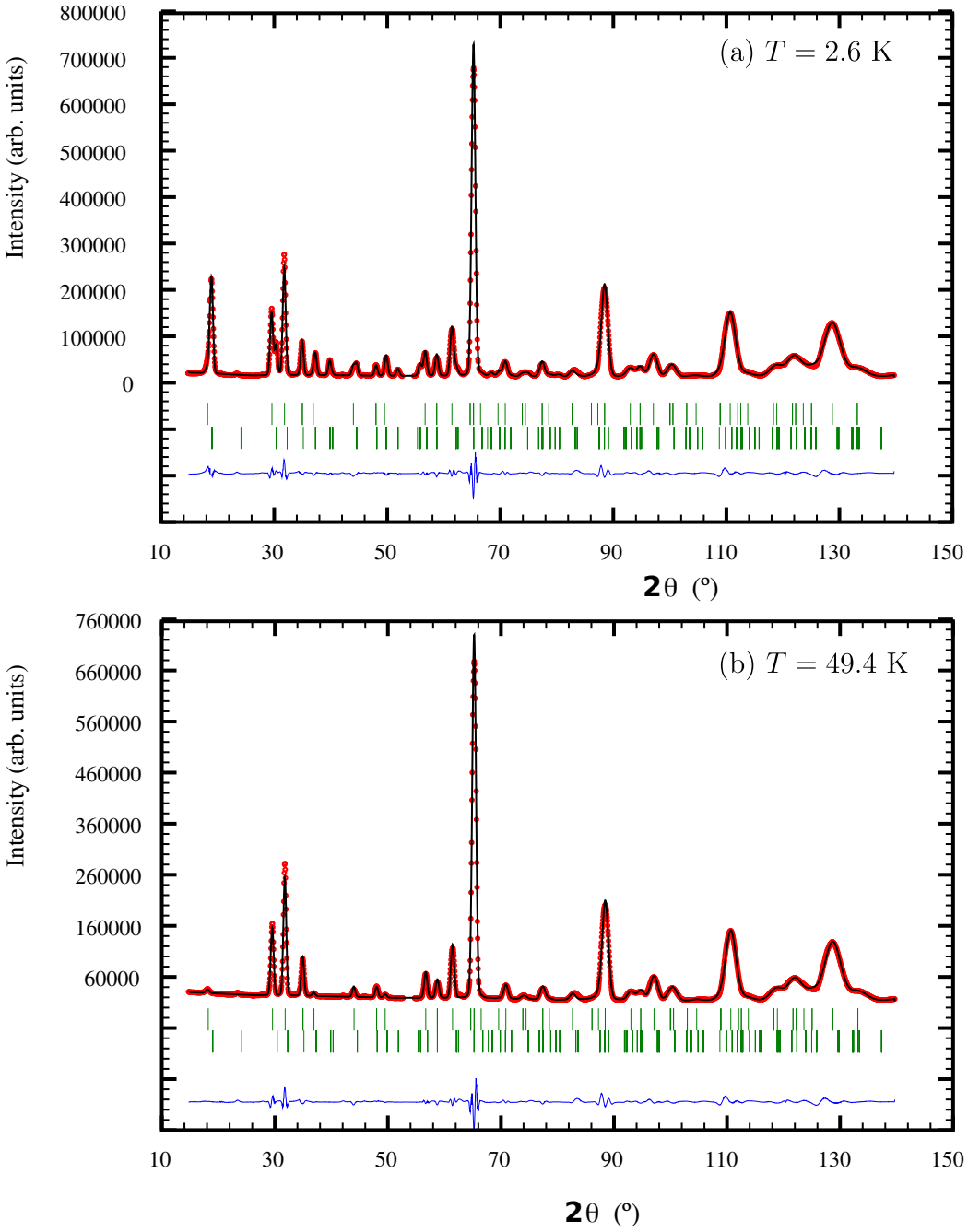

Figure D.2 Rietveld refinement (black lines), neutron powder diffraction data (red points) and measured at (a) $T = 2.6\,\mathrm{K}$ and (b) $T = 49.4\,\mathrm{K}$. Top and bottom ticks indicate respectively the $MnSb_2O_6$ nuclear and magnetic peaks. $T = 2.6\,\mathrm{K}$. The difference curve (observed-calculated) is shown in blue lines.

the octahedral distortion. The corresponding angles are shown in Fig. D.4 as a function of the temperature. We note that the calculations on FULLPROF are performed until the first digit of the angles.

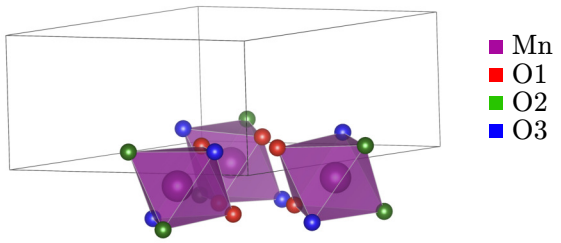

Figure D.3 MnO_6 octahedra are composed of a Mn atom (purple) surrounded by six O atoms with three inequivalent Wyckoff positions (in red, green and blue).

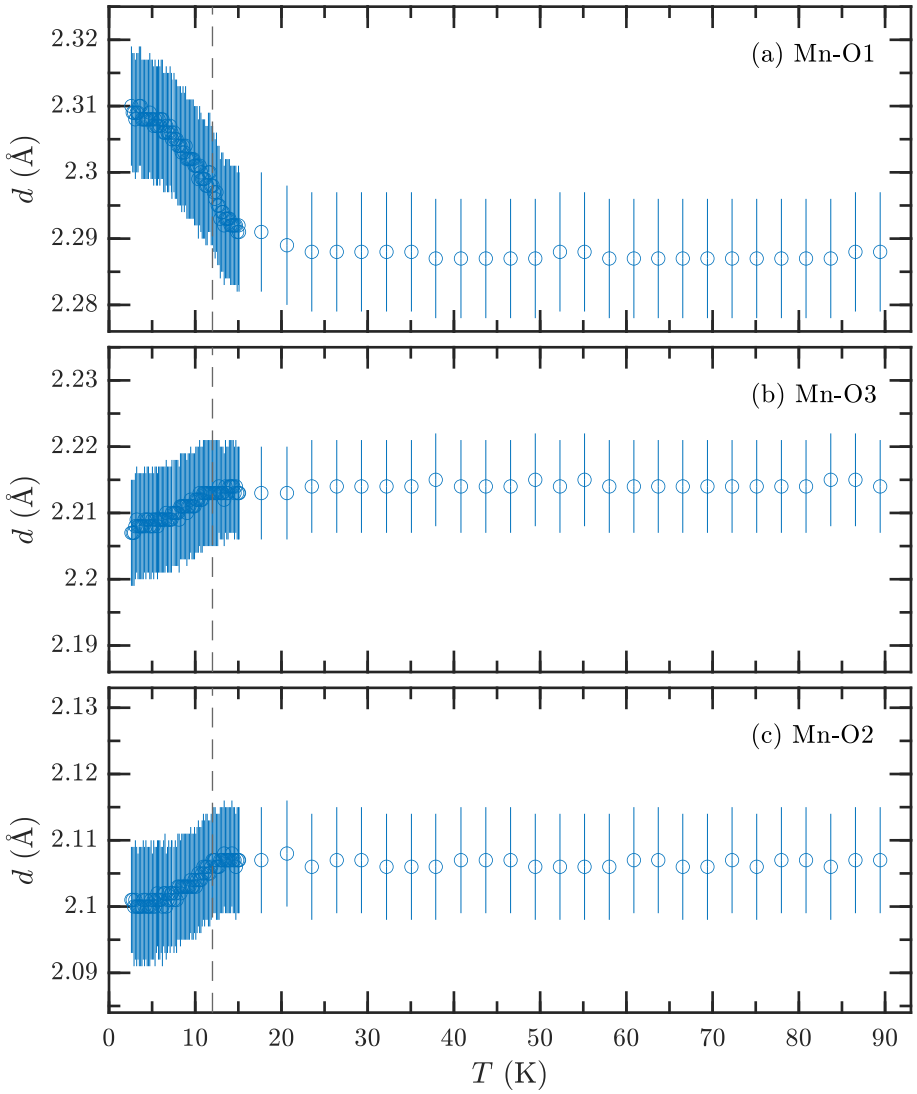

Figure D.4 Temperature dependence of the bond distances within a MnO_6 octahedron between Mn and (a) O1, (b) O3, and (c) O2.

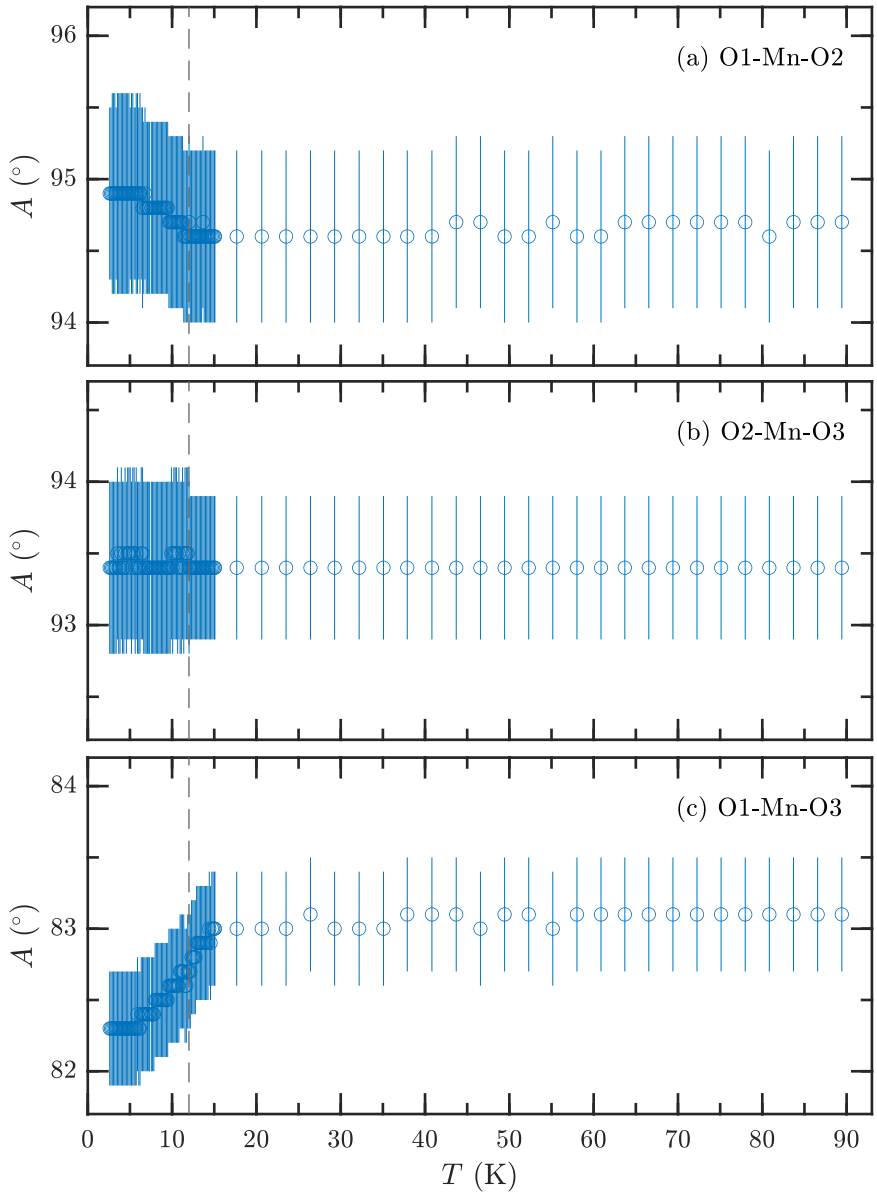

Figure D.5 Temperature dependence of the angles within a MnO_6 octahedron for (a) O1-Mn-O2, (b) O2-Mn-O3, and (c) O1-Mn-O3.

Appendix E

Single crystal sum rules analysis

E.1 Integration methods for first moment

As the first moments are computed by a numerical integration, it is important to make sure that the integration methods do not have a significant impact on the results of the analysis. This section outlines five integration methods, and the resulting γ parameters are compared in Fig. E.1, following a L-scan analysis on the $E_\mathrm{f} = 2.4\,\mathrm{meV}$ dataset.

In Section IV.3.4.2, the constant-$\boldsymbol{Q}$ scans are fitted to two Gaussians as shown in Fig. IV.9, and then the first moments were calculated by numerically integrating with a trapezoidal rule with the background removed from the fit to a two-Gaussian model. The results are shown with bars (C). Of course, the first moments can also be computed without removing the background, resulting with bars (B). Then, they can be computed analytically using the fit parameters of the two-Gaussian model, shown with the bars (A) in Fig. E.1. In order to avoid the mixture of elastic scattering and one-magnon scattering, the elastic line can be fitted to a third Gaussian, while the actual data above $E = 0.2\,\mathrm{meV}$ are fitted to two Gaussians. Then, the first moments can be again calculated analytically with the fitted parameters of these two Gaussians in the good energy range. This is shown in bars (D). Finally, the trapezoidal integration can be performed, removing the background from this three-Gaussian model, as shown in bars (E). Finally, it can be seen that all the fitted parameters agree within uncertainties. We have rather chosen to adopt trapezoidal integration, removing the background

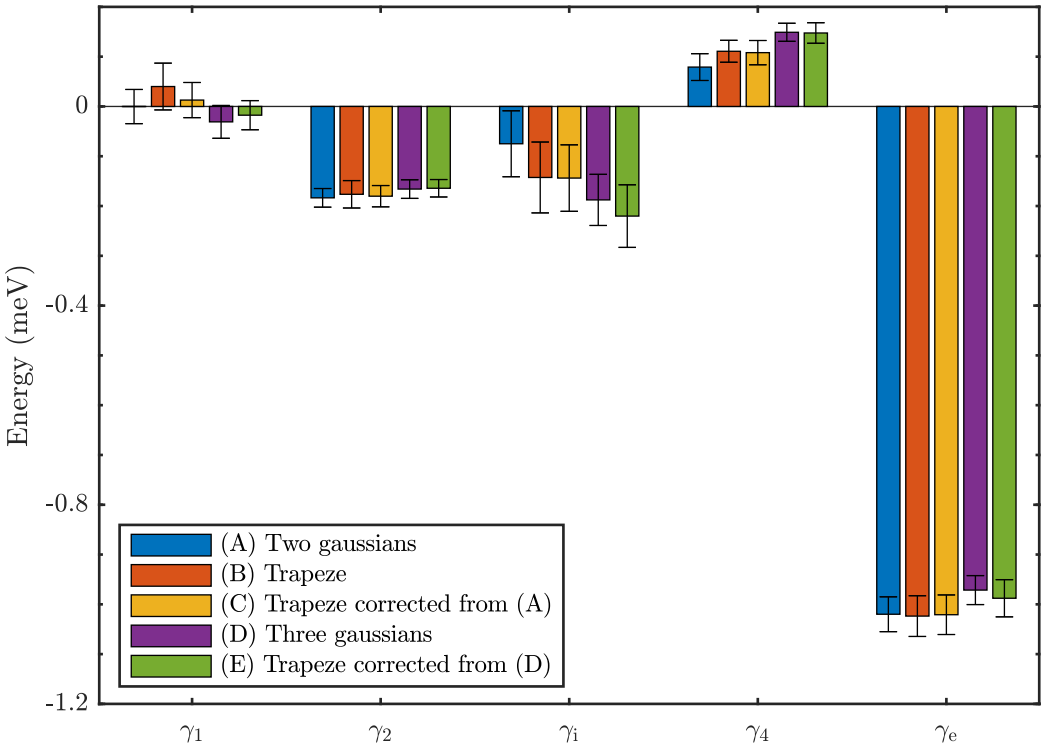

Figure E.1 Fitted parameters for different integrations methods to compute the first moments, from the $E_f = 2.4\,\text{meV}$ dataset.

from the two-Gaussian fit, to deal with any deviation from a two-mode spin-wave spectrum.

E.2 H-scan

In Section IV.3.4.2, we have described the first moment sum rule analysis of the single crystal data, by fixing some H_0 and calculating the first moment as a function of L. We can perform the same analysis considering $\boldsymbol{Q} = (H, H, L_0)$ with H varying for a chosen L_0 (H-scan). For each interaction indexed by spins i and j, the corresponding term in the cosine in Eq. (IV.15) can be written now:

$$\boldsymbol{Q} \cdot \boldsymbol{d}_{ij} = 2\pi H(d_{ij,x} + d_{ij,y}) + 2\pi L_0 d_{ij,z}, \tag{E.1}$$

where the distances are expressed in lattice units, and the scattering vector in reciprocal lattice units. Similarly as in Eq. (IV.18), a general formula for the first moment can be derived for a fixed L_0, using trigonometric identities:

$$\begin{aligned}\langle E\rangle(H, L_0) = A_{\mathrm{i}}(L_0)\cos(2\pi\delta_1 H) + ... \\ A_{\mathrm{e}}(L_0)[\cos(2\pi\delta_2 H) + ... \\ \cos(2\pi\delta_3 H) + \cos(2\pi\delta_4 H)] + C(L_0),\end{aligned} \tag{E.2}$$

where we have now three functions A_{i}, A_{e} and C which are L_0-dependent, expressed by:

$$A_{\mathrm{i}}(L_0) = \frac{4}{3}[\gamma_1 + \gamma_i \cos(2\pi L_0)] \tag{E.3}$$

$$A_{\mathrm{e}}(L_0) = \frac{4}{3}[\gamma_2 + \gamma_e \cos(2\pi L_0)] \tag{E.4}$$

$$\begin{aligned}C(L_0) = -\frac{2}{3}[2\gamma_1 + 6\gamma_2 + 3\gamma_i + 3\gamma_4 + 6\gamma_e] + ... \\ \frac{2}{3}\cos(2\pi L_0)(\gamma_i + 3\gamma_4).\end{aligned} \tag{E.5}$$

Fig. E.2(a)-(c) shows some constant-$\boldsymbol{Q}$ cuts for $(H, H, L_0 = 0.4)$ and their fit to two gaussians. The first moments are again calculated numerically using trapezoidal integration and the background is removed from the two-gaussian fit. These computed first moments are the red data points in Fig. E.2(d), along with the H-dependence of the computed first moment, and the fit to Eq. (E.2), to extract A_{i}, A_{e} and C. This operation is repeated for several L_0, as shown in Fig. E.2(e)-(f).

Finally, a total of 999 first moments $\langle E\rangle(\boldsymbol{Q})$ are computed for this analysis on this $E_{\mathrm{f}} = 2.4\,\mathrm{meV}$ dataset, and plotted against the fitted first moments in Fig. E.3(a). The γ parameters are then obtained by fitting the measured A_{i}, A_{e} and C to their theoretical values, as shown in Fig. E.3(b)-(d), where the red data points are the coefficients calculated in Fig. E.2(d)-(f). As for the L-scan analysis, some remaining background can be included in the computation of C. For this reason, the L_0-independent part of Eq. (E.5), which corresponds to an overall constant to the first moment sum rule, is not used to get the γ parameters and hence the exchange constants J_i.

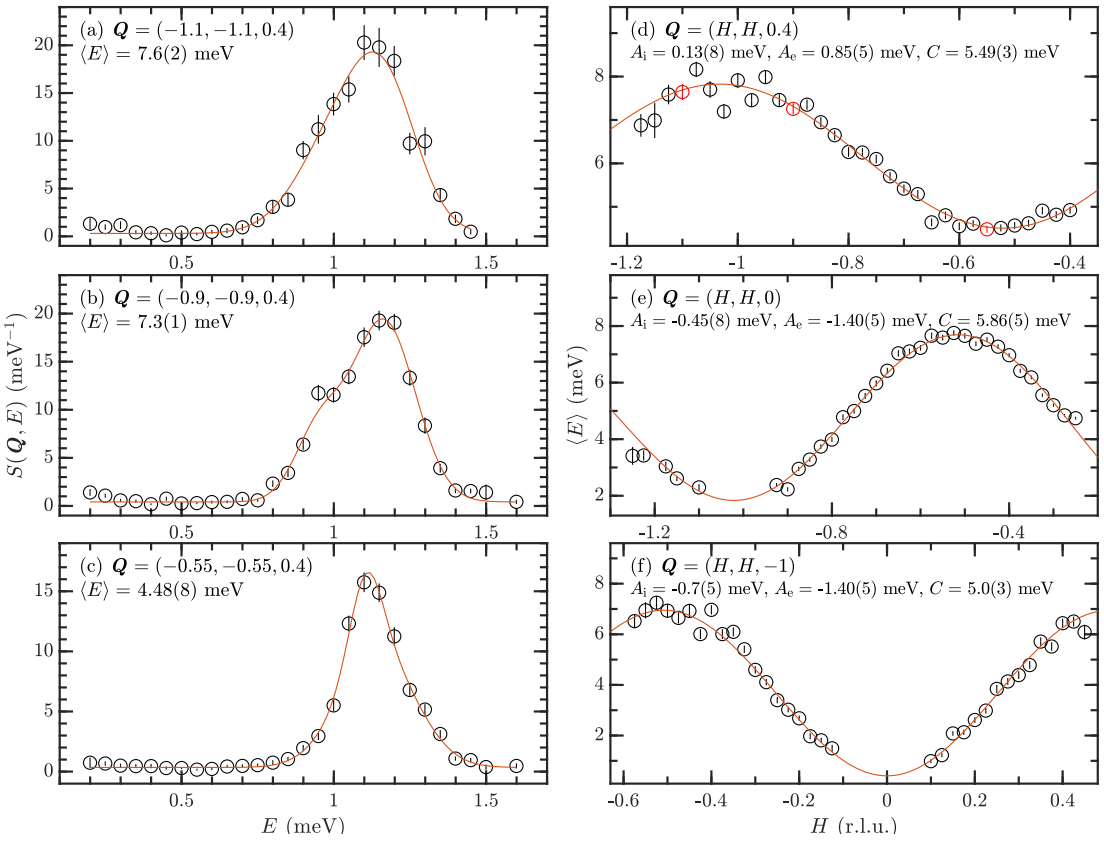

Figure E.2 (a)-(c) Constant-$\boldsymbol{Q}$ scans for different $\boldsymbol{Q} = (H, H, L_0 = 0.4)$. A fit to a double gaussian is shown in red, and the first moment is calculated from trapezoidal integration where the background is removed from the gaussian fit. (d) First moment as a function of H for $L_0 = 0.4$, fitted to its theoretical expression (red curve). The red data points correspond to the first moments calculated in the cuts plotted in (a)-(c). (e)-(f) First moment as a function of H for (e) $L_0 = 0$ and (f) $L_0 = -1$, fit to theoretical expression in red.

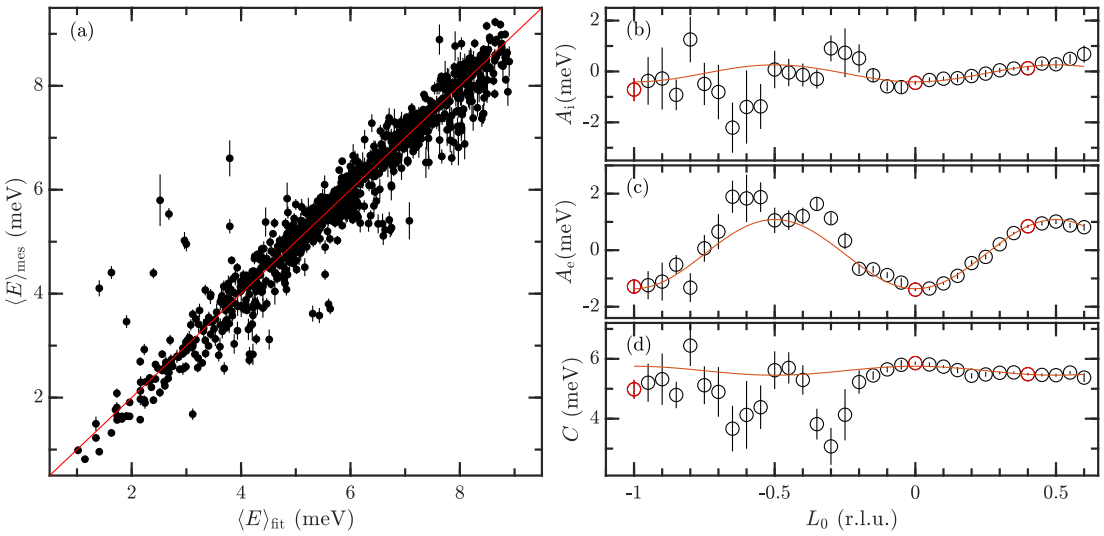

Figure E.3 (a) Measured first moments versus fitted first moments for H-scan analysis, for the $E_{\mathrm{f}} = 2.4\,\mathrm{meV}$ dataset. A total of 999 $\langle E\rangle(\boldsymbol{Q})$ were taken into account. (b)-(d) Fitting of coefficients (b) A_{i}, (c) A_{e} and (d) C giving the γ parameters. The red data points show the values calculated in Fig. E.2(d)-(f).

	J_1	J_2	J_3	J_4	J_5	J_6	J_7
Fig. 14 (b)	0.0988	0.2859	0.1500	0.3491	-0.1011	1.0222	0.1161
Fig. 14 (c)	0.0988	0.2859	0.2000	0.3491	-0.0155	0.9972	0.0732
Fig. 14 (d)	0.0988	0.2859	0.2500	0.3491	0.0702	0.9722	0.0304

Table E.1 The parameters for the calculations performed in SpinW displayed in Fig. IV.13(b)-(d). Parameters varied for the three calculations are highlighted in blue.

E.3 Second dataset results

The single crystal first moment sum rule analysis was repeated on the second dataset measured on MACS with $E_{\mathrm{f}} = 3.7\,\mathrm{meV}$. The results of the L-scan (469 computed first moments) and H-scan (487 computed first moments) analyses are respectively shown in Fig. E.4 and Fig. E.5.

E.4 Parameters for Figure 14

The sum rule analysis had an ambiguity in the set of equations resulting from the fact that several exchange constants corresponded to the same bond distance.

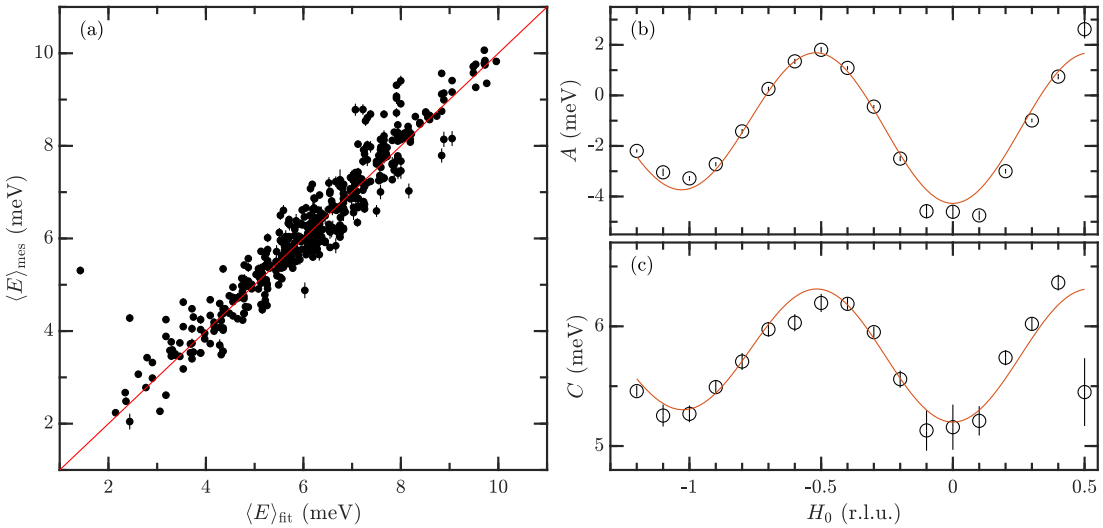

Figure E.4 (a) Measured first moments versus fitted first moments for L-scan analysis, for the $E_{\mathrm{f}} = 3.7\,\mathrm{meV}$ dataset. A total of 469 $\langle E\rangle(\boldsymbol{Q})$ were taken into account. (b)-(c) Fitting of coefficients (b) A and (c) C giving the γ parameters.

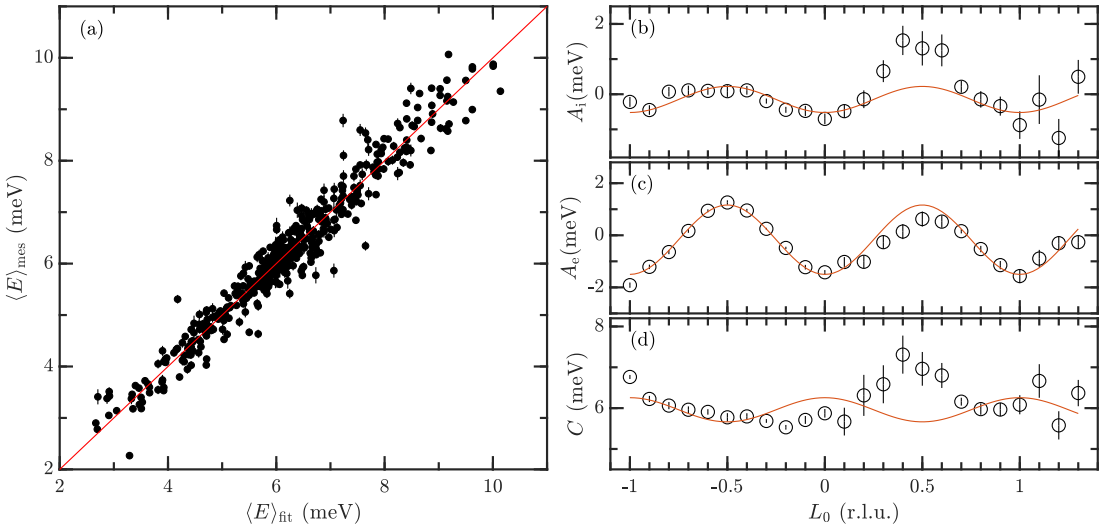

Figure E.5 (a) Measured first moments versus fitted first moments for H-scan analysis, for the $E_{\mathrm{f}} = 3.7\,\mathrm{meV}$ dataset. A total of 487 $\langle E\rangle(\boldsymbol{Q})$ were taken into account. (b)-(d) Fitting of coefficients (b) A_{i}, (c) A_{e} and (d) C giving the γ parameters.

We therefore needed to fix one exchange constant through a comparison to the single crystal dispersion as discussed in the main text. This qualitative analysis is described in Fig. IV.13. The parameters for the calculations are listed in Table E.1.

Appendix F

VI_3 diffraction patterns

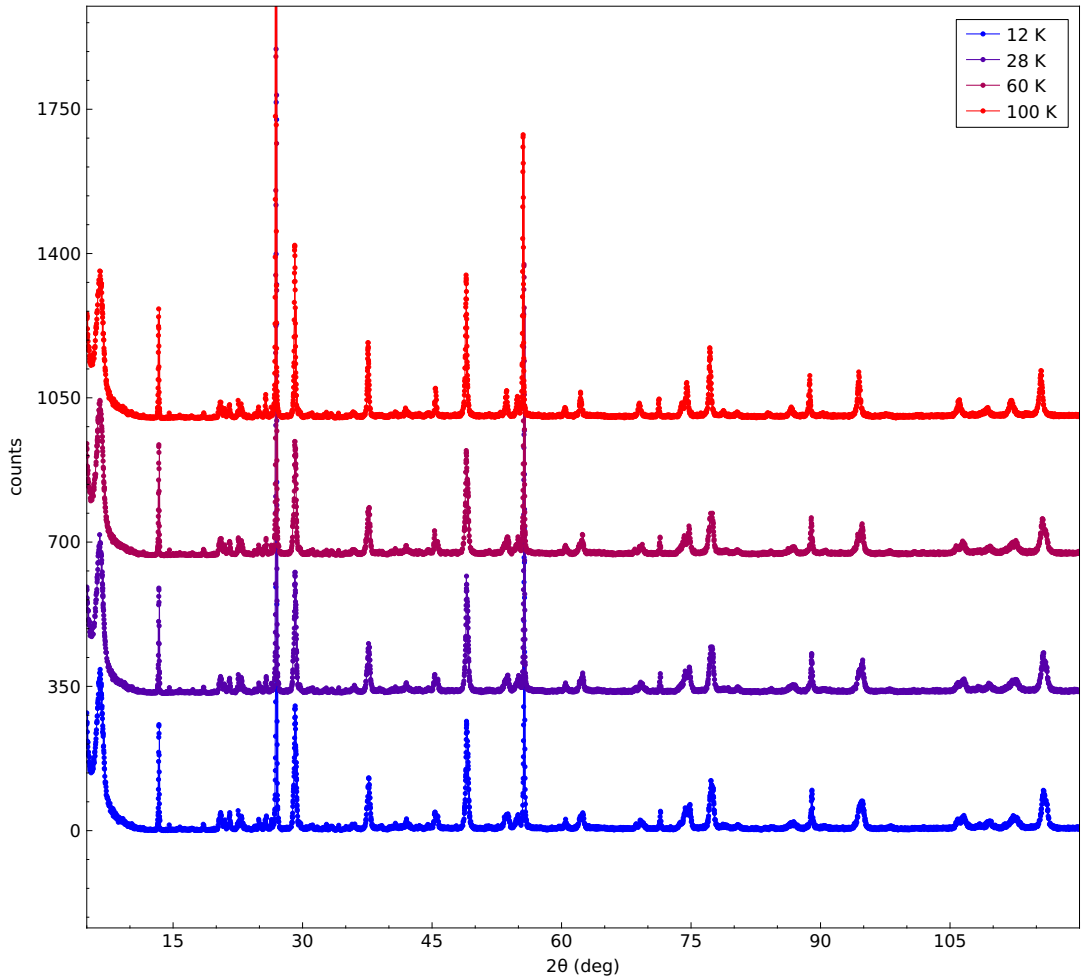

Figure F.1 Stacked plots of the X-ray powder diffraction patterns for four temperatures.

Full diffraction patterns with a 2θ-range $[5, 120]^\circ$ were measured at 12, 28, 60 and 100 K, as shown in Fig. F.1. Smaller 2θ-range $[42.5, 57]^\circ$ datasets were measured between 20 K and 150 K (36 temperatures). Raw diffraction patterns are shown in Fig. F.2 for selected temperatures. Some peak splittings are observed below 80 K, evidencing a structural transition in VI_3.

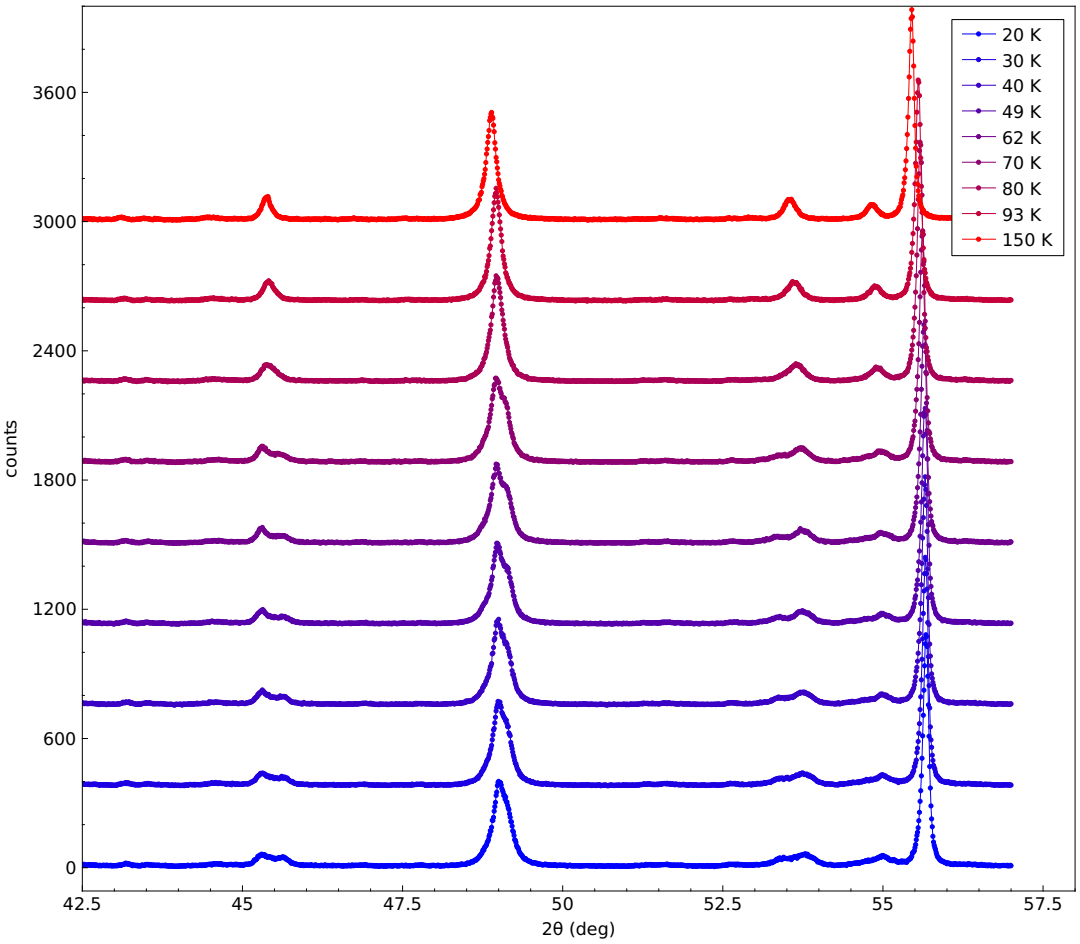

Figure F.2 Stacked plots of the X-ray powder diffraction patterns for selected temperatures.

Bibliography

[1] E. Chan, J. Pásztorová, R. D. Johnson, M. Songvilay, R. A. Downie, J.-W. G. Bos, O. Fabelo, C. Ritter, K. Beauvois, C. Niedermayer, S.-W. Cheong, N. Qureshi, and C. Stock, Phys. Rev. B **106**, 064403 (2022).

[2] E. Chan, H. Lane, J. Pásztorová, M. Songvilay, R. D. Johnson, R. Downie, J.-W. G. Bos, J. A. Rodriguez-Rivera, S.-W. Cheong, R. A. Ewings, N. Qureshi, and C. Stock, Physical Review B **107**, 144420 (2023).

[3] C. Trainer, O. R. Armitage, H. Lane, L. C. Rhodes, E. Chan, I. Benedičič, J. A. Rodriguez-Rivera, O. Fabelo, C. Stock, and P. Wahl, Phys. Rev. B **106**, L081405 (2022).

[4] É. du Trémolet de Lacheisserie, D. Gignoux, and M. Schlenker, *Magnetism, Fundamentals, Materials and Applications*, edited by É. du Trémolet de Lacheisserie, D. Gignoux, and M. Schlenker (Springer, New York, NY, 2002).

[5] S. J. Blundell, *Magnetism: A Very Short Introduction* (Oxford University Press, 2012).

[6] C. G. Shull and J. S. Smart, Phys. Rev. **76**, 1256 (1949).

[7] L. Néel, Comptes Rendus Hebdomadaires Des Seances De L Academie Des Sciences **203**, 304 (1936).

[8] M. N. Baibich, J. M. Broto, A. Fert, F. N. Van Dau, F. Petroff, P. Etienne, G. Creuzet, A. Friederich, and J. Chazelas, Phys. Rev. Lett. **61**, 2472 (1988).

[9] G. Binasch, P. Grünberg, F. Saurenbach, and W. Zinn, Phys. Rev. B **39**, 4828 (1989).

[10] E. Dagotto, Rev. of Mod. Phys. **66**, 763 (1994).

[11] Web of Science.

[12] P. Curie, J. Phys. Theor. Appl. **3**, 393 (1894).

[13] I. Dzyaloshinskii, Sov. Phys. JETP **10**, 628 (1960).

[14] D. Astrov, Sov. Phys. JETP **11**, 708 (1960).

[15] V. J. Folen, G. T. Rado, and E. W. Stalder, Phys. Rev. Lett. **6**, 607 (1961).

[16] E. Ascher, H. Rieder, H. Schmid, and H. Stössel, J. App. Phys. **37**, 1404 (1966).

[17] H. Schmid, Ferroelectrics **162**, 317 (1994).

[18] K. Aizu, Phys. Rev. B **2**, 754 (1970).

[19] J. F. Scott, Nat. Mater. **6**, 256 (2007).

[20] M. Gajek, M. Bibes, S. Fusil, K. Bouzehouane, J. Fontcuberta, A. Barthélémy, and A. Fert, Nat. Mater. **6**, 296 (2007).

[21] N. A. Spaldin, S.-W. Cheong, and R. Ramesh, Phys. Today **63**, 38 (2010).

[22] N. A. Hill, J. Phys. Chem. B **104**, 6694 (2000).

[23] W. Eerenstein, N. D. Mathur, and J. F. Scott, Nature **442**, 759 (2006).

[24] M. Fiebig, J. Phys. D: App. Phys. **38**, R123 (2005).

[25] N. A. Spaldin and M. Fiebig, Science **309**, 391 (2005).

[26] S.-W. Cheong and M. Mostovoy, Nat. Mater. **6**, 13 (2007).

[27] J. Wang, J. B. Neaton, H. Zheng, V. Nagarajan, S. B. Ogale, B. Liu, D. Viehland, V. Vaithyanathan, D. G. Schlom, U. V. Waghmare, N. A. Spaldin, K. M. Rabe, M. Wuttig, and R. Ramesh, Science **299**, 1719 (2003).

[28] T. Kimura, T. Goto, H. Shintani, K. Ishizaka, T. Arima, and Y. Tokura, Nature **426**, 55 (2003).

[29] N. Hur, S. Park, P. A. Sharma, J. S. Ahn, S. Guha, and S.-W. Cheong, Nature **429**, 392 (2004).

[30] R. Ramesh and N. A. Spaldin, Nat. Mater. **6**, 21 (2007).

[31] K. Wang, J.-M. Liu, and Z. Ren, Adv. Phys. **58**, 321 (2009).

[32] Y. Tokura, S. Seki, and N. Nagaosa, Rep. Prog. Phys. **77**, 076501 (2014).

[33] R. D. Johnson and P. G. Radaelli, Annu. Rev. Mater. Res. **44**, 269 (2014).

[34] S. Dong, J.-M. Liu, S.-W. Cheong, and Z. Ren, Adv. Phys. **64**, 519 (2015).

[35] M. Fiebig, T. Lottermoser, D. Meier, and M. Trassin, Nat. Rev. Mater. **1**, 16046 (2016).

[36] N. A. Spaldin and R. Ramesh, Nat. Mater. **18**, 203 (2019).

[37] D. Khomskii, Phys. **2**, 20 (2009).

[38] G. Catalan and J. F. Scott, Adv. Mat. **21**, 2463 (2009).

[39] D. Lebeugle, D. Colson, A. Forget, and M. Viret, App. Phys. Lett. **91**, 022907 (2007).

[40] R. D. Johnson, L. C. Chapon, D. D. Khalyavin, P. Manuel, P. G. Radaelli, and C. Martin, Phys. Rev. Lett. **108**, 067201 (2012).

[41] T. Kimura, Annu. Rev. Mater. Res. **37**, 387 (2007).

[42] M. Mostovoy, Phys. Rev. Lett. **96**, 067601 (2006).

[43] J. Rodríguez-Carvajal and J. Villain, Comptes Rendus Physique **20**, 770 (2019).

[44] D. I. Khomskii, in *Multiferroic Materials*, Chap. 1, edited by J. Wang (CRC Press, 2016).

[45] N. Nagaosa, in *Spin Current*, Chap. 10, edited by S. Maekawa, S. O. Valenzuela, E. Saitoh, and T. Kimura (Oxford University Press, 2017) pp. 160–184.

[46] I. A. Sergienko and E. Dagotto, Phys. Rev. B **73**, 094434 (2006).

[47] H. Katsura, N. Nagaosa, and A. V. Balatsky, Phys. Rev. Lett. **95**, 057205 (2005).

[48] I. Dzyaloshinskii, J. Phys. Chem. Solids **4**, 241 (1958).

[49] T. Moriya, Phys. Rev. Lett. **4**, 228 (1960).

[50] K. Yosida, *Theory of Magnetism* (Springer, New York, 1996).

[51] T. Finger, D. Senff, K. Schmalzl, W. Schmidt, L. P. Regnault, P. Becker, L. Bohatỳ, and M. Braden, Phys. Rev. B **81**, 054430 (2010).

[52] P. Babkevich, A. Poole, R. D. Johnson, B. Roessli, D. Prabhakaran, and A. T. Boothroyd, Phys. Rev. B **85**, 134428 (2012).

[53] T. Honda, J. S. White, A. B. Harris, L. C. Chapon, A. Fennell, B. Roessli, O. Zaharko, Y. Murakami, M. Kenzelmann, and T. Kimura, Nat. Commun. **8**, 15457 (2017).

[54] J. A. Rodríguez-Velamazán, O. Fabelo, J. Campo, J. Rodríguez-Carvajal, N. Qureshi, and L. C. Chapon, Sci. Rep. **8**, 10665 (2018).

[55] T.-h. Arima, J. Phys. Soc. Jpn. **76**, 073702 (2007).

[56] Y. J. Choi, H. T. Yi, S. Lee, Q. Huang, V. Kiryukhin, and S.-W. Cheong, Phys. Rev. Lett. **100**, 047601 (2008).

[57] R. D. Johnson, K. Cao, L. C. Chapon, F. Fabrizi, N. Perks, P. Manuel, J. J. Yang, Y. S. Oh, S.-W. Cheong, and P. G. Radaelli, Phys. Rev. Lett. **111**, 017202 (2013).

[58] M. Kinoshita, S. Seki, T. J. Sato, Y. Nambu, T. Hong, M. Matsuda, H. B. Cao, S. Ishiwata, and Y. Tokura, Phys. Rev. Lett. **117**, 047201 (2016).

[59] K. S. Novoselov, A. K. Geim, S. V. Morozov, D. Jiang, Y. Zhang, S. V. Dubonos, I. V. Grigorieva, and A. A. Firsov, Science **306**, 666 (2004).

[60] K. S. Novoselov, D. Jiang, F. Schedin, T. J. Booth, V. V. Khotkevich, S. V. Morozov, and A. K. Geim, Proc. Natl. Acad. Sci **102**, 10451 (2005).

[61] A. K. Geim, Science **324**, 1530 (2009).

[62] S. Z. Butler, S. M. Hollen, L. Cao, Y. Cui, J. A. Gupta, H. R. Gutiérrez, T. F. Heinz, S. S. Hong, J. Huang, A. F. Ismach, E. Johnston-Halperin, M. Kuno, V. V. Plashnitsa, R. D. Robinson, R. S. Ruoff, S. Salahuddin, J. Shan, L. Shi, M. G. Spencer, M. Terrones, et al., ACS Nano **7**, 2898 (2013).

[63] P. Ajayan, P. Kim, and K. Banerjee, Phys. Today **69**, 38 (2016).

[64] A. K. Geim and I. V. Grigorieva, Nature **499**, 419 (2013).

[65] Y. Liu, N. O. Weiss, X. Duan, H.-C. Cheng, Y. Huang, and X. Duan, Nat. Rev. Mat. **1**, 1 (2016).

[66] K. S. Novoselov, A. Mishchenko, A. Carvalho, and A. H. Castro Neto, Science **353**, aac9439 (2016).

[67] N. D. Mermin and H. Wagner, Phys. Rev. Lett. **17**, 1133 (1966).

[68] M. Gibertini, M. Koperski, A. F. Morpurgo, and K. S. Novoselov, Nat. Nanotechnol. **14**, 408 (2019).

[69] L. Onsager, Phys. Rev. **65**, 117 (1944).

[70] C. A. F. Vaz, J. A. C. Bland, and G. Lauhoff, Rep. Prog. Phys. **71**, 056501 (2008).

[71] J. L. Miller, Phys. Today **70**, 16 (2017).

[72] C. Gong and X. Zhang, Science **363**, eaav4450 (2019).

[73] L. J. De Jongh and A. R. Miedema, Adv. Phys. **50**, 947 (2001).

[74] J.-G. Park, J. Phys. Condens. Matter **28**, 301001 (2016).

[75] C.-T. Kuo, M. Neumann, K. Balamurugan, H. J. Park, S. Kang, H. W. Shiu, J. H. Kang, B. H. Hong, M. Han, T. W. Noh, and J.-G. Park, Sci. Rep. **6**, 20904 (2016).

[76] M.-W. Lin, H. L. Zhuang, J. Yan, T. Z. Ward, A. A. Puretzky, C. M. Rouleau, Z. Gai, L. Liang, V. Meunier, B. G. Sumpter, P. Ganesh, P. R. C. Kent, D. B. Geohegan, D. G. Mandrus, and K. Xiao, J. Mater. Chem. C **4**, 315 (2015).

[77] K.-z. Du, X.-z. Wang, Y. Liu, P. Hu, M. I. B. Utama, C. K. Gan, Q. Xiong, and C. Kloc, ACS Nano **10**, 1738 (2016).

[78] X. Wang, K. Du, Y. Y. F. Liu, P. Hu, J. Zhang, Q. Zhang, M. H. S. Owen, X. Lu, C. K. Gan, P. Sengupta, C. Kloc, and Q. Xiong, 2D Mater. **3**, 031009 (2016).

[79] J.-U. Lee, S. Lee, J. H. Ryoo, S. Kang, T. Y. Kim, P. Kim, C.-H. Park, J.-G. Park, and H. Cheong, Nano Lett. **16**, 7433 (2016).

[80] N. Samarth, Nature **546**, 216 (2017).

[81] B. Huang, G. Clark, E. Navarro-Moratalla, D. R. Klein, R. Cheng, K. L. Seyler, D. Zhong, E. Schmidgall, M. A. McGuire, D. H. Cobden, W. Yao, D. Xiao, P. Jarillo-Herrero, and X. Xu, Nature **546**, 270 (2017).

[82] C. Gong, L. Li, Z. Li, H. Ji, A. Stern, Y. Xia, T. Cao, W. Bao, C. Wang, Y. Wang, Z. Q. Qiu, R. J. Cava, S. G. Louie, J. Xia, and X. Zhang, Nature **546**, 265 (2017).

[83] K. S. Burch, D. Mandrus, and J.-G. Park, Nature **563**, 47 (2018).

[84] X. Jiang, Q. Liu, J. Xing, N. Liu, Y. Guo, Z. Liu, and J. Zhao, App. Phys. Rev. **8**, 031305 (2021).

[85] C. Dai, P. He, L. Luo, P. Zhan, B. Guan, and J. Zheng, Sci. China Mater. **66**, 859–876 (2023).

[86] H.-J. Deiseroth, K. Aleksandrov, C. Reiner, L. Kienle, and R. K. Kremer, Eur. J. Inorg. Chem. **2006**, 1561 (2006).

[87] H. Wang and X. Qian, 2D Mater. **4**, 015042 (2017).

[88] Y. Gao, M. Gao, and Y. Lu, Nanoscale **13**, 19324 (2021).

[89] J. Chadwick, Proc. R. Soc. Lond. A **136**, 692 (1932).

[90] C. G. Shull, Rev. of Mod. Phys. **67**, 753 (1995).

[91] B. Jacrot, R. Ghosh, and A. Filhol, *Neutrons for science: the history of the Institut Laue-Langevin, an exceptionally successful international collaboration*, Sciences & histoire (EDP sciences, Les Ulis, 2021).

[92] B. N. Brockhouse and A. T. Stewart, Phys. Rev. **100**, 756 (1955).

[93] G. L. Squires, *Introduction to the Theory of Thermal Neutron Scattering*, 3rd ed. (Cambridge University Press, Cambridge, 2012).

[94] S. W. Lovesey and S. W. Lovesey, *Theory of Neutron Scattering from Condensed Matter: Volume I: Nuclear Scattering*, International Series of Monographs on Physics (Oxford University Press, Oxford, 1986).

[95] S. W. Lovesey, *Theory of Neutron Scattering from Condensed Matter: Volume II: Polarization Effects and Magnetic Scattering*, International Series of Monographs on Phys. (Oxford University Press, Oxford, 1986).

[96] G. Shirane, S. M. Shapiro, and J. M. Tranquada, *Neutron Scattering with a Triple-Axis Spectrometer: Basic Techniques* (Cambridge University Press, Cambridge, 2002).

[97] T. Chatterji, ed., *Neutron Scattering from Magnetic Materials*, 1st ed. (Elsevier, Amsterdam, 2006).

[98] A. Furrer, J. Mesot, and T. Strässle, *Neutron Scattering in Condensed Matter Phys.*, Series on Neutron Techniques and Applications (World Scientific, 2009).

[99] A. T. Boothroyd, *Principles of neutron scattering from condensed matter*, 1st ed. (Oxford University Press, New York, 2020).

[100] A. Czarnecki, W. J. Marciano, and A. Sirlin, Phys. Rev. Lett. **120**, 202002 (2018).

[101] Particle Data Group, R. L. Workman, V. D. Burkert, V. Crede, E. Klempt, U. Thoma, L. Tiator, K. Agashe, G. Aielli, B. C. Allanach, C. Amsler, M. Antonelli, E. C. Aschenauer, D. M. Asner, H. Baer, S. Banerjee, R. M. Barnett, L. Baudis, C. W. Bauer, J. J. Beatty, et al., Prog. Theor. Exp. Phys. **2022**, 083C01 (2022).

[102] J. K. Cockcroft, Powder diffraction course material: Nuclear Reactors, Birkbeck College, University of London (2006).

[103] V. F. Sears, Neutron News **3**, 26 (1992).

[104] N. W. Ashcroft and N. D. Mermin, *Solid State Phys.* (Saunders college, Philadelphia, Pa., 1976).

[105] M. Enderle, Collection SFN **13**, 01002 (2014).

[106] P. J. Brown, in *International Tables for Crystallography*, Vol. C, Chap. 4.4.5, edited by E. Prince (2006) 1st ed., pp. 454–461.

[107] O. Halpern and M. H. Johnson, Phys. Rev. **55**, 898 (1939).

[108] C. G. Shull, E. O. Wollan, and W. C. Koehler, Phys. Rev. **84**, 912 (1951).

[109] R. Nathans, C. Shull, G. Shirane, and A. Andresen, J. Phys. Chem. Solids **10**, 138 (1959).

[110] M. Blume, Phys. Rev. **130**, 1670 (1963).

[111] S. V. Maleev, V. G. Bar'yakhtar, and R. A. Suris, Sov. Phys.-Solid State (English Transl.), **4** (1963).

[112] V. Simonet, M. Loire, and R. Ballou, Eur. Phys. J.: Spec. Top. **213**, 5 (2012).

[113] J. Schweizer, in *Neutron Scattering from Magnetic Materials*, edited by T. Chatterji (Elsevier Science, Amsterdam, 2006) pp. 153–213.

[114] N. J. Giles-Donovan, *Characterisation of Competing Orders in Dielectric Oxides*, Ph.D. thesis, University of Glasgow (2021).

[115] P. J. Brown, in *Neutron Scattering from Magnetic Materials*, Chap. 5, edited by T. Chatterji (Elsevier Science, Amsterdam, 2006) pp. 215–244.

[116] R. M. Moon, T. Riste, and W. C. Koehler, Phys. Rev. **181**, 920 (1969).

[117] N. Qureshi, M. T. F. Díaz, L. C. Chapon, A. Senyshyn, W. Schweika, and M. Valldor, Phys. Rev. B **97**, 064404 (2018).

[118] J.-R. Soh, F. de Juan, N. Qureshi, H. Jacobsen, H.-Y. Wang, Y.-F. Guo, and A. T. Boothroyd, Phys. Rev. B **101**, 140411 (2020).

[119] N. Giles-Donovan, N. Qureshi, R. D. Johnson, L. Y. Zhang, S.-W. Cheong, S. Cochran, and C. Stock, Phys. Rev. B **102**, 024414 (2020).

[120] F. Tasset, P. J. Brown, and J. B. Forsyth, J. Appl. Phys. **63**, 3606 (1988).

[121] F. Tasset, Phys. B: Condens. Matter **156-157**, 627 (1989).

[122] F. Tasset, P. Brown, E. Lelièvre-Berna, T. Roberts, S. Pujol, J. Allibon, and E. Bourgeat-Lami, Phys. B: Condens. Matter **267–268**, 69 (1999).

[123] J. Schwinger, Phys. Rev. **73**, 407 (1948).

[124] G. P. Felcher and S. W. Peterson, Acta Crystallogr. A **31**, 76 (1975).

[125] N. Qureshi, A. Bombardi, S. Picozzi, P. Barone, E. Lelièvre-Berna, X. Xu, C. Stock, D. F. McMorrow, A. Hearmon, F. Fabrizi, P. G. Radaelli, S.-W. Cheong, and L. C. Chapon, Phys. Rev. B **102**, 054417 (2020).

[126] P. Barnes, S. Jacques, and M. Vickers, Powder diffraction course material: Powder Diffraction.

[127] T. C. Hansen, P. F. Henry, H. E. Fischer, J. Torregrossa, and P. Convert, Meas. Sci. Technol. **19**, 034001 (2008).

[128] D20 - High-intensity two-axis diffractometer with variable resolution, Institut Laue-Langevin website.

[129] H. M. Rietveld, J. Appl. Crystallogr. **2**, 65 (1969).

[130] B. Ouladdiaf, J. Archer, G. McIntyre, A. Hewat, D. Brau, and S. York, Phys. B: Condens. Matter **385-386**, 1052 (2006).

[131] OrientExpress - Laue Diffractometer, Institut Laue-Langevin website.

[132] D9 - Hot neutron four-circle diffractometer, Institut Laue-Langevin website.

[133] J. Rodríguez-Carvajal, Phys. B **192**, 55 (1993).

[134] N. Qureshi, J. Appl. Crystallogr. **52**, 175 (2019).

[135] B. H. Toby, Powder Diff. **21**, 67 (2006).

[136] N. Qureshi, EPJ Web of Conferences **155**, 00002 (2017).

[137] W. Heil, J. Dreyer, D. Hofmann, H. Humblot, E. Lelievre-Berna, and F. Tasset, Phys. B: Condens. Matter **267–268**, 328 (1999).

[138] M. Janoschek, S. Klimko, R. Gähler, B. Roessli, and P. Böni, Phys. B: Condens. Matter **397**, 125 (2007).

[139] F. Semadeni, B. Roessli, and P. Böni, Phys. B: Condens. Matter **297**, 152 (2001).

[140] Description - TASP, Paul Scherrer Institut website.

[141] J. A. Rodriguez, D. M. Adler, P. C. Brand, C. Broholm, J. C. Cook, C. Brocker, R. Hammond, Z. Huang, P. Hundertmark, J. W. Lynn, N. C. Maliszewskyj, J. Moyer, J. Orndorff, D. Pierce, T. D. Pike, G. Scharfstein, S. A. Smee, and R. Vilaseca, Meas. Sci. Technol. **19**, 034023 (2008).

[142] E. N. Maslen, A. G. Fox, and M. A. O'Keefe, in *International Tables for Crystallography*, Vol. C, edited by E. Prince (2006) 1st ed., pp. 554–595.

[143] M. Kenzelmann, A. B. Harris, S. Jonas, C. Broholm, J. Schefer, S. B. Kim, C. L. Zhang, S.-W. Cheong, O. P. Vajk, and J. W. Lynn, Phys. Rev. Lett. **95**, 087206 (2005).

[144] K. Marty, V. Simonet, E. Ressouche, R. Ballou, P. Lejay, and P. Bordet, Phys. Rev. Lett. **101**, 247201 (2008).

[145] M. Loire, V. Simonet, S. Petit, K. Marty, P. Bordet, P. Lejay, J. Ollivier, M. Enderle, P. Steffens, E. Ressouche, A. Zorko, and R. Ballou, Phys. Rev. Lett. **106**, 207201 (2011).

[146] C. Stock, L. C. Chapon, A. Schneidewind, Y. Su, P. G. Radaelli, D. F. McMorrow, A. Bombardi, N. Lee, and S.-W. Cheong, Phys. Rev. B **83**, 104426 (2011).

[147] L. Chaix, R. Ballou, A. Cano, S. Petit, S. de Brion, J. Ollivier, L.-P. Regnault, E. Ressouche, E. Constable, C. V. Colin, A. Zorko, V. Scagnoli, J. Balay, P. Lejay, and V. Simonet, Phys. Rev. B **93**, 214419 (2016).

[148] C. Stock, R. D. Johnson, N. Giles-Donovan, M. Songvilay, J. A. Rodriguez-Rivera, N. Lee, X. Xu, P. G. Radaelli, L. C. Chapon, A. Bombardi, S. Cochran, C. Niedermayer, A. Schneidewind, Z. Husges, Z. Lu, S. Meng, and S.-W. Cheong, Phys. Rev. B **100**, 134429 (2019).

[149] K. Momma and F. Izumi, J. Appl. Crystallogr. **44**, 1272 (2011).

[150] H. D. Flack, Helv. Chim. Acta **86**, 905 (2003).

[151] J. N. Reimers and J. E. Greedan, J. Solid State Chem. **79**, 263 (1989).

[152] J. Werner, C. Koo, R. Klingeler, A. N. Vasiliev, Y. A. Ovchenkov, A. S. Polovkova, G. V. Raganyan, and E. A. Zvereva, Phys. Rev. B **94**, 104408 (2016).

[153] P. Bak and M. H. Jensen, J. Phys. Condens. Matter **13**, L881 (1980).

[154] A. M. Nakua and J. E. Greedan, J. Cryst. Growth **154**, 334 (1995).

[155] C. Stock, O. R. Fabelo Rosa, N. Qureshi, and M. Songvilay, The Nuclear Structure of MnSb2O6 in single crystals: (2021), type: dataset.

[156] E. Chan, K. Beauvois, N. Qureshi, J. A. Rodriguez Velamazan, M. Songvilay, C. Stock, and A. Stunault, Magnetic and electric field switching of magnetic domains in MnSb2O6 (2021), type: dataset.

[157] C. Stock, L. Chapon, J. Pasztorova, N. Qureshi, M. Songvilay, and A. Stunault, Coupled structural and magnetic chirality in MnSb2O6: (2017), type: dataset.

[158] E. Chan, N. Qureshi, C. Ritter, and C. Stock, The Detailed Magnetic Structure of MnSb2O6 ; Helix or Ellipse? (2021), type: dataset.

[159] T. Hahn and H. Klapper, in *International Tables for Crystallography*, Vol. D, Chap. 3.3, edited by A. Authier (2013) 2nd ed., pp. 413–487.

[160] S. Parsons, Acta Crystallogr. D **59**, 1995 (2003).

[161] E. Koch, in *International Tables for Crystallography*, Vol. C, Chap. 1.3, edited by E. Prince (2006) 1st ed., pp. 10–14.

[162] N. Chandra, K. R. Acharya, and P. C. E. Moody, Acta Crystallogr. D **55**, 1750 (1999).

[163] L. D. Barron, J. Am. Chem. Soc. **108**, 5539 (1986).

[164] J. Villain, J. Phys. Condens. Matter **10**, 4793 (1977).

[165] J. Jerphagnon and D. S. Chemla, J. Chem. Phys. **65**, 1522 (1976).

[166] X. Wang, F.-T. Huang, J. Yang, Y. S. Oh, and S.-W. Cheong, APL Mater. **3**, 076105 (2015).

[167] M. A. Prosnikov, A. N. Smirnov, V. Y. Davydov, Y. Araki, T. Arima, and R. V. Pisarev, Phys. Rev. B **100**, 144417 (2019).

[168] M. Campostrini, M. Hasenbusch, A. Pelissetto, P. Rossi, and E. Vicari, Phys. Rev. B **65**, 144520 (2002).

[169] H. Kawamura, J. App. Phys. **63**, 3086 (1988).

[170] N. Qureshi, M. Zbiri, J. Rodríguez-Carvajal, A. Stunault, E. Ressouche, T. C. Hansen, M. T. Fernández-Díaz, M. R. Johnson, H. Fuess, H. Ehrenberg, Y. Sakurai, M. Itou, B. Gillon, T. Wolf, J. A. Rodríguez-Velamazan, and J. Sánchez-Montero, Phys. Rev. B **79**, 094417 (2009).

[171] S. Cheon, H.-W. Lee, and S.-W. Cheong, Phys. Rev. B **98**, 184405 (2018).

[172] P. C. Hohenberg and W. F. Brinkman, Phys. Rev. B **10**, 128 (1974).

[173] J. des Cloizeaux and J. J. Pearson, Phys. Rev. **128**, 2131 (1962).

[174] G. Müller, H. Thomas, H. Beck, and J. C. Bonner, Phys. Rev. B **24**, 1429 (1981).

[175] Y. Endoh, G. Shirane, R. J. Birgeneau, P. M. Richards, and S. L. Holt, Phys. Rev. Lett. **32**, 170 (1974).

[176] R. Coldea, D. A. Tennant, and Z. Tylczynski, Phys. Rev. B **68**, 134424 (2003).

[177] D. A. Tennant, T. G. Perring, R. A. Cowley, and S. E. Nagler, Phys. Rev. Lett. **70**, 4003 (1993).

[178] S. E. Nagler, D. A. Tennant, R. A. Cowley, T. G. Perring, and S. K. Satija, Phys. Rev. B **44**, 12361 (1991).

[179] B. Lake, D. A. Tennant, J.-S. Caux, T. Barthel, U. Schollwöck, S. E. Nagler, and C. D. Frost, Phys. Rev. Lett. **111**, 137205 (2013).

[180] M. B. Stone, D. H. Reich, C. Broholm, K. Lefmann, C. Rischel, C. P. Landee, and M. M. Turnbull, Phys. Rev. Lett. **91**, 037205 (2003).

[181] M. Mourigal, M. Enderle, A. Kloepperpieper, J.-S. Caux, A. Stunault, and H. M. Ronnow, Nat. Phys. **9**, 435 (2013).

[182] I. U. Heilmann, J. K. Kjems, Y. Endoh, G. F. Reiter, G. Shirane, and R. J. Birgeneau, Phys. Rev. B **24**, 3939 (1981).

[183] T. Huberman, R. Coldea, R. A. Cowley, D. A. Tennant, R. L. Leheny, R. J. Christianson, and C. D. Frost, Phys. Rev. B **72**, 014413 (2005).

[184] M. Songvilay, E. Rodriguez, R. Lindsay, M. Green, H. Walker, J. Rodriguez-Rivera, and C. Stock, Phys. Rev. Lett. **121**, 087201 (2018).

[185] P. R. Hammar, D. H. Reich, C. Broholm, and F. Trouw, Phys. Rev. B **57**, 7846 (1998).

[186] G. Xu, Z. Xu, and J. M. Tranquada, Rev. Sci. Instrum. **84**, 083906 (2013).

[187] S. Nakatsuji, K. Kuga, K. Kimura, R. Satake, N. Katayama, E. Nishibori, H. Sawa, R. Ishii, M. Hagiwara, F. Bridges, T. U. Ito, W. Higemoto, Y. Karaki, M. Halim, A. A. Nugroho, J. A. Rodriguez-Rivera, M. A. Green, and C. Broholm, Science **339**, 559 (2012).

[188] I. A. Zaliznyak and S.-H. Lee, in *Mod. Techniques for Characterizing Magnetic Materials*, edited by Y. Zhu (Springer, Boston, MA, 2005) pp. 3–64.

[189] P. M. Sarte, *Neutron Inelastic Scattering Studies of Effective Spin-1/2 Magnets*, Ph.D. thesis (2019).

[190] P. M. Sarte, A. M. Arévalo-López, M. Songvilay, D. Le, T. Guidi, V. García-Sakai, S. Mukhopadhyay, S. C. Capelli, W. D. Ratcliff, K. H. Hong, G. M. McNally, E. Pachoud, J. P. Attfield, and C. Stock, Phys. Rev. B **98**, 224410 (2018).

[191] C. Stock, L. C. Chapon, O. Adamopoulos, A. Lappas, M. Giot, J. W. Taylor, M. A. Green, C. M. Brown, and P. G. Radaelli, Phys. Rev. Lett. **103**, 077202 (2009).

[192] M. B. Stone, Y. Chen, J. Rittner, H. Yardimci, D. H. Reich, C. Broholm, D. V. Ferraris, and T. Lectka, Phys. Rev. B **65**, 064423 (2002).

[193] M. Matsumoto, J. Phys. Soc. Jpn. **90**, 014701 (2021).

[194] M. Songvilay, J. Robert, S. Petit, J. A. Rodriguez-Rivera, W. D. Ratcliff, F. Damay, V. Balédent, M. Jiménez-Ruiz, P. Lejay, E. Pachoud, A. Hadj-Azzem, V. Simonet, and C. Stock, Phys. Rev. B **102**, 224429 (2020).

[195] M. Songvilay, S. Petit, F. Damay, G. Roux, N. Qureshi, H. C. Walker, J. A. Rodriguez-Rivera, B. Gao, S.-W. Cheong, and C. Stock, Phys. Rev. Lett. **126**, 017201 (2021).

[196] R. A. Cowley, J. Phys.: Condens. Matter **15**, 4143 (2003).

[197] C. Stock, R. A. Cowley, J. W. Taylor, and S. M. Bennington, Phys. Rev. B **81**, 024303 (2010).

[198] S. Toth and B. Lake, J. Phys. Condens. Matter **27**, 166002 (2015).

[199] J. S. Smart, *Effective field theories of magnetism* (Saunders, Philadelphia, 1966).

[200] P. M. Sarte, M. Songvilay, E. Pachoud, R. A. Ewings, C. D. Frost, D. Prabhakaran, K. H. Hong, A. J. Browne, Z. Yamani, J. P. Attfield, E. E. Rodriguez, S. D. Wilson, and C. Stock, Phys. Rev. B **100**, 075143 (2019).

[201] H. Lane, E. Pachoud, J. A. Rodriguez-Rivera, M. Songvilay, G. Xu, P. M. Gehring, J. P. Attfield, R. A. Ewings, and C. Stock, Phys. Rev. B **104**, L020411 (2021).

[202] H. Lane, E. E. Rodriguez, H. C. Walker, Ch. Niedermayer, U. Stuhr, R. I. Bewley, D. J. Voneshen, M. A. Green, J. A. Rodriguez-Rivera, P. Fouquet, S.-W. Cheong, J. P. Attfield, R. A. Ewings, and C. Stock, Phys. Rev. B **104**, 104404 (2021).

[203] H. Lane, M. Songvilay, R. A. Ewings, and C. Stock, Phys. Rev. B **106**, 054431 (2022).

[204] Y. Wang, C. Xian, J. Wang, B. Liu, L. Ling, L. Zhang, L. Cao, Z. Qu, and Y. Xiong, Phys. Rev. B **96**, 134428 (2017).

[205] Y. Liu, E. Stavitski, K. Attenkofer, and C. Petrovic, Phys. Rev. B **97**, 165415 (2018).

[206] Y. Deng, Y. Yu, Y. Song, J. Zhang, N. Z. Wang, Z. Sun, Y. Yi, Y. Z. Wu, S. Wu, J. Zhu, J. Wang, X. H. Chen, and Y. Zhang, Nature **563**, 94 (2018).

[207] B. Chen, J. Yang, H. Wang, M. Imai, H. Ohta, C. Michioka, K. Yoshimura, and M. Fang, J. Phys. Soc. Jpn. **82**, 124711 (2013).

[208] H. L. Zhuang, P. R. C. Kent, and R. G. Hennig, Phys. Rev. B **93**, 134407 (2016).

[209] Y.-P. Wang, X.-Y. Chen, and M.-Q. Long, App. Phys. Lett. **116**, 092404 (2020).

[210] Z. Fei, B. Huang, P. Malinowski, W. Wang, T. Song, J. Sanchez, W. Yao, D. Xiao, X. Zhu, A. F. May, W. Wu, D. H. Cobden, J.-H. Chu, and X. Xu, Nat. Mater. **17**, 778 (2018).

[211] X. Wang, J. Tang, X. Xia, C. He, J. Zhang, Y. Liu, C. Wan, C. Fang, C. Guo, W. Yang, Y. Guang, X. Zhang, H. Xu, J. Wei, M. Liao, X. Lu, J. Feng, X. Li, Y. Peng, H. Wei, et al., Sci. Adv. **5**, eaaw8904 (2019).

[212] A. F. May, S. Calder, C. Cantoni, H. Cao, and M. A. McGuire, Phys. Rev. B **93**, 014411 (2016).

[213] V. Y. Verchenko, A. A. Tsirlin, A. V. Sobolev, I. A. Presniakov, and A. V. Shevelkov, Inorg. Chem. **54**, 8598 (2015).

[214] X. Kong, G. D. Nguyen, J. Lee, C. Lee, S. Calder, A. F. May, Z. Gai, A.-P. Li, L. Liang, and T. Berlijn, Phys. Rev. Mat. **4**, 094403 (2020).

[215] J. Yi, H. Zhuang, Q. Zou, Z. Wu, G. Cao, S. Tang, S. A. Calder, P. R. C. Kent, D. Mandrus, and Z. Gai, 2D Mater. **4**, 011005 (2016).

[216] S. W. Jang, H. Yoon, M. Y. Jeong, S. Ryee, H.-S. Kim, and M. J. Han, Nanoscale **12**, 13501 (2020).

[217] X. Xu, Y. W. Li, S. R. Duan, S. L. Zhang, Y. J. Chen, L. Kang, A. J. Liang, C. Chen, W. Xia, Y. Xu, P. Malinowski, X. D. Xu, J.-H. Chu, G. Li, Y. F. Guo, Z. K. Liu, L. X. Yang, and Y. L. Chen, Phys. Rev. B **101**, 201104 (2020).

[218] S. Calder, A. I. Kolesnikov, and A. F. May, Phys. Rev. B **99**, 094423 (2019).

[219] S. Bao, W. Wang, Y. Shangguan, Z. Cai, Z.-Y. Dong, Z. Huang, W. Si, Z. Ma, R. Kajimoto, K. Ikeuchi, S.-i. Yano, S.-L. Yu, X. Wan, J.-X. Li, and J. Wen, Phys. Rev. X **12**, 011022 (2022).

[220] C. Stock, N. Ayape Katcho, E. Chan, O. R. Fabelo Rosa, H. Lane, E. Pachoud, and N. Qureshi, The nuclear structure of CVT grown Fe3-xGeTe2 (2021), type: dataset.

[221] H. Lane, *From Local Degrees of Freedom to Correlated States in Anisotropic 3d Transition Metal Compounds*, Ph.D. thesis (2022).

[222] P. Gambardella, S. Rusponi, M. Veronese, S. S. Dhesi, C. Grazioli, A. Dallmeyer, I. Cabria, R. Zeller, P. H. Dederichs, K. Kern, C. Carbone, and H. Brune, Science **300**, 1130 (2003).

[223] Y. Kamihara, T. Watanabe, M. Hirano, and H. Hosono, J. Am. Chem. Soc. **130**, 3296 (2008).

[224] J. W. Lynn and P. Dai, Phys. C: Supercond. **469**, 469 (2009).

[225] D. C. Johnston, Adv. Phys. **59**, 803 (2010).

[226] J. Paglione and R. L. Greene, Nature Phys. **6**, 645 (2010).

[227] A. Chubukov and P. J. Hirschfeld, Phys. Today **68**, 46 (2015).

[228] R. M. Fernandes, A. I. Coldea, H. Ding, I. R. Fisher, P. J. Hirschfeld, and G. Kotliar, Nature **601**, 35 (2022).

[229] S. Li, C. de la Cruz, Q. Huang, Y. Chen, J. W. Lynn, J. Hu, Y.-L. Huang, F.-C. Hsu, K.-W. Yeh, M.-K. Wu, and P. Dai, Phys. Rev. B **79**, 054503 (2009).

[230] Y. Mizuguchi, F. Tomioka, S. Tsuda, T. Yamaguchi, and Y. Takano, App. Phys. Lett. **94**, 012503 (2009).

[231] B. C. Sales, A. S. Sefat, M. A. McGuire, R. Y. Jin, D. Mandrus, and Y. Mozharivskyj, Phys. Rev. B **79**, 094521 (2009).

[232] E. E. Rodriguez, C. Stock, P.-Y. Hsieh, N. P. Butch, J. Paglione, and M. A. Green, Chem. Sci. **2**, 1782 (2011).

[233] P. Babkevich, M. Bendele, A. T. Boothroyd, K. Conder, S. N. Gvasaliya, R. Khasanov, E. Pomjakushina, and B. Roessli, J. Phys.Cond. Matter **22**, 142202 (2010).

[234] M. Bendele, P. Babkevich, S. Katrych, S. N. Gvasaliya, E. Pomjakushina, K. Conder, B. Roessli, A. T. Boothroyd, R. Khasanov, and H. Keller, Phys. Rev. B **82**, 212504 (2010).

[235] Y. Sun, T. Yamada, S. Pyon, and T. Tamegai, Sci. Rep. **6**, 32290 (2016).

[236] E. E. Rodriguez, C. Stock, P. Zajdel, K. L. Krycka, C. F. Majkrzak, P. Zavalij, and M. A. Green, Phys. Rev. B **84**, 064403 (2011).

[237] S. Rößler, D. Cherian, W. Lorenz, M. Doerr, C. Koz, C. Curfs, Yu. Prots, U. K. Rößler, U. Schwarz, S. Elizabeth, and S. Wirth, Phys. Rev. B **84**, 174506 (2011).

[238] I. A. Zaliznyak, Z. J. Xu, J. S. Wen, J. M. Tranquada, G. D. Gu, V. Solovyov, V. N. Glazkov, A. I. Zheludev, V. O. Garlea, and M. B. Stone, Phys. Rev. B **85**, 085105 (2012).

[239] C. Stock, E. E. Rodriguez, P. Bourges, R. A. Ewings, H. Cao, S. Chi, J. A. Rodriguez-Rivera, and M. A. Green, Phys. Rev. B **95**, 144407 (2017).

[240] W. Bao, Y. Qiu, Q. Huang, M. A. Green, P. Zajdel, M. R. Fitzsimmons, M. Zhernenkov, S. Chang, M. Fang, B. Qian, E. K. Vehstedt, J. Yang, H. M. Pham, L. Spinu, and Z. Q. Mao, Phys. Rev. Lett. **102**, 247001 (2009).

[241] D. Parshall, G. Chen, L. Pintschovius, D. Lamago, Th. Wolf, L. Radzihovsky, and D. Reznik, Phys. Rev. B **85**, 140515 (2012).

[242] E. E. Rodriguez, D. A. Sokolov, C. Stock, M. A. Green, O. Sobolev, J. A. Rodriguez-Rivera, H. Cao, and A. Daoud-Aladine, Phys. Rev. B **88**, 165110 (2013).

[243] C. Trainer, C. M. Yim, C. Heil, F. Giustino, D. Croitori, V. Tsurkan, A. Loidl, E. E. Rodriguez, C. Stock, and P. Wahl, Sci. Adv. **5**, eaav3478 (2019).

[244] C. Trainer, M. Songvilay, N. Qureshi, A. Stunault, C. M. Yim, E. E. Rodriguez, C. Heil, V. Tsurkan, M. A. Green, A. Loidl, P. Wahl, and C. Stock, Phys. Rev. B **103**, 024406 (2021).

[245] C. Stock, E. Chan, A. Stunault, and R. Travers, Neutron polarimetry study of the spin density wave phase in Fe1+xTe (2021), type: dataset.

[246] U. Stuhr, B. Roessli, S. Gvasaliya, H. M. Rønnow, U. Filges, D. Graf, A. Bollhalder, D. Hohl, R. Bürge, M. Schild, L. Holitzner, C. Kaegi, P. Keller, and T. Mühlebach, Nucl. Instrum. Methods Phys. Res. A **853**, 16 (2017).

[247] M. McGuire, Crystals **7**, 121 (2017).

[248] M. A. McGuire, H. Dixit, V. R. Cooper, and B. C. Sales, Chem. Mater. **27**, 612 (2015).

[249] W.-B. Zhang, Q. Qu, P. Zhu, and C.-H. Lam, J. Mater. Chem. C **3**, 12457 (2015).

[250] H. Wang, F. Fan, S. Zhu, and H. Wu, Europhys. Lett. **114**, 47001 (2016).

[251] J. L. Lado and J. Fernández-Rossier, 2D Mater. **4**, 035002 (2017).

[252] S. Jiang, L. Li, Z. Wang, K. F. Mak, and J. Shan, Nat. Nanotechnol. **13**, 549 (2018).

[253] D. R. Klein, D. MacNeill, J. L. Lado, D. Soriano, E. Navarro-Moratalla, K. Watanabe, T. Taniguchi, S. Manni, P. Canfield, J. Fernández-Rossier, and P. Jarillo-Herrero, Science **360**, 1218 (2018).

[254] N. Sivadas, S. Okamoto, X. Xu, Craig. J. Fennie, and D. Xiao, Nano Lett. **18**, 7658 (2018).

[255] K. O. Berry, R. R. Smardzewski, and R. E. McCarley, Inorg. Chem. **8**, 1994 (1969).

[256] D. Juza, D. Giegling, and H. Schäfer, Z. Anorg. Allg. Chem. **366**, 121 (1969).

[257] J. He, S. Ma, P. Lyu, and P. Nachtigall, J. Mater. Chem. C **4**, 2518 (2016).

[258] S. Son, M. J. Coak, N. Lee, J. Kim, T. Y. Kim, H. Hamidov, H. Cho, C. Liu, D. M. Jarvis, P. A. C. Brown, J. H. Kim, C.-H. Park, D. I. Khomskii, S. S. Saxena, and J.-G. Park, Phys. Rev. B **99**, 041402 (2019).

[259] S. Tian, J.-F. Zhang, C. Li, T. Ying, S. Li, X. Zhang, K. Liu, and H. Lei, J. Am. Chem. Soc. **141**, 5326 (2019).

[260] T. Kong, K. Stolze, E. I. Timmons, J. Tao, D. Ni, S. Guo, Z. Yang, R. Prozorov, and R. J. Cava, Adv. Mat. **31**, 1808074 (2019).

[261] P. Doležal, M. Kratochvílová, V. Holý, P. Čermák, V. Sechovský, M. Dušek, M. Míšek, T. Chakraborty, Y. Noda, S. Son, and J.-G. Park, Phys. Rev. Mat. **3**, 121401 (2019).

[262] T. Marchandier, N. Dubouis, F. Fauth, M. Avdeev, A. Grimaud, J.-M. Tarascon, and G. Rousse, Phys. Rev. B **104**, 014105 (2021).

[263] E. Gati, Y. Inagaki, T. Kong, R. J. Cava, Y. Furukawa, P. C. Canfield, and S. L. Bud'ko, Phys. Rev. B **100**, 094408 (2019).

[264] Y. Liu, M. Abeykoon, and C. Petrovic, Phys. Rev. Research **2**, 013013 (2020).

[265] A. Koriki, M. Míšek, J. Pospíšil, M. Kratochvílová, K. Carva, J. Prokleška, P. Doležal, J. Kaštil, S. Son, J.-G. Park, and V. Sechovský, Phys. Rev. B **103**, 174401 (2021).

[266] Y. Hao, Y. Gu, Y. Gu, E. Feng, H. Cao, S. Chi, H. Wu, and J. Zhao, Chin. Phys. Lett. **38**, 096101 (2021).

[267] K. Yang, F. Fan, H. Wang, D. I. Khomskii, and H. Wu, Phys. Rev. B **101**, 100402 (2020).

[268] G.-D. Zhao, X. Liu, T. Hu, F. Jia, Y. Cui, W. Wu, M.-H. Whangbo, and W. Ren, Phys. Rev. B **103**, 014438 (2021).

[269] Z. Zhou, S. K. Pandey, and J. Feng, Phys. Rev. B **103**, 035137 (2021).

[270] C. Huang, F. Wu, S. Yu, P. Jena, and E. Kan, Phys. Chem. Chem. Phys. **22**, 512 (2020).

[271] D. Hovančík, J. Pospíšil, K. Carva, V. Sechovský, and C. Piamonteze, Nano Lett. **23**, 1175 (2023).

[272] M. Bartkowiak, J. S. White, H. M. Rønnow, and K. Prša, Rev. Sci. Instrum. **85**, 026112 (2014).

[273] A. Pimenov, A. A. Mukhin, V. Y. Ivanov, V. D. Travkin, A. M. Balbashov, and A. Loidl, Nat. Phys. **2**, 97 (2006).

[274] L. Chaix, S. de Brion, F. Lévy-Bertrand, V. Simonet, R. Ballou, B. Canals, P. Lejay, J. B. Brubach, G. Creff, F. Willaert, P. Roy, and A. Cano, Phys. Rev. Lett. **110**, 157208 (2013).